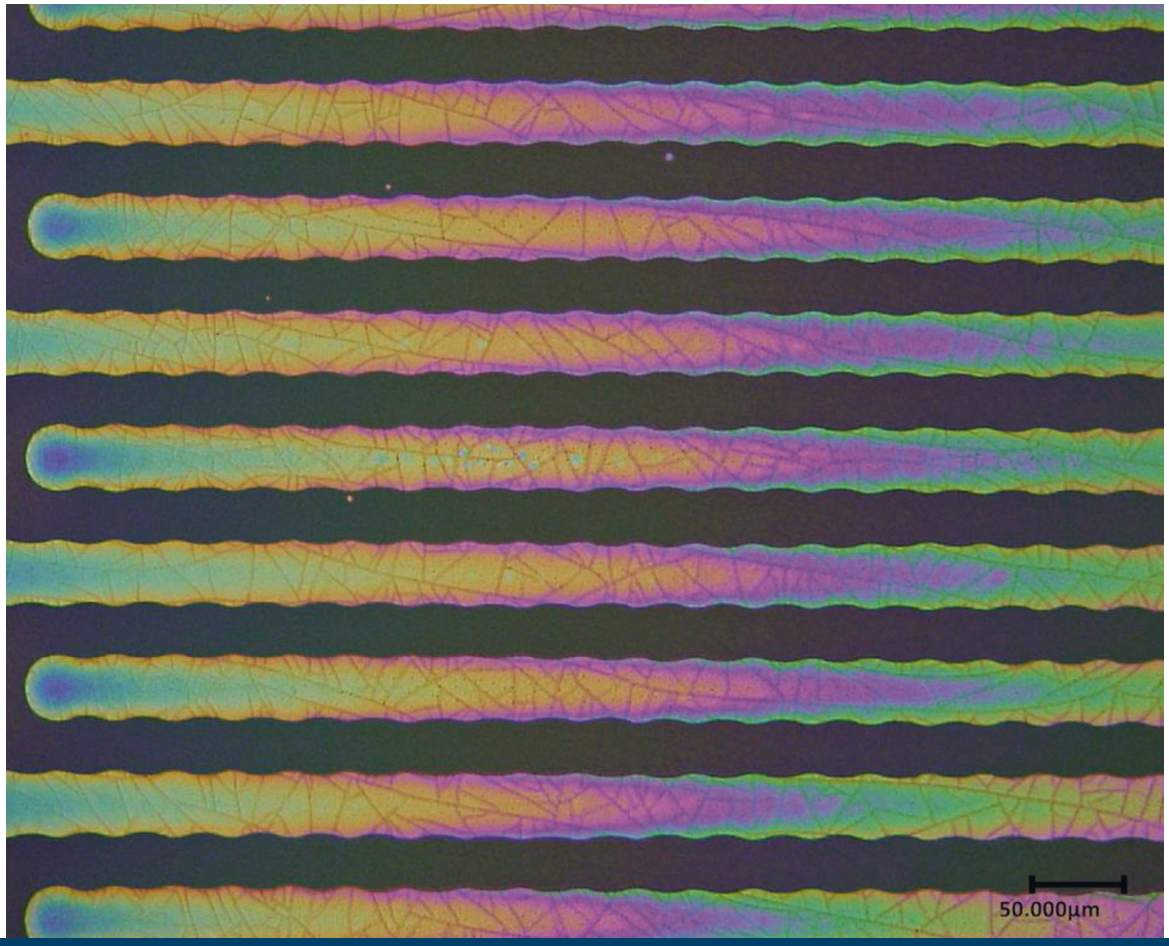

Development of a New, Miniaturized and Flexible Temperature Sensor

Stefanie Hamacher

Schlüsseltechnologien / Key Technologies
Band / Volume 303
ISBN 978-3-95806-863-6

Mitglied der Helmholtz-Gemeinschaft

JÜLICH
Forschungszentrum

Schriften des Forschungszentrums Jülich
Reihe Schlüsseltechnologien / Key Technologies Band / Volume 303

Forschungszentrum Jülich GmbH
Institut für Biologische Informationsprozesse (IBI)
Bioelektronik (IBI-3)

Development of a New, Miniaturized and Flexible Temperature Sensor

Stefanie Hamacher

Schriften des Forschungszentrums Jülich
Reihe Schlüsseltechnologien / Key Technologies Band / Volume 303

ISSN 1866-1807 ISBN 978-3-95806-863-6

Bibliografische Information der Deutschen Nationalbibliothek.
Die Deutsche Nationalbibliothek verzeichnet diese Publikation in der
Deutschen Nationalbibliografie; detaillierte Bibliografische Daten
sind im Internet über http://dnb.d-nb.de abrufbar.

Herausgeber und Vertrieb:	Forschungszentrum Jülich GmbH Zentralbibliothek, Verlag 52425 Jülich Tel.: +49 2461 61-5368 Fax: +49 2461 61-6103 zb-publikation@fz-juelich.de www.fz-juelich.de/zb
Umschlaggestaltung:	Grafische Medien, Forschungszentrum Jülich GmbH
Druck:	Grafische Medien, Forschungszentrum Jülich GmbH
Copyright:	Forschungszentrum Jülich 2025

Schriften des Forschungszentrums Jülich
Reihe Schlüsseltechnologien / Key Technologies, Band / Volume 303

D 82 (Diss. RWTH Aachen University, 2025)

ISSN 1866-1807
ISBN 978-3-95806-863-6

Vollständig frei verfügbar über das Publikationsportal des Forschungszentrums Jülich (JuSER)
unter www.fz-juelich.de/zb/openaccess.

Eidesstattliche Erklärung

Stefanie Hamacher
erklärt hiermit, dass diese Dissertation und die darin dargelegten Inhalte die eigenen sind und selbstständig, als Ergebnis der eigenen originären Forschung, generiert wurden.
Hiermit erkläre ich an Eides statt

1. Diese Arbeit wurde vollständig oder größtenteils in der Phase als Promovierender dieser Fakultät und Universität angefertigt;

2. Sofern irgendein Bestandteil dieser Dissertation zuvor für einen akademischen Abschluss oder eine andere Qualifikation an dieser oder einer anderen Institution verwendet wurde, wurde dies klar angezeigt;

3. Wenn immer andere eigene- oder Veröffentlichungen Dritter herangezogen wurden, wurden diese klar benannt;

4. Wenn aus anderen eigenen- oder Veröffentlichungen Dritter zitiert wurde, wurde stets die Quelle hierfür angegeben. Diese Dissertation ist vollständig meine eigene Arbeit, mit der Ausnahme solcher Zitate;

5. Alle wesentlichen Quellen von Unterstützung wurden benannt;

6. Wenn immer ein Teil dieser Dissertation auf der Zusammenarbeit mit anderen basiert, wurde von mir klar gekennzeichnet, was von anderen und was von mir selbst erarbeitet wurde;

7. Ein Teil oder Teile dieser Arbeit wurden zuvor veröffentlicht und zwar als Deutsche Patentanmeldung 102019004120.8 „Sensoranordnung, Verfahren zur Herstellung sowie Verwendung der Sensoranordnung"

20.10.2025

Stefanie Hamacher

It always seems impossible, until it is done.
Nelson Mandela

Für Uli, Sue, Tina und Saskia
Danke dafür, dass ihr das *Unmögliche* möglich erscheinen ließt.

Abstract

Temperature is one of the most important scientific quantities and plays a fundamental part in our daily life. While permanent temperature sensors were primarily used to control air conditioning, fridges and freezers, nowadays they are utilized in many more fields, such as healthcare, manufacturing and agriculture. Over the centuries several different devices were developed that were able to determine changes in temperature. In the beginning, such a thermometer was simply based on the expansion and contraction of air or water and the dilation of liquids is still in use in the common mercury thermometer. However, many more devices are known today that are based on the change of different physical quantities that can be related to temperature. Common examples are the change in resistance used in resistance temperature detectors (RTDs) or thermistors or the change in spectral characteristics detected via IR measurements. Depending on the purpose of the temperature measurement an appropriate technique is chosen, since all of the known devices have their advantages and drawbacks, e.g. a small temperature range or low relative change of the specific parameter per degree. To overcome such drawbacks, a miniaturized temperature sensor based on a new approach was developed in this work. As a sensing principle, the dependence of the diffusion coefficient on fluid viscosity, which in turn is temperature dependent, was exploited. Using Faradaic electrochemical currents from a redox mediator dissolved in fluid, a relation between current and temperature can be obtained. Here, three different ionic liquids (ILs) and mixtures of them were investigated along with different redox species, such as ferrocene, hydroquinone and methylene blue to establish a stable temperature sensor that is suitable over a large temperature range and shows long-term stability. Several thin-film sensor prototypes were fabricated and characterized using custom-made electronics as well as a potentiostat. First, the peak current dependence on temperature using cyclic voltammetry (CV) was demonstrated. Afterwards a screening of the most feasible redox species was conducted using CV. Thereby it was found that ferrocene is not stable over a longer period of time, which is why other redox couples were examined and methylene blue was found to be the best. Additionally, the IL 1-ethylimidazolium nitrate ([EIM][NO3]) was used as redox species and solvent medium simultaneously. In order to establish an easy to handle sensor, the sensitive layer had to be fixed upon the substrate. This was achieved by adding two monomers and a photo initiator to the IL mixture that were cured using UV light. Finally, the prepared temperature sensors were characterized using the chronoamperometric technique and four different pulse lengths. Compared to standard resistance temperature detectors, this novel sensor shows a higher per degree sensitivity and can be utilized in a broad temperature range, for example for cold-chain monitoring of perishables.

Zusammenfassung

Die Temperatur ist eine der wichtigsten naturwissenschaftlichen Größen und spielt eine essenzielle Rolle in unserem täglichen Leben. Das Einsatzgebiet von permanent messenden Temperatursensoren hat sich in den letzten Jahren stark erweitert. In der Klimatechnik sowie in Kühl- und Gefrierschränken werden solche Sensoren schon lange eingesetzt, während ihr Einsatz im Gesundheitswesen, in industriellen Herstellungsprozessen und der Landwirtschaft erst in der jüngeren Vergangenheit Einzug gehalten hat. Über die Jahrhunderte hinweg wurden viele unterschiedliche Geräte entwickelt, die in der Lage sind, die Änderung der Temperatur zu messen. Anfangs wurde die Temperaturmessung durch die Ausbreitung bzw. Kontraktion von Luft oder Wasser bestimmt und auch heutzutage wird dieses Prinzip in Quecksilberthermometern noch genutzt. Jedoch gibt es mittlerweile eine ganze Reihe weiterer Geräte, die unterschiedliche physikalische Größen nutzen, um Temperaturmessungen durchzuführen. Bekannt sind vor allem Widerstandsthermometer, so genannte RTDs, oder auch Thermistoren, die eine Änderung des Widerstands in Relation zur Temperatur setzen sowie Geräte, die auf Thermographie, z.B. Wärmebildkameras, basieren und die Änderung der spektralen Charakteristika durch IR-Messung sichtbar machen. Welche Art von Thermometer eingesetzt wird, hängt in erster Linie davon ab, was und wie genau gemessen werden soll, denn alle bekannten Techniken haben ihre Vor- und Nachteile, wie beispielsweise einen geringen Temperaturbereich oder eine relativ kleine Änderung des gerätespezifischen Parameters pro Grad Celsius. Um diese Nachteile zu umgehen, wurde in dieser Arbeit ein miniaturisierter Temperatursensor, basierend auf einem neuen Arbeitsprinzip, entwickelt. Als Sensorprinzip wurde die Abhängigkeit des Diffusionskoeffizienten von der Viskosität von Flüssigkeiten verwendet. Die Viskosität ist wiederum abhängig von der Temperatur. Diese Abhängigkeit wurde durch den Einsatz von in Flüssigkeit gelösten Redox-Mediatoren, die anschließend elektrochemisch vermessen wurden, gezeigt. In diesem speziellen Fall wurden drei unterschiedliche ionische Flüssigkeiten (ILs) sowie Mischungen aus diesen verwendet. Zusätzlich wurden verschiedene Redox Spezies, wie z.B. Ferrocen, Hydroquinon und Methylenblau, getestet, um einen stabilen Temperatursensor zu entwickeln, der über einen großen Temperaturbereich funktioniert und langzeitstabil ist. Dazu wurden mehrere Dünnschicht Prototyp-Sensoren hergestellt und mithilfe von Custom-made Elektronik bzw. Potentiostate charakterisiert. Zunächst wurde mittels Cyclovoltammetrie (CV) die Abhängigkeit des Peakstroms von der Temperatur gezeigt. Um die geeignetste Redox-Spezies zu identifizieren, wurde anschließend ein Screening verschiedener Derivate der o. g. Redox-Spezies mittels CV durchgeführt. Es wurde festgestellt, dass Ferrocen nicht über einen längeren Zeitraum stabil ist und der Sensor nach wenigen Tagen seine Funktionalität verliert, weshalb die anderen Redox-Spezies untersucht wurden. Dabei stellte sich Methylenblau als am besten geeignet heraus. Außerdem wurde eine der eingesetzten ionischen Flüssigkeiten, 1-Ethylimidazolium Nitrat ([EIM][NO3]), gleichzeitig sowohl als Redox-Spezies als auch als Lösungsmittel eingesetzt. Damit der hergestellte Sensor flexibel einsetzbar und gut händelbar ist, musste die temperatursensitive Schicht auf dem Substrat fixiert werden. Dazu wurde eine Mischung aus zwei Monomeren und einem Photoinitiator zur IL-Mischung hinzugegeben. Durch UV-Aktivierung wurde die Polymerisation der Monomere gestartet, wodurch eine auf dem Substrat fixierte Schicht entstand. Letztlich wurde der hergestellte Temperatursensor mittels chronoamperometrischen Messungen bei vier unterschiedlichen Pulslängen charakterisiert.

Verglichen zu Standard RTDs, zeigt dieser Sensor eine größere Sensitivität pro Grad Celsius und kann gleichzeitig über einen großen Temperaturbereich eingesetzt werden, z. B. zur Überwachung der Kühlkette von verderblichen Lebensmitteln.

Contents

List of Figures

List of Tables

List of Abbreviations

acac	Acetylacetone
AD	Anno Domini
BC	Before Christ
BSTO	Barium Strontium Titanate
BTO	Barium Titanate
CV	Cyclic Voltammetry
DMF	N, N-Dimethylformamide
DMSO	Dimethylsulfoxide
EDL	Electrochemical Double Layer
EDX	Energy Dispersive X-Ray Spectroscopy
emf	Electromotive Force
FSE	Fractional Stokes-Einstein
HSP	Hansen Solubility Parameters
ICP-OES	Inductively Coupled Plasma Atomic Emission Spectroscopy
IL	Ionic Liquid
IoT	Internet of Things
MB	Methylene Blue
MEA	Microelectrode Array
NE	Nernst-Einstein
NTC	Negative Temperature Coefficient
PET	Polyethylene Terephthalate
PEN	Polyethylene Naphthalate
PTC	Positive Temperature Coefficient
PTCR	Positive Temperature Coefficient of Resistance
RTD	Resistance Temperature Detector

SEM Scanning Electron Microscopy

SNR Signal-to-Noise Ratio

STO Strontium Titanate

TEM Transmission Electron Microscopy

THF Tetrahydrofuran

VFT Vogel-Fulcher-Tamman

WE Working Electrode

XRD X-Ray Diffraction

1 Introduction

Nowadays, sensors have improved our daily life significantly in almost every field, e.g. health care, manufacturing processes and smart homes. A sensor is a device that detects changes in its environment and formulates a respective meaningful response. Thereby, the general working principle is always the same: starting with a change in a physical quantity, such as pressure, mass, temperature, humidity, that is then detected by a sensor and converted into an electric signal, e.g. voltage, current, frequency, which is recorded, read out or further processed [1].
In the last ten years (2011 - 2021) the global sensors market showed an extraordinary growth from US$ 62 billion in 2011 to over US$ 190 billion in 2021 [2]. These numbers give an impression about how many different sensors are available at the market. Level sensors, for example, are important in industrial and consumer markets and are mostly based on optical detection methods [1, 3, 4]. Pressure sensors are another type which are commonly used, for example in maintenance of complete water and heating systems. Furthermore, they enable the creation of IoT (Internet of Things) systems that monitor pressure driven devices such as airbags in cars [1, 5]. Infrared (IR) sensors are also widely used, especially in the field of biomedical and healthcare applications to monitor the blood flow and blood pressure or to detect heat radiation of objects. Due to the latter they are also deployed in environmental monitoring [1]. There are quite a number of different sensors types available nowadays, which are mentioned and described in the review of *Javaid et. al* [1] and as can be seen each quantity (e.g. pressure, temperature etc.) can be determined by a number of different techniques.
While IR is a relatively modern way of measuring temperature, the first thermometers were based on the dilatation of matter, although the actual definition of temperature itself was developed along the thermometers over the centuries. *Max Planck* (1858 - 1947) made a quite simple definition around 1900: "Temperature is defined as the degree of hotness or coldness of a body" [6, 7]. However, to give an exact definition of *temperature* was a task on which many scientists worked over the centuries.

Besides time, temperature is probably the most measured quantity and a fundamental part of our life. The concept of temperature is most important and ever present in the biological, physical and chemical world. Depending on the temperature of the air, we choose our clothing appropriately. If we are sick our body temperature increases, and if it increases too much it might become life threatening. Then, there are things we should not touch with our bare hands because they are just too hot or too cold. The processing and manufacturing of certain materials require a special temperature to be successful, e.g. the forging of metal. Nowadays we are well aware of the fact that the temperature in the universe is around 4 K (-269°C), while the temperature of the star *Vega* is on its surface around 9.602 K (9.329 °C). All of this was true (although not always known) long before we were able to develop thermometers and temperature sensors to measure temperature very precisely.
So it is not surprising that already the ancient Greeks in the second century BC knew that air expands if it is heated and contracts if it is cooled. In this way *Philo of Byzantium* conducted the first temperature measurement experiments and constructed a kind of thermoscope. A thermoscope is a device consisting of a glass bulb and a long tube. The tube is connected to a jug of water and connected with the glass bulb which is filled with air. If the bulb is placed in the sun,

the temperature of the air is increased and thereby expands, bubbles can be observed inside the water jug. Contrary, if the bulb is then moved into the shade, the tube gets filled with water due to the contraction of the air. However, there was no scale as such on the thermoscope which made it impossible to measure the temperature change quantitatively. Moreover, the thermoscope was an open system which means that the change of the liquid level inside the tube was also dependent on the barometric pressure. Additionally, the expansion or contraction of the liquid itself was neglected at this time [6]. So, the first "thermometer" was more like a barometer, but it also was the base for further development in this regard.

Almost 2000 years later, in the beginning of the 17^{th} century, *Galileo* and *Fludd* developed independently from each other, another version of the thermoscope. While *Galileo's* experiments are based on the work of *Heron of Alexandria* (10 AD - ca. 70 AD) and were conducted in or before 1603, *Fludd* used the manuscript of *Philo of Byzantium* some years later. The main contribution of *Fludd* comprises the more practical arrangement of the air bulb and the water jug. Instead of using a bent tube connecting the water jug and the air filled sphere, he arranged everything vertically [6]. In the following years, many such thermoscopes were developed, however, none of them was calibrated in any way, which made them incomparable with each other. In 1613, *Sagredo* used a thermoscope to investigate the temperature of several lakes and also measured the temperature difference of the winter snow and the summer heat. He classified his readings as *degrees of heat* and with that used his thermoscope as a "real" thermometer [6]. Since he used for all measurements the same device, the recorded data was actually comparable, although the device itself was not calibrated.

The thermometer known as the *Galileo thermometer* was only named after the famous physicist but not invented by him. Literature indicates that either a group of academics, among them one of *Galileo's* students, or the *Grand Duke of Tuscany, Ferdinand II, one of the great family of Medici* were the actual inventors of this specific thermometer [6, 8].

Over the years in the 17^{th} century several scientists invented thermometers and noticed soon that they need to define fixed points of temperature to make them more accurate. In 1632, the first big improvement of *Galileo's* air-based thermoscope was achieved by the French physician, *Jean Rey*, who just inverted the usage of air and water. Thus, water was now rising or sinking in the tube due to temperature changes and expansion/contraction effects [9]. However, also *Rey's* version of a thermometer was an open system which resulted in a lot of inaccuracy due to the evaporation of water as well as the change in barometric pressure. Another 25 years passed until the first sealed-in, liquid-in-glass thermometer was invented. This also was the first time something like a scale was fused onto the tube, although this scale was dependent on the geometry of the device itself, which again caused the problem that the thermometer was not reproducible. So, instead of using the properties of the device, scientists came to the conclusion it would be more feasible to use two fixed points of temperature and divide the space between them into equidistant parts [9]. However, which temperatures were suitable as fixed points and which were not, varied a lot over the years. Some of them used the cold of winter and the heat of summer, others used only either the freezing point of water or its boiling point, not realizing that they needed two points. Still others used the temperature of the human blood or the body temperature of cows and deer.

In 1714, *Daniel Fahrenheit* invented the nowadays well-known mercury thermometer as well as an alcohol thermometer. Finally, in 1724, he used an ice-water mixture with salammonic or sea salt and defined this temperature point as 0. The pure mixture of water and ice obtained a temperature of 32° according to him, while the alcohol of his thermometer expanded to 96° if held into the mouth or under the armpit of a healthy person. Dividing the distance between these three points into equal parts resulted in the Fahrenheit scale that is used until today in the US [9]. Several years later, in 1742, the Swedish astronomer *Andreas Celsius* defined the boiling point

of water as 0° and the freezing point of water as 100°. He subdivided the distance between these points in 100 parts. Although the temperature scale used in Germany and Europa is named after Celsius, the scale we know was defined by a colleague of Celsius, *Märten Strömer*, who inverted the two fixed points so that the freezing point of water is 0°C and the boiling point accounts for 100°C [9, 10].
Already in 1702, *Guillaume Amontons* suggested that there is a lower limit below which temperature can never fall. According to his data this temperature lied around -239.5°. *Lambert* repeated *Amonton's* experiments with more accuracy and obtained a value of -270.3° [9]. Again many years passed, when in the beginning of the 19^{th} century, *Wiliam Thomas* (later *Lord Kelvin*) took up this topic and published 1848 his paper *On an Absolute Thermometric Scale* in which he estimated the almost correct value of the absolute zero, -273°C, and used the degree Celsius as its unit increment. Until 2019, the absolute zero was defined as the triple point of water - there, liquid water, ice and water steam are coexisting at a pressure of 0.006 bar - at 273.16 K or 0.01 °C [11]. To honor *Kelvin's* work the absolute thermodynamical temperature scale is named after him and is used today as the standard temperature scale in science [6, 10]. However, also the triple point of water has its disadvantages as exact definition since it depends on the isotopic composition of the water under investigation. This led to the adoption of a new definition based on the fixed numerical value of the *Boltzmann constant k*, which is $1.380\ 649 \cdot 10^{-23}$ J/K and equals to kg m^2 s^{-2} K^{-1}, where the kilogram, meter and second are defined in terms of the Planck constant *h*, the speed of light in vacuum *c* and the unperturbed ground state hyperfine transition frequency of the caesium 133 atom $\Delta\nu_{Cs}$ [12, 13]. This system was chosen because the natural constants, such as the *Planck constant* or *Boltzmann constant*, are today the most precisely determined values which will only change if our way of determining them becomes even more accurate than it is now.

As derived in the previous section, *Lord Kelvin* established the absolute thermodynamical temperature scale which already indicates that the science of thermodynamics is the base to achieve an exact definition of temperature. Considering the simple definition of *Max Planck* and extend it by its relation to energy one gets a simple, qualitative definition: temperature can be considered to be the level of thermal energy [6]. However, measuring the level of thermal energy, i.e. temperature, is not a trivial task, although temperature is one of the fundamental units (base units) of science. Furthermore, it cannot be measured directly, which makes it necessary to obtain the change of other physical phenomena that are related to temperature, e.g. resistance, volumetric expansion or spectral characteristics. Since temperature measurements are important in many fields, e.g. medicine and health care, various manufacturing and industrial processes as well as smart agriculture and the food industry to guarantee high quality, a wide range of different measurement techniques and devices are available [14, 15]. The most common ones will be described in chapter 2.1.
Nowadays, in many applications and processes it is necessary to detect even the slightest temperature changes at the level of a few tens of millikelvin. Therefore, a wide variety of temperature sensors are available, all based on different detection mechanisms and combining attributes such as sensitivity, range, precision, time response, spatial resolution, stability, degree of interference and processability to a different degree [16, 17].

The aim of this thesis is the development of a flexible temperature sensor that shows a high enough sensitivity and is stable over a wide temperature range to allow the use of low-power Internet of Things (IoT) applications. Such a sensor would dismiss many of the drawbacks that current temperature measurement devices exhibit. Several state of the art temperature sensors are introduced in chapter 2.1. All of them rely on different working principles, e.g. a change

in resistance, expansions of fluids or a change in color with thermal energy. The most common temperature sensor is the mercury thermometer that uses the dilation of mercury with increasing temperature. However, nowadays the mercury is replaced by other liquids such as alcohols or ionic liquids [18]. Thermistors and thermocouples are electronic temperature sensors which use the change in resistance or voltage, respectively, to monitor changes in temperature. However, all of those sensors show drawbacks such as a restriction in shape and size, no recording of temperature and either a small temperature range or a low relative change in a certain parameter per degree. Due to the last point usually high-end devices are needed to measure small temperature changes.
To address these problems, a new, flexible and miniaturized temperature sensor was developed. Using Faradaic electrochemical currents from a redox couple dissolved in an IL or using a pure IL as redox molecule, a relation between current and temperature could be obtained. Compared to standard RTDs this novel sensor shows a higher per degree sensitivity and can be utilized in a broad temperature range depending on the IL chosen. The measurement principle is based on the change of viscosity with temperature and correlated to that with the diffusion of redox active molecules through the IL yielding higher currents at elevated temperatures.
Another attempt was based on barium strontium titanate (BSTO) that shows a quite strong positive temperature coefficient of resistance (PTCR) effect around its Curie Temperature (T_C). In order to use this material for a flexible temperature sensor BSTO nanoparticles were required. Therefore, different sol gel synthesis routes were examined to obtain such nanoparticles and apply them onto a flexible electrode system.
While Chapter 2 provides an overview over the theoretical background relevant to this field, Chapter 3 describes the materials and methods used during this work. Chapter 4 is concerned with the development of a flexible temperature sensor that shows a high enough sensitivity and is stable over a wide temperature range to allow the use of low-power applications. Here, the two approaches, using BSTO or ILs, respectively, as temperature sensitive material, are described in detail. In Chapter 5, the achieved results from the previous chapter concerning the IL approach will be correlated with some physical models, e.g. Stokes-Einstein and Nernst-Einstein. Since these models combine the current measurements and the viscosity measurements, the viscosity data is also presented here. Finally, a summary is given that also provides impulses for further investigations.

2 Fundamentals

This chapter starts with a detailed overview of different, but already well established, measurement techniques to determine temperature. Afterwards, the basics of two different sensor materials and setups which were investigated and improved during this work are described. The two approaches followed the aim to develop a new and flexible temperature sensor that shows a high sensitivity as well as a high stability over a wide temperature regime. The first of these sensors is based on barium strontium titanate (BSTO) that shows a great PTCR effect close to the so called Curie temperature. The second sensor uses the viscosity-dependent diffusion coefficient of fluids, in this case ionic liquids (ILs), to measure temperature. Both materials are not new by themselves, but the application setup for measuring temperature is. This includes the usage of microelectrodes which are described at the end of the chapter.

2.1 Overview of Well-Established Techniques to Measure Temperature

Temperature cannot be measured directly, which means that other effects that show a temperature dependence need to be measured and afterwards correlated to temperature. Furthermore, thermometers can also be categorized by the interaction between the thermometer and the medium to be measured. One can differentiate between invasive, semi-invasive and non-invasive techniques. Most techniques described in this chapter belong to the invasive category, since they are most commonly used in science. Among these temperature devices are the typical liquid-in-glass thermometer, thermistors, thermocouples and bimetallic thermometers. All of them have some advantages and disadvantages depending on the planned experiment. However, they also have one drawback which needs to be considered in common. As soon as the device gets in contact with the medium of interest it causes a disturbance of its temperature, mostly due to the fact that the temperature sensor has another temperature as the medium in the beginning. Following this, the temperature of sensor and medium will be equalized due to heat transfer upon contact and therefore change throughout the medium. How large the magnitude of this change will be depends on the temperature difference of sensor and medium before contact. Conclusively, this means the measured value will be different from the actual value and therefore, each temperature measurement will have an error that should be considered during data analysis. However, the disturbance of the temperature due to the immersion of the sensor is not the only source for errors or inaccuracy. Even if the sensor and medium are in thermal equilibrium with each other, the measurement itself can be incorrect due to the processing of the data and the fact that the measurement, e.g. change in resistance or rising of a liquid in a glass tube, entails the exchange of energy in order to detect a temperature. In order to make a temperature measurement meaningful the temperature device needs to be calibrated beforehand [7].

2.1.1 Heat Transfer

In order to evaluate a temperature measurement and its possible uncertainties it is important to understand the principles behind both. As already known from the previous section, the different

temperatures of two objects will get equalized over time if the objects are getting in contact with each other. This phenomenon is called heat transfer and can be distinguished into three categories based on the physical mechanism the heat gets transferred: conduction, convection and radiation.

Conduction

If a temperature gradient exists in an object and the temperature equalizes due to collisions between molecules or atoms, this phenomenon is called conduction. Here, the thermal conductivity, a property of the material the object is made of, indicates how fast the heat flow will be and therefore, how fast the equilibrium state can be reached. Thereby, the thermal conductivity is independent of temperature for small temperature regions [7].
It is known that temperature correlates with the kinetic energy, which represents the movement of molecules or atoms within an object. This movement is different for metals, non-metals, liquids and gases and therefore, the thermal conductivity varies greatly. However, one general rule applies for all materials; the energy (temperature) is always transferred from molecules/atoms with high energy to ones with lower energy. In a gas, this transfer occurs due to collisions between molecules. As single molecules are distributed over a certain volume, the density of the gas molecules are quite small so that collisions rarely occur which means gases are bad conductors. In case of a given kinetic energy, light molecules obtain higher velocities and move faster which results in more collisions. Therefore, the thermal conductivity of hydrogen or helium is highest.
In a solid, the atoms are constrained at fixed positions in a crystal lattice and cannot move freely compared to gases. However, with higher temperature (more kinetic energy) the vibration of the atoms around their position increases and yields in the transport of energy through the lattice due to interatomic forces. Solids can generally be distinguished between metals and non-metals. In the case of metals, the freely moving electrons increase the amount of energy that can be transported which makes metals very good conductors (thermal and electrical). These electrons are comparable with gases with respect to the freedom of movement. This means, in metals the conduction consists of two principles, one, the lattice vibrations and second, the movement of electrons, while in non-metals only the former process takes place. Additionally, the impurities and defects in the crystal lattice decrease the diffusion of heat through the solid and reduce therefore its conduction. The nature of liquids lies between gases and solids which means for the process of conduction that the molecules are closely packed as in solids, but the energy transfer occurs due to collisions between molecules. Since the molecules are not constrained to fixed positions within the liquid, the scattering of energy happens randomly [19].
Independent of the exact mechanism, conduction can be described by *Fourier's law* since the rate of heat flow is always proportional to temperature difference:

$$\dot{q}_{cond} = k\ A\ \frac{(T_1 - T_2)}{(X_1 - X_2)}, \tag{2.1}$$

where $\dot{q}$ is the heat conducted per unit time in watts, k is the thermal conductivity of the material in W m^{-1} K^{-1}, A is the cross-sectional area perpendicular to the direction of heat flow and T_1 and T_2 are the temperatures at the positions X_1 and X_2, respectively [7, 19]. As can be seen from equation 2.1, the higher the temperature difference, the higher the heat flow. Following that, the heat transfer is highest at the beginning of contact between two objects and decreases over time if the heat distributes evenly throughout them (and Δ T becomes smaller) [19].

Convection

The second mechanism of heat flow is called convection and consists of two parts. One part is still the conduction (movement on the molecular level), discussed above, extended by the macroscopic movement of the bulk. From a scientific point of view, the convection between a fluid and a solid is of most interest. Considering a solid object immersed into a flowing liquid, the heat transfer can be described as follows. Close to the surface of the solid object the velocity of the liquid flow is almost zero, while it is almost unaffected at some distance away. This creates a region within the fluid that varies between zero and the natural, macroscopic velocity and is called boundary layer. This layer determines the heat transfer rate from the solid to the liquid. At the surface of the solid the heat is only transferred due to conduction, while farther away the part of the convection processes increases. This can be described by Newton's law of cooling [7, 19]

$$\dot{q} = h\ A\ (T_S - T_\infty) \tag{2.2}$$

Here, T_S represents the temperature at the surface of the solid and T_∞ the temperature of the bulk liquid (beyond the boundary layer). h is comparable to k and denotes the convection heat transfer coefficient in W m^{-2} K^{-1}.

Radiation

The third mode is called radiation and occurs due to the emission of electromagnetic waves by matter. In contrast to the previously described modes of heat transfer, radiation does not require direct physical contact between the objects or a physical medium that transfers heat. The exact mechanism is also based on the vibration of the atoms in an object, but instead of passing the energy through the lattice, the atoms emit photons with a specific energy. This energy is related to the wavelength of the emitted radiation by

$$E = h\ \nu = h\ \frac{c}{\lambda} \tag{2.3}$$

with E = Energy in J
h = Planck constant: $6.626 \cdot 10^{-34}\ Js$
ν = Frequency in s^{-1}
c = Speed of Light: $2.9979 \cdot 10^{8}\ m\ s^{-1}$
λ = Wavelength in m

Equation 2.3 shows that the emitted radiation can range from very long wavelengths (low energy) such as radio waves, microwaves or infrared radiation to very short wavelength (high energy) such as X-rays or γ-rays. Since the energy of an object is also related to temperature it can be concluded that every matter emits radiation as soon as its temperature is above 0 K. This can be described by the Stefan-Boltzmann law [19] :

$$E = \epsilon\ \sigma\ T^4, \tag{2.4}$$

where σ is known as the Stefan-Boltzmann constant ($5.67051 \cdot 10^{-8}$ W m^{-2} K^{-4}) and ϵ is the total surface emissivity of an object. The emissivity characterizes an object as either black body ($\epsilon = 1$) or white body ($\epsilon = 0$) or something in between ($0 < \epsilon < 1$) and with that gives an indication about the ability to emit radiation. As can be seen by equation 2.4 the energy is proportional to temperature with an exponent of 4, which means that the rate of emission is quite large at high temperatures. Even at room temperature (298 K) the radiation rate equals

470 W m^{-2} which also includes the human body. The reason why this emission is not important to our life is that all the matter around us is also emitting at that rate, which creates a kind of balance of emitting and absorbing energy. Considering this balance the heat flux by radiation can be formulated as follows:

$$\dot{q}_{\text{rad}} = \epsilon\ \sigma\ A(T_{\text{s}}^4 - T_{\text{surf}}^4) \tag{2.5}$$

Here, T_s represents the temperature of the surroundings of an object and T_{surf} gives the temperature at the surface of the object and A is the area of the object's surface. In case the surrounding of the object is not homogeneous, equation 2.5 becomes more complex by introducing two- or three-dimensional equations [7, 19].

2.1.2 Temperature Measurements Based on the Dilatation of Matter

The expansion and contraction of matter (solid, liquid and gas) with temperature is a well-known phenomenon in science. It is used in a variety of thermometers, e.g. bimetallic thermometers, liquid-in-glass-thermometers or gas thermometers. In the following each of these types will be shortly introduced and the measurement principle explained.

Bimetallic Thermometers

Bimetallic thermometers consist of strips of two different metals that are bonded together. Since each metal has a different coefficient of thermal expansion, a change in temperature leads to a different degree of expansion of the two metals and this results in a bending of the bimetallic strip (see figure 2.1). The bending can be translated into a temperature measurement by a mechanical linkage without the need of an external power supply. Usually, the bimetallic strip is arranged in a spiral or helical configuration to achieve a high enough sensitivity. The operating range of such thermometers lies between -70°C and 600°C while their accuracy amounts to ± 1°C [7, 20].

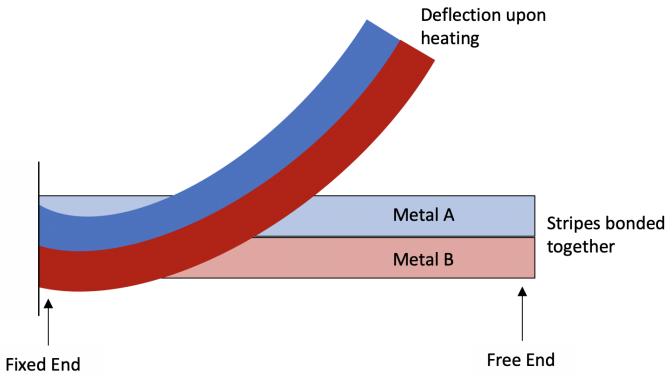

Figure 2.1. Bimetallic thermometer: the two metal stripes are bonded together and fixed on one end (left), while the other is free to bend at elevated temperatures. Metal B shows a higher thermal expansion coefficient (expands more) than metal A. Image adapted from [7].

Liquid-in-Glass-Thermometers

The mercury thermometer belongs to the class of liquid-in-glass-thermometers and was invented by *Daniel Fahrenheit* in 1714 [9]. Generally, these kind of thermometers are well known and used in almost every part of life and science for almost 200 years. It consists of a glass column that can be distinguished into the reservoir (bulb) and the capillary tube supported in a stem. The bulb and capillary tube are connected with each other and filled with the liquid, e.g. mercury [6, 7, 19].
Besides mercury, also other liquids, such as alcohols, aromatic compounds and nowadays, ionic liquids (ILs), are used. Which liquid is chosen depends on the actual application, temperature range or accuracy needed. These specifications are defined by the properties of the respective liquid. The most important properties are the melting and boiling point (in case of ILs it is the decomposition point) as well as the thermal expansion coefficient. Table 2.1 shows different liquids and their respective working range and thermal expansion coefficient [7, 19].

Table 2.1. Working Range and thermal expansion coefficient of different liquids used in liquid-in-glass-thermometers [19].

Thermometric Liquid	Working Range (°C)	Thermal Expansion Coefficient (K^{-1})
Mercury	-35 to 510	$1.6 \cdot 10^{-4}$
Ethanol	-80 to 60	$1.04 \cdot 10^{-3}$
Pentane	-200 to 30	$1.45 \cdot 10^{-3}$
Toluene	-80 to 100	$1.03 \cdot 10^{-3}$
Ionic Liquid [21–24]	-100 to 400	$\sim 5 - 7 \cdot 10^{-4}$

Ionic liquids show a quite large temperature range between their melting and decomposition point depending on the chosen anion and cation.

Since also the glass is in contact with the medium to be measured, both, the glass as well as the liquid in the capillary tube will expand or contract if the temperature changes. However, the thermal expansion coefficient of glass lies in the range of $2 \cdot 10^{-5}$ 1/K [7] and $5 \cdot 10^{-7}$ 1/K [25] depending on the exact glass composition and is therefore much smaller than the coefficient of liquids [7, 19].

Gas Thermometers

Gas thermometers were also already invented in the 17^{th} century. *Robert Boyle* was the first one who described the product of volume V and pressure p to be constant.

$$p \cdot V = \text{constant} \tag{2.6}$$

Jospeh L. Gay-Lussac further discovered in 1802 that every gas has approximately the same thermal expansion coefficient of 1/267 K^{-1}. This value was corrected in 1847 by *Victor Renault* to be 1/273 K^{-1}. Nowadays, experiments show that the coefficient slightly varies for each gas. In 1834, *Emile Clapeyron* finally established the well-known perfect gas law, where p represents the pressure, V the volume, n the amount of substance, R the ideal gas constant and T the absolute temperature in Kelvin.

$$p \cdot V = n \cdot R \cdot T \tag{2.7}$$

Gas thermometers can be divided into two categories: either they are based on constant volume or constant pressure. In order to determine a special temperature, the thermometer has to be calibrated first. Meaning the value of pV is measured for two known temperatures, e.g. the freezing and boiling point of water. Afterwards, any temperature can be determined by measuring pV and calculating T as

$$\frac{T_2}{T_1} = \frac{(pV)_{T_2}}{(pV)_{T_1}}, \tag{2.8}$$

where T_1 is the temperature that is to be determined, T_2 is the temperature of the freezing point, and $(pV)_{T_1}$ and $(pV)_{T_2}$ are the values determined at the respective temperature [7].

Galileo Thermometer

As already mentioned during the journey through history (see chapter 1), one of the early scientists who worked on temperature measurements was *Galileo Galilei*. Although, he did not invent the quite famous *Galileo thermometer*, he was one of the first who discovered that the density of a substance changes with temperature. This phenomenon is part of the working principle of a *Galileo thermometer*, which was actually invented by the *Grand Duke of Tuscany, Ferdinand II*. The second effect of this temperature measurement is based on *Archimedes'* principle: in a sealed glass cylinder, filled with a transparent liquid (nowadays hydrocarbons) several small glass bulbs, each filled with a different colored liquid are submerged. The glass bulbs are having all the same size and are all filled with liquid. The actual nature of this liquid or its color is not relevant for the functionality, but the difference in density is the crucial part. Furthermore, at each glass bulb a small metal plate is attached which shows the temperature between 18°C and 25°C. Depending on the calibration, the glass bulb which represents the actual temperature, is either floating in the middle of the glass cylinder or is the lowest of the ones which are at the top most position. If the temperature changes, the density of the surrounding liquid as well as the liquid within the glass bulbs is changing. If the density of the glass bulbs is smaller than the density of the surrounding liquid, these bulbs are rising in the cylinder and vise verca. However, this process is quite slow, which is why this thermometer is also called *Galileo's termometro lento* (slow, or lazy thermometer) [6, 8].

2.1.3 Temperature Measurements Based on the Change of Resistance

The field of thermometers that are based on the change of resistance can be divided into several classes depending on the material used and the mechanism behind the measurement. This includes platinum resistance thermometers and thermistors.

Resistance Temperature Detectors (RTDs)

The main part of an RTD is the resistance element made of platinum, nickel or copper, that is in contact with the medium/object of interest. This element is electrically connected to a device that is able to detect the change in resistance and correlate this to a meaningful measure of temperature.
The resistance of a metal follows *Ohm's* law and depends on the movement of electrons within the crystal lattice, the vibration of the atoms in this lattice as well as the impurities of the lattice structure. If a potential is applied on a metal wire, an external electrical field is created that forces the electrons within the metal to move in one direction. The motion of the electrons is impeded

by the vibrations of the atoms in the lattice which will increase with increasing temperature. Therefore, the resistance of metals is proportional to temperature:

$$R_T = R_0 \, (1 + \alpha T) \tag{2.9}$$

where R_0 is the resistance at 0°C, R_T the resistance at any temperature, α the temperature coefficient of resistance for a certain material and T the temperature. The temperature coefficient of resistance is a material property and can be calculated from

$$\alpha = \frac{R_{100} - R_0}{100°C \cdot R_0} \tag{2.10}$$

where R_{100} is the resistance at 100°C in Ω. For platinum α equals $3.927 \cdot 10^{-3}$ K^{-1} [6, 7, 19]. Today, there are a variety of platinum RTDs available which are labeled according to their resistance at 0°C: Pt100, Pt500 or Pt1000 have a resistance of 100 Ω, 500 Ω or 1000 Ω at this temperature, respectively. The higher the resistance at 0° the better the resolution of the sensor.

Thermistors

In contrast to RTDs, thermistors are made of ceramic semiconductors which exhibit very high sensitivities that are roughly a hundred times higher than that of platinum RTDs and even a thousand times higher than that of thermocouples. Typical semiconductors consist of mixtures of metal oxides, e.g. nickel, manganese, iron, copper, cobalt or titanium, as well as doped ceramics and can be divided into two classes: Negative Temperature Coefficient (NTC) and Positive Temperature Coefficient (PTC) thermistors.
The main difference between the two classes is the behavior of resistance with temperature. In the case of NTCs the resistance decreases and for PTCs the resistance increases with increasing temperatures, respectively. The latter is mostly based on barium titanate and its derivatives. Such devices are especially used for temperature sensing, switching or protection of windings in electric motors and transformers, because upon a certain temperature the current flow will be significantly diminished and overheating is not possible [7].
NTCs show a dramatically decrease in resistance with temperature and have therefore a broad range of applications. Depending on the manufacturing process and the chosen oxides they exhibit resistance values between 10 Ω and 5 MΩ at 25°C. Contrarily to RTDs the relation of resistance and temperature does not show a linear behavior but can be expressed by

$$R_T = A \, e^{\frac{\beta}{T}} \tag{2.11}$$

with R_T = resistance at temperature T in Ω
A = constant for the particular thermistor under consideration in Ω
β = constant for the particular thermistor under consideration in K
T = absolute temperature in K

It is important to note that equation 2.11 is only valid in a small temperature regime where the characteristics of $\ln(R)$ versus $1/T$ show an approximately linear behavior [7].

2.1.4 Temperature Measurements Based on the Production of an Electromotive Force (emf)

A third group of modern temperature sensors are thermocouples. They consist, similar as bimetallic thermometers, of two different metal wires that are connected at one end (thermo-

electric junction). However, their working principle is based on the formation of an emf due to the movement of electrons from one wire to the other if a temperature difference is present between the thermoelectric junction and the terminus connection (see figure 2.2) [7].

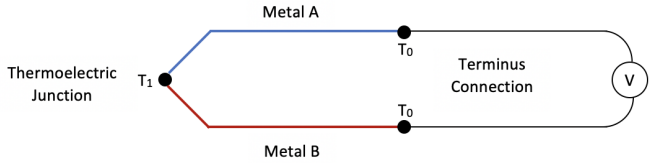

Figure 2.2. Simple thermocouple circuit: The two metals A and B are connected with each other at the thermoelectric junction. Due to a flow of electrons from the metal with higher energy to the one with lower energy, a potential is produced that can supply heat at the terminus connection if the two junctions experience different temperatures. Image adapted from [7].

According to the band theory of metals the electrons of the outer atomic shells are arranged in a quasi-free electron cloud around the nuclei to fulfill the *Pauli* exclusion principle. This means, the electrons are collected in a so called valance band which overlaps with an unoccupied conduction band and enables the flow of electrons due to an applied field. Since every metal has a unique electronic and crystalline structure, the allowed energy states will also be unique, resulting in a flow of electrons from the metal with higher energy into the metal with lower energy upon contact at the thermoelectric junction. This flow continues until the metal with lower energy experiences an excess of electrons, leading to the formation of a reverse emf that opposes the flow. Finally, a common *Fermi* energy is reached that lies between the energies of the two metals and a potential is produced (called *Peltier* EMF) that can supply heat at the terminus connection if this is kept at a different temperature as the thermoelectric junction. A second term that has to be considered is the *Thomson* voltage that expresses the heat forming due to the flow of a current through the wires. It depends mainly on the variation of the *Fermi* energy of each conductor. Combining the *Peltier* and *Thomson* potential, the *Seebeck* potential can be obtained. [6].

$$dV_S = \alpha_{AB}\, dT \tag{2.12}$$

where V_S expresses the *Seebeck* potential in μV, α_{AB} denotes the difference of the *Seebeck* coefficient for the thermoelements A and B (α_A - α_B) in μV K^{-1} and dT is the temperature difference between thermoelectric junction and the terminus connection in K. The *Seebeck* coefficient is unique for each material, but since it is difficult to determine the absolute values, the coefficients are determined with respect to a reference material (usually platinum). [6, 7].

2.2 Barium Strontium Titanate Sol-Gels and Nanocrystals as Temperature Sensitive Material

2.2.1 Barium Titanate ($BaTiO_3$): General Features

In chapter 2.1.3 the main features of materials that show a PTCR effect are already mentioned: they are mostly based on ceramic semiconductor materials such as barium titanate ($BaTiO_3$; BTO) that changes their electrical behavior upon reaching a material specific temperature, called Curie Temperature T_C. While below T_C these materials are conductive, the current flow will be significantly diminished above T_C. Figure 2.3 shows the typical characteristic of a PTC material. Below the Curie temperature (up to 100°C) as well as above 200°C a negative temperature coefficient can be observed, while in between these temperatures a significant increase of resistivity about several orders of magnitude can be seen [26].

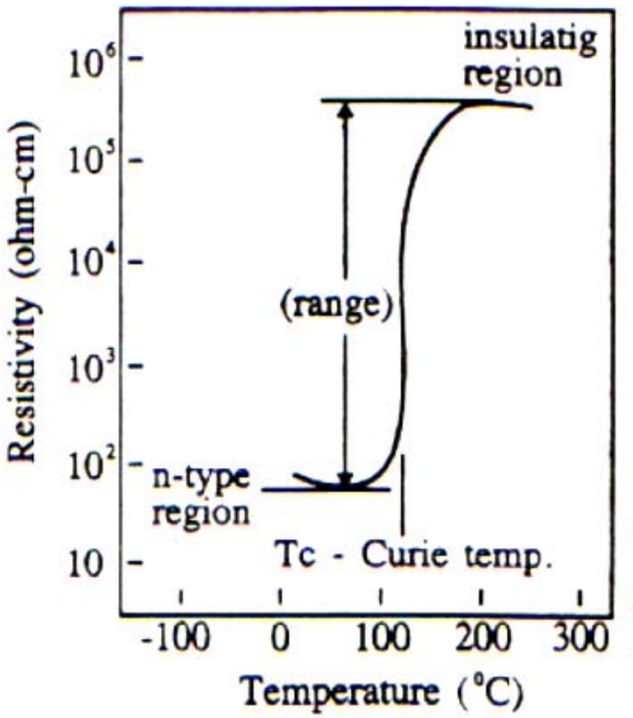

Figure 2.3. Typical characteristic of a PTC material, e.g. $BaTiO_3$. Image from [27].

This increase in resistivity can be explained by the change of the crystal lattice. Barium titanate belongs to the group of minerals called *pereovskite* with the generalized crystal structure ABO_3. Above T_C (130°C), the unit cell of the $BaTiO_3$ lattice is cubic and the ions are arranged as shown in figure 2.4. The Ba^{2+}- and O^{2-}-ions (AO_3) show a cubic-closed packed assembly, meaning the Ba^{2+}-ions sit on the corners of a cube while the O^{2-}-ions occupy the face-centered position. The Ti^{4+}-ion is located at the body-center position.

Below T_C, the unit cell structure gets distorted to the tetragonal form at which the *c* direction is elongated and a dipole moment is induced. Around 0°C another structural transformation

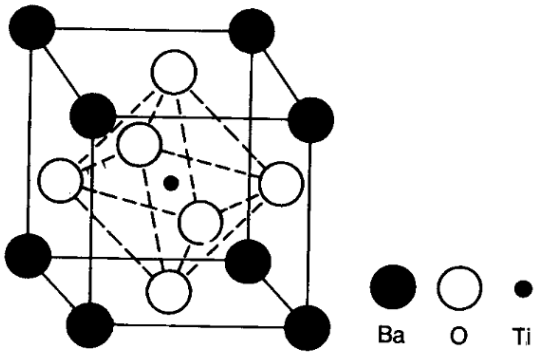

Figure 2.4. Structure of a unit cell of $BaTiO_3$. Image from [26].

occurs and the unit cell becomes orthorhombic, with the polar axis parallel to the face diagonal. The fourth unit cell structure can be found below -90°C and is called rhombohedral, where the polar axis is along a body diagonal (see figure 2.5) [26].

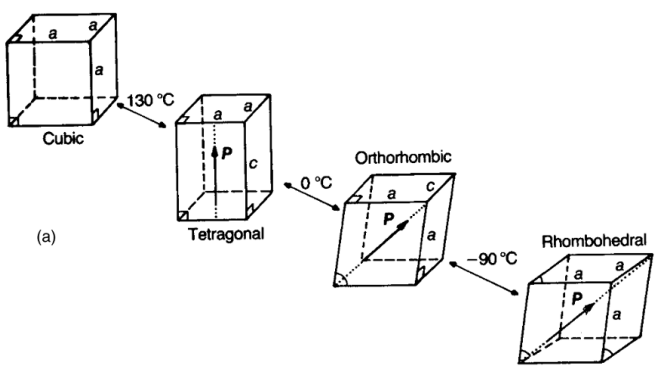

Figure 2.5. Unit cell distortion of a $BaTiO_3$ unit cell. Image from [26].

Besides the change in resistivity with temperature, the dielectric constant also changes along the phase transition as shown in figure 2.6 and therefore, BTO exhibits different properties. Below T_C, the three phases exhibit ferroelectric properties, while above T_C, the cubic phase has a paraelectric property [28].

The dielectric and resistive properties of BTO can be altered by doping, meaning the partial substitution of isovalent or heterovalent cations at either Ti-sites (B-sites) or Ba-sites (A-sites) [29–31]. Substituting the Ba^{2+}-cation by Sr^{2+} or Pb^{2+} yield in a lower or higher Curie point, respectively. Doping the B-site by substitution of Ti^{4+} with Zr^{4+} results also in a significant reduction of T_C as can be seeen in figure 2.7 [30, 31].

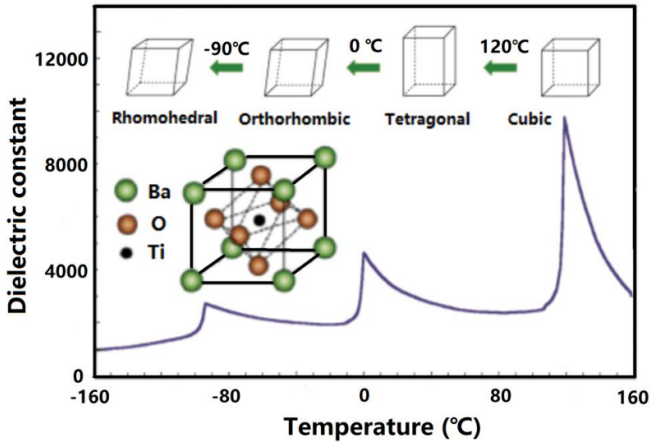

Figure 2.6. Temperature dependence of dielectric constant of $BaTiO_3$. Image from [28].

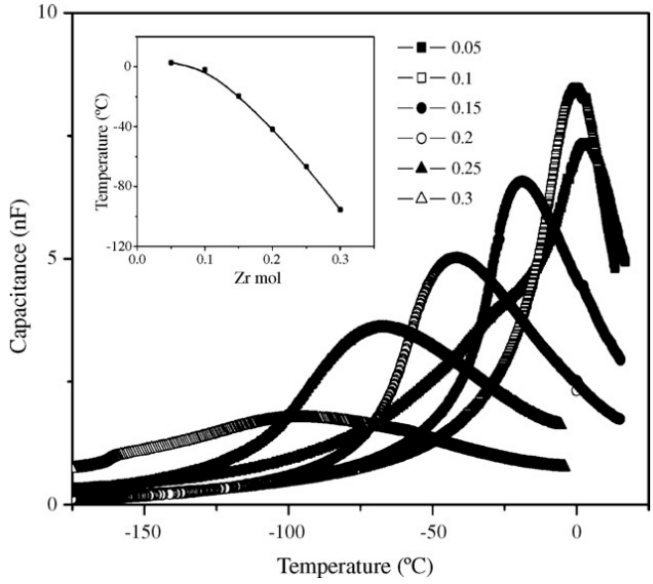

Figure 2.7. The capacitance as a function of temperature and the Curie temperature, T_C, as a function of x (inlet) for $(Ba_{0.6}Sr_{0.4})(Ti_{1-x}Zr_x)O_3$. Image from [30].

2.2.2 Different Synthesis Routes of $BaTiO_3$ and its Derivatives

Nowadays, a variety of synthesis routes are known that all result in BTO ceramics. They can be divided into three main categories: solid-state synthesis, hydrothermal synthesis and sol-gel synthesis.

2.2.2.1 Solid-State Synthesis of $BaTiO_3$

The solid-state synthesis is the classical method to obtain BTO and is just mentioned for completion. There, $BaCO_3$ and TiO_2 are mixed and calcinated at high temperatures (> 1000°C). The $BaCO_3$ reacts at the surface of the TiO_2 particles to form $BaTiO_3$ which then diffuses into the center of the TiO_2 particles.

$$BaCO_3 + TiO_2 \rightarrow BaTiO_3 + CO_2 \tag{2.13}$$

The grain size of these particles depend mainly on the grain size of the TiO_2 precursor, but also on the sintering temperature and duration of the sintering process [28, 32–35].

2.2.2.2 Sol-Gel Synthesis of $BaTiO_3$

In contrast to the solid-state synthesis, the sol-gel method enables the production of ceramics at considerably lower temperatures. The most important class of precursors for the sol-gel synthesis are metal alkoxides, which undergo a two-step transition: first, hydrolysis that leads to a polymerization and second a condensation that results in a 3-D solid phase network. [36, 37]. Another commonly used material class are metallic salts, which have an ionic structure [38]. Here, the metal alkoxide precursors are described in detail.
Metal alkoxides are commonly written as $[M(OR)_z]_n$, where M represents a metal with valence z (here, $M = Ti^{4+}$), R is an organic residue, e.g. alkyl or alkenyl group, and n stands for the molecular association. Usually they are obtained from a reaction of an alcohol with a metal and since there a numerous alcohols available a large number of different metal alkoxides can be found. Due to their polar M-OR bonds, which are caused by the different electronegativity of the metal and the oxygen atom, they are typically Lewis acids. Thus, they are quite sensitive towards a nucleophilic substitution of water molecules that results in the formation of metal hydroxides (M-OH) and the respective alcohol (see equation 2.14) [36, 38, 39]. However, it should be mentioned that Kessler et al. [40] argues that metal alkoxides are rather Lewis bases that undergo a proton assisted S_N1 mechanism through hydrolysis. For the purpose of this thesis the classical model, in which metal alkoxides are seen as Lewis acids, will be used.

$$M(-OR)_z + zH_2O \rightarrow M(-OH)_z + zROH \tag{2.14}$$

To prevent an uncontrollable hydrolysis due to the presence of water, it might be necessary to work under an inert atmosphere and use stabilizing agents, e.g. acetylacetone for the metal alkoxides [36, 38]. Figure 2.8 shows the mechanism of the hydrolysis, where the water molecule acts as a Lewis base and attacks the metal ion of the alkoxide. This is followed by the formation of transition state I, in which a proton transfer from the water molecule towards the alkoxide occurs. Thereby, increasing temporarily the coordination number N of the metal atom. Finally, the alcohol group is released and a transition state is obtained.

The condensation sets in as soon as the formation of the M-OH intermediate occurred, yielding the desired metal-oxygen-metal bonds. However, there are two possibilities how the condensation step takes place. Since there are both, the original alkoxide, M-OR, as well as the hydrolyzed species, M-OH, present, both can undergo the condensation, resulting in a M-O-M species. The first reaction is called alkoxolation while the second one is called oxolation. Figure 2.9 shows the two condensation pathways, in which first an "ol"-bridge is formed due to the nucleophilic attack of the lone electron pair of the oxygen atom from the M-OH species. This is followed by the proton transfer yielding an "oxo"-bridge and the leaving group, R-OH or HOH, respectively.

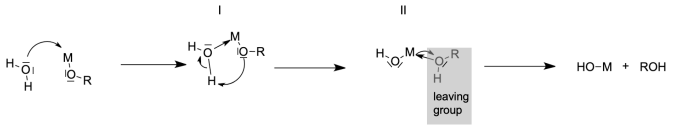

Figure 2.8. Schematic representation of the hydrolysis mechanism, including the nucleophilic attack of a water molecule at the metal atom yielding the transition state I and followed by the departure of the leaving group (II), resulting in the release of an alcohol group and the formation of a transition state that enters the condensation. The *arrows* indicate the donor character of the lone electron pairs of the oxygen atoms. Image from [36, 38].

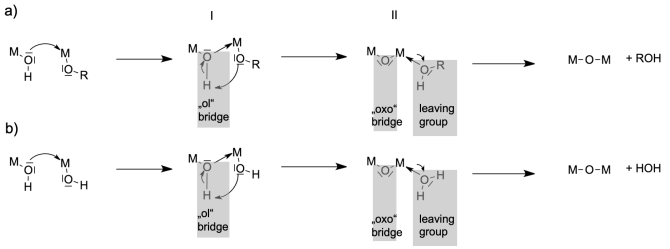

Figure 2.9. Schematic representation of the condensation mechanism, including the nucleophilic attack of a M-OH molecule at the metal atom of either an alkoxide molecule (a) or another M-OH molecule (b), yielding the transition state I in which an "ol" bridge is formed. This is followed by the departure of the leaving group and the formation of an "oxo" bridge (II), resulting in the release of an alcohol or water molecule and the formation of a M-O-M bond. The *arrows* indicate the donor character of the lone electron pairs of the oxygen atoms. Image from [36, 38].

The above described reactions are all involved in the formation of a sol-gel by developing a 3-D network. In case of the formation of barium titanate, titantium (IV) isopropoxide or titanium (IV) n-butoxide are often used as precursors for the sol-gel synthesis. Thereby, tetrahedral units of $Ti(OR)_4$, with R = ^{i}Pr or ^{n}Bu, or octahedral units of $Ti_2(OR)_8(LH)_2$, with R = ^{i}Pr and L = NHPr, are formed as alkoxide (see figure 2.10).

Depending on the degree of this polymerization process a stable suspension of colloidal solid particles or polymers in a liquid (*sol*) will form, which is transformed into the *gel* (solid phase) at a later stage. The hydrolysis and condensation reactions can be influenced by temperature and pH adjustments according to the shown mechanisms, which in turn defines the size of the obtained particles. [36]
Using the sol-gel method, thin films can be applied onto flexible polymer substrates such as polyethylene terephthalate (PET) and subsequently photonically sintered. This sintering method will be described in section 2.2.4.

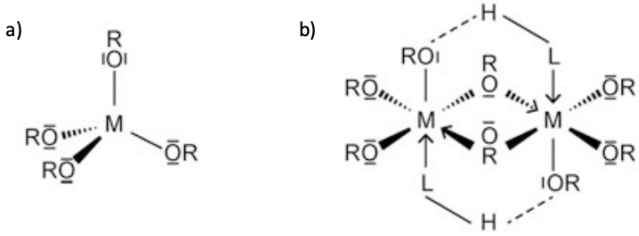

Figure 2.10. Schematic representation of two possible Ti-alkoxides formed during the sol-gel process. a) shows a tetrahedron structure of $Ti(OR)_4$, with R = ^{i}Pr or nBu, b) represents octahedral units consisting of $M_2(OR)_8(LH)_2$ with solvent adduct L-H (L = R' or NHR") which forms additional hydrogen bridges M = Ti; R = O^{i}Pr ; L = NHPr. Image from [36, 41].

2.2.3 Properties of $BaTiO_3$-Nanoparticles

The physical and chemical properties of nanoparticles depend mainly on their size and shape. In case of BTO nanoparticles it was found that the ferroelectricity is decreasing with decreasing particle size and vanishes below a critical size. This is called the size effect [42–47]. *Hoshina et al.* [44] investigated the dependence of particle size with the lattice parameters a and c as well as the tetragonality (c / a ratio), while *Wada et al.* [45] examined the relation of the dielectric constant with particle size.
Another size effect of BTO nanoparticles is the peak broadening and low intensity in common XRD measurements, which makes the analysis with high-energy synchrotron radiation x-ray necessary. Using this technique to analyze BTO nanoparticles with several sizes, i. e. 20 nm, 30 nm, 40 nm, 85 nm, 140 nm, 215 nm, 430 nm and 1000 nm, it was found that at room temperature the crystal symmetries of the particles with 20 nm and 30 nm were cubic, while the crystal symmetry of the particles over 40 nm were tetragonal. [44, 46] The particle size dependence of the lattice parameters a and c as well as of the tetragonality (a/c ratio) can be seen in figures 2.11 and 2.12. With decreasing particle size the lattice parameters a and c increase and decrease, respectively, up to the particle size of 30 nm at which they become equal. This is supported by the analysis of the tetragonality, shown in figure 2.12, which decreases also with decreasing particle size until the a/c ratio is 1.000 at a size of 30 nm and smaller. The ratio of 1.000 reflects a cubic symmetry of the crystal lattice. Furthermore, the cell volume increased for particle sizes below 140 nm (figure 2.11), which indicates that the surface starts to affect the entire crystal structure from this point on, while additionally the dielectric maximum of 5000 was also found for particles of 140 nm and is therefore accounted to the surface effect.

In a second step, *Hoshina et al.* [44] investigated the temperature dependence of the crystal structure of the BTO nanoparticles. Thereby, only the sizes between 20 nm to 430 nm were considered. For these particle sizes the lattice parameter of the a- and c-axis as well at the cell volume were determined at temperatures between 30°C and 150°C. In figure 2.13 a) to d), two transition temperatures, T_I and T_{II}, are shown. While T_I represents the phase transition from tetragonal to cubic symmetry (also called Curie temperature T_C), T_{II} marks the temperature at which the cell volume expansion took place. As can be seen, the phase transition temperature T_I is size independent and is for all particle sizes 135°C. T_{II} on the other hand decreases with decreasing particle size, i. e. for particles with size 430 nm T_I equals T_{II}, while for particles

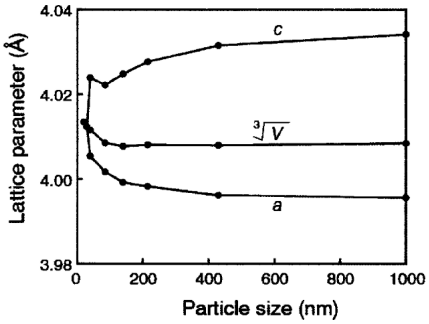

Figure 2.11. Change of lattice parameters (a- and c-axis) and the cube root of cell volume ($V^{1/3} = (a^2c)^{1/3}$) with different particles sizes at 24°C for BTO nanoparticles between 20 nm and 1000 nm. Image from [44].

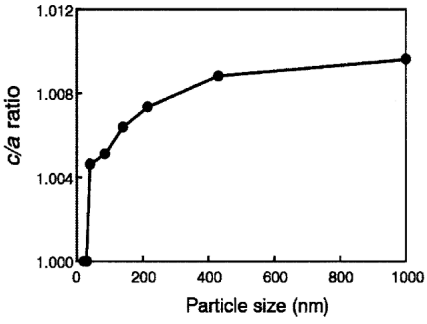

Figure 2.12. Tetragonality (a/c ratio) for different BTO particles sizes, i. e. 20 nm to 1000 nm, at 24°C. Image from [44].

with size 140 nm and 40 nm T_{II} lies at 110°C and 77°C, respectively. Since the particles of 30 nm are cubic at each temperature, T_I and T_{II} are not determinable.

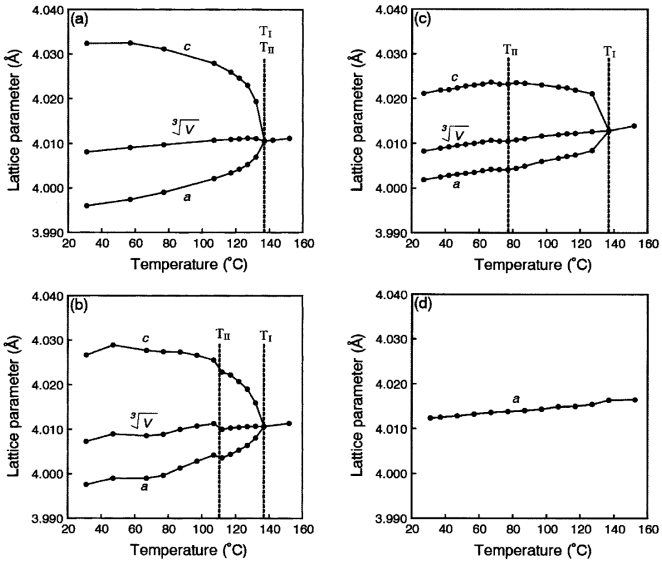

Figure 2.13. Temperature dependence of the lattice parameters (a- and c-axis) and the cube root of cell volume ($V^{1/3} = (a^2c)^{1/3}$) of BTO nanoparticles with sizes of a) 430 nm, b) 140 nm, c) 40 nm and d) 30 nm. Image from [44].

2.2.4 Photonic Sintering of $BaTiO_3$-Sol-Gels

The sol-gel method provides basically two ways of obtaining BTO functional layers. First, synthesizing BTO nanocrystals in benzyl alcohol using titanium (IV) isopropoxide as Ti-source ac-

cording to *Veldhuis* et al. [48]. Second, using the sol-gel-route according to *Schneller* et al. [36] which results in a BTO-sol that can be applied as thin film onto flexible polymer substrates. In a second step, this thin film has to be sintered in order to achieve a crystal BTO layer. Since the polymer substrates are temperature sensitive the conventional sintering temperatures of 800-1000°C cannot be used to obtain a crystalline film. Therefore, a new method, the so called photonic sintering, was developed and used for different oxide films as well as silver and cooper oxide inks. [39, 49–52]

Kim et al. [50] developed a photonic sintering technique for strontium titanate ($SrTiO_3$; STO) using white light as well as deep UV- and near IR-irradiation to sinter the sol-gel-film applied onto a polymer substrate. In order to find the best sintering parameters, they tested a energy density range of 5-25 J cm^{-2} and applied for each energy density a single pulse of 20 ms. Thereby they found that 5 J cm^{-2} proved to be insufficient to obtain a crystal layer. The crystallization was determined by measuring the dielectric constant, which only started to increase at 10 J cm^{-2}. For 15 J cm^{-2} the dielectric constant was highest and decreased again for higher energy densities. Furthermore, the number of pulses applied were also investigated while the total energy was maintained at 15 J cm^{-2}. It was found that a single pulse yields the highest dielectric constant, while splitting the energy into several pulses decreased the dielectric constant again. Finally, the pulse length was varied and the effect on the dielectric constant investigated. Again, the total energy was maintained at 15 J cm^{-2}, which results in higher pulse intensities for shorter pulse lengths. This lead to damaging the substrate for pulse lengths below 15 ms. These results are shown in figure 2.14 a to c. Figure 2.14 d shows the XRD patterns of the STO film before and after sintering. It can be seen that the characteristic peaks (211), (210) and (110) of crystal STO increased after the photonic sintering.

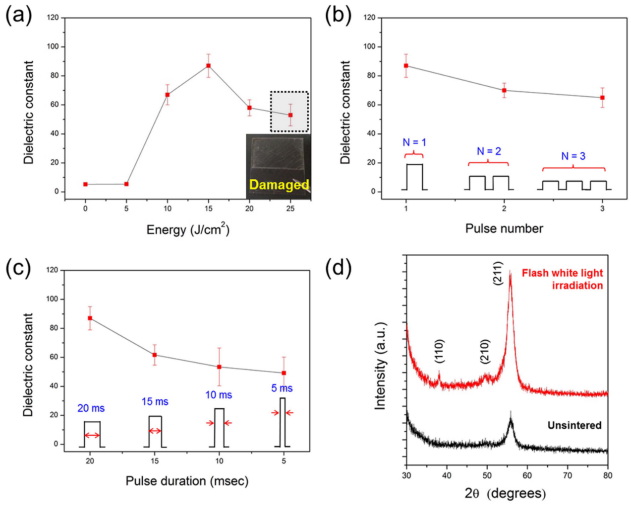

Figure 2.14. Photonic sintering of a STO thin film using flash white light. The dielectric constant was measured for a) several energy densities, b) pulse numbers and c) pulse duration. Additionally, the XRD patterns of the STO thin film before and after sintering are shown (d). Image from [50].

To improve the above shown results further, deep UV as well as near IR irradiation was additionally used to the white light irradiation. For the deep UV a range of 30 to 90 mW cm^{-2} was tested and used in combination with a white light irradiation of 15 J cm^{-2} (single pulse with a

duration of 10 ms). The best results were obtained for 30 mW cm^{-2} deep UV during the white light sintering process. Applying additionally near IR irradiation to the combination of deep UV and white light sintering the photonic sintering was even more efficient. Therefore, near IR with a power of 3 W cm^{-2} was irradiated for 0 -180 s before the white light sintering. The results show that the highest dielectric constant was obtained for a irradiation of 180 s with near IR followed by white light sintering at again 15 J cm^{-2}. The results are shown in figure 2.15. [50]

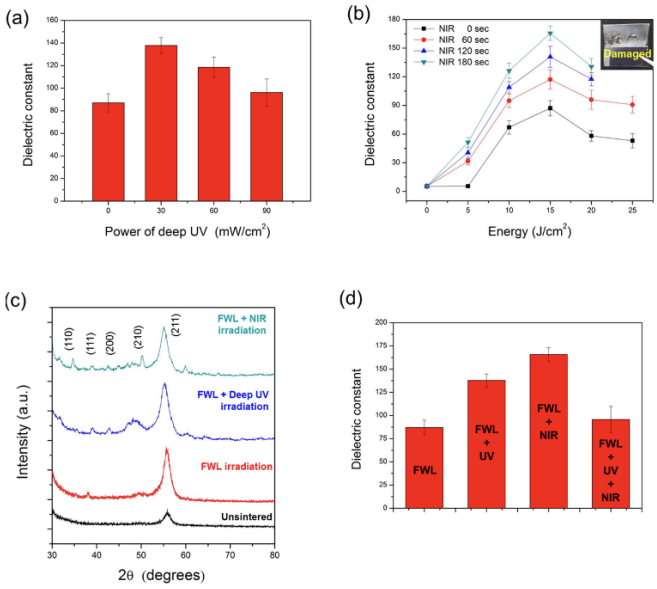

Figure 2.15. Photonic sintering of a STO thin film using flash white light in combination with deep UV and near IR. The dielectric constant was determined in correlation with a) different power of the deep UV and b) several duration times of near IR pre-treatment. The flash white light parameters were kept at 15 J cm^{-2}. with a single pulse of 20 ms The XRD pattern of the three sintering processes as well as the unsintered state are shown in c). In d) the comparison of the combination of the before described sintering parameters are shown. Figure adapted from [50].

2.3 Ionic Liquids and Their Viscosity-Dependent Diffusion Coefficient as Temperature Sensitive Material

2.3.1 Ionic Liquids (ILs): General Features

Ionic Liquids (ILs) are known for more than a century, but they only gained an increase attention in the last three decades as neoteric solvents [18]. A common used definition of ILs is that ionic liquids are salts with a melting point below the boiling point of water, i.e. 100°C [53]. The salts which are classified as IL exhibit very often a melting point around room temperature or even below due to the structure of the cation and anion [18,54–56]. Usually the cation is larger compared to common salts and shows a more diffuse and asymmetric charge distribution. Widely used as cations in ILs are N-heterocyclic compounds such as 1-Alkyl-3-methylimidazolium $[C_nC_1im]^+$ or 1-Alkyl-1-methylpyrrolidinium $[C_nC_1pyrr]^+$ as well as quarternised ammonium and phosphonium [55, 57, 58]. IL anions can be of organic or inorganic nature. In many cases, the negative charge is also distributed over several atoms with the exception of halide anions [57]. The asymmetrical structure of ILs is mainly responsible for their low melting point, because it inhibits local packing. Additionally, the charge-diffuse nature of the cation leads to repulsive forces between the charge-neutral organic entities and the highly ionic components of the cation which also impede the formation of a crystal structure [58–60]. Furthermore, ILs exhibit several more interesting properties, such as a negligible vapor pressure, high thermal stability which leads rather to decomposition than evaporation upon heating, high loading capacity, large electrochemical windows, high conductivities and tuneable solvent properties [59–62]. A representative selection of commonly used cations and anions are shown in figure 2.16.

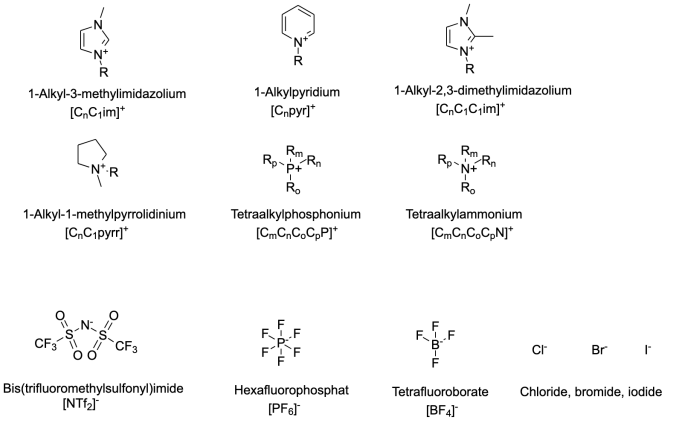

Figure 2.16. Some common cations (1^{st} and 2^{nd} row) and anions (3^{rd} row).

In principle, the combination of cations and anions can be chosen arbitrarily or according to a desired functionallity, e.g. specific thermophysical or physicochemical property, that shall be obtained. [63, 64]. This results in approx. 10^6 possible simple ILs and even more (ca. 10^{18}) binary systems (ILs containing one cation and two different anions or two different cations and one anion) [57, 64]. Since the structure of an IL and its properties are closely related it is important to gain a general understanding of the interactions the ions of an IL are under-

going. The nature of these inter- and intramolecular interactions range from weak, nonspecific and isotropic forces such as *van der Waals*, solvophobic and dispersion forces [56, 65] to strong and long-ranged *Coulombic* forces [65, 66], specific and anisotropic forces, e.g. hydrogen bonding [55, 56, 65], halogen bonding, dipole-dipole [66], magnetic dipole, electron pair donor/acceptor interactions [56]. In a well-chosen system (i.e. cation and anion combination), the ion-ion interactions and the symmetry of the ions are balanced in a way that the melting point lies around RT. For instance, the length of the alkyl chain of the cation reduces the *Coulomb* forces and thus, disrupts the lattice packing, which lowers the melting point and determines the viscosity of the IL [56]. In addition, *van der Waals* interactions, π-π-stacking of aromatic cations, and hydrogen bonding between polar groups are also present and influence the physical properties of a respective IL. Since hydrogen bonds are quite directional, they can destroy the charge symmetry of the IL and cause defects within the *Coulombic* network which in turn increases the dynamics of the ions and therefore decreases the viscosity. Hence, while the hydrogen bonds are much weaker compared to *Coulomb* interactions, they play a major role for designing the desired IL [67]. In the following some of these aspects are discussed in greater detail.

2.3.2 Influence of the Structure of Cation and Anion in ILs

As mentioned above, the physicochemical properties of ILs depend mainly on the structure of the cation and anion, respectively, as well as the combination of cation and anion. In order to predict these properties and design specific ILs machine learning methods are utilized. Among these methods, artificial neural networks are a leading and effective technique. The review of Racki et al. [68] gives an insight in the recent advances of the application of artificial neural networks to model the properties of ILs.
Furthermore, several other groups investigated the influence of different anion-cation couplings as well as the influence of alkyl chain lengths and impurities, e.g. water, by conducting viscosity, density and other measurements [69–81].

2.3.2.1 Miscibility of ILs with Water and Other Organic Solvents

Depending on the chosen anion the IL becomes water-soluble, e.g. Cl^-, Br^-, I^-, NO_3^-, $[Al_2Cl_7]^-$, $[AlCl_4]^-$ (decomp.), or water-insoluble, e.g. $[PF_6]^-$, $[NTf_2]^-$. The water solubility of $[BF_4]^-$ depends on two factors: first, the temperature of the IL, i.e. $[C_4mim][BF_4]$ is soluble in water at room temperature but forms a biphasic system at 5°C. Second, the length of the alkyl chain at the cation, i.e. $[C_nmim][BF_4]$ with n > 4 form also biphasic systems. However, also the solubility of ILs with other anions, such as $[PF_6]^-$, depends on the alkyl chain length and decreases with increasing length (see figure 2.17) [82].

According to *Bonhôte* et al. [83] the miscibility with other liquids, e.g. organic solvents, depends on the dielectric constant of that liquid. Solvents with medium to high dielectric constants ϵ, such as low alcohols and ketones, dichloromethane ($\epsilon = 8.93$), and THF ($\epsilon = 7.58$) are all miscible with dialkylimidazolium based ILs (used anions: triflates (TfO^-, $[CF_3SO_3]^-$), bis(trifluoromethylsulfonyl)imide (NTf_2^-, $[(CF_3SO_2)_2N]^-$), nonaflate (NfO^-, $[C_4F_9SO_3]^-$), acetate (AcO^-, $[CH_3COO]^-$, trifluoroacetate (TA^-, $[CF_3COO]^-$), heptafluorobutanoate (HB^-, $[C_3F_7COO]^-$)). Alkanes, dioxane ($\epsilon = 2.01$), toluene ($\epsilon = 2.38$) and diethyl ether ($\epsilon = 4.33$) are immiscible with these ILs. Ethyl acetate ($\epsilon = 6.02$) seems to be the border of miscibility, meaning that the ILs $[C_2mim]^+$ TfO^-, NfO^-, and Tf_2N^- are still miscible, while the ILs comprising TA^- and HB^- as anions are only slightly soluble. Increasing the alkyl chain length from C_2 to C_4 also increases the solubility. The miscibility of these ILs with water depends on the ability

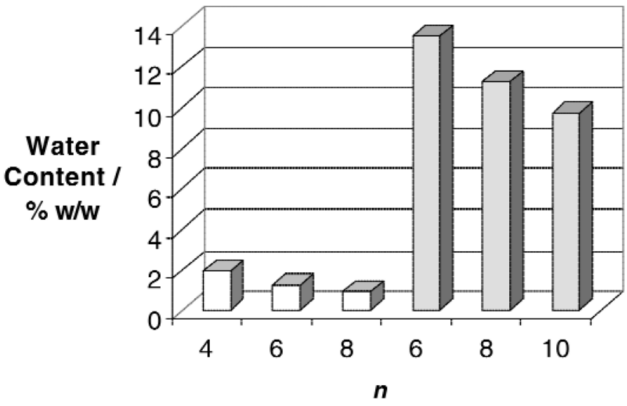

Figure 2.17. Water content of $[C_n mim][PF_6]$ with n = 4, 6, 8 (white) and $[C_n mim][BF_4]$ with n = 6, 8, 20 (grey) at ambient temperature. Image from [82].

of the anion to form hydrogen bonds, resulting in the immiscibility of the NTf_2^- containing ILs. Here, the alkyl chain length shows only an insignificant contribution [83].

2.3.2.2 Hydrogen Bonds

Hydrogen bonds are one of the important intermolecular interactions occurring in ILs. Depending on the structure of the cation, a variation of different hydrogen bonds can be established. The main contribution in forming a hydrogen bond is the *Coulombic* interactions between the partial positive and negative charges on the hydrogen atom and the acceptor atom, respectively [84]. Usually the H-bond donor is a C-H unit within the cation. However, in an imidazolium based IL for instance are several such C-H units present which leads to the conclusion that there are several different possibilities of forming an H-bond, i.e a C-H on the aromatic ring or a C-H of the alkyl chains [55]. Many groups did a large variety of computational calculations and experiments, e.g. classical molecular dynamics simulations [58, 85–89], ab initio calculations [90, 91], density functional theory [61, 92–94], NMR, IR and Raman spectroscopy [62, 63, 84, 95–99], crystallographic examinations [84, 100–102], neutron diffraction [103, 104], and others [105–108] to identify the internal structure of ILs and explain their extraordinary properties. Especially vibrational spectroscopy methods are a useful tool in studies which aim to determine the internal structure of ILs. Already in the 1980's several groups used spectroscopical methods to investigate the structure of halogenoaluminate ILs. Among them, *Tait et al.* [109], *Abdul-Sada et al.* [110] and *Dieter et al.* [62], who investigated the system of 1-ethyl-3-methylimidazolium chloride/bromide/iodide and aluminum chloride ($[[C_2C_1im]][Cl]$-$AlCl_3$, $[C_2C_1im]][Br]$-$AlCl_3$, $[C_2C_1im]][I]$-$AlCl_3$). Depending on the mole fraction (N) of $AlCl_3$ this system either shows acidic ($N > 0.50$) behavior due to the presence of $Al_2Cl_7^-$ or basic ($N < 0.50$) behavior due to the presence of Cl^- ions [62, 109]. At ca. 3050 cm^{-1} a so called "Cl^- interaction band" appears in IR spectra the more basic the system gets (see figure 2.18). This happens due to the presence of chloride ions that can be assigned to stretching vibrations of C^2-H...Cl^-, C^4-H...Cl^- and C^5-H...Cl^- hydrogen bonds. Similar to the chloride containing system, Br^- and I^- interaction bands were found between 3050 cm^{-1} and 3080 cm^{-1} in the spectra of $[C_2C_1im]][Br]$ and $[C_2C_1im]][I]$ [110].

XRD studies by *Elaiwi et al.* [100] confirmed that each cation is H-bonded by three Cl^--anions

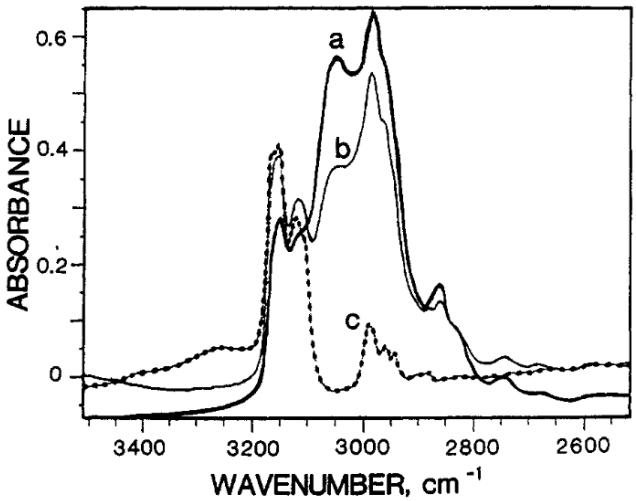

Figure 2.18. IR spectra of CH bands of $[C_2C_1im]^+$ in $[C_2C_1im][Cl]$-$AlCl_3$ at a) $N = 0.33$, b) $N = 0.40$, and c) $N = 0.50$. The higher the amount of $AlCl_3$ ($N > 0.50$), the more acidic is the composition and the peak at 3050 cm^{-1} decreases. Image from [62].

which are lying in the plane of the imidazolium ring and forming hydrogen bonds to the C^2-H, C^4-H and C^5-H site. This is shown in figure 2.19 for a single $[C_2C_1im]^+$ cation and in 2.20 the packing of several ions are shown. *Turner et al.* [91] showed via ab initio calculations that the C^2-H site has a local energy minimum because it contains the most acidic proton. However, the global minimum corresponds to the configuration at which the halogen is positioned above the ring in a close proximity to C^2-H. The exact position depends on the size of the anion. While smaller anions tend to position above the C^2-H group, larger ones are more likely to be above the ring [55].

These findings were confirmed by several other groups [59, 61, 87, 90] over the last years, however, they also suggest that the H-bond in the plane of the ring is not linear, as the Cl^- sits slightly displaced forming a weaker secondary H-bond, with one of the alkyl groups (chelated H-bonds). This is shown in figure 2.21 [55] in which all possible H-bonds which are in plane of the imidazolium ring of $[C_4C_1im][Cl]$ are displayed together with the association sites of the chloride anion. The primary site (1) for H-bond interactions is, of course, the C^2-H position since this carries the most positive partial charge. As mentioned above, the anion can also be located at the back of the imidazolium ring around the C^4-H and C^5-H bonds (2). These H-bonds are influenced more by the electronic character and steric impact of the alkyl groups due to their rotational ability. This also can lead to the formation of secondary H-bonds (4) with C-H units along the chain. The N-C-H units (3a and 3b) of the alkyl chains experiencing a higher variability and show longer bond distances depending on the local conformation of the alkyl chain. However, the calculations of *Turner et al.* show that the anion tends to position itself closer to the methyl substituent as opposed to the longer alkyl chain (see fig. 2.21 front-Me) [91]. Compared to the primary site, these H-bonds are of medium strength. Finally, it is also possible that the anion interacts with the hydrogen atoms of the terminal methyl groups (5a and 5b) of the alkyl chain. Since the cation interacts at least with two hydrogens [91] at the same time, the anion can be kept in the local vicinity if one H-bond is broken until it is reformed [55].

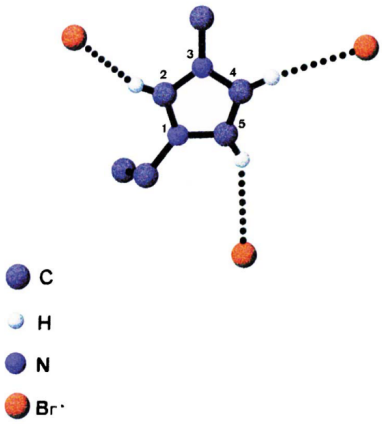

Figure 2.19. Possible, in plane positions of the halide anion around a single $[C_2C_1im]^+$-cation. Image from [100].

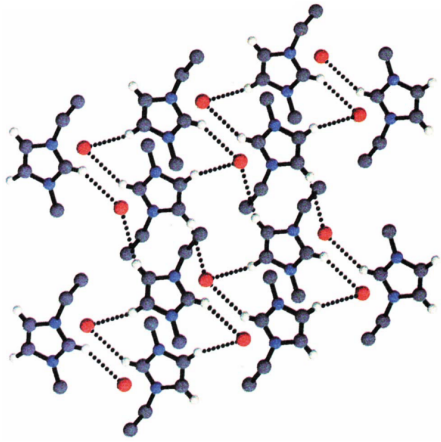

Figure 2.20. Ion packing of $[C_2C_1im]X$ ($X = Br^-$ or I^-) viewed along the b axis. Image from [100].

The interactions of the hydrogens bound to $C^{8/9}$ depend mainly on the size of the anion and were found to be present in 1-ethyl-3-methylimidazolium dicyanamide. In order to form such H-bonds, the alkyl chain needs to twist according to the arrangement of the electronegative atoms in the anion. However, these H-bonds are expected to be weak and have not been studied in detail [55].

Noack et al. [63] investigated the effect of methylating the C^2 position in a $[C_2C_1im]^+$ and $[C_4C_1im]^+$ cation, using $[NTf_2]^-$ as cation. Besides spectroscopic measurements (IR, Raman and NMR) they also measured phyiscochemical properties such as the melting point, thermal decomposition temperature, density and viscosity and compared the methylated ILs with the non-methylated ones. Generally, the viscosity, melting point and thermal decomposition temperature increase drastically due to the methylated C^2 position, while the density decreases slightly. The spectroscopical data shows shifting of several peaks associated with the C^2-atom. These effects can be explained by the altered electron density distribution of the cation that leads to a change in the interionic interaction, i.e. increased *Coulomb* and decreased *van der Waals* interactions, due to the methylation.

The change of certain physicochemical properties are discussed in the next section with respect to several parameters, e.g. alkyl chain length, effect of impurities.

2.3.3 Physicochemical Properties of ILs

In literature, a large amount of articles is available that describe the physicochemical behavior of various ILs, i.e. the temperature dependence of viscosity, density and conductivity, diffusion coefficients of cations and anions, thermal expansion, surface tension etc. [69–78]. Often, these properties are investigated with respect to different alkyl chain lengths on the cation or varying anions for one cation and vice versa. In general, it can be said that the density of ILs ranges between 1.0 to 1.6 g cm^{-3}, the viscosity lies typically in the range of 10 to 500 mPa s at ambient temperature and the thermal expansion coefficient is approx. twice as high as water and amounts to $5 \cdot 10^{-4}$ K^{-1} [71]. Furthermore, the influence of impurities, such as water, organic solvents or halides, play a major role when measuring the viscosity, density or conductivity of

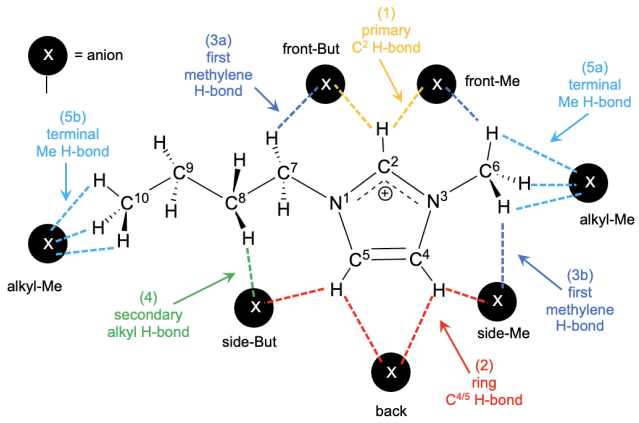

Figure 2.21. Representation of the possible H-bonds and anion association sites (in plane) in the 1-butyl-3-methylimidazolium cation. The anion is displayed as black, filled circle with a withe X. In clockwise direction the H-bonds are: front-Me, alkyl-Me, side-Me, back, side-But, alkyl-Me, front-But. To distinguish between the H-bonds, they are color coded and numbered: (1) primary with C^2 of the ring (yellow), (2) with $C^{4/5}$ at the rear of the ring (red), first methylene (3a) or first methyl (3b) with the C^7 or C^6 groups on the alkyl chains (dark blue), (4) secondary with interactions of the CH_2 groups along the alkyl chains (green) and terminal-methyl (5) with interactions at the terminal methyl groups on the alkyl chains C^6 or C^{10} (light blue). Image adapted from [55].

ILs, especially, if the obtained results are compared to other values found in literature. Many authors are not specifying the amount of water or other impurities in their ILs, which results in unreliable data that makes them incomparable and can lead to serious problems if ILs are used in industrial applications [70, 73, 75, 106].

2.3.3.1 Viscosity, Density and Conductivity of ILs

In this section an overview of the most important findings with respect to temperature dependent behavior of viscosity, density and conductivity is given. Furthermore, the influence of impurities or added organic solvents is briefly discussed.
In general, the viscosity and density decrease with increasing temperature, while the conductivity shows the opposite trend.

Viscosity

The viscosity can be described by *Arrhenius* equation (see equation 2.15). However, for glass-forming liquids, such as ILs, this equation is not satisfactory and the *Vogel-Fulcher-Tamman (VFT)* equation (see equation 2.16) results in a better fit [69, 74, 75, 111].

$$\eta = \eta_\infty \cdot e^{\left(\frac{E_A}{R \cdot T}\right)} \tag{2.15}$$

$$\eta = \eta' \cdot e^{\left(\frac{B}{T-T_0}\right)} \tag{2.16}$$

In the *Arrhenius* equation 2.15, η_∞ denotes the viscosity at infinite temperature, E_A the activation energy for viscous flow and R the universal gas constant. For the VFT equation 2.16, η' represents also a material constant, T_0 corresponds to the glass transition temperature and B is another constant that yields the activation energy of Arrhenius if multiplied by R. If the IL under investigation yields a linear correlation of $\ln(\eta)$ vs. T^{-1}, the Arrhenius model can be used otherwise the VFT equation needs to be considered. Figure 2.22 shows a typical viscosity plot, where the line displays the best fit of the data according to equation 2.16.

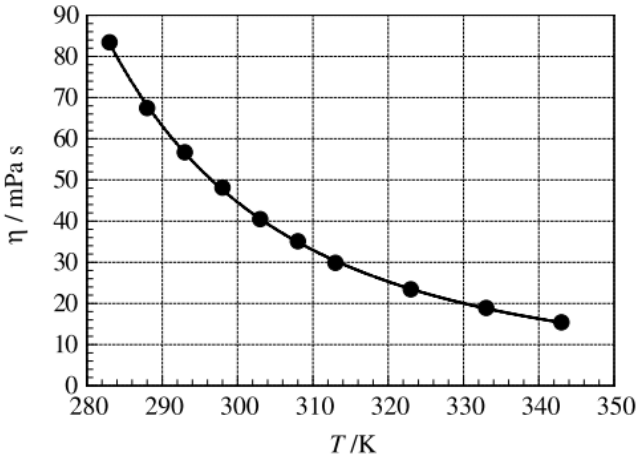

Figure 2.22. VFT plot of 1:2 trimethylsulfonium bromide–$AlCl_3$ ($r^2 > 0.999$). Image from [69].

According to *Okoturo et al.* [69], which model, Arrhenius or VFT, yields the better result depends on the cation and anion, respectively. In their study they investigated the viscosity behavior of 23 different ILs and concluded that ILs that contain either 1-butyl-3-methylimidazolium cations in combination with a symmetrical anion, e.g. $[BF_4]^-$, or an $[NTf_2]^-$ anion with less symmetric cations, e.g. 1-butyl-1-methyl- pyrrolidinium, can be well fitted by Arrhenius.
For ILs which are not fitted satisfactorily by Arrhenius, the plot of $\ln(\eta)$ vs. T^{-1} does not result in a linear behavior as can be seen in figure 2.23. Here, the plot shows a downward curvature and a relatively low r^2 value for the temperature dependence of viscosity [69].

For such ILs the VFT equation results in more accurate fittings. This is generally true for chloroaluminate ILs with cations that are either small and symmetrical with low molar mass ($<$ 100 g mol^{-1}) or larger with shorter alkyl groups as well as an aromatic group around the onium atom (100 g mol^{-1} $<$ molar mass $<$ 151 g mol^{-1}). In case of the $[NTf_2]^-$ anion, the combination with cations having a high molar mass (100 - 140 g mol^{-1}) also fit the VFT model well [69]. *Seddon et al.* [111] investigated the effect of the alkyl chain length on 1-alkyl-3-methylimdazolium ($[C_n mim]^+$ with n = 2 - 14) cations with various anions ($[BF_4]^-$, $[PF_6]^-$, $[NO_3]^-$, $[CF_3SO_3]^-$ and $[Cl]^-$) and found an increase in viscosity with increasing chain length for all tested ILs. This can be explained by the increasing *van der Waals* forces due to longer hydrophobic alkyl chains. In case of n $>$ 12, the length of the alkyl chain is large enough that a separation of the ionic head group and the alkyl chain occurs. This leads to a discontinuous viscosity behavior, as is

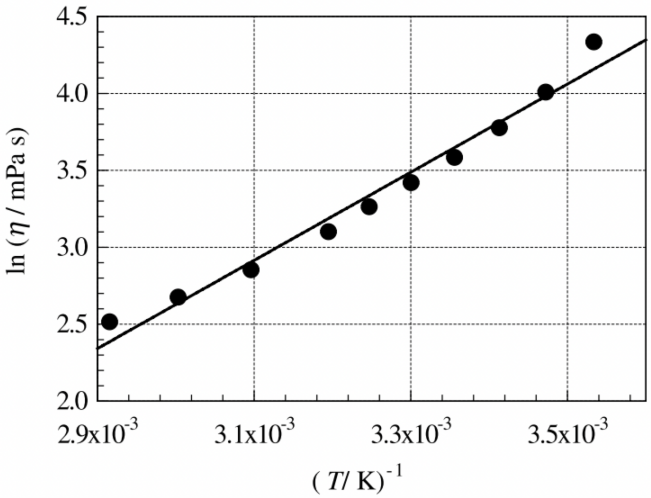

Figure 2.23. Arrhenius plot for 1:1.5 acetamidine hydrochloride-$AlCl_3$ showing a downward curvature ($r^2 > 0.97$). Image from [69].

displayed in figure 2.24. For n = 2 - 10, the viscosity shows the typical exponential decreasing behavior with increasing temperature, while for n > 10 this behavior shows drastic changes due to the formation of a liquid crystal phase. Furthermore, it can be seen that the viscosity increases with increasing length of the aliphatic alkyl chain, however, this increase is also not linear as shown in figure 2.25.

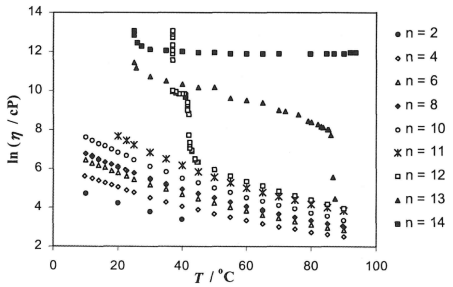

Figure 2.24. Viscosity behavior of $[C_n mim][BF_4]$ with increasing temperature. Image from [111].

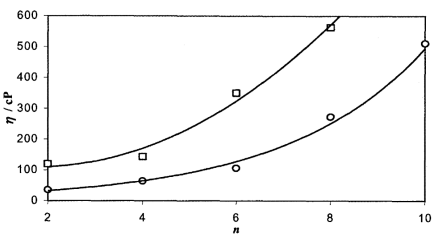

Figure 2.25. Change in viscosity with increasing alkyl chain length for $[C_n mim][NO_3]$ (□) and $[C_n mim][CF_3SO_3]$ (○). Image from [111].

Almeida et al. [112] investigated the temperature dependence of viscosity for several pure ILs and binary IL mixtures. They showed that the viscosity decreases in the following order for pure ILs containing a common cation, i.e. $[C_4mim]^+$, at a given temperature, i.e. 298.15 K: $[(CH_3O)_2PO_2]^- > [CH_3CO_2]^- > [PF_6]^- > [BF_4]^- > [CF_3SO_3]^- > [SCN]^- > [NTf_2]^- > [N(CN)_2]^- \approx [C(CN)_3]^-$. This order depends on two factors, namely size of the anion and its ability to strongly interact with the other ions. As can be seen, the non-fluorinated anions show the highest viscosity, because they are able to form strong H-bonds with other ions. In case of the $[(CH_3O)_2PO_2]^-$ anion the bulky size (large molar volume) contributes additionally and

increases the viscosity further compared to $[CH_3CO_2]^-$. Considering the low viscous ILs, containing cyano groups, the effect of the size is contrariwise to the fluorinated anions. Here, the bulkier ones also show a lower viscosity that is related to the intermolecular interactions in the bulk liquid [112, 113].
A binary system, containing one cation and two different anions, shows also a systematic increase or decrease in viscosity depending on the exact composition of the IL mixture. In general, the viscosity of the mixtures are between the viscosities of the pure ILs. If the $[C_4mim][NTf_2]$ is the basic IL and a more viscous IL, e.g. $[C_4mim][SCN]$, is added, the viscosity of the mixture increases. Contrary, if a lower IL, e.g. $[C_4mim][NN(CN)_2]$, is used, the mixtures' viscosity decreases [112]. The group of *Vieira* [114] also examined the viscosity behavior for three different binary IL mixtures, i.e. $[C_4mim]\{[NO_3]_{(x)}[CH_3SO_3]_{(1-x)}\}$, $[C_4mim]\{[NO_3]_{(x)}[Cl]_{(1-x)}\}$, $[C_4mim]\{[CH_3SO_3]_{(x)}[Cl]_{(x-1)}\}$. They observed that the viscosity increases with increasing amount of the chloride containing IL. This is probably due to the better ability of Cl^- to form H-bonds with the imidazolium ring compared to the NO_3^- and $CH_3SO_3^-$ anions, which is also in agreement with the observations of *Almeida* and his group [112]. All experimental data were fitted according to the logarithmic VFT equation

$$\ln(\eta) = \ln(\eta_0) + \frac{B}{T - T_0} \tag{2.17}$$

which showed good agreement. Figure 2.26 shows exemplarily the aforementioned trend for the mixture $[C_4mim]\{[NO_3]_{(x)}[Cl]_{(1-x)}\}$ [114].

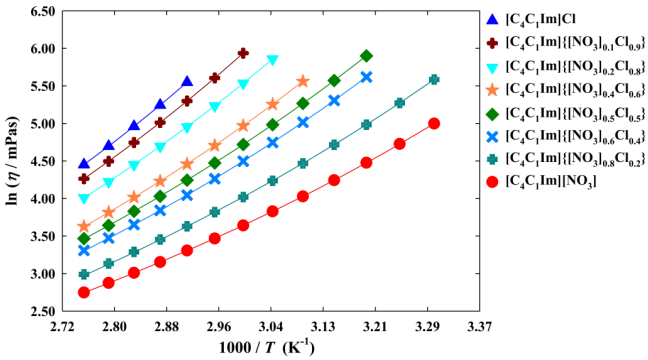

Figure 2.26. Temperature dependence of viscosity for the mixture of $[C_4mim]\{[NO_3]_{(x)}[Cl]_{(1-x)}\}$. Image from [114].

As already mentioned before, the purity of ILs is an important factor that needs to be considered. Over the last decades, many publications appeared which investigated the physicochemical properties of various ILs and tried to compare the results with previous results from other groups [22, 70, 71, 75, 112, 115, 116]. Very often significant deviations were found, which can be explained by several facts: the same ILs are purchased by different sources or synthesized individually and thereby the purification processes are different which results in differing impurities and purification results; the handling and storage of ILs, the sample preparation (e.g. drying) and the measurement technique itself (e.g. rotational rheometer vs. falling ball viscosimeter) add further uncertainties that yields in high variations of the results. Common impurities are water and halides due to absorption of moisture from air or residues of the synthesis, respectively, that show great impact on the viscosity.
Queiros et al. [116] investigated the influence of water on the thermophysical properties, i.e

density, speed of sound, viscosity, electrical and thermal conductivity as well as the refractive index, of 1-ethyl-3-methylimidazolium acetate. Figure 2.27 shows the viscosity dependence on temperature as a function of the mole fraction of water. It can be clearly seen that the viscosity decreases drastically with increasing water content. Another representation is shown in figure 2.28, where the viscosity is displayed as function of temperature for several IL-water mixtures using a VFT fit.

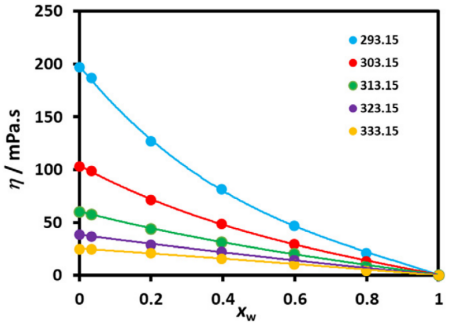

Figure 2.27. Viscosity of $[C_2C_1im][CH_3CO_2]$ - water mixtures as function of the molar fraction of water at different temperatures: • 293.15 K, • 303.15 K, • 313,15 K, • 323,15 K, • 333,15 K. Image from [116].

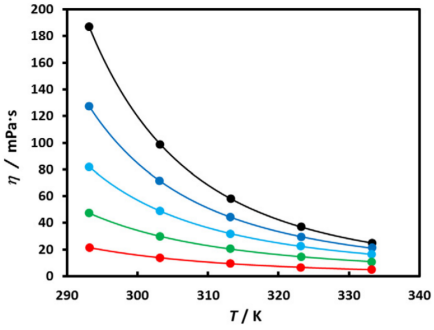

Figure 2.28. Viscosity of $[C_2C_1im][CH_3CO_2]$ - water mixtures as function of temperature represented as a VFT fit for different mole fractions of IL: • pure $[C_2C_1[CH_3CO_2]$ ($x_{IL} = 0.9660$), • $x_{IL} = 0.8022$, • $x_{IL} = 0.6049$, • $x_{IL} = 0.4017$, • $x_{IL} = 0.2013$. Image from [116].

The influence of impurities gets even more clear, if the obtained data of several groups for the same ILs are compared. As displayed in figure 2.29 the deviations in viscosity (100 (($\eta_{epx.}$ - $\eta_{lit.}$)/$\eta_{lit.}$)) for the same IL in the same temperature range can be quite large. *Almeida* and his group [117] measured nine different ILs with a common cation and different anions and compared their results with data from several groups found in literature. For the IL $[C_4C_1im][CH_3CO_2]$ especially large deviations, down to -34% (meaning, the viscosity of the references was much higher), were found. Furthermore, the ILs $[C_4C_1im][SCN]$, $[C_4C_1im][CF_3SO_3]$ and $[C_4C_1im]$-$[(CH_3O)_2PO_2]$ also show deviations of up to 10%. All other ILs, i.e. $[C_4C_1im][NTf_2]$, $[C_4C_1im]$-$[N(CN)_2]$, $[C_4C_1im][C(CN)_3]$, $[C_4C_1im][BF_4]$ and $[C_4C_1im][PF_6]$, show only small divergences, ranging from 0.08% to 3.80%.

Similar results were also found by other groups [22, 70, 71, 75, 112, 115] that compared their experimental data with data found in literature. This shows how important the information about impurities are in order to analyze and compare experimental viscosity data.

Density

As previously mentioned, the density decreases with temperature, but in contrast to viscosity it usually shows a linear behavior. However, in literature different fitting equations can be found. Mostly, a linear equation, such as

$$\rho = a + b(T) \tag{2.18}$$

is used, where a and b are adjustable parameters [71, 73, 111, 112]. On the other hand, several

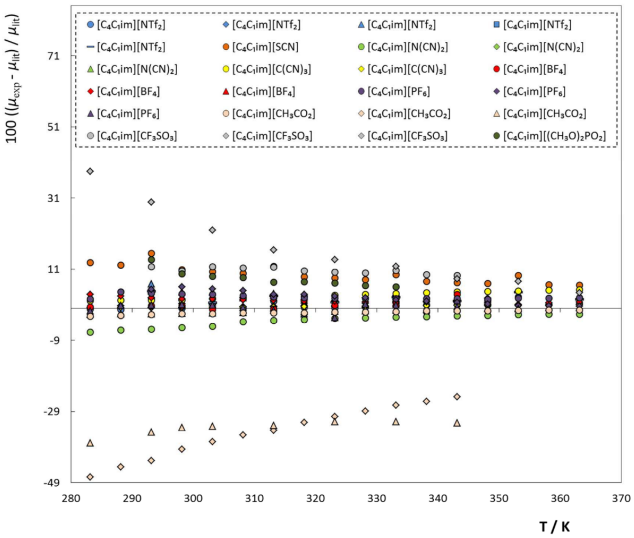

Figure 2.29. Comparison of viscosity data with several previously reported data sets by plotting the relative deviations of the experimental viscosity (in the work of *Almeida et al.* [117]: $\mu_{exp.}$) and the literature viscosity ($\mu_{lit.}$) against the temperature. Different symbols represent different references, while the same color corresponds to the same IL. Image from [117].

groups [118–121] also use polynomials of second order to describe the density dependence on temperature.

$$\rho = \rho_0 + \rho_1 T + \rho_2 T^2 \tag{2.19}$$

Here, T is the absolute temperature in K and ρ_0, ρ_1 and ρ_2 are fitting parameters. Which equation to use it part of a controversy discussion [112]. Using the temperature-dependent density data, the isobaric thermal expansion coefficient, α_p, of an IL can be determined by the following equation

$$\alpha_p = -\left(\frac{\partial \ln\rho}{\partial T}\right)_p \tag{2.20}$$

where p is the pressure [71,119,122]. In general, the thermal expansion coefficient of most ILs decreases slightly with increasing temperature and lies around (5 - 8) $\cdot 10^{-4}$ K^{-1}. The exception are the two ILs [C_8C_1im][Br] and [C_8C_1im][I] for which α_p increases weakly with increasing temperature. Furthermore, the thermal expansion coefficient does not significantly vary with temperature, which is why an average thermal expansion coefficient independent of temperature can be provided [119].
A second parameter that depends inversely on density is the molar volume, $V_{m,\,exp}$, that represents the miscibility of two ILs with each other. It is defined as follows

$$V_{\mathrm{m,exp}} = \frac{xM_1 + (x-1)M_2}{\rho} \tag{2.21}$$

where x and M are the mole fraction and molecular weight of IL 1 and IL 2, respectively, and ρ is the density of the pure IL or the mixture of two ILs depending on the mole fraction used. If equation 2.21 results in a linear correlation for all molar fractions, ideal mixing occurs for the ILs used. Deviations of this ideal behavior are usually quite small for most of the IL mixtures. However, to acknowledge the differences of experimental molar volumes from ideality, the excess molar volume can be calculated according to [112]

$$V_m = V_{\mathrm{m,\,exp}} \cdot \left(\frac{x M_1}{\rho_1} + \frac{(x-1) M_2}{\rho_2} \right) \tag{2.22}$$

The variation of parameters, e.g. size of cation and anion, alkyl chain length of the cation, water content etc. influences also the density of ILs. *Almeida et al.* [112] investigated the influence of the anion size for a common cation, $[C_4C_1im]$. They found, with few exceptions, that the smaller the anion the smaller the density is and presented the following order of anions for $[C_4C_1im]$: $[NTf_2]^-$ (ρ = 1.4372 g cm^{-3}, V_m = 291.80 cm^3 mol^{-1}) > $[CF_3SO_3]^-$ (ρ = 1.2963 g cm^{-3}, V_m = 222.39 cm^3 mol^{-1}) > $[PF_6]^-$ (ρ = 1.3676 g cm^{-3}, V_m = 209.99 cm^3 mol^{-1}) > $[BF_4]^-$ (ρ = 1.2016 g cm^{-3}, V_m = 188.16 cm^3 mol^{-1}) > $[(CH_3O)_2PO_2]^-$ (ρ = 1.1579 g cm^{-3}, V_m = 228.03 cm^3 mol^{-1}) > $[CH_3CO_2]^-$ (ρ = 1.0528 g cm^{-3}, V_m = 188.32 cm^3 mol^{-1}). Especially, the cyano-based ILs show the opposite behavior, i.e. with increasing molar volume the density decreases. This can be explained by the non-homologous central atoms and yields the order $[SCN]^-$ (ρ = 1.0702 g cm^{-3}, V_m =) 184.36 cm^3 mol^{-1}) > $[N(CN)_2]^-$ (ρ = 1.0602 g cm^{-3}, V_m =) 193.60 cm^3 mol^{-1}) > $[C(CN)_3]^-$ (ρ = 1.0476 g cm^{-3}, V_m =) 1218.86 cm^3 mol^{-1}) [112, 119].
The group of *Kolbeck* [119] also investigated the influence of different cations on the density using $[NTf_2]^-$ as common anion. More specifically, they addressed three different aspects: First, the length of the alkyl chain on the imidazolium, second, the functionalization of the chain with hydrophilic groups, third, the head group of the cation. In general, the density decreases with increasing alkyl chain length due to increasing dispersive interactions that lead to a separation of the polar cationic head groups and anions and the non-polar alkyl chains. The introduction of hydrophilic groups into the alkyl chain, e.g. ethylene glycol, yields an increase in density compared to a nonfunctionalized IL comprising a similar alkyl chain length (e.g. $[C_7C_1im][NTF_2]$). This increase can be explained due to the formation of inter- and intramolecular H-bonds that are not present in the nonfunctionalized ILs. The third examined aspect, the exchange of the cationic head group, results in no clear statement, yet, since different groups found different trends. However, *Kolbeck et al.* [119] found that exchanging the imidazolium ($[C_4C_1im][NTf_2]$) by pyrrolidinium ($[C_4C_1pyrr][NTf_2]$) reduces the density from 1.435 g cm^{-3} to 1.394 g cm^{-3}. This finding is also confirmed by others [72,90] and a possible explanation is the planar configuration of the imidazolium cation compared to the pyrrolidinium one that allows a denser packing. However, *Sánchez et al.* [123] found the opposite trend using the dicyanamide anion, arguing that the anion influences the preferential conformation of the cation that effects the density.
In contrast to the previously discussed influence of water on viscosity, water shows only an insignificant impact on density. This is probably due to large difference in molecular weight (190 - 640 g mol^{-1} for ILs vs. 18 g mol^{-1} for water) and the similarity in density (1.0 - 1.6 g cm^{-3} for ILs vs. 1.0 g cm^{-3} for water) [119]. This is also confirmed by the quite small relative deviations between experimental results and literature data ($\pm$ -0.70 - 0.5 %) given by several groups [112, 123, 124]. Figure 2.30 displays the effect of different cations and anions, respectively as well as the influence of the alkyl chain length at the cation and the introduction of an hydrophilic group or the exchange of the head group from imidazolium to pyrrolidinium.

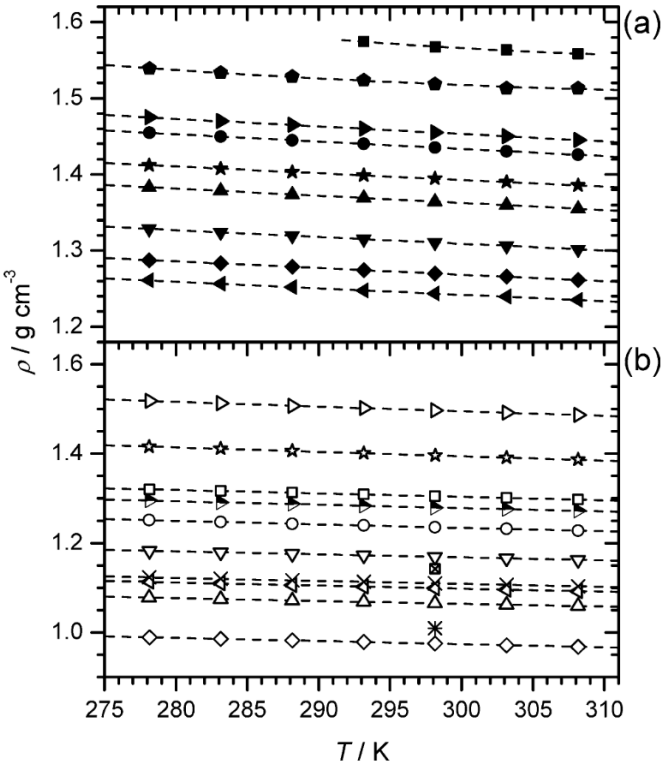

Figure 2.30. Temperature dependent density behavior of a) different $[NTf_2]^-$ salts: ■ $[C_1C_1im][NTf_2]$, ⬟ $[C_2C_1im][NTf_2]$, ● $[C_4C_1im][NTf_2]$, ▲ $[C_6C_1im][NTf_2]$, ▼ $[C_8C_1im][NTf_2]$, ◆ $[C_{10}C_1im][NTf_2]$, ◀ $[C_{12}C_1im][NTf_2]$, ★ $[C_4C_1pyrr][NTf_2]$, ▶ $[Me(EG)_2C_1im][NTf_2]$ and b) different $[C_8C_1im]^+$ salts: ▷ $[C_8C_1im][FAP]$, ☆ $[C_8C_1im][NPf_2]$, □ $[C_8C_1im]I$, ○ $[C_8C_1im][PF_6]$, ▽ $[C_8C_1im]Br$, ⊠ $[C_8C_1im][OTf]$, × $[C_8C_1im][CH_3OSO_3]$, ◁ $[C_8C_1im][BF_4]$, △ $[C_8C_1im][NO_3]$, ∗ $[C_8C_1im]Cl$, ◇ $[C_8C_1im][B(CN)_4]$, ▷ $[C_2C_1im][BF_4]$. Image from [119].

Ionic Conductivity

The ionic conductivity, κ, is another important physicochemical property of ILs and indirectly related with viscosity. Thus, it is not surprising that the alkyl chain length of the cation and the purity of the IL have a great influence on κ and hence, a large deviation of values for κ can be found in literature. In general, the ionic conductivity increases with increasing temperature and decreases with increasing alkyl chain length [125, 126]. This is shown in figures 2.31 to 2.34.

Stoppa et al. [125] determined the ionic conductivity of four different imidazolium-based ILs with increasing alkyl chain length from -35°C to 195°C. Similar to the viscosity, the behavior of κ with temperature can be described by a Vogel-Fulcher-Tamman equation (this equation applies to all transport properties of glass-forming liquids, i.e. ILs, above their glass-transition temperature (T_g)). Here, it has the following form:

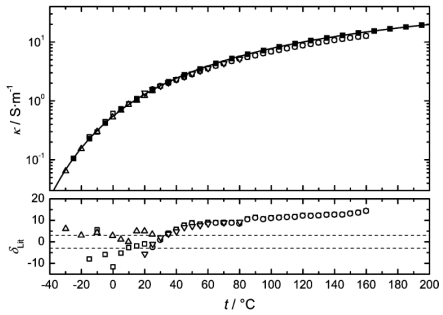

Figure 2.31. Comparison of ionic conductivities (κ) of $[C_2C_1im][BF_4]$ as well as relative deviations (δ_{Lit}) from several references. ■ displays the data determined by *Stoppa et al.* [125]; □, ○, △ and ▽ are values found in literature. The solid line represents a VFT fit according to equation 2.23; the dashed lines display an arbitrary margin of ± 3 for δ_{Lit}. Image from [125].

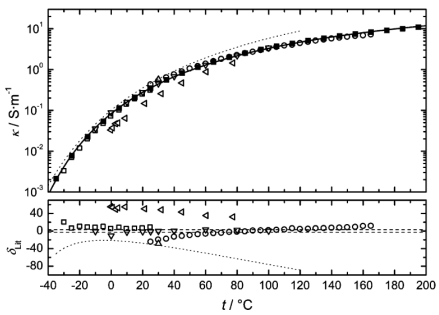

Figure 2.32. Comparison of ionic conductivities (κ) of $[C_4C_1im][BF_4]$ as well as relative deviations (δ_{Lit}) from several references. ■ displays the data determined by *Stoppa et al.* [125]; □, ○, △ and ▽ are values found in literature. The solid line represents a VFT fit according to equation 2.23; the dashed lines display an arbitrary margin of ± 3 for δ_{Lit}. Image from [125].

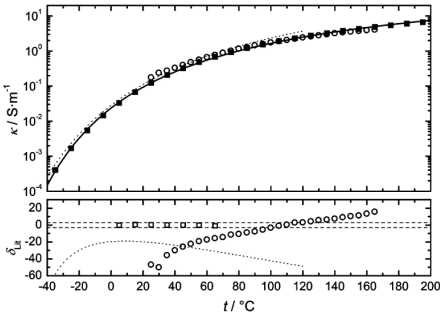

Figure 2.33. Comparison of ionic conductivities (κ) of $[C_6C_1im][BF_4]$ as well as relative deviations (δ_{Lit}) from several references. ■ displays the data determined by *Stoppa et al.* [125]; □ and ○, are values found in literature. The solid line represents a VFT fit according to equation 2.23; the dashed lines display an arbitrary margin of ± 3 for δ_{Lit}. Image from [125].

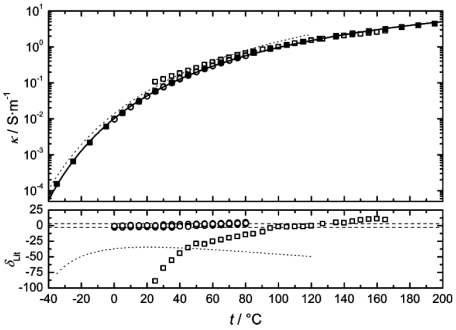

Figure 2.34. Comparison of ionic conductivities (κ) of $[C_8C_1im][BF_4]$ as well as relative deviations (δ_{Lit}) from several references. ■ displays the data determined by *Stoppa et al.* [125]; □, ○, are values found in literature. The solid line represents a VFT fit according to equation 2.23; the dashed lines display an arbitrary margin of ± 3 for δ_{Lit}. Image from [125].

$$\ln(\kappa) = \ln(\kappa') + \frac{B_\kappa}{T - T_{0,\kappa}} \tag{2.23}$$

κ' and B_κ are fit parameters and $T_{0,\kappa}$ is the so called VFT-temperature. $T_{0,\kappa}$ usually lies 20 - 30 K below the T_g values that can be determined using differential scanning calorimetry.
The large deviations ($\delta_{Lit} = 100(\kappa - \kappa_{Lit})/\kappa$) are mainly due to two reasons. First, during the measurement of κ the electrode polarization is neglected or inappropriately treated. However,

the groups that corrected their data with respect to the electrode polarization show good agreement with the data of *Stoppa et al.* (see ▽ figure 2.32 and ○ figure 2.34). The second reason usually is the degree of impurity of the ILs that is not always stated in literature. A main contribution onto the latter reason is the hydrolysis of the BF_4^- anion, either during the synthesis or the conductivity measurement itself [125].
The conductivity range of ILs is rather broad, ranging from 0.1 mS cm^{-1} up to 20 mS cm^{-1} [83]. Especially, ILs belonging to the imidazolium family exhibit relative high conductivities around 10 mS cm^{-1}, while the highest conductivity of *N,N*-dialkyl-pyrrolidinium [NTf_2] salts lie at 2 mS cm^{-1}. The combination of imidazolium cations with the dicyanamide ([$N(CN)_2$]) anion results in the highest conductivities (up to 36 mS cm^{-1}) [127]. However, compared to the conductivity of common electrolytes, e.g. concentrated aqueous KOH solutions (29,4 wt%) applied in alkaline batteries, that show values of 540 mS cm−1, the conductivity of ILs is considerable lower [128]. Combining the ionic conductivity, the density and the molecular weight (while $\rho/M = c$, the molarity) of an IL, the molar conductivity, Λ can be calculated.

$$\Lambda = \frac{\kappa M}{\rho} = \frac{\kappa}{c} \tag{2.24}$$

Again, the temperature dependence can be well described by the VFT equation. Applying the so called *Walden* rule,

$$\Lambda \cdot \eta = \text{constant} \tag{2.25}$$

and displaying the data as log-log plot of Λ vs. η^{-1} (fluidity) the dissociation of the IL can be judged. In figure 2.35 the Walden plot of the four ILs [C_2C_1im][BF_4], [C_4C_1im][BF_4], [C_6C_1im][BF_4] and [C_8C_1im][BF_4] are presented. The solid line shows the "ideal" KCl line, which represents a completely dissociated electrolyte. Since the data of all ILs are quite close to this "ideal" KCl line, which means the ILs can be classified as "high-ionicity". The deviation from the ideality increases with increasing alkyl chain length in the order $[C_2C_1im]^+ > [C_4C_1im]^+ > [C_6C_1im]^+ \approx [C_8C_1im]^+$, which means the conductivity decreases. This is probably due to the separation of the hydrophobic alkyl chain and the hydrophilic head group of the cation, reflecting the increasing nanosegregation [125].
Tokuda et al. [126] as well as *Noda et al.* [129] presents a second method to determine the degree of dissociation of an IL. Therefore, they determined the molar conductivity in two different ways, namely by impedance spectroscopy and NMR measurements. Λ_{NMR} was calculated using the *Nernst-Einstein* relation.

$$\Lambda_{NMR} = \frac{N_A e^2 (D_{cation} + D_{anion})}{kT} = \frac{F^2 (D_{cation} + D_{anion})}{RT} \tag{2.26}$$

where N_A is the *Avogadro* number, e is the electric charge on each ion, F is *Faraday's* constant and R is the universal gas constant.
Afterwards, they calculated the ratio $\Lambda_{imp}/\Lambda_{NMR}$ and claimed that the non-unity indicates that not all diffusive species within an IL contribute to the ionic conduction, i.e. ionic aggregates and/or clusters are formed. In case of the NMR measurements, it is important to note that the process of association/disassociation is much faster than the intrinsic NMR time scale (10^{-9} - 10^{-10} s), which means that it is not possible to distinguish between a free ion and an associated one. Contrary to that, during the electrochemical impedance measurement an individual ion may migrate due to an applied electric field for a characteristic time when it exists as charged species. However, during this measurement the ion can also form a noncharged species by associating for another characteristic time, in which it does not contribute any more to the conduction.

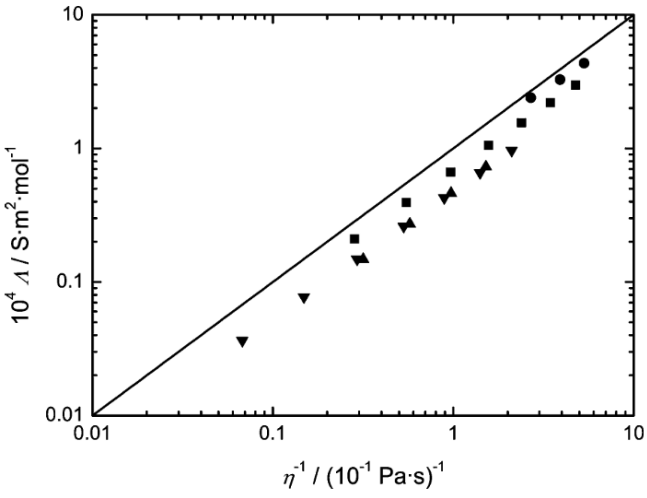

Figure 2.35. Walden plot of the ILs: ● $[C_2C_1im][BF_4]$, ■ $[C_4C_1im][BF_4]$, ▲ $[C_6C_1im][BF_4]$ and ▼ $[C_8C_1im][BF_4]$. The solid line represents the "ideal" KCl line. Image from [125].

2.3.4 Nernst-Einstein and Stokes-Einstein model

The previously discussed conductivity depends on the migration of the ionic species within an IL. This, of course, depends on the degree of dissociation of the IL into free ions which can be displayed by the Walden plot. However, to compare ILs with an ideal electrolyte (usually 1 M aqueous KCl solution) is somewhat difficult since the ion-solvent interactions of an electrolyte differs from the ion-ion interactions present in ILs [130]. Therefore, another principle based on the Nernst-Einstein equation (see equation 2.27) was introduced.

$$\Lambda = \frac{F^2}{RT}(v_+ z_+^2 D_{S+} + v_- z_-^2 D_{S-})(1 - \Delta) \tag{2.27}$$

v_i and z_i are stoichiometric and charge numbers, respectively, for a salt that dissociates in the way

$$A_{v+}B_{v-} \rightleftharpoons v_+ A^{z+} + v_- B^{z-} \tag{2.28}$$

while F, R and T denote the Faraday constant, the universal gas constant and the temperature in K and Δ is the Nernst-Einstein (NE) deviation parameter.

$$\Delta = 1 - \frac{RT\Lambda}{F^2(v_+ z_+^2 D_{S+} + v_- z_-^2 D_{S-})} = 1 - \frac{\Lambda}{\Lambda_{NE}} = 1 - Y \tag{2.29}$$

Here, the ionicity (denoted as $Y = \Lambda/\Lambda_{NE} < 1$) is defined as the ratio of the measured molar conductivity Λ of the IL to that calculated from ionic self-diffusion coefficients D_{Si} [131]. Self-diffusion is a kind of transport property of fluids and results from intermolecular collisions within the fluid. Δ equals 0 only in case of non-interacting ions, e.g. in infinitely diluted electrolyte solution. The ions in ILs, however, are in close contact with each other since the liquid structure is highly ordered due to Coulombic forces. This means that Δ contains information about the cation-cation-, anion-anion- and cation-anion-interactions. Depending on the nature of the IL, e.g. protic vs. aprotic, the values of Δ vary considerably. For instance, $\Delta = 0.41$ for

the aprotic IL $[C_4C_1im][BF_4]$, while $\Delta = 0.79$ for the protic IL $[PyrOMe][BF_4]$. With that, Δ can be seen as a substitute for the Walden plot, where the conductivity vs. viscosity was compared to a "ideal" KCl line [132].

The hydrodynamic Stokes-Einstein model can be used to examine the effect of ion size and charge. It links the interdiffusion coefficient D of a molecule with radius r and its shear viscosity η based on three assumptions. First, the size of the diffusing particle is much larger than the solvent molecules, second the interaction of diffusing particles can be ignored due to their low concentration and third the shape of the diffusing particle is spherical. These assumptions are not directly applicable for ionic liquids. However, *Ohtori et al.* showed that the Stokes-Einstein equation holds within the statistical errors also for non spherical liquids [133]. Equation 2.30 represents the classical Stokes-Einstein equation

$$D = \frac{kT}{n\pi\eta r} \tag{2.30}$$

with D as diffusion coefficient, k as *Boltzmann* constant, T as absolute temperature, η as shear viscosity, r as molecule radius and n as Stokes-Einstein number or the so called *Sutherland coefficient* that describes the hydrodynamic limits of a perfectly sticking surface or sliding sphere [134–136]. According to *Sutherland* [134], n can be expressed as follows:

$$n = 6\left(\frac{1 + 2\eta/\beta r}{1 + 3\eta/\beta r}\right) \tag{2.31}$$

where β depends on the viscosity and expresses the coefficient of sliding friction. For a perfect sticking surface $\beta = \infty$, while for a perfect sliding sphere $\beta = 0$, which means n lies between 6 and 4, respectively. The Stokes-Einstein model was derived for tracer molecules moving in a solvent continuum, e.g. colloidal and macromolecular systems. Resulting from this, the Stokes-Einstein number n has to be viscosity dependent.
Tokuda et al. [137] determined n for several ILs to gain a better understanding of the microscopic ion dynamics. Table 2.2 summarizes the results for the diffusion of the cation $[C_4C_1im]^+$ in five different ILs, i.e. $[C_4C_1im][(C_2F_5SO_2)_2N]$, $[C_4C_1im][NTf_2]$, $[C_4C_1im][CF_3SO_3]$, $[C_4C_1im][PF_6]$, $[C_4C_1im][BF_4]$, as well as the diffusion of the respective anion in those ILs. Additionally, figure 2.36 shows the experimental data as D vs. T η^{-1} plots.

Table 2.2. The Stokes-Einstein numbers for the diffusion of the cation $[C_4C_1im]^+$ and the respective anions in the ILs $[C_4C_1im][(C_2F_5SO_2)_2N]$, $[C_4C_1im][NTf_2]$, $[C_4C_1im][CF_3SO_3]$, $[C_4C_1im][PF_6]$, $[C_4C_1im][BF_4]$ [137].

IL	van der Waals radii r (nm)	Stokes-Einstein number n of cation	Stokes-Einstein number n of anion
$[C_4C_1im]^+$	0.330		
$[(C_2F_5SO_2)_2N]^-$	0.362	3.3	4.1
$[NTf_2]^-$	0.326	3.4	4.3
$[CF_3SO_3]^-$	0.267	3.4	5.0
$[PF_6]^-$	0.254	3.0	4.6
$[BF_4]^-$	0.227	3.3	4.6

The obtained values indicate that the cation diffuses faster, because the n values are smaller, than the anion if they have the same *van der Waals* radii. Interestingly, this is still true for $[C_4C_1im][BF_4]$, although the radii of cation and anion show a large discrepancy, with the anion

having the smaller radius. However, the Stokes-Einstein number of the cation is smaller which means that the diffusion of the cation is still faster than the diffusion of the $[BF_4]^-$ anion [137].

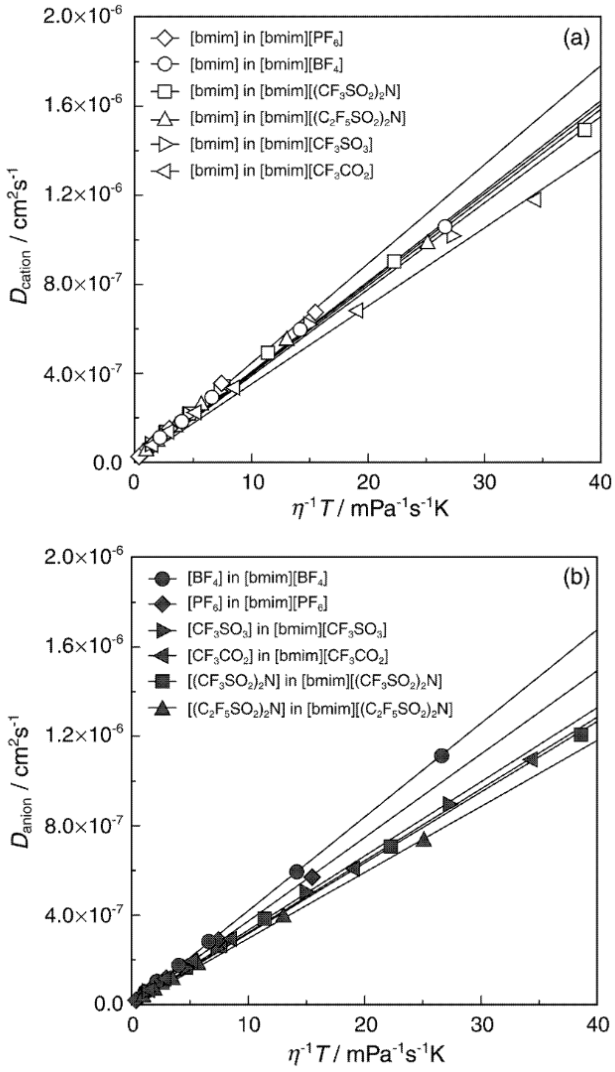

Figure 2.36. Relationship of T η^{-1} and self-diffusion coefficients for a) the cation and b) the anion in $[C_4C_1im]$ based ILs. Image from [137].

As alternative to the classical Stokes-Einstein relation, the so called fractional Stokes-Einstein equation (FSE) can be used to describe self-diffusion in ILs (and other liquids).

$$D \propto \left(\frac{1}{\eta}\right)^t \tag{2.32}$$

where t is a fitted constant ranging between $0 < t < 1$. The viscosity dependent Stokes-Einstein number can than be expressed as follows:

$$\ln(n) = \ln(n_0) + (t-1)\ln(\eta) \tag{2.33}$$

with n_0 representing n at unit viscosity and t is experimentally found to be between 2/3 and 1 and increases with increasing molar volume of the diffusive species. [131, 136, 138].
Furthermore, in literature are two forms of the temperature dependent FSE available. The first form is an extension of equation 2.30

$$\frac{D}{T} \propto \left(\frac{1}{\eta}\right)^t \tag{2.34}$$

The second one can be written as

$$D \propto \left(\frac{T}{\eta}\right)^s \tag{2.35}$$

The exponents t and s are usually determined by calculating the slope of experimental log-log plots. Although, t and s depend on the used units for D and η, experience showed that the difference is mostly negligible [136].
Combining the approaches of Nernst-Einstein and Stokes-Einstein, an expression called fractional Walden relation is obtained that includes the molar conductivity Λ since Λ is proportional to the sum of the self-diffusion coefficients in equation 2.27 [136].

$$\Lambda T \propto D \propto \left(\frac{T}{\eta}\right)^s \tag{2.36}$$

Harris et al. [77, 139] showed that Δ, the Nernst-Einstein deviation parameter, is independent of temperature and pressure and that the exponent s lies around 0.90 ± 0.05. The group of *Zech* [140] also found values for s that agree well with the previously reported ones. For instance, good fits were obtained for values of $s = 0.86$ for $[C_4C_1im][BF_4]$, $s = 0.88$ for $[C_4C_1im][CF_3SO_3]$ and $s = 0.86$ for $[C_4C_1im][CF_3CO_2]$ (see figure 2.37).

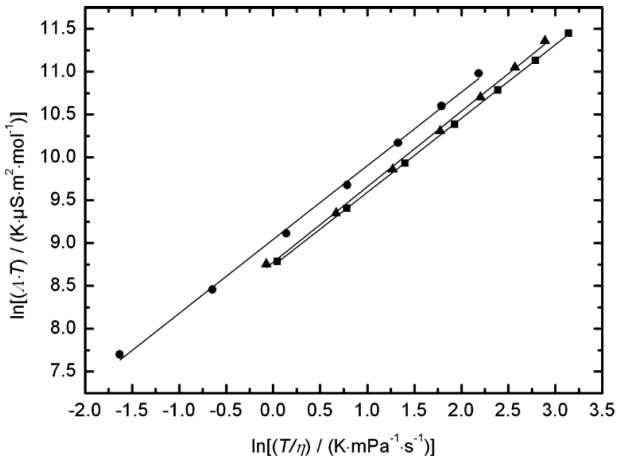

Figure 2.37. Fractional Walden plot with [ln(Λ T) vs. ln(T η^{-1})] for the ILs ● $[C_4C_1im][PF_6]$, ▲ $[C_4C_1im][CF_3SO_3$ and ■ $C_4C_1im][CF_3CO_2]$. The solid lines represent linear least square fits of the form ln[(Λ T)/(K μS m^2 mol^{-1}] = t · ln[(T η^{-1})/(K mPa^{-1}s^{-1})] + C. Image from [140].

2.3.5 Electrochemistry of ILs

The unique properties of ILs make them of interest in many fields of application. One of these properties is the large electrochemical window in which they are stable. Together with the high conductivity, ILs are suitable for the broad field of electrochemistry. However, in contrast to classical electrolytes that are obtained by dissolving a salt into a molecular solvent which results in a mixture of solvated ions, their neutral or charged combinations and solvent molecules, ILs only comprise charged ions. This makes them quite different from normal electrolytes which yields the necessity to derive some new concepts to describe the processes taking place during electrochemical experiments. In the following, the main aspects of ILs in electrochemistry are introduced.

2.3.5.1 Electrochemical Window

One important feature that makes ILs interesting for electrochemistry is the broad electrochemical window in which they are redox-robust. This window can be as large as 7 V, however, most ILs show a range of 4.5 - 5 V between the cathodic and anodic limit [128, 141]. Important to note is that these windows depend on the system configuration that was chosen to measure it, i.e. the working and reference electrodes. Very often the working electrode and the reference system found in literature differ which makes it difficult to compare results [128]. Moreover, the purity of the ILs play also here an significant role and can change the width of the electrochemical window. The cathodic and anodic limit is defined as the potential at which the cation gets reduced and the anion gets oxidized, respectively, and both are always depending on the counterion. Nevertheless, a general trend can be observed, showing that quarternary ammonium and pyrrolidinium salts are more stable than the corresponding imidazolium salts due to the acidic C^2-H-group that yields a quite stable carbene configuration upon reduction. Considering the anions, the fluorinated ones, especially [NTf_2], show a high stability against oxidation [83, 141].

2.3.5.2 Electrochemical Double Layer (EDL)

In classical electrochemistry, several models were developed to describe the electrode-electrolyte interface, which can be viewed as parallel-plate.capacitor. In 1879, Helmholtz [142] was the first who described the interface of an electrode and an electrolyte. Around 30 years later, Gouy and Chapman [143, 144], independently of each other, proposed a different model which again was adapted by Stern [145] in 1924. Since then, several more changes were proposed to describe the metal-electrolyte interface [146].
Helmholtz described the EDL as parallel-plate-capacitor in which the metal surface carries for instance a positive charge and the electrolyte layer closest to the metal surface a negative one. The distance between the metal surface and the counterions adsorbed to it corresponds to the radius of the solvated ion, labeled with H in figure 2.38a, and is also called the *Helmholtz double layer*. This means that the interface as such must be electroneutral. However, this model is insufficient since it can only explain the existence of a capacitance but not its dependence on potential. For a planar electrode the specific capacitance of the Helmholtz double layer can be expressed as [147, 148]

$$C_s^H = \frac{\epsilon_0 \epsilon_r}{H} \tag{2.37}$$

where ϵ_0 and ϵ_r are the permittivity of free space ($8.8542 \cdot 10^{-12}$ $C^2J^{-1}m^{-1}$) and the ratio between the permittivity of the solvent and the free space, also called dielectric constant, respectively.

The approach of Gouy and Chapman [143, 144] takes into account that the ions are mobile due to random thermal motion (diffusion) to balance the concentration through the solution while at the same time influenced by the electrostatic forces of the electrode surface. This is called *diffusive layer* and can be described by the well-known *Boltzmann equation* in which the ions are treated as point charges [147, 148].

$$c_i = c_{i,\infty} e^{\frac{-z_i e \Psi}{k_B T}} \tag{2.38}$$

Here, c_i and $c_{i,\infty}$ represent the equilibrium and bulk concentration of species *i*, respectively, z_i is the charge of the ion, *e* the elementary charge, Ψ the potential at distance x and k_B and T are the *Boltzman* constant and absolute temperature, respectively. The local electric potential Ψ in the diffusive layer can be determined by the Poisson-Boltzmann equation assuming constant solution permittivity and considering some boundary conditions: $\Psi(0) = \Psi_D$ and $\Psi(\infty) = 0$. With that the specific capacitance of a planar electrode can be defined as [147, 148]

$$C_s^D = \frac{q_s}{\Psi_D} = \frac{4zeN_A c_\infty \lambda_D}{\Psi_D} \sinh\left(\frac{ze\Psi_D}{2k_B T}\right) \tag{2.39}$$

with q_s denoting the surface charge density, N_A as *Avogadro's* number ($N_A = 6.022 \cdot 10^{23}$ mol^{-1}) and λ_D is the Debye length. The latter is defined as [147]

$$\lambda_D = \left(\frac{\epsilon_0 \epsilon_r k_B T}{2e^2 z^2 N_A c_\infty}\right)^{1/2} \tag{2.40}$$

and gives the distance of the charged surface at which the potential has decayed by a factor of $1/e$ (here, *e* is Euler's number).
Since the Helmholtz double layer corresponds to a parallel plate capacitor the potential Ψ_s decays linearly, as displayed in figure 2.38a. The diffusive layer of Gouy and Chapman, however, decreases exponentially due to the Debye length as shown in figure 2.38b.

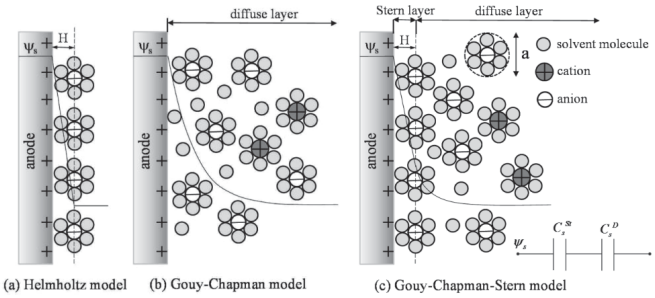

Figure 2.38. Schematic presentation of a) the Helmholtz model, b) the Gouy-Chapman model and c) the Gouy-Chapman-Stern model. Image from [147].

Unfortunately, neither the Helmholtz nor the Gouy-Chapman model are able to explain the experimental findings by itself. Only the combination of the two models, done by *Stern* in 1924, results in good agreement of theory and experiment. As figure 2.38c shows, *Stern* postulated a thin layer of ions at the electrode surface that represents the Helmholtz layer, also called Stern layer, and a diffusive layer as Gouy and Chapman described it. The total electric double layer capacitance can therefore be represented as the Stern and diffusive layer capacitance in series

and shows a potential and concentration dependency [147, 148].
Applying these models to pure and solvent-free ionic liquids bears several problems, though. For one, the models are developed for diluted electrolyte solutions, while ILs are purely ionic and therefore show very high ion concentrations. Another point that has to be taken into account is that the Helmholtz model treats the ions as hard spheres and the Gouy-Chapman model considers the ions as point charges - both assumptions are not applicable to ILs. However, there exist a few studies of ILs and their double-layer capacitance characteristics which show that the values of these double-layer capacitances are comparable to those of non-aqueous solvent/electrolyte systems [149,150].To explain these findings, Oldham [146] developed an Gouy-Chapman-Stern model for the metal-IL-interface. Around the same time Kornyshev et al. [151–156] started to develop a model based on the mean-field theory and used molecular dynamics simulations to describe the differential capacitance of electrode-IL-interfaces which was extended by the group of Yan [157] in 2014. Here, only a brief description of the main aspects of these models will be given. For further details see references [146, 151–157].
In the first approach of Kornyshev et al. [151], they introduced a so called mean-field lattice-gas model in which he assumed that the ions occupy certain spaces within a lattice while there are also free voids. Yan et al. [157] extended this model by considering the different sizes of cations and anions. Figure 2.39 shows a two-dimensional representation of such a lattice-gas model.

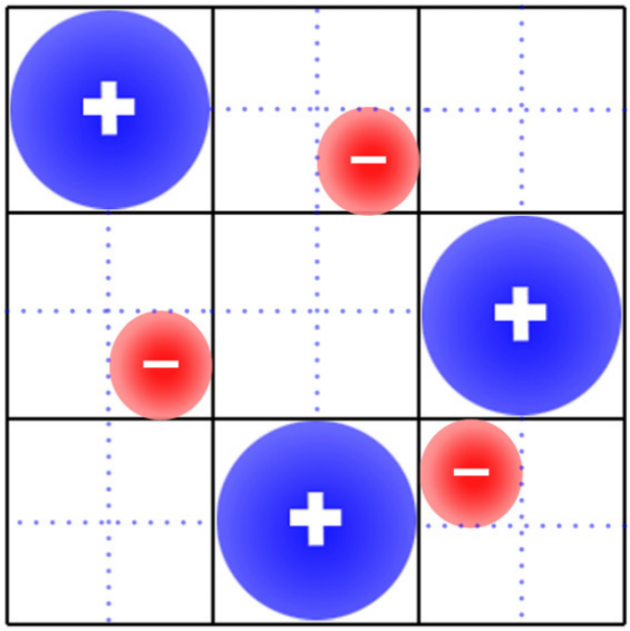

,

Figure 2.39. Schematic, two-dimensional presentation of a lattice-gas model. The cations are displayed in blue and the anions in red, representing the different sizes of the ions. Image from [157].

Kornyshev introduced a parameter γ, the compacity or packing parameter (see figure 2.40), which puts the total number of ions in the bulk ($\bar{N}$) in relation to the available sites for them (N) or in other words, assuming there is no change in total volume, it is the relation of the ions' concentration (c_0) to the maximal possible local concentration of ions (c_{max}) [151].

$$\gamma = \frac{\bar{N}}{N} = \frac{2c_0}{c_{max}} \tag{2.41}$$

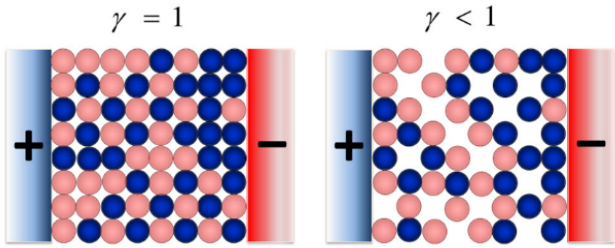

,

Figure 2.40. Schematic representation of the compacity parameter γ for an IL between two electrodes. The red spheres display the anions, the blue ones depict the cations while the free spaces in the lattice represent the voids. The left picture shows a lattice for $\gamma = 1$, the right one for $\gamma = 0.75$. Image from [158].

With that the finite size of the ions are taken into consideration, because it does not matter how the system (comprising electrode and electrolyte) is polarized, the maximal possible concentration cannot be exceeded. It turned out that $\gamma = 1/3$ represents a boundary condition that influences the shape of the capacitance curve due to a phenomenon called *electrostriction* [151]. The capacitance curve of the Gouy-Chapman-Stern model shows an U-shaped form, while the capacitance curves according to the mean-field lattice-gas model shows either a bell-shaped ($\gamma > 1/3$) or a camel-shaped ($\gamma < 1/3$) form as shown in figure 2.41. In addition an experimental capacitance curve of the IL $[C_6C_1im][Cl]$ is displayed. For the simulations, three different models were defined, representing different lengths of the alkyl chains of common (imidazolium) cations. The one bead model (1 BM) is comparable to the $[C_2C_1im]^+$ cation and consists of one charged bead (blue thin solid line in figure 2.41). The two (green dash-dotted line) and three (red dashed line) bead models (2 BM and 3 BM, respectively) comprises one and two neutral beads and one charged bead, respectively, and represent $[C_6C_1im]^+$ and $[C_9C_1im]^+$ cations.

As can be seen, the experimental data in figure 2.41 are quite well matched by the simulations for the two and three bead models. Both showing a camel-shaped curve at which the anodic peak is higher than the cathodic one and exhibiting a local minimum at 0 V. The maxima of the two bead model are located at 0.35 V and -0.4 V and for the three bead model at 0.4 V and -0.5 V, respectively. Important to note is that the overall bead density is for all three models the same. [154, 155]

The change in shape of the capacitance curve can be explained by the geometry of the cation. In the 2BM and 3BM models the neutral beads represent the different alkyl chain length of common (imidazolium) cations. The packing parameter for the one bead model, representing the $[C_2C_1im]^+$ cation with a quite short alkyl chain, was estimated to be $\gamma_{1BM} = 0.3$ for which a bell-shaped curved is expected. This expectation goes along with a relative high density of charged beads. Contrary to that, the one and two neutral beads of the 2BM and 3BM, respectively, represent much longer alkyl chains which can cause voids or act as spacers within the IL and in turn reduces the density of charged beads and with that the capacitance itself. Having a closer look at the experimental data, it can be seen that the anodic capacitance maximum lies at a higher anodic polarization than the simulation predicts. This can be explained by the fact that the tail of the cations (neutral beads) are assumed to be rigid in the simulations while in reality the

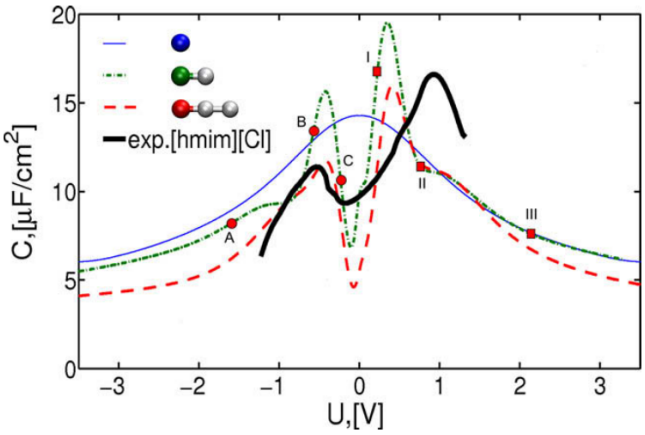

Figure 2.41. Differential capacitance curves obtained from simulations for three model systems which differ in cation geometry. For comparison, a one bead cation, e.g. $[C_2C_1im]^+$ (blue; thin solid line) was used showing a maximum value of capacitance at 0 V. A dumbbell model consisting of one charged and one neutral bead (green; dash-dotted line) was used to indicate the elongated shape of the cation, e.g. $[C_6C_1im]^+$. The three bead model comprising two neutral and one charged bead (red; dashed line) represents an even more elongated tail of the cation, e.g. $[C_9C_1im]^+$. For both, the two and three bead model a camel-shaped curve was obtained with maxima at 0.35 V/-0.4 V and 0.4V/-0.5 V, respectively. The anion was in all cases the same and simulated as one single charged bead. Additionally, the experimental curve of $[C_6C_1im][Cl]$ (black; thick solid line) is shown. The points (A) - (C) and (I) - (III) indicate the positions for which the neutral bead number densities were computed and are shown in figure 2.42. Image from [154, 155].

$[C_6C_1im]^+$ cation has a rather long flexible alkyl chain. This in turn results in the need of higher electrode charge densities, σ, to exchange the tails of the cations with their heads [154, 155]. Therefore, Kornyshev and his group [154, 155] computed the neutral bead number densities ($n^0(z)$) for cathodic and anodic polarization of the 2 BM as can be seen in figure 2.42. The different curves (A) - (C) and (I) - (III) correspond to the values of the electrode charge densities σ indicated in figure 2.41.

Depending on the electrode charge density σ, the cations show different orientations with respect to the electrode surface. For low $|\sigma|$, they are either oriented with the neutral heads towards the electrode or they lie flat on the surface. For higher $|\sigma|$ the orientation changes depending on the kind of polarization of the electrode. For a high cathodic polarization, the tails of the cations are pointing away from the electrode surface and are located in the "second" layer of the double layer. In case of anodic polarization, the cations are replaced by anions in the first layer, close to the electrode, and no clear orientation of the cations can be found anymore. This results in local maximal values of charge density for both cathodic and anodic polarization, which do not need to be equal to each other necessarily. These values could also be considerably larger than the average charge density in the bulk. The amplitude of this increase depends mainly on the length of the tail of the cation and with that on the number of voids or spacers with in the

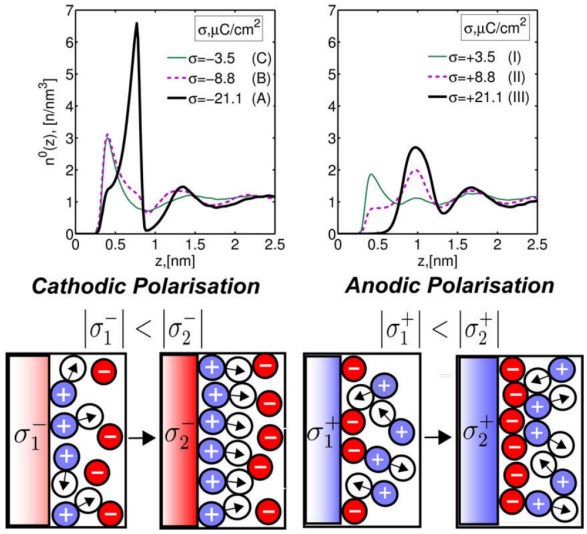

Figure 2.42. Top: Neutral bead number densities for cathodic (left) and anodic (right) polarization of the 2 BM system at the positions of the electrode charge densities σ indicated in figure 2.41. With increasing polarization the neutral bead number density decreases in both cases, i.e. the neutral beads are expelled from the region closest to the electrode surface. For very high cathodic polarization a peak maximum around $z \approx 0.75$ nm can be observed due to the alignment of the cations with their neutral bead away from the electrode surface. For very high anodic polarization the neutral beads are expelled from the region close to the electrode surface due to the accumulation of anions at this site which can be seen by the peak around $z \approx 1$ nm.
Bottom: The lower part displays a cartoon-like picture of the orientation of the cations and anions for different polarizations. It can be seen that the neutral beads (indicated by the arrows) of the cations tend to align away from the electrode surface for high cathodic polarization and thereby form a layer that separates the cations from the anions. On the other hand, high anodic polarization yields in the close alignment of anions to the electrode surface while the second layer comprises the cations with no preferential orientation. This also explain the broader peak in the right top plot. Image from [154, 155].

IL [154]. This phenomenon is also called *overscreening* because the ion layer adjacent to the electrode surface contains more charge than required to compensate the charge of the electrode. Thus, the second ion layer also exhibits an excess of co-charges, followed by another layer with surplus counter-charges, and so on. Impedance measurements suggest that these reorientation processes are slow and take place at the time scale of seconds [159].
In case of high electrode potential, the electrode charge cannot be compensated by one single layer of counter-ions anymore, but rather by an accumulation of them. This effect is called lattice saturation and causes a decay of the differential interfacial capacitance with $C_{int} \sim \Delta\varphi^{-1/2}$. The transition from overscreening to lattice saturation can take place in quite a large potential range

as shown by Vatamanu et al. via molecular dynamics simulations [160]. They also found that the lattice saturation effect only will take place at potentials (± 15 V) beyond the electrochemical window in which ILs are stable. Mao et al. [161] gives an comprehensive review about the ionic structures of ILs as well as the theoretical models of their EDLs and some computationald methods.

Besides the potential of the electrode, the purity of the IL and the temperature at which the differential capacitance is measured influences the interfacial structure of the EDL. Especially ILs with PF_6^- or BF_4^- as anion are prone to hydrolysis. Moreover, the BF_4^- anion never shows a stable behavior in the presence of water, which makes it difficult to handle under experimental conditions. The influence of temperature on the interfacial capacitance is less clear, though. Drüschler et al. [159] investigated the influence of temperature on the interfacial capacitance of the system 1-butyl-1-methylpyrrolidinium tris(pentafluoroethyl)trifluorophosphate ($[C_4C_1pyrr][FAP]$)/Au(111). The interface was modeled by a simple RC equivalent circuit where the resistance represents the ion transport within the IL and the capacitance expresses the EDL. This yields in the expression for the double layer charging time of $\tau = RC$. As discussed before (see section 2.3.3.1), the ionic conductivity of ILs increases with increasing temperature, which means that the resistance R decreases at elevated temperatures as well as τ. The same can be expected of the interfacial processes and thus for the capactiance C [159]. However, in literature different results can be found. Lockett et al. [162] for example found that for $[C_4C_1im][BF_4]$ the differential capacitance increases with increasing temperature, while the local minimum is shifted at elevated temperatures about 0.1 V towards more negative potentials, which indicates a more weakly specifically adsorption of the cation onto the electrode surface. In contrast to that, many theoretical models predict the opposite beahvior, namely the decrease of differential capacitance at elevated temperatures or a rather complicated behavior [156, 163]. Moreover, the experimental investigations (electrochemical impedance spectroscopy) of Drüschler et al. [159] also show a decrease of differential capacitance with increasing temperature. However, if they only choose one frequency (here 10 Hz, because the impedance phase angle is close to -90° which represents ideal capacitive behavior) and investigate the temperature dependence there, they also find an increase of capacitance with temperature. Plotting the data in a complex capacitance plane reveals that the position of the data points measured at 10 Hz exhibits a strong temperature dependence. They conclude that the found increase of capacitance with temperature at a single frequency is therefore an artifact resulting from the temperature dependence of two capacitive processes [159].

2.4 Microelectrodes as Versatile Tool for Electrochemical Processes

The characteristics, e.g. size, geometry, arrangement of the electrode play an important role in electrochemical measurements, because the electrode behavior changes with its dimension. Although there is not a strict definition of microelectrodes, Bard and Faulkner [164], Buzzeo et al. [149] as well as Aoki [165] suggest the following aspects need to be fulfilled: one, the electrode has to be smaller than the scale of the diffusion layer in typical experiments and two, one dimension has to be smaller than 25 μm (called: critical dimension). Consequently, compared to macroelectrodes, three phenomena can be observed that change due to the smaller geometric dimension: first, the current density increases, second, the current decreases (not proportional to the electrode area reduction) and third, the mass transport changes from linear to 2- or 3-D diffusion, which is an important feature [165]. The decrease in current can be compensated by using an array of microelectrodes, which additionally, improves the signal-to-noise ratio. Otherwise, the change in mass transport is the most crucial phenomena to be considered and depends on two factors: one, the size of the microelectrodes relative to the size of the diffusion zones; two, the size of the diffusion zones relative to the size of the insulating material that separates two adjacent microelectrodes (this is also called the center-to-center separation d of the electrodes) [166]. Taking these two factors into account, four possible categories can be defined. Category 1 comprises microelectrodes which are separated far enough from each other to only obtain individual, small diffusion layers with a linear diffusion (see figure 2.43 1). In category 2, the thickness of the diffusion layer δ is larger than the microelectrodes themselves, but still not large enough to overlap (see figure 2.43 2). According to Davies et al. [166], this is the most common scenario, since the microelectrode arrays yield the best signal to noise ratio. In category 3, the diffusion zones grow thus large that they start overlapping each other and with that the adjacent microelectrodes deplete the same region of solution resulting in a decrease of current (compared to the previous category). The diffusion layer thickness δ of category 4 exceeds the size of the insulating layer leading to a complete overlap and therefore linear diffusion (see figure 2.43 4) [166].

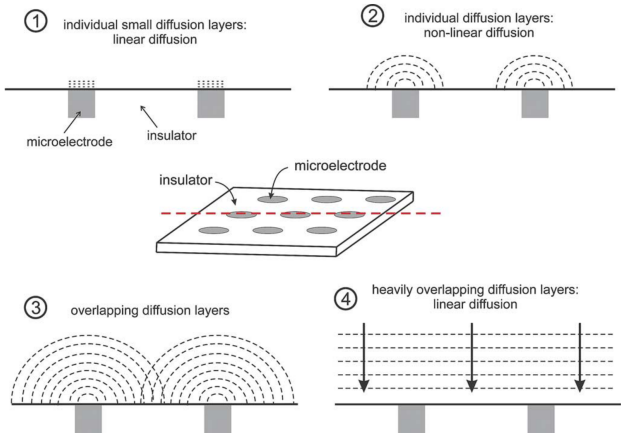

Figure 2.43. Scheme of the four possible categories of a diffusion profile at microelectrodes. Image from [166].

The mass transport in categories 1 and 4 can be described as 1-D problem due to the linear

diffusion, while for category 2 already a 2-D approach is needed. The overlapping diffusion layers of category 3 lead to an even more complex problem since the entire electrode surface needs to be considered instead of one single microelectrode [166]. Davies et al. developed [166] and validated [167] a method that is based on the diffusion domain approximation (first introduced by Amatore et al. [168]) to simplify such problems.
Considering the mass transport for a redox process at microelectrodes, the thickness of the diffusion layer, δ, that is depleted of reactant depends on the experimental time scale. For short times, δ is smaller than the electrode radius, r_e, which results in linear diffusion and can be described by the well-known Cottrell-equation [169–171]

$$i = nFAc_{\text{bulk}}\sqrt{\frac{D}{\pi t}} \tag{2.42}$$

where n is the number of transferred electrons, F is the Faraday constant, A is the geometry of the electrode (for a disc of radius r_e the area $A = \pi\, r_e^2$) c_{bulk} is the concentration of the redox species, D represents the diffusion coefficient and t the time. For longer times, the mass transport is dominated by radial diffusion and a steady-state current is obtained since the electron transfer across the electrode/solution interface equals the diffusion rate of the molecules towards the electrode. This can be described by a similar equation, found by Saito [169–171]:

$$i_{ss} = \frac{nFAc_{\text{bulk}}D}{r_e} \tag{2.43}$$

Compton et al. [171] investigated the size of electrodes necessary to show the chronoamperometric behavior predicted by the Cottrell equation and found that for smaller electrodes (microelectrodes) the Shoup-Szabo-equation [172–174] is better suited to predict and describe the observed behavior.

$$i = 4nFDr_e c_0 f(\tau) \tag{2.44}$$

$$f(\tau) = 0.7854 + 0.8862\tau^{-\frac{1}{2}} + 0.2146e^{-0.7823\tau^{-\frac{1}{2}}} \tag{2.45}$$

$$\tau = 4Dtr_e^{-2} \tag{2.46}$$

Where τ is the dimensionless time.

3 Materials & Methods

3.1 Chemicals

3.1.1 Barium Titanate and Barium Strontium Titanate

Synthesis Route 1: BTO/BSTO-Sol-Gel Route

Barium acetate ($Br(CH_3COOH)_2$, 99%) and strontium acatate ($Sr(CH_3COOH)_2$, 97 %), titanium (IV) isopropoxide ($Ti(i\text{-}OC_3H_7)_4$, 99.999%), acetyl acetone (acac, 99.0 %), 2-methoxy-ethanol (99.8 %) and glacial acetic acid (99.7 %) were purchased from Sigma Aldrich, Germany and used as-received from the supplier without any further purification. Titanium (IV) isopropoxide was stored and handled under an inert Argon atmosphere.

Synthesis Route 2: BTO-/BSTO-Nanocrystals Using Ultrasound

Barium chloride dihydrate ($BaCl_2 \cdot 2\ H_2O$, 99 %), strontium chloride hexahydrate ($SrCl_2 \cdot 6\ H_2O$, 99 %), titanium tetrachloride ($TiCl_4$, 99.9%), ethanol (99.9 %) and sodium hydroxide (NaOH, anhydrous, 98%) were purchased from Sigma Aldrich, Germany and used as-received from the supplier without further purification. Titanium chloride was stored and handled under an inert Argon atmosphere.

Synthesis Route 3: Nanocrystalline BTO/BSTO in Benzyl Alcohol at Room Temperature

Titanium(IV) isopropoxide ($Ti(i\text{-}OC_3H_7)_4$, 99.999%), barium hydroxide octahydrate ($Ba(OH)_2 \cdot 8\ H_2O$, 98.0%), benzyl alcohol (99.0 %) and 2-propanol (99.5%) were purchased from Sigma Aldrich, Germany. Benzyl alcohol was distilled under Argon before usage. All other chemicals were used as-received from the suppliers without any further purification. Both titanium(IV) isopropoxide and benzyl alcohol were stored and handled in a water-free environment.

3.1.2 Ionic Liquids

The ionic liquids, 1-butyl-1-methylpyrrolidinium bis(trifluoromethylsulfonyl)imide [BMPy][NTF2] (**IL1**), 1-hexyl-3-methylimidazolium tetrafluoroborate [HMIM][BF4] (**IL2**) and 1-ethylimidazolium nitrate [EIM][NO3] (**IL3**) were purchased from IoLiTec Ionic Liquids Technologies GmbH and used as-received.
The electrochemical window for these ILs are given from IoLiTec as follows:

- **IL1:** [BMPy][NTF2]: -2.5 V(cathodic limit) to 2.8 V (anodic limit)
- **IL2:** [HMIM][BF4]: -2.4 V (cathodic limit) to 2.7 V (anodic limit)
- **IL3:** [EIM][NO3]: not available, therefore the window for [EIM][NTF2] is used as orientation -0.8 V (cathodic limit) to 2.6 V (anodic limit)

3.1.3 Redox Species

The used redox species, 1,1-ferrocene dicarboxylic acid, 1,1-ferrocene dimethanol, 1,1-dimethylferrocene, 6-(ferrocenyl-)hexanethiol, 1,1-(ferrocenyl-)undecanethiol and ferrocene carboxaldehyd as well as the methylene blue and the quinone-hydroquinone derivatives, tetrafluoroparaquinone, 2,6-dimethylparaquinone, 1,4-benzoquinone, were purchased from Sigma Aldrich, Germany and used as-received.

3.1.4 UV-Matrix

The acrylate monomers, 1,6-hexadiol acrylate **M1** and trimethyolpropanthoxylat triacrylate **M2**, as well as the photo initiator, 2-hydroxy-2-methyl propiophenone **1** were purchased from Sigma Aldrich, Germany and used as-received.

3.2 Preparation and Characterization of BSTO-Sol-Gels and Nanoparticles

The following synthesis routes are described for the synthesis of BSTO nanoparticles. However, each route can also be used to obtain pure BTO- or STO-sol-gels and nanoparticles by just adding the pure Ba^{2+}- or Sr^{2+}-salt instead of a mixture of both salts.

3.2.1 Synthesis Route 1: Acetate-Sol-Gel-Route of BSTO According to *Schneller* et. al [36]

In a first step, the titanium isopropoxide needs to be stabilized with acetyl acetone (acac) since it is sensitive to moisture/water. Therefore, a ratio of two moles of acetyl acetone per one mole of titanium isopropoxide is added. With the following equation the volume of the needed acetyl acetone can be calculated.

$$V_{\mathrm{acac}} = \left(\frac{M_{\mathrm{acac}} \cdot c_{\mathrm{stock}} \cdot V_{\mathrm{total}}}{\rho} \right) \cdot 2 \tag{3.1}$$

with
- V_{acac} = volume of acetyl acetone
- M_{acac} = molecular weight of acetyl acetone [100.12 g mol^{-1}]
- c_{stock} = concentration of stock solution [mol l^{-1}]
- V_{total} = total volume of stock solution
- ρ = density of acetyl acetone [0.97 g ml^{-1}]

The volume of the stock solution is set to be 25.00 ml in this case which results in 1.55 ml of acetyl acetone. In a next step, the difference of the total volume of stock solution and the volume of acetyl acetone yields the volume of the solvent, i. e. 23.45 ml. The solvent comprises a mixture of three parts acetic acid and one part 2-methoxyethanol, i. e. 5.86 ml 2-methoxyethanol and 17.58 ml acetic acid.
The above demonstrated calculations of the different components are based on idle behavior of all chemicals, i. e. no mixing effects occur. In reality the composition will slightly vary due to such mixing effects, however, this is insignificant for the preparation of the sol-gel since it is highly reproducible.

In a second step, a mixture of barium acetate and strontium acetate in the respective molar ratio, e. g. 60% : 40%, was prepared and dissolved in glacial acid. During the dissolution step, the titanium isopropoxide is stabilized using the above calculated amounts of 2-methoxyethanol, acetyl acetone and acetic acid (glacial). This is done under an inert atmosphere. Finally, the barium and strontium salt mixture is added to the titanium isopropoxide solution and the final amount of acetic acid (glacial) is added to adjust the concentration.

3.2.2 Synthesis Route 2: BSTO-Nanocrystals Using Ultrasound According to *Moghtada* et. al [175]

Barium chloride dihydrate and strontium chloride hexahydrate were mixed in an 70/30% molar ratio and dissolved in 5 ml deionized MilliQ water that was beforehand degassed by bubbling argon at 70°C for 30 min through with subsequent boiling for another 30 min. A stoichiometric amount of titanium tetrachloride were dissolved in 5 ml ethanol under argon atmosphere. The titanium tetrachloride solution was added into the salt solution and stirred for 30 min at 60°C. Afterwards 10 ml NaOH solution (pH = 14) was added and the so obtained precursor solution (containing all three solutions) was placed into an ultrasound bath at 50°C for 40 min. Finally, the precipitation was filtered, washed using MilliQ water and dried at 100°C in an oven.

3.2.3 Synthesis Route 3: Nanocrystalline BSTO in Benzyl Alcohol at Low Temperature According to *Veldhuis* et. al [48]

First, a 200 mmol l^{-1} solution of titanium (IV) isopropoxide in benzyl alcohol was prepared under an argon atmosphere and refluxed for 2 h at 120°C. Then, 70 mol-% of a 1:1 mixture containing barium hydroxide octahydrate and strontium hydroxide octahydrate were added and again refluxed for 2 h at 120 °C. After reaction the obtained powder was centrifuged and the benzyl alcohol replaced by 2-propanol. Subsequently, the as-prepared powder was washed several times with 2-propanol and finally dried in an oven at 100°C.

3.2.4 Characterization by X-ray Diffraction (XRD)

X-Ray diffraction measurements were performed by means of a Bruker D8 high-resolution diffractometer utilizing the Cu $K_{\alpha 1}$ wavelength (λ = 1.54 Å). The system is equipped with a 4 crystal monochromator and a Göbel mirror in order to collimate and monochromatize the x-ray radiation. A scintillator detector is employed to collect the diffracted intensity. In front of the detector, a 3 mm wide mechanical slit is used. Symmetric 2Theta/theta scans were performed in a range 2Theta = 3-140° with a angular resolution of 0.1°. The integration time of each point amounts to 1s.

3.2.5 Characterization by Scanning Electron Microscopy (SEM) and Transmission Electron Microscopy (TEM)

SEM:
Device: Magellan XHR 400 L FE-SEM-FEI and Zeiss LEO 1550.
Wafer: SiO2 with a native oxid layere (2 nm) or PEN and PET polymer substrates.
Sample preparation SEM: The wafers were cleaned in acetone and *i*-propanol twice. Then, one to two drops of the respective sample was placed onto the wafer and the sample was dried in air. Afterwards, oxygen plasma (0.8 mbar, 20% power, 30 s) was applied to remove organic residues.

TEM:
Device: Tecnai F20 microscope operated at 200 kV.
Wafer: Cu grid covered with carbon film.
Sample preparation: The particles were dispersed in ethanol and titrated on Cu grid covered with carbon film. The Cu grids were dried on a plate oven at 75°C.

3.2.6 Characterization by Inductively Coupled Plasma Atomic Emission Spectroscopy (ICP-OES)

A Thermo Scientific ICP-OES 6500 and 7600 were used to determine the composition of the obtained BSTO nanocrystals according route 3 at the ZEA-3 institute of the Forschungszentrum Jülich. Therefore, two samples of 50 mg were dissolved in an 50 ml volumetric flask with 3 ml HCl / 3 ml H_2O_2 and filled up to the mark with water. Then, two aliquots were diluted by 1:100 and analyzed.

3.3 Sensor Geometry

3.3.1 Laser Ablated Structures

3.3.1.1 BSTO-based Sensor

Planar gold IDEs were chosen for the sensor design. To produce the structures, layers of titanium and gold, with thicknesses of 5 nm and 50 nm, respectively, were evaporated onto a flexible polyethylene terephthalate (PET; DuPont PCS) substrate. Using laser ablation (RDX 500 Laser Machine, Pulsar Photonics GmbH, Germany) the gold layer was structured to establish an IDE pattern with 40 digits having a length of ∼3500 μm, a gap of ∼50 μm, and a width of ∼50 μm. Before applying the BSTO-layer, the IDEs were sonicated with 1 v/v % Aquet detergent (concentrate, Scienceware) in Milli-Q water for 10 minutes, followed by 10 minute sonication in isopropanol.

3.3.1.2 IL-based Sensor

A planar two electrode system was chosen for the sensor design. To produce the structures, layers of titanium and gold, with thicknesses of 5 nm and 50 nm, respectively, were evaporated onto a flexible polyethylene terephthalate (PET) substrate. Using laser ablation the gold layer was structured to establish a two electrode system. The spacing between the working and counter electrodes was 200 μm, and the feedlines as well as parts of the working electrode were passivated by printing a mixture of SU8 and γ-butyrolactone on top of the gold layer using an OmniJet 300 inkjet printer. By this, three microelectrodes, having dimensions of 50 μm x 500 μm, were left open at which the gold was in contact with the ionic liquid solution that was applied directly on top of the gold (see figure 3.1). On top of the feedlines a connector was glued using silver paste to connect the sensor to a commercial potentiostat or custom made readout electronics via cables.

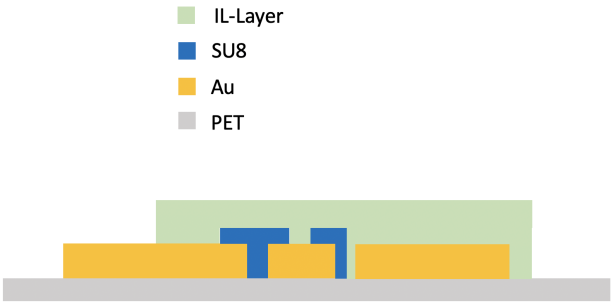

Figure 3.1. Cross-section of a laser ablated gold electrode, passivated with SU8 to define the contact area of Au and IL.

3.3.2 Cleanroom Fabricated MEAs

3.3.2.1 BSTO-based Sensor

Flexible, planar IDEs were produced in-house in the cleanroom of the Helmholtz Nanoelectronic Facility (HNF) Jülich. Therefore, layers of titanium (acts as adhesion material between the PET substrate and the gold) and gold, with thicknesses of 5 nm and 50 nm, respectively, were evaporated onto a flexible polyethylene terephthalate (PET) substrate. In a subsequent wet chemical etching step using TechniEtch™ACl2 (for 1 min with a ratio of TechniEtch™ACl2/DI-water 1:1 and following that for 2-3 min with pure TechniEtch™ACl2; Microchemicals), the metal structure was defined. Afterwards the gold structures were passivated applying SU8 via spin coating on top. On this passivation, a photolithography was performed to create circular openings of 80 μm diameter into the passivation layer on top of the electrodes, which defines the digits and gaps between adjacent digits that is exposed to the BSTO. Additionally, the bond pads were opened by reactive ion etching to be able to clue a connector using silver paste on top.

3.3.2.2 IL-based Sensor

Flexible, planar microelectrode arrays were produced in-house in the cleanroom of the Helmholtz Nanoelectronic Facility (HNF) Jülich. The process was as follows: layers of titanium (acts as adhesion material between the PET substrate and the gold) and gold, with thicknesses of 5 nm and 50 nm, respectively, were evaporated onto a flexible polyethylene terephthalate (PET) substrate. In a subsequent wet chemical etching step using TechniEtch™ACl2 (for 1 min with a ratio of TechniEtch™ACl2/DI-water 1:1 and following that for 2-3 min with pure TechniEtch™ACl2; Microchemicals), the metal structure was defined. Afterwards the gold structures were passivated using SU8 that was applied by spin coating. On this passivation, a photolithography was performed to create circular openings of 80 μm diameter into the passivation layer on top of the electrodes, which defines the electrode area that is exposed to the ionic liquid. The chip dimensions are 5 mm x 5 mm with three openings of 80 μm and feedlines of 200 μm length (see figure 3.2).

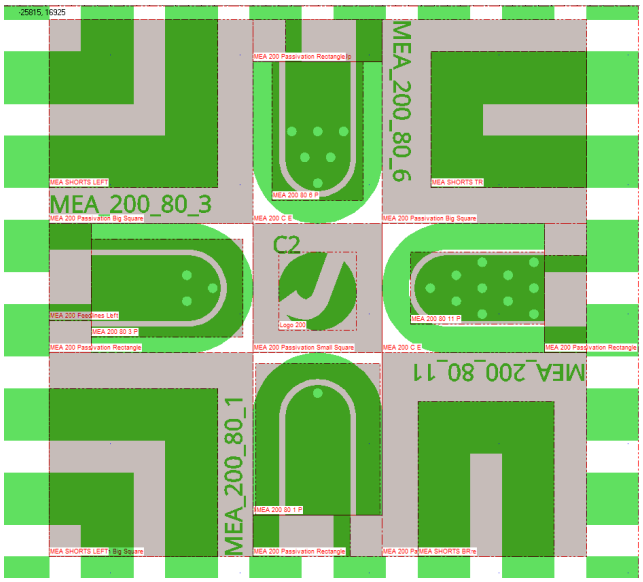

Figure 3.2. Layout of a cleanroom fabricated MEA: light green displays the exposed Au layer, dark green the passivated Au parts and grey is the passivation layer. One chip comprises four MEA structures with different numbers of working electrodes; here always the MEA with three openings were used.

3.4 Sensor Preparation

3.4.1 BSTO-based Sensor

3.4.1.1 Sol-Gel-BSTO

The BSTO sol was synthesized according to the above described route 1. The sol was then diluted in a 60:40 wt% ratio with ethylene glycol to obtain a inkjet printable ink. The ink was printed on top of the IDE structures using an OmniJet 300 printer (Unijet Co., Ltd., South Korea), as well as 1 and 10 pL Dimatix cartridges (FUJIFILM Dimatix, Inc., USA). Depending on the wetting of the ink on top of the substrate and the IDE structures, the substrate was activated using oxygen plasma with the following parameters: 20 %, 0.2 mbar, 0.1 min.
Afterwards, the sensor was dried using a hot plate at 120°C to dry the printed layer, before flash lamp annealing it with a PulseForge 1200 (Novacentrix, USA). The exact parameters are given in chapter 4.2.1.

3.4.1.2 BSTO Nanoparticles

The BSTO particles were synthesized according to the above described routes 2 and 3. Afterwards, the as-synthesized particles were suspended in a solvent to obtain a stable suspension which can be applied by either drop casting or spin coating on top of the IDEs. Therefore, BSTO suspensions were prepared, using benzyl alcohol, isopropanol or *N,-N*-dimethylformamide (DMF) as suspension solvent. The suspension comprised 20 wt% BSTO particles and was sonicated for five minutes. Finally, 2 μl were applied onto the IDE. The sensor was then dried using a hot plate at 80 °C.

3.4.2 IL-based Sensor

3.4.2.1 Proof-of-Principle Experiment Using Cyclic Voltammetry

For a proof-of-principle experiment, ferrocene dimethanol was dissolved in 1-butyl-1-methylpyrrolidinium bis(trifluoromethylsulfonyl)imide (0.2 M) and applied via drop casting onto the planar sensor system (laser ablated structure with complete working electrode). Subsequently, the as-prepared sensor was examined using cyclic voltammetry at various temperatures. The temperature was varied between 0°C to 60°C in 10°C steps.

3.4.2.2 Long Term Experiments Using Chronoamperometry

In this study, three different IL layers were investigated: first, a 4 : 1 mixture of 1-butyl-1-methylpyrrolidinium bis(trifluoromethylsulfonyl)imide [BMPy][NTF2] (**IL1**) and 1-hexyl-3-methylimidazolium tetrafluoroborate [HMIM][BF4] (**IL2**) in which methylene blue (0.04 M) as redox molecule was dissolved (sensor type 1), second, pure 1-ethylimidazolium nitrate [EIM]-[NO3] (**IL3**) was used as a redox molecule and transport medium simultaneously (sensor type 2), and third, a 1 : 3 mixture of [HMIM][BF4] and [EIM][NO3] in which the [HMIM][BF4] was added to reduce the melting point of [EIM][NO3] (sensor type 3) was investigated. For fixating the ionic liquid solution on a planar sensor system, a UV-curable matrix was added consisting of two acrylate monomers (1,6-hexadiol acrylate : Trimethylolpropanthoxylat tri acrylate in a ratio of 10.5 wt% : 5.5 wt%) and the photo initiator 2-hydroxy-2-methyl propiophenone (0.6 wt%). After deposition of 2 µl solution by drop casting, the obtained layer was photocured using a UV lamp (MUA-165, Mejiro Genossen, Japan) for several seconds and heating the sensor to 125°C for 30 min to remove the volatile solvents.

3.5 Measurement Settings

3.5.1 Viscosity Measurements

The viscosity measurements were done using a Brookfield Rheometer LV DV3T that was temperature controlled using a Thermostat F32 from Julabo. The measurement principle is based on a cone-plate geometry, using a CPA-40Z spindle as plate, with a given shear rate to determine the fluid viscosity of a sample (1 ml). The viscosity of the used ILs in this work were determined in the temperature range between 20°C and 60°C in 5°C or 10°C steps, respectively. At each temperature the viscosity was recorded for 180 s, while the data points were collected at 1-second intervals, and the average value as well as the standard deviation were calculated. Due to measurement artifacts the first 15 points of each measurement were dismissed until the viscosity showed a constant behavior.

3.5.2 Automatic Temperature Setup

The temperature setup consists of a peltier element (TEG 127-230-32, thermalforce.de) that was glued on top of a liquid cooler to keep the lower side at a constant temperature (here 8°C). It was supplied with a power supply for varying the potential to heat or cool the top side. The heating and cooling was done by a self-written program that varied the potential in a way that the temperature range of -20°C to 60°C was covered. Each temperature was kept constant for 180 s before the next point was set. The temperature range was cycled in 10°C steps for several times. On top of the element, a reference thermocouple device was fixated that was connected to

a computer to record the actual temperature. Besides the thermocouple the sensor under investigation was located and heated/cooled by the peltier element. The sensor under investigation was thereby connected to potentiostate (PalmSens 4 + MUX8, PalmSens BV; The Netherlands). The peltier element and temperature sensors were located in a closed box that was flushed with nitrogen to prevent condensation of humidity from the air at lower temperatures.

3.5.3 Electrochemical Measurements

3.5.3.1 Cyclic Voltammetry (CV) Experiment

A PalmSens 4 potentiostat (Palms Sens BV; The Netherlands) was used for electrochemical characterization of the sensor. The pre-characterization was done using cyclic voltammetry to determine the reduction and oxidation peak position using a potential range of -1.0 V to 0.5 V for the sensor comprising methylene blue and -0.5 V to 0.5 V for the sensor comprising ferrocene dimethanol. A scan rate of 0.05 V/s were used. Once the peak positions were determined, chronoamperometry was utilized for the actual temperature measurements by using methylene blue as redox molecule.

3.5.3.2 Chronoamperometry Experiments

For all three layer compositions the change in current over temperature was recorded for several cycles using a chronoamperometric technique provided by a PalmSens 4 + MUX8 (PalmsSens BV, The Netherlands) device. To this end, the temperature was changed in the range of -20°C to 60°C in 10°C steps as described above. Each temperature was kept stable for 180 s. During this time interval, several chronoamperometric measurements were conducted by applying a potential of -1.0 V at the working electrode (WE) of the sensor and recording the resulting current. For each sensor, different measurement pulse lengths between 0.1 s and 10 s were used. The current was recorded every 1 ms for the pulse lengths of 0.1 s, 0.5 s and 1.0 s and every 10 ms for a pulse length of 10.0 s. Between two consecutive measurements a delay time of 30 s was introduced to avoid accumulation of charge and reduce the depletion of redox molecules in the vicinity of the electrode. For each sensor and applied pulse length, several heating and cooling cycles were recorded. The average and standard deviation was calculated for all measurements at the same temperature during two cooling and heating cycles. A 50 Hz notch filter was applied to the raw current data to increase the signal to noise ratio. Afterwards, the current data was averaged over the last 20 ms of each measurement for pulse lengths 0.05 s, 0.1 s and 0.5 s and over 200 ms and 2 s for pulse lengths 1.0s and 10.0 s, respectively.

4 Results & Discussion

4.1 Objectives

In this chapter the obtained outcomes during the work of this thesis are discussed. The aim of this thesis was the development of a flexible temperature sensor that shows a high enough sensitivity and is stable over a wide temperature range to allow the use of low-power Internet of Things (IoT) applications. Such a sensor would overcome many of the drawbacks current temperature measurement devices exhibit. Several state of the art temperature sensors were introduced in chapter 2.1. All of them rely on different working principles, e.g. a change in resistance, expansions of fluids or a change in color with thermal energy. The most common temperature sensor is the mercury thermometer that uses the dilation of mercury with increasing temperature. However, nowadays the mercury is replaced by other liquids such as alcohols or ionic liquids [18]. Thermistors and thermocouples are electronic temperature sensors which use the change in resistance or voltage, respectively, to monitor changes in temperature. However, all of those sensors show drawbacks such as a restriction in shape and size, no direct recording of temperature possible (e.g. for mercury thermometers) and either a small temperature range or a low relative change in a certain parameter per degree. Due to the last point usually high-end electronics are needed to measure small temperature changes.
To address these problems, a new, flexible and miniaturized temperature sensor was developed. Thereby, two strategies were investigated. One, using the sol-gel method to develop a printable barium strontium titanate ink, which is crystallized in a photo curing step or synthesizing barium strontium titanate nanoparticles, which are suspended in an appropriate solvent for printing in order to measure the change in resistance with temperature. Second, using Faradaic electrochemical currents from a redox couple dissolved in an IL or using a pure IL as redox molecule, to establish a relation between current and temperature.
While the first approach, using BSTO as temperature sensitive material, did not yield the expected and desired results, the second approach, utilizing ILs, lead to three prototypes of a highly sensitive temperature sensor. Compared to standard RTDs this novel sensor shows a higher per degree sensitivity and can be utilized in a broad temperature range depending on the chosen IL. The measurement principle is based on the change of viscosity with temperature and correlated to that with the diffusion of redox active molecules through the IL yielding higher currents at elevated temperatures.
In the first part of this chapter the BSTO approach is discussed and it will be shown why this material and the different methods investigated to obtain it with the desired properties, failed. In the second part, the feasibility of using ionic liquids and different redox couples to measure temperature is demonstrated. This is followed by the attempt to explain the findings by connecting the results with physical models and equations, e.g. Stokes-Einstein and Nernst-Einstein adapted for usage with ILs in the next chapter (see chapter 5.2).

4.2 Development of a Temperature Sensor Based on Barium Strontium Titanate

The use of barium titanate and its derivatives as temperature sensitive material is well known and utilized in commercially available thermistors. BSTO belongs to the so called PTCs, since it shows a positive temperature coefficient, which means that the resistance increases with increasing temperature. The approach to use BSTO to develop a flexible temperature sensor with high sensitivity makes it necessary to consider new synthesis methods of BSTO, which are compatible with the setup of a polymer-based, flexible sensor. The most common polymer substrates for such sensors are based on polyethylene terephthalate (PET) or polyethylene naphthalate (PEN), which results in a temperature restriction during the development process. As described previously in chapter 2.2 the classical method to obtain such ceramic materials is the solid-state synthesis that requires temperatures of > 1000°C. Therefore, two different approaches were investigated that require much lower temperatures: one, the sol-gel method, which produces an amorphous 3-D network of M-O-M species (M = Ti^{4+}) as shown in figure 2.10. This so called *sol* is in a second step photonically sintered using a PulseForge 1200 (Novacentrix, USA) with a xenon flash lamp. Two, BSTO nanoparticles were synthesized, characterized and subsequently suspended in an appropriate solvent. This suspension was then applied onto a flexible IDE substrate via drop casting or spin coating and the sensor dried on a hot plate.
In the following sections both attempts are discussed in detail and the respective results are shown.

4.2.1 BSTO Sol-Gel Approach with Subsequent Flash Light Sintering to Form a Temperature Sensitive Layer

The BSTO sol-gel was prepared according to *Schneller* et. al [36] and the procedure is described in chapter 3.2.1. As result, one obtained a liquid-like sol that was adjusted to serve as an inkjet printable ink. Therefore, the physicochemical properties such as surface tension and viscosity were determined and adjusted accordingly. The surface tension of the pure sol lies around 28.9 mN m^{-1} and the viscosity around 6.7 mPa s. While the surface tension is already suitable for inks, the viscosity is too low and was adjusted by adding ethylene glycol. Finally, a ratio of 60 wt% sol to 40 wt% ethylene glycol was chosen and results in a viscosity value of 10.3 mPa s and a surface tension of 34.2 mN m^{-1}. This ink as well as the pure sol-gel was then printed on top of gold IDE structures as described previously (see chapter 3.4.1.1).

4.2.1.1 Finding Appropriate PulseForge Parameters

For the first experiments regarding the photonic sintering process the prepared BSTO ink was printed on top of some gold and silver IDEs as a continuous area. Figure 4.1 shows a schematic and figure 4.2 a microscopic picture with fivefold magnification of the layout.

As can be seen in a larger magnification (twenty- and fiftyfold), the BSTO layer shows cracks after drying, which usually hints toward too high of a layer thickness (see figure 4.3 and 4.4). Therefore, thickness measurements were also done using the Keyence X-150 laser microscope (Keyence, Japan). These show two significantly different height profiles, depending on the measured position. One height measurement was done at the edge of the pure sol-gel layer and a second on a part that was printed on top of the gold IDE. In both cases the clean substrate was used as a reference point. While the height for the pure sol-gel layer varies between 1.5 μm and 2.1 μm, the height on top of the gold IDE lies between 0.05 μm and 0.17 μm (see figures 4.5 and 4.6).

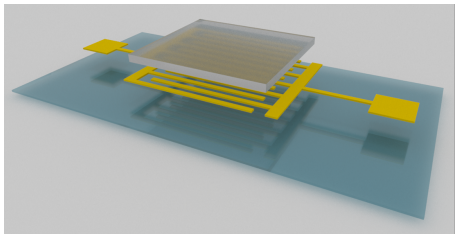

Figure 4.1. Scheme of a continuous BSTO ink layer on top of an IDE structure.

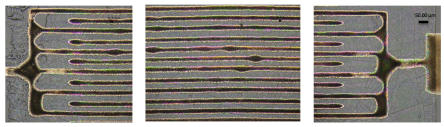

Figure 4.2. Microscopic picture of a continuous BSTO ink layer after printing on top of an IDE structure with fivefold magnification.

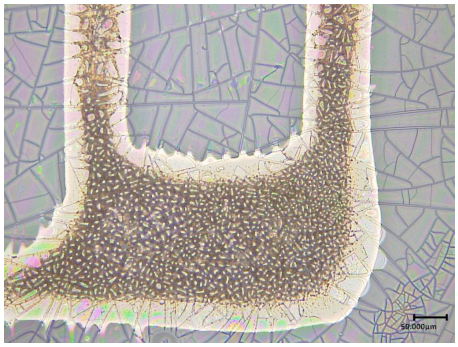

Figure 4.3. Microscopic image at twentyfold magnification showing several cracks of the BSTO layer after drying at 120°C.

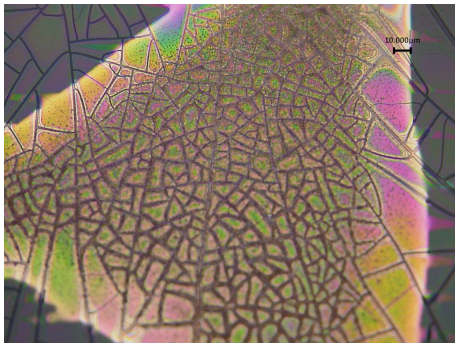

Figure 4.4. Microscopic image at fiftyfold magnification showing several cracks of the BSTO layer after drying at 120°C.

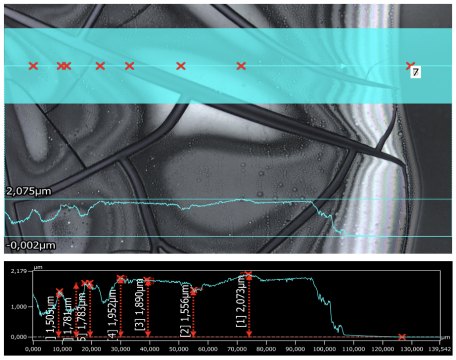

Figure 4.5. Height measurement at hundredfold magnification on the pure BSTO layer. Seven measurement points were taken and the height varies between 1.505 μm and 2.073 μm, which indicates a relatively thick layer (compared to other positions; see figure 4.6).

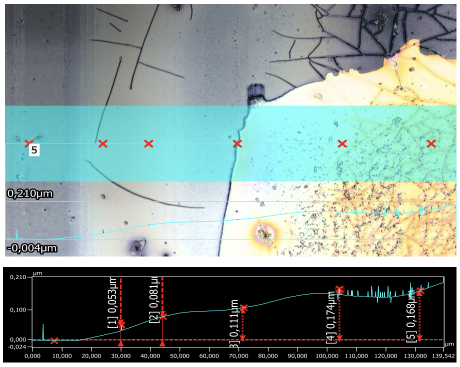

Figure 4.6. Height measurement at hundredfold magnification of the BSTO layer on top of the gold IDE. Five measurement points were taken and the height varies between 0.053 μm and 0.168 μm, which indicates a relatively thin and smooth layer.

The height measurements at the two different positions of the same sensor indicate an uneven layer thickness. This might be due to some flowing effects during the printing of the layer,

which are induced by the movement of the substrate holder. Another reason might be a too high resolution setting (DPI) during the printing, which results in too large an overlap of adjacent ink drops and therefore, in too much ink. However, these structures were usable for the first flash light sintering tests and were therefore used to test some PulseForge parameters. In table 4.1 the settings of the photonic curing experiments can be found. Figures 4.7 to 4.12 show the corresponding microscope images of the sensor after each flash lamp treatment (for the first flash lamp treating no image is available). In total six flash lamp sintering steps were carried out at the same IDE structure. This means, the images shown in figures 4.7 to 4.12 represent the results of the added flash lamp treatments in their succession of application. Thereby, the energy was increased continuously by varying the applied voltage and pulse length (envelope). Furthermore, each light pulse was divided in so called μpulses (as they are referred to by the manufacture), meaning the 2000 μs of the first parameter settings were divided into 2 μpulses with the following values: 1500 μs applying the respective voltage (high), 250 μs pause (low), 500 μs applying voltage (high), 250 μs pause (low).

Table 4.1. PulseForge settings for the first photonic curing experiments of a BSTO layer on top of a gold IDE structure.

Energy (J cm^{-2})	**Voltage** (V)	**Pulse Length** (μs)	**μpulses**	**high** (μs)	**low** (μs)	**Duty Cycle** (%)
0.497	350	2000	2	1500 500	250 250	80
2.562	300	2000	2	1500 500	250 250	80
3.151	320	2000	2	1500 500	500 250	80
3.859	320	2600	2	2500 100	500 250	78
4.981	350	2600	2	2500 100	500 250	78
6.028	360	3100	2	3000 100	500 250	81

The first two flash lamp treatments caused only a slight change in coloring of the BSTO layer as well as the formation of more cracks (compare figures 4.7 and 4.8). This indicates that the applied energy is not high enough to start the crystallization process of the BSTO sol-gel. Therefore, four more flash lamp treatments were carried out with increasing energy each time. Figure 4.9 shows the first real change in appearance by having several blackened spots at the IDE digits and a broadening of same. These appearance changes increased for the following treatments until in figure 4.11 almost the entire IDE digits are black and in figure 4.12 even the area between digits appears to be burned.
Due to the short, but energetic light pulses the surface temperature of the sample can increase up to several hundred degree Celsius without heating up the entire substrate. Thereby, the BSTO layer should change from amorphous to crystalline while the gold structure as well as the PET substrate are not significantly heated. However, as figures 4.9 to 4.12 indicate, this was not achieved with the chosen parameters.

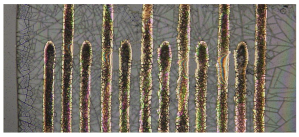

Figure 4.7. Microscope image (5 x) of a BSTO layer on top of a gold IDE before flash lamp treatment. It can be seen that the BSTO layer shows already some cracks before photonically cured.

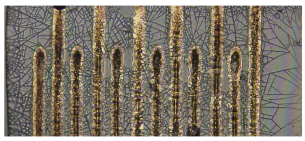

Figure 4.8. Microscope image (5 x) of a BSTO layer on top of a gold IDE after two flash lamp treatments (2.562 J cm^{-2}, 300 V, 2000 μs, 2 μpulses with 80% duty cycle). A slight color change can be observed as well as the formation of more cracks.

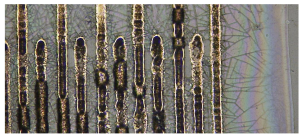

Figure 4.9. Microscope image (5 x) of a BSTO layer on top of a gold IDE after three flash lamp treatments (3.151 J cm^{-2}, 320 V, 2000 μs, 2 μpulses with 80% duty cycle). Along some parts of the IDE digits a broadening and blackening of the structure can be seen. This indicates some burning of material.

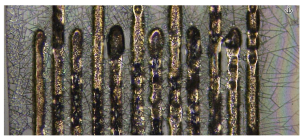

Figure 4.10. Microscope image (5 x) of a BSTO layer on top of a gold IDE after four flash lamp treatments (3.859 J cm^{-2}, 320 V, 2600 μs, 2 μpulses with 78% duty cycle). The broadening and blackening of the IDE digits is more pronounced.

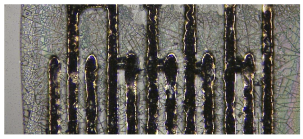

Figure 4.11. Microscope image (5 x) of a BSTO layer on top of a gold IDE after five flash lamp treatment (4.981 J cm^{-2}, 350 V, 2600 μs, 2 μpulses with 78% duty cycle). Almost the entire digits are blackend due to the photonic curing. However, the BSTO layer beside the gold structures is mostly unchanged.

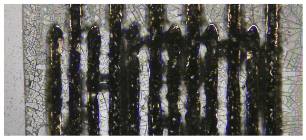

Figure 4.12. Microscope image (5 x) of a BSTO layer on top of a gold IDE after six flash lamp treatments (6.028 J cm^{-2}, 360 V, 3100 μs, 2 μpulses with 81% duty cycle). The entire gold IDE is blackend as well as several parts between the gold structure. This indicates that also the substrate (PET) itself is burned at several positions.

4.2.1.2 Adjusting the Properties of the BSTO Ink

One reason why also the gold structure in the previously described experiments was affected might be due to the low absorption rate of the transparent, lightly yellow BSTO ink. Using a bolometer, which was an accessory of the PulseForge, the absorption of different ink compositions were determined. In two inks 1 wt% of carbon black or methyl violet was added, respectively, to increase the absorption ability of the ink. Then, the emitted energy for a cetain set of curing parameters was measured: first without substrate, second the pure substrate, third three substrates with different ink compositions (pure BSTO ink, BSTO ink with carbon black and methyl violet, respectively). These samples were exposed to three different parameter setting of the PulseForge. The settings as well as the absorption results are presented in table 4.2. The absorption is calculated by putting the measured energy without any substrate in relation to the energy values of the subsequent measurements with substrate and inks.

Table 4.2. Determining the absorption ability of different ink compositions using carbon black and methyl violet, respectively, as additives (1 wt %) for three different parameter settings.

Parameters: 350 V, 5 ms, 5 pulses, 0.1 Hz, 5 counts		
Sample	**Energy** (J cm^{-2})	**Absorption** (%)
Without Substrate	3.926 ± 0.061	-
Pure Substrate	3.137 ± 0.036	20.1
Pure BSTO Ink	3.113 ± 0.025	20.7
BSTO Ink + 0.1 wt% Carbon Black	2.925 ± 0.037	25.5
BSTO Ink + 0.1 wt% Methyl Violet	2.562 ± 0.029	34.7
Parameters: 300 V, 3 ms, 5 pulses, 0.1 Hz, 5 counts		
Sample	**Energy** (J cm^{-2})	**Absorption** (%)
Without Substrate	1.626 ± 0.023	-
Pure Substrate	1.290 ± 0.014	20.7
Pure BSTO Ink	1.278 ± 0.009	21.4
BSTO Ink + 0.1 wt% Carbon Black	1.197 ± 0.018	26.4
BSTO Ink + 0.1 wt% Methyl Violet	1.065 ± 0.019	34.5
Parameters: 290 V, 20 ms, 1 pulse, 0.1 Hz, 5 counts		
Sample	**Energy** (J cm^{-2})	**Absorption** (%)
Without Substrate	7.068 ± 0.078	-
Pure Substrate	5.745 ± 0.036	18.7
Pure BSTO Ink	5.704 ± 0.033	19.3
BSTO Ink + 0.1 wt% Carbon Black	5.380 ± 0.017	23.9
BSTO Ink + 0.1 wt% Methyl Violet	4.818 ± 0.032	31.8

As can be seen, methyl violet as an additive increased the absorption by a factor of approx. 40% compared to the pure BSTO ink. Conclusively, 40% less energy should be necessary to cure the BSTO ink with the additive. Additionally, further experiments were based on the presented results in chapter 2.2.4 of *Kim* et. al [50] since strontium titanate and barium strontium titanate are similar materials with respect to their properties and synthesis parameters. Therefore, the parameters, single pulse of 10 to 20 ms and an energy density around 15 J cm^{-2}, by *Kim* et. al were used. Table 4.3 shows the parameter settings of the flash lamp sintering with considerably higher energies due to significantly longer light pulses. The corresponding microscope images are shown in figures 4.13 to 4.20.

Table 4.3. PulseForge settings based on the results of *Kim* et. al [50] with a BSTO ink containing 1 wt% methyl violet as additive to increase the light absorption of the flash lamp pulses. The pulse length was kept constant at 20 ms, while the voltage was adjusted. Each experiment represents a single light pulse (the 20 ms were not divided into μpulses).

No.	**Energy** (J cm^{-2})	**Voltage** (V)	**Pulse Length** (μs)	**Figure**
1	7.068 ± 0.078	290	20	4.14
2	8.946 ± 0.034	320	20	4.15
3	9.637 ± 0.044	330	20	4.16
4	10.339 ± 0.054	340	20	4.17
5	11.790 ± 0.052	360	20	4.18
6	12.591 ± 0.049	370	20	4.19
7	15.013 ± 0.042	400	20	4.20

The pulse length of the different experiments were kept constant while the energy level was adjusted by increasing the applied voltage step by step. Each experiment consisted of a single light pulse of 20 ms, which was not, as before, divided into several μpulses. The energy was set between 7 J cm^{-2} and 15 J cm^{-2} to approximate the given parameters from literature slowly and be able to observe the change of the sol-gel layer.

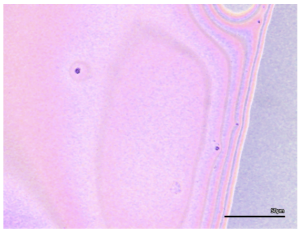

Figure 4.13. Microscope image (5 x): BSTO ink with 1 wt% methyl violet as additive on a pure PEN substrate before flash lamp treatment. It can be seen that the BSTO layer has a violet coloring, but no cracks are visible.

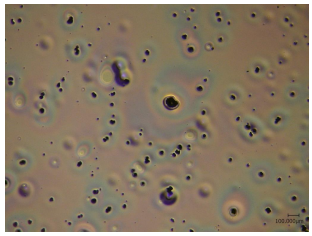

Figure 4.14. Microscope image (5 x): BSTO ink with 1 wt% methyl violet on a pure PEN substrate. Flash lamp treatment: 7.068 $\pm$ 0.078 J cm^{-2}, 290 V, 20 ms. Changes in color and surface appearance can be observed.

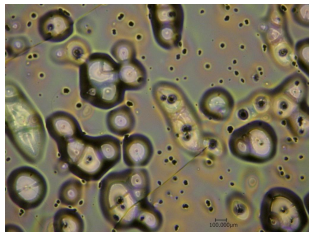

Figure 4.15. Microscope image (5 x): BSTO ink with 1 wt% methyl violet on a pure PEN substrate. Flash lamp treatment: 8.946 $\pm$ 0.034 J cm^{-2}, 320 V, 20 ms. Here, the formation of "bubbles" can be observed.

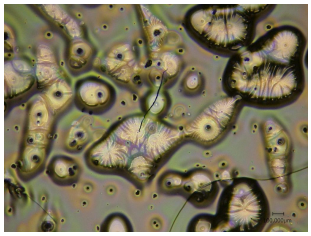

Figure 4.16. Microscope image (5 x): BSTO ink with 1 wt% methyl violet on a pure PEN substrate. Flash lamp treatment: 9.637 $\pm$ 0.044 J cm^{-2}, 330 V, 20 ms. The extend of "bubble" formation is similar to the previous experiment.

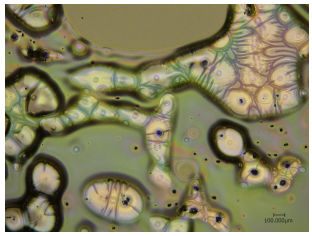

Figure 4.17. Microscope image (5 x): BSTO ink with 1 wt% methyl violet on a pure PEN substrate. Flash lamp treatment: 10.339 $\pm$ 0.054 J cm^{-2}, 340 V, 20 ms. The "bubble" formation occurs in a similar extend as with 9.637 J cm^{-2} .

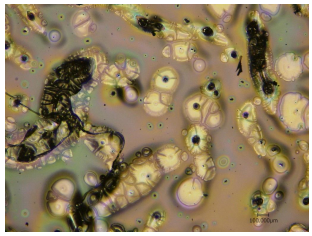

Figure 4.18. Microscope image (5 x): BSTO ink with 1 wt% methyl violet on a pure PEN substrate. Flash lamp treatment: 11.790 $\pm$ 0.052 J cm^{-2}, 360 V, 20 ms. The formation of "bubbles" is still comparable to the previous experiment.

The series of experiments show clearly a change of coloring even after the first light pulse of 7.068 J cm^{-2} (compare figures 4.13 and 4.14). This indicates that the methyl violet is decomposed due to the irradiation with the flash lamp and the elevated surface temperature of the sample. The PulseForge has an integrated SimPulse software, based on Beer's law, to calculate the temperature at each layer, which reads for this first pulse a temperature of 225°C at the surface. Furthermore, some small spots can be observed, which decreases the surface smoothness.

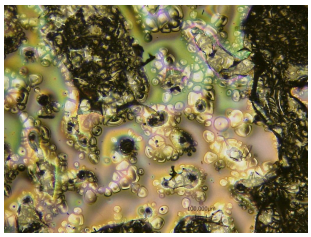

Figure 4.19. Microscope image (5 x): BSTO ink with 1 wt% methyl violet on a pure PEN substrate . Flash lamp treatment: 12.591 ± 0.049 J cm^{-2}, 379 V, 20 ms. The "bubble" formation increases slightly and some blackened spots can be observed.

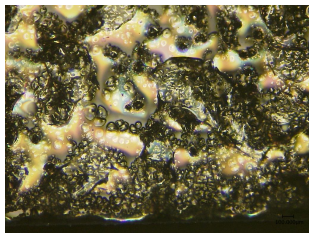

Figure 4.20. Microscope image (5 x): BSTO ink with 1 wt% methyl violet on a pure PEN substrate.Flash lamp treatment: 15.013 ± 0.042 J cm^{-2}, 400 V, 20 ms. The energy seemed too high, since the sol gel layer and the substrate are mostly burned.

Increasing the energy by approx. 1 J cm^{-2} for the next four experiments, respectively, the formation of some kind of "bubbles" can be observed (see figure 4.15 to 4.18). However, the change in appearance of these samples is insignificant. A further increase of energy, however, lead finally to the burning of the sol-gel layer as well as the substrate due to temperatures of around 440°C at the surface (see figures 4.19 and 4.20).
The laser microscope images only show a change in appearance, however, to determine if this change is due to the formation of some crystal structures or due to other processes, the samples were also investigated using the scanning electron microscope (SEM) and X-ray diffraction (XRD) measurements. Especially, the latter is important to determine the crystal structure of materials. Figures 4.21 to 4.23 represent the SEM images of the PulseForge experiments 7, 5 and 3 with the energy parameters 15.013 J cm^{-2}, 11.790 J cm^{-2} and 9.637 J cm^{-2}, respectively. The XRD measurements cannot be done on a PEN substrate since these materials have an amorphous structure and result therefore in a noisy background signal which makes it difficult to determine single peaks of the BSTO structure. Hence, the BSTO ink was applied onto a SiO_2 wafer that only shows very defined peaks and was treated with similar flash lamp parameters as the samples on the PEN substrate. The SiO_2 wafers were oxygen plasma treated to increase the spreading of the BSTO ink containing methyl violet and after the spin coating process they were dried on a hot plate at 111°C for 2 h to remove the solvent. Afterwards two wafers were treated with the following PulseForge parameters presented in table 4.4.

Table 4.4. Flash lamp settings of the SiO_2 wafer sintering. Wafer 1 was treated with three different parameter settings, while wafer 2 was only sintered with the highest applied energy of wafer 1.

Wafer1

Energy (J cm^{-2})	**Voltage** (V)	**Pulse Length** (ms)	**No. of Pulses**
9.637 ± 0.044	330	20	1
15.013 ± 0.042	400	20	1
16.072 ± 0.052	450	15	5

Wafer2			
16.072 ± 0.052	450	15	5

Figures 4.24 and 4.25 show the XRD patterns of the SiO_2 wafer after the PulseForge treatment. These XRD pattern represent substitutionally the results of the flash lamp treatment shown in figures 4.21 to 4.23.

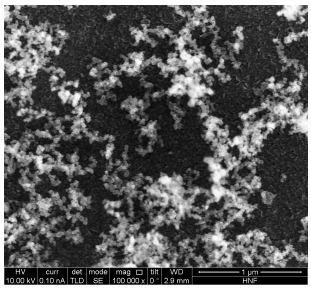

Figure 4.21. SEM image (100.000 x) of a BSTO ink layer with 1 wt% methyl violet on a pure PEN substrate after a flash lamp treatment with the following settings: 15.013 ± 0.042 J cm^{-2}, 400 V, 20 ms. The image shows some particles that could be nanocrystals. However, this needs to be confirmed by XRD measurements.

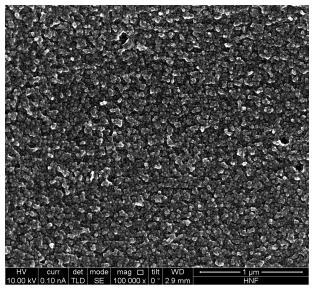

Figure 4.22. SEM image (100.000 x) of a BSTO ink layer with 1 wt% methyl violet on a pure PEN substrate after a flash lamp treatment with the following settings: 11.790 ± 0.052 J cm^{-2}, 360 V, 20 ms. The image also shows nanoparticles which could be BSTO crystals.

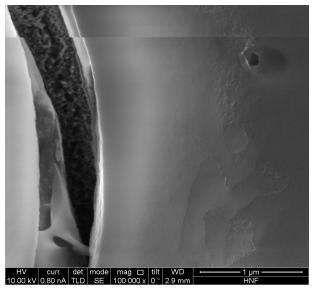

Figure 4.23. SEM image (100.000 x) of a BSTO ink layer with 1 wt% methyl violet on a pure PEN substrate after a flash lamp treatment with the following settings: 9.637 ± 0.044 J cm^{-2}, 330 V, 20 ms. Here, the layer seems mostly unchanged and smooth, while the crack on the left side shows a rougher surface.

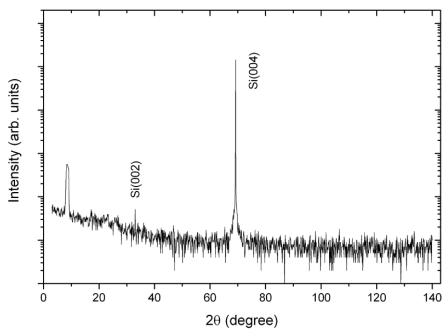

Figure 4.24. XRD pattern of wafer 1 after PulseForge treatment with three different settings. The added flash lamp treatments yield in a peak at $2\theta = 8.3$ °.

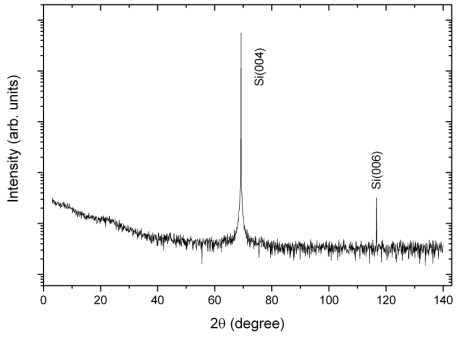

Figure 4.25. XRD pattern of wafer 2 after a single PulseForge treatment. No peaks, except of the SiO_2 wafer were detected.

The XRD results lead to two conclusions. First, the used PulseForge parameters (which were similar to the ones published by *Kim* et. al [50]) did not yield in the expected BSTO crystal

structure since no XRD peaks of this material were detected. The one peak at $2\theta = 8.3$ ° does not belong to BSTO crystal structure, but could correspond to $Sr_3Ti_2O_7$. However, without further peaks no conclusion can be made. Second, the subsequent treatment with three flash lamp settings of wafer 1 show that the succession of several flashes might have an effect on the formation of a crystal structure, compared to a single treatment with only the highest energy of wafer 2, which did not yield in any detectable peak.
Conclusively, the flash lamp sintering approach using the PulseForge 1200 did not yield the expected results, which is why another synthesis route was tested.

4.2.2 BSTO Nanocrystals Suspended in Organic Solvents as Temperature Sensitive Layer

Since the flash lamp sintering approach was not successful, another approach, in which the BSTO nanocrystals were directly synthesized and afterwards applied onto the sensor, was tested. The BSTO nanocrystals were prepared according to *Moghtada* et. al [175] and *Veldhuis* et. al [48], respectively. Both approaches are done at low temperatures and described in chapter 3.2.2 and 3.2.3. Afterwards, the obtained nanocrystals were suspended in an organic solvent, which was chosen according to *Hansen Solubility Parameters* (HSP). For further details on the *Hansen Solubility Parameters* consider the literature [176]. In short, the HSP express quantitatively the cohesion energy that is the sum of the three energies caused due to dispersion interactions (E_D, dispersion cohesive energy), permanent dipole-permanent dipole interactions (E_P, polar cohesive energy) and hydrogen bonding (E_H). Materials with a high affinity towards each other also show similar HSP [176]. In case of the BSTO nanocrystals 24 different suspensions were prepared using different solvents (e.g. water, several alcohols [methanol, ethanol, isopropanol, butanol, cyclohexanol], toluene, acetone, benzylacetate, γ-butyrolactone, several gylcols [diethylene glycol, triethylene glycol monomethyl ether, dipropylene glycol], chloroform, cyclohexane, ethylacetate, butylacetate, acetonitiril, THF, DMF, 1-methyl-2-pyrrolidone, DMSO, dichlormethane, propylenecarbonate) to determine which one yields the most stable suspension.

4.2.2.1 Preparation of BSTO Nanocrystals Using Ultrasound

According to *Moghtada* et. al [175, 177–179] $XTiO_3$ (where X can be Ba, Sr, Ni) nanocrystals can be obtained in a fast one-step synthesis using ultrasound at 50°C according to the following reaction pattern:

$$BaCl_2\ (aq) + TiCl_4\ (l) + 6\ NaOH\ (aq) \rightarrow BaTiO_3\ (s) + 6\ NaCl\ (aq) + 3\ H_2O \tag{4.1}$$

The obtained precipitate was examined by XRD, SEM and EDX. The XRD data was analyzed using *Jana2006*, which is a freely available software that is able to calculate certain XRD spectra according to given parameters. In figure 4.26 the XRD data of the obtained nanocrystals is shown. The upper spectrum represents the measured (black) and calculated (red) data of the expected BSTO nanocrystals, while the lower spectrum shows the calculated δ of the data sets (measured vs. calculated), which should be zero, if the measured and calculated data match.

As can be seen, the measured data does not fit the calculated one since in the upper spectra several peaks are missing where according to the calculated spectra peaks are expected. Additionally, the lower spectra, which shows the δ of measured and calculated data, is not a straight line, which is expected if the measured data would fit. Conclusively, the obtained nanocrystals are not BSTO. Therefore, the powder was also examined using SEM and EDX to determine

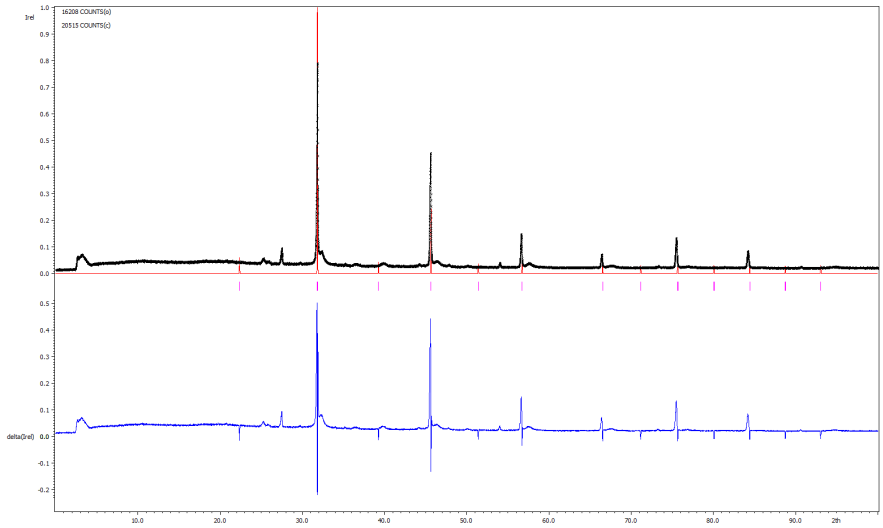

Figure 4.26. Top: Measured (black) and calculated (red) XRD data of the obtained nanocrystals according to Moghtada et. al [175] and BSTO, respectively.
Bottom: Calculated δ of the measured and calculated data based on BSTO.
Both spectra indicate that the measured particles do not have the crystal structure of BSTO, since the δ is quite significant and according to the upper spectrum not all expected XRD peaks are present.

of which elements the powder consists. The SEM (figure 4.27) shows cuboidal crystals whose composition were determined using EDX in the two marked spots. The EDX results are shown in table 4.5, where the upper line represents the values in wt% and the lower line in atomic %, respectively for both spots. It can be seen that the main components are sodium and chlorine instead of barium, strontium, titanium and oxygen. The negative values of strontium in the second spot indicate that this element was not detected. These findings lead to the conclusion that the obtained crystals are rather NaCl instead of the expected BSTO, which also explains the mismatch of the XRD data shown above.

Analyzing the measured XRD data again based on the NaCl crystal, the XRD spectrum matches nicely. Since this synthesis route was published several times, but no exact concentrations were mentioned in the respective experimental part, some variations were tested. Additionally, also the amount and concentration of NaOH and the time of sonication were varied. However, the results were always the same, namely the main part of the particles consisted of NaCl which is the byproduct of the above shown reaction scheme. Extensive washing of the received particles was also unsuccessful, which is why a third synthesis route was used.

4.2.2.2 Preparation of BSTO Nanocrystals Based on Benzyl Alcohol at Room Temperature

4.2.2.2.1 Characterization of the Obtained BSTO Nanocrystals

Following the recipe of *Veldhuis* et. al [48] (see chapter 3.2.3), the expected BSTO nanocrystals were obtained. Figure 4.28 represents the corresponding XRD spectrum, showing the expected peaks with their corresponding orientation of the crystal. The calculated red line is hardly visible because the measured data yields in a quite broad spectrum indicating the existence of nanocrys-

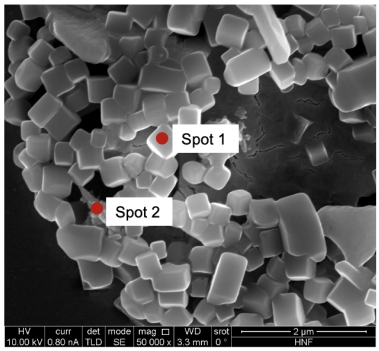

Figure 4.27. SEM image of the obtained nanocrystals. The two marked spots show the position at which the EDX measurement was done.

Table 4.5. Composition of the measured spots using EDX in wt% (upper line) and atomic % (lower line). The negative values for strontium indicate that in the chosen spot this element was not detectable. Otherwise show the results that the main elements are sodium and chlorine, meaning the sample consists mainly of NaCl.

	C	O	Na	Cl	Ti	Sr	Ba
1	1.84	3.54	11.98	26.10	0.12	1.03	55.38
	7.5	10.9	25.6	36.1	0.1	0.006	19.8
2	7.10	15.0	21.48	26.2	2.41	-13.98	41.8
	16.6	26.4	26.3	20.8	1.4	-0.047	8.6

tals. However, the lower spectrum, representing the δ of measured and calculated data sets, is almost zero and confirms that the measured particles are BSTO.

Additionally, the obtained nanocrystals were analyzed using TEM to determine the particles size, since the magnification of the SEM was not high enough. In figures 4.29 and 4.30 two TEM images with magnifications of 38.000 and 450.000 are displayed. As can be seen the particle size is around 10 nm in diameter, which is significantly below 30 nm, the found critical size at which the ferroelectrical properties of the BSTO vanish.

Furthermore, ICP-OES was used to determine the Ba:Sr ratio in the nanocrystals. The analysis showed a 49.9 : 50.1 atomic % ratio of Ba:Sr, which fits the ratio of the starting material. However, the Ti:(Ba/Sr) ratio yields 46.7 : 53.3 atomic %. The permittivity was determined by measuring the capacitance of a BSTO pellet (diameter: 10 mm and height: 8.1 mm) using a LCR meter and calculating the permittivity using the "partial capacitance model" [180]. The capacitance for two sample resulted in $C = 5.93$ pF and $C = 7.35$ pF and the corresponding permittivity yields $\epsilon = 17.7$ and $\epsilon = 21.4$, respectively. The calculation of permittivity assumes a homogenous BSTO crystal, which was not the case for the prepared BSTO pallet in this case. However, the values give a good indication of the permittivity and are in the same range as the ones presented by Wada et. al [45]. Finally, also the temperature dependence of the obtained nanocrystals were measured using the LCR meter ST2826 (Sourcetronic GmbH, Germany). Figures 4.31 and 4.32 show the temperature dependence of resistance and capacitance for the BSTO nanocrystal pallet. The temperature was varied from room temperature (approx. 20°C) to 309°C. As can be seen, there is no PTC effect visible as would be expected for BSTO, since the resistance decreases with increasing temperature. In the temperature regime of 40-120°C, the Curie Temperature, T_C, would be expected (due to the chosen Ba:Sr ratio), however, no significant change in resistance is detected. Since the crystal size lies below the critical size of 30 nm, this behavior was to be expected. For the capacitance measurement a continuous increase was found.

4.2.2.2.2 Sensor Fabrication with Three Different BSTO Suspensions

Nevertheless, the obtained nanocrystals were suspended in three appropriate solvents, selected according to *Hansen Solubility Parameters*, i.e. benzyl alcohol, isopropanol and DMF. These

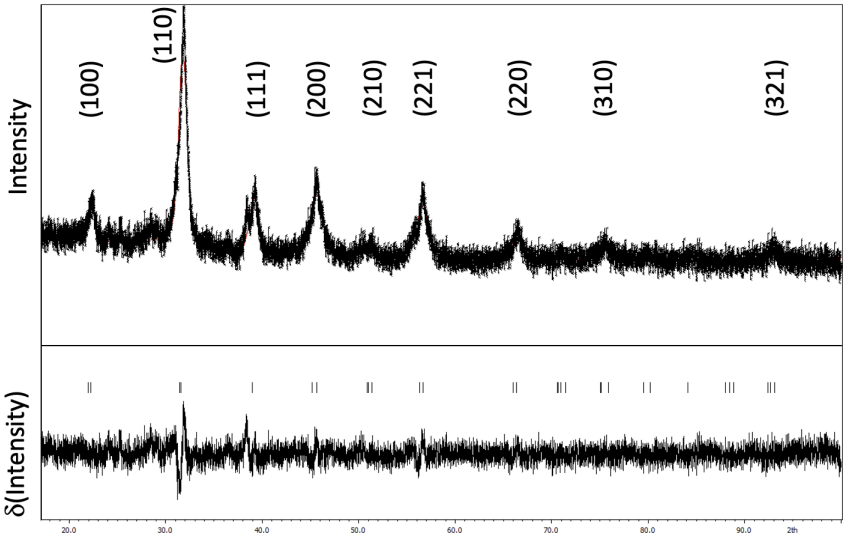

Figure 4.28. Top: Measured (black) and calculated (red) XRD data of the obtained nanocrystals according to Veldhuis et. al [48] and BSTO, respectively. The calculated red line is hardly visible because the measured data yields in a quite broad spectrum indicating the existence of nanocrystals. **Bottom:** Calculated δ of the measured and calculated data based on BSTO.

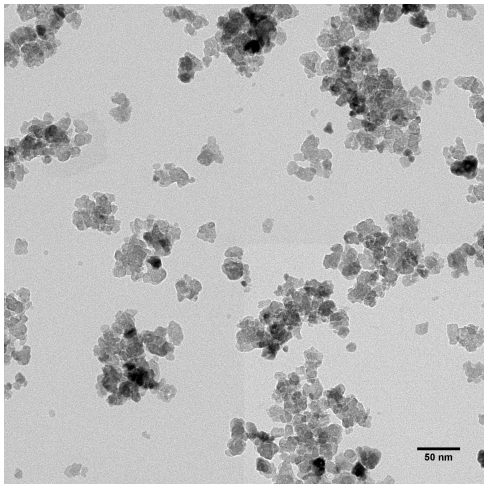

Figure 4.29. TEM image of BSTO nanocrystals at a magnification of 38.000.

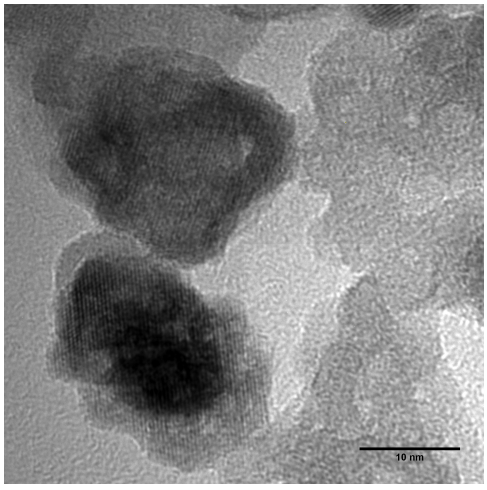

Figure 4.30. TEM image of BSTO nanocrystals at a magnification of 450.000. The particle size lies around 10 nm.

suspensions were then applied onto IDEs (laser ablated structures as well as cleanroom fabricated ones, see chapter 3.3.2). To be able to measure the change in resistance or impedance with increasing temperature, a dense coverage of the IDE surface is necessary. This was examined by SEM at which the particle distribution on top of and in between the IDE fingers was

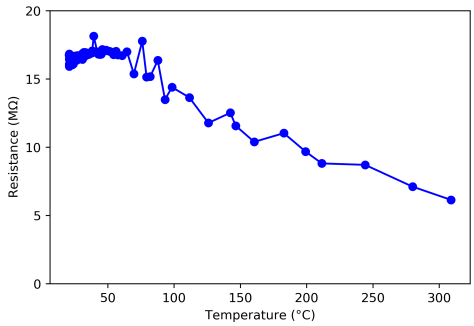

Figure 4.31. Temperature dependence of the resistance of BSTO nanocrystals. The temperature was measured from room temperature to 309°C. In the temperature regime of 40-120°C, the Curie Temperature, T_C, would be expected due to the chosen Ba:Sr ratio. However, no PTC effect is observable in the entire temperature range, which indicates that the size of the nanocrystals is below the critical size of 30 nm.

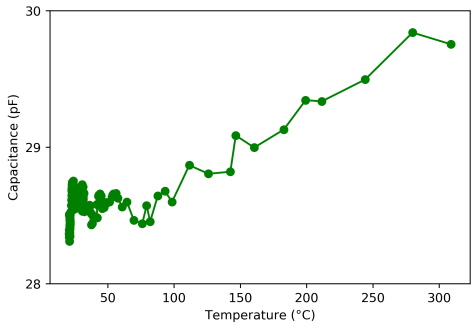

Figure 4.32. Temperature dependence of the capacitance of BSTO nanocrystals. The temperature was measured from room temperature to 309°C. In this regime the capacitance increases continuously.

imaged. Figures 4.33 and 4.34 show two SEM images at 1.300 and 40.000 magnification after the BSTO suspension using benzyl alcohol as solvent was applied once. In figure 4.35 an image of a completely covered IDE is shown, which is the result of a second drop casting of this BSTO suspension. The brighter areas in figure 4.33 represent the gold fingers of the IDE while the darker parts are the gaps in between these fingers, where most of the BSTO nanocrystals are accumulated. Only a few isolated particles can be seen on top of the gold fingers. Since this would be problematic for any electrochemical measurements, the suspension was applied a second time (see figure 4.35). Thus, the IDE shows a complete coverage, but the areas of the fingers and gaps can still be distinguished (bright: gap, dark: fingers). The larger magnification in figure 4.34 shows after the first drop casting already a quite dense layer in the gaps.

The same procedure was done using isopropanol and DMF as solvents for the BSTO suspensions. Both solvents resulted in suitable suspensions but showed a bad IDE coverage as can be seen in figures 4.36 to 4.39. In figures 4.36 and 4.38 the BSTO layer on top of a laser ablated IDE is displayed with magnifications of 1.300 and 3.000, respectively. Figures 4.37 and 4.39 show the BSTO coverage of cleamroom fabricted IDEs. Instead of a continuous layer, the particles agglomerated during the drying process and therefore, only covered some parts of the IDE.

At this point, the concept of preparing a flexible and miniaturized temperature sensor containing BSTO as sensitive layer was given up due to several reasons:

1. The finally obtained BSTO nanocrystals were too small in size and therefore lost their temperature sensitive abilities, i. e. the change in crystal structure from tetragonal to cubic upon reaching the Curie temperature (PTC effect).

2. Therefore, the synthesis route of *Veldhuis* et. al [48] would have needed to be adjusted to obtain crystallite sizes above the critical size of 30 nm in order to still have the desired PTC effect. This could have been done in two ways:

    - Either the concentration of the benzyl alcohol solution could have been varied, since *Veldhuis* et. al [48] hypothesized that the small size of the nanocrystals is achieved

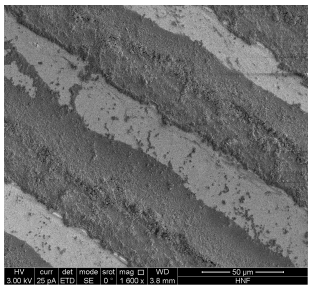

Figure 4.33. SEM image of an laser ablated IDE covered with BSTO nanocrystals suspended in benzyl alcohol (10 wt%) at a magnification of 1.300. The brighter areas are the golf finger of the IDE, the darker parts are the gaps between two fingers, in which most of the particles are accumulated.

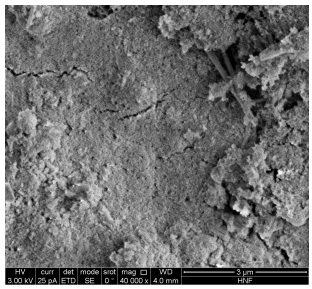

Figure 4.34. SEM image of an laser ablated IDE covered with BSTO nanocrystals suspended in benzyl alcohol (10 wt%) at a magnification of 40.000. The accumulated particles in the IDE gaps form a quite dense layer.

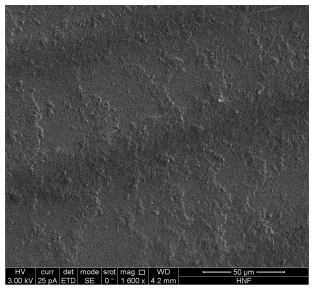

Figure 4.35. SEM image of a laser ablated IDE covered with BSTO nanocrystals suspended in benzyl alcohol (10 wt%) at a magnification of 1.600, after a second drop casting of the BSTO suspension. Now the entire IDE is covered with BSTO nanocrystals in a dense layer.

due to the formation of a capping layer by the benzyl alcohol molecules on top of the BSTO crystallites' surface that hinders the continuous growth

- Or an additional amount of water, e.g. 1 mol water per 1 mol of Ti alkoxide, could have been added, since *Veldhuis* et. al [181] showed that the variation of water influences the crystallite growth

3. However, even using the small size of approx. 10 nm of the BSTO particles to form stable suspensions that covers the surface of IDEs homogeneously was insufficient. Larger sized particles could increase the challenge to create stable suspensions or in a next step even printable inks. Especially inkjet inks have some additional requirements regarding the agglomeration and stability of suspended particles in solvents, since the solvents need to fit certain criteria of physicochemical properties, e.g. certain range of viscosity and surface tension need to be met.

In addition to the above mentioned reasons to stop working on the BSTO based temperature sensor, first promising results using ionic liquids (ILs) were achieved. The experiments and respective results are presented in the next chapter.

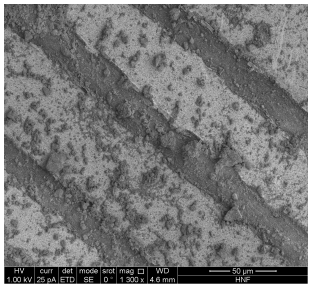

Figure 4.36. SEM image of an laser ablated IDE covered with BSTO nanocrystals suspended in isopropanol (10 wt%) at a magnification of 1.300. The brighter areas are the golf finger of the IDE, the darker parts are the gaps between two fingers.

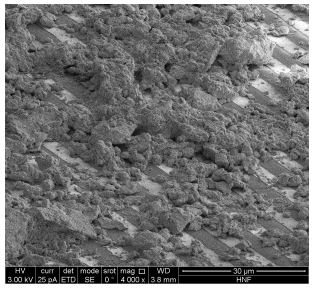

Figure 4.37. SEM image of an cleanroom fabricated IDE covered with BSTO nanocrystals suspended in isopropanol (10 wt%) at a magnification of 4.000.

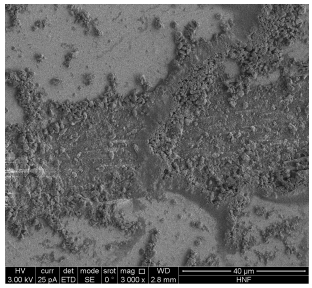

Figure 4.38. SEM image of an laser ablated IDE covered with BSTO nanocrystals suspended in DMF (10 wt%) at a magnification of 3.000. Here, the darker parts correspond to the gold fingers while the brighter ones represent the gap in between two adjacent fingers.

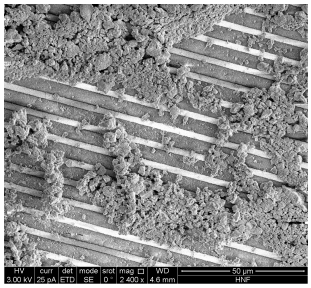

Figure 4.39. SEM image of an cleanroom fabricated IDE covered with BSTO nanocrystals suspended in DMF (10 wt%) at a magnification of 2.400. The bright lines correspond to the gold fingers, the darker parts are the gaps in between two fingers.

4.3 Development of a Temperature Sensor Based on Ionic Liquids and Their Viscosity-Dependent Diffusion Coefficient

Ionic liquids (ILs) are used for several decades in all kinds of fields, e.g. material science and technology applications due to their broad variety of properties. In this work, three different ILs were used as temperature sensitive material. Here, the change in viscosity, and thereby of the diffusion coefficient, with temperature was used as working principle of the sensor. Therefore, the change in current due to electrochemical processes at the surface of an electrode was measured and recorded with increasing and decreasing temperature using either cyclic voltammetry (CV) or chronoamperometry. In addition, different redox couples such as ferrocene and its derivatives, several quinone-hydroquinone couples as well as methylene blue (MB) were tested to investigate the influence of such molecules on the sensitivity and stability of the sensor. Moreover, also a combination of the three utilized ILs were tested to vary the temperature range in which the sensor is working as well as to check if this shows an impact on the sensitivity.
In the following, the development of three IL-based sensor prototypes are described and discussed. Starting with the first proof-of-principle experiment, followed by testing different redox couples and finally discussing the results of the chronoamperometric measurements.

4.3.1 Proof-of-Principle Experiment

As a first experiment, ferrocene dimethanol was dissolved in 1-butyl-1-methylpyrrolidinium bis-(trifluoromethylsulfonyl)imide ($[C_4C_1pyrr][NTf_2]$, **IL1**) with a concentration 0.2 M. From this solution a ca. 20 μl drop was placed on top of the planar, laser ablated electrode structure. Without further treatment, cyclic voltammograms at different temperatures of this setup were recorded using a scan rate of 0.05 V/s. The temperature was varied between 0°C and 60° and were changed in 10°C steps. Figures 4.40 and 4.41 show the voltammograms of these measurements as well as the peak current of the oxidation and reduction process as function of temperature.

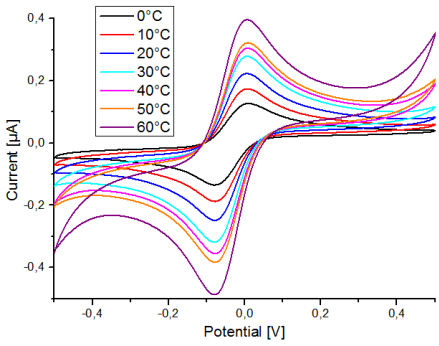

Figure 4.40. CV curves of ferrocene dimethanol in $[C_4C_1pyrr][NTf_2]$ (0.2 M) at different temperatures.

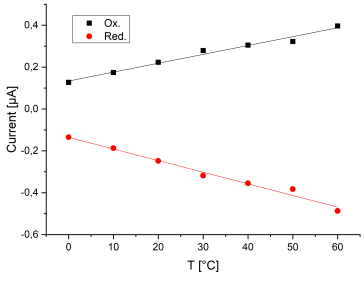

Figure 4.41. Current of oxidation and reduction peaks as function of temperature. The sensitivity and linearity yield (4.23 ± 0.27) nA/°C and r^2 0.9901 as well as (-5.56 ± 0.33) nA/°C and r^2 0.9911 for reduction and oxidation, respectively.

It can be seen that the peak current for both processes, oxidation and reduction, show a linear dependence on temperature as well as a good sensitivity. The linearity yield r^2 values of 0.9901 and 0.9911 for the reduction and oxidation functions. However, at 50°C both values, for reduction and oxidation, show a higher deviation from the linearity than the current values for the other temperatures. The sensitivity for the reduction and oxidation process accounts for (4.23 ± 0.27) nA/°C and (-5.56 ± 0.33) nA/°C, respectively. Due to the high cathodic and anodic limit of the IL (2.8 V and -2.5 V) it is assumed that the IL itself is not changed by the cyclic voltammetry.
Starting from here, a more advanced sensor setup was developed. This included the utilization of microelectrodes as well as testing of different redox couples of the ferrocene class, e.g. 1,1-ferrocene dicarboxylic acid, 1,1-ferrocene dimethanol, 1,1-dimethylferrocene, 6-(ferrocenyl)-hexanethiol, 1,1-(Ferrocenyl)undecanethiol and ferrocenecarboxaldehyde, the quinone-hydroquinone couple and methylene blue. Additionally, a UV-curable polymer matrix was added to the IL-redox couple solution that should fixate the IL-layer on top of the electrodes.

4.3.2 Improving the Sensor System

4.3.2.1 Microelectrodes

To improve the signal-to-noise ratio (SNR) microelectrodes were used. They were either obtained directly during the cleanroom fabrication or for the laser ablated ones they were defined by passivating most parts of the working electrode with a SU8 photoresist using the OmniJet 300 inkjet printer. In order to increase the measured current values an array of three microelectrodes were actually used.
For the microelectrodes used in this work probably all four cases, explained in chapter 2.4, occurred during the electrochemical measurements. While in chapter 2.4 the diffusion constant was considered as constant, here the conducted experiments were operated at different temperatures and since the diffusion coefficient is temperature dependent it changes during the experiments. Furthermore, several ILs and mixtures of them with different viscosities were utilized in the measurements and thereby changing the diffusion coefficient of each prototype. Therefore it is probable that the equations describing the sensor system is only at certain experimental conditions accurately and merge into each other during the change of temperature.
The microelectrodes utilized in this work are much smaller than the electrodes Compton et al. [171] used to determine the validity of the Cottrell-equation. Therefore, the Shoup-Szabo-equation will be applied to describe the observed sensor behavior in chapter 5.2.

4.3.2.2 UV-Matrix

Applying the IL-redox couple solution onto the planar sensor system can be done via drop casting or inkjet printing for instance. However, this solution needs to be fixed on the surface for practical applications. Hence, a UV-curable polymer matrix was added to the solution which will polymerize upon UV-curing and with that form a porous matrix in which the IL solution is "trapped" but still able to diffuse. Here, a mixture of 1,6-hexanediol diacrylate (**M1**) and trimethylolpropane ethoxylate triacrylate (**M2**) in a 1:1 molar ratio and 3 wt% photoinitiator (2-hydroxy-2-methyl-propiophenone; **1**) was used and irradiated for some seconds with UV light. In the beginning, also a variation of **M1** : **M2** ratio was tested, while for the chronoamperometric measurements always a 1:1 ratio was used. Therefore, the 1:1 molar mixture is labeled with UV1, a 1:3 molar ratio is labeled with UV2 and a 3:1 molar ratio is labeled with UV3. To all mixtures always 3 wt% of the photoinitiator was added.
The chosen photoresist **1** is split into two radicals **2a** and **2b** upon UV irradiation and initiates the

polymerization reaction by attacking the double bonds of the two monomers **M1** and **M2**. Since **M1** is a linear molecule while **M2** is branched a cross-linked network with different pore sizes can be obtained by varying the molar ratio of **M1** and **M2**. A schematic of the polymerization process is shown in scheme 1. The cross-linking of the two monomers with each other is not shown, although very likely to happen frequently.

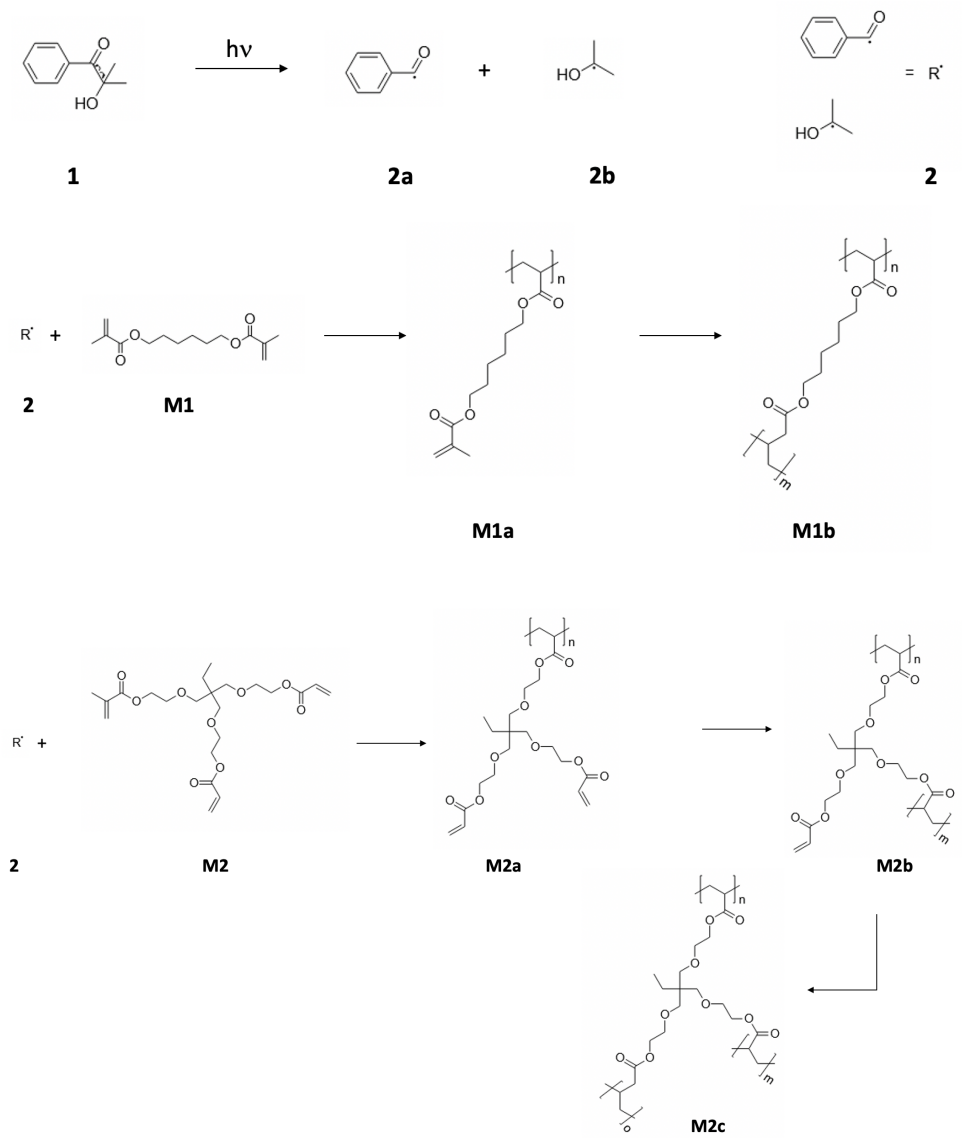

Scheme 1. Scheme of the polymerization process. In the first row the radical formation of the photoresist **1** upon UV irradiation is shown. In the middle and last row the polymerization reaction of the monomers **M1** and **M2** are displayed.

Unfortunately, this procedure has one major drawback, namely the decomposition of the ferrocene redox molecule due to the UV irradiation [182]. However, even without curing the polymer matrix using UV light, the ferrocene molecule would decompose over time due to sunlight

irradiation and is therefore not the best choice for a stable sensor. Following this, several other redox systems were tested to find a stable redox molecule that can be reduced and oxidized repeatedly.

4.3.3 Testing Different Redox Couples

First, several other ferrocene derivatives were tested to check their stability over time and their general redox behavior. Among them were 1,1-ferrocene dicarboxylic acid, 1,1-ferrocene dimethanol, 1,1-Dimethylferrocene, 6-(ferrocenyl)hexanethiol, 1,1-(ferrocenyl)undecanethiol and ferrocene carboxaldehyd as already mentioned. However, all of them proved to be not appropriate as redox couple for this application as will be explained in the subsequent section. Then, other redox systems, such as quinone-hydroquinone and methylene blue (MB) were investigated. From the quinone-hydroquinone system also several derivatives, e.g. tetrafluoroparaquinone, 2,6-dimethylparaquinone, were examined, which showed a greater stability than the ferrocene couple. One reason, why this system was of interested is the fact that there are also ionic liquids available that show a quinone moiety which could have been used as solvent and redox active material in one. On the other side is the redox reaction of a quinone-hydroquinone system quite complicated, because it is not just a simple electron transfer but the oxidation process includes also an acid-base equilibrium. The oxidation of a simple hydroquinone molecule (**3**) to a 1,4-benzoquinone (**4**) is shown in figure 4.42.

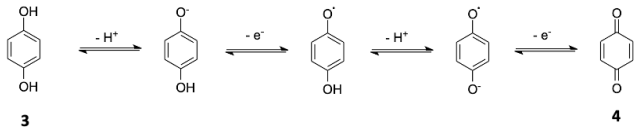

Figure 4.42. Oxidation mechanism of hydroquinone (**3**) to 1,4-benzoquinone (**4**).

Due to the complicated redox mechanism, the resulting CV is also hard to interpret and becomes even harder if at some point a mixture of hydroquinone (**3**) and benzoquinone (**4**) are present simultaneously. The CV of a 1:1 mixture of **3** and **4** as well as a CV of the pure hydroquinone in **IL1** is shown in figure 4.44. The concentration was 85 mM for each solution and the 1:1 mixture was based on a volumetric ratio. As can be seen, is the CV of the mixture quite complex comprising several oxidation and reduction peaks. Therefore, this system was found to be not suitable and was not further investigated. Instead another common redox molecule, namely methylene blue, was tested. Figure 4.43 shows methylene blue (**5**) and its reduced form **6** [183].

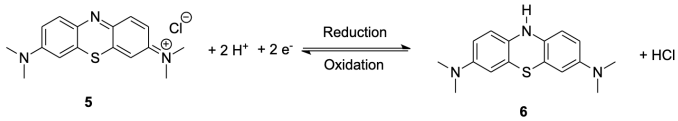

Figure 4.43. Methylene blue (**5**) and its reduced form **6** [183].

Although the methylene blue molecule as such is quite large the oxidation and reduction is a two electron transfer reaction and with that much more simple than for the quinone-hydroquinone system. In figure 4.45 the CV of methylene blue (**5**) in **IL1** (ca. 20 mM) is shown.

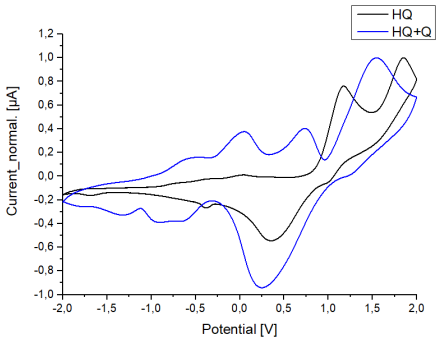

Figure 4.44. CV of pure hydroquinone (**3**) as well as a 1:1 mixture of hydroquinone (**3**) and 1,4-benzoquinone (**4**).

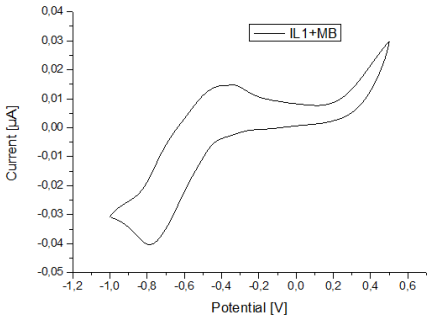

Figure 4.45. CV of methylene blue (**5**) in **IL1** at a concentration of 20 mM.

4.3.4 Comparison of Ferrocene and Methylene blue as Redox Molecule

In the following the stability of the temperature sensitive layer comprising either ferrocene or methylene blue as redox molecule is demonstrated. Therefore, for every step of the preparation of the sensitive layer CVs were recorded. This means, first, the pure redox molecule dissolved in **IL1** were applied onto the electrode configuration (2 μl) and CVs were recorded. Second, the **IL1** solution was removed and a mixture of redox molecule in **IL1** and the UV matrix (4:1 volume ratio) was applied without curing (again 2 μl). Third, the sensor was cured using a UV lamp and then a number of CVs were recorded over several days. The corresponding CVs (always the fifth cycle of each recording is shown) are displayed in figures 4.46 - 4.49. As can be seen the functionality of the sensitive layer stops a few days after the curing process took place and no reduction or oxidation peaks can be detected anymore, if ferrocene was used as redox molecule. The increase in current after the addition of the UV matrix solution and its curing is probably caused by the presence of additional electrons from the unreacted monomers and the free radical of the photo initiator after UV irradiation. The same procedure was done using methylene blue as redox species. Since the solubility of MB in the respective ILs is much lower, only a concentration of 40 mM was used. Figures 4.50 to 4.53 show the behavior of a methylene blue containing temperature sensitive layer. As can be seen, figure 4.53 shows still clear redox peaks, therefore, the temperature sensitivity was tested next. Thus, the sensor was fixated onto the temperature measurement setup (described in chapter 3.5.2) and several CVs were recorded at different temperatures. First, only the change between room temperature and 42°C and back to room temperature were checked. Afterwards, the temperature was increased again to 42°C and then further to 60°C and back to room temperature. This is shown in figures 4.54 and 4.55, respectively. The indices behind the temperature in the legend of these figures indicates the number of the heating or cooling cycles.

There are mainly two things to observe: first, the amplitude of the peak is increasing/decreasing with higher/lower temperatures; second, at higher temperatures (42°C and 60°C) a second reduction peak can be seen that also disappears again at room temperature. Additionally, the peaks at elevated temperatures shift slightly in potential. For the reduction process, the potential shifts towards lower values, while the oxidation process does not show a continuous shift in one direction (see table 4.6). The appearance of this second peak might be due to some intermolecular interactions between the MB molecules and the IL which can only be seen at higher temper-

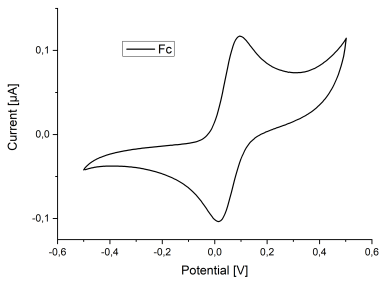

Figure 4.46. CV curve of ferrocene in **IL1** (0.2 M).

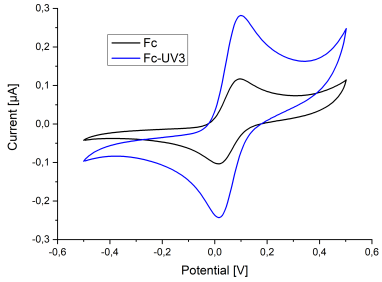

Figure 4.47. CV curves of ferrocene in **IL1** and after the addition of UV3 solution (4:1 ratio).

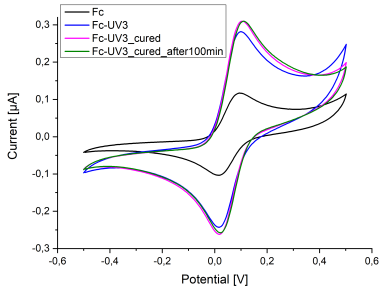

Figure 4.48. CV curves of ferrocene in **IL1**, after the addition of UV3 solution (4:1 ratio) and immediately after the layer was cured as well as after 100 minutes post curing.

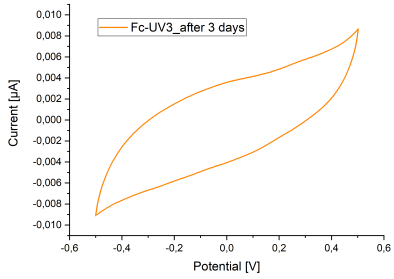

Figure 4.49. CV curve of the temperature sensitive layer, three days after curing.

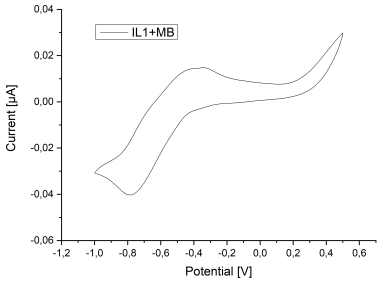

Figure 4.50. CV curve of methylene blue in **IL1** (40 mM).

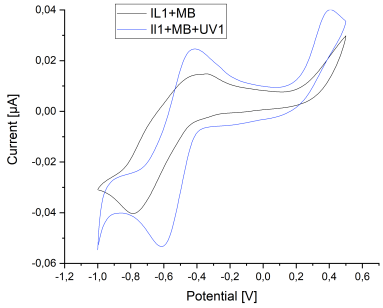

Figure 4.51. CV curves of methylene blue in **IL1** and after the addition of UV1 solution (4:1 ratio).

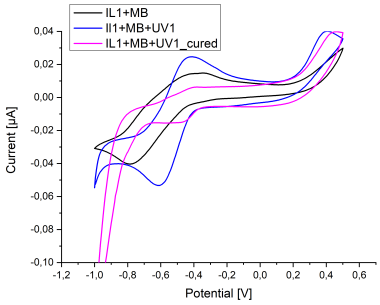

Figure 4.52. CV curves of methylene blue in **IL1**, after the addition of UV1 solution (4:1 ratio) and immediately after the layer was cured.

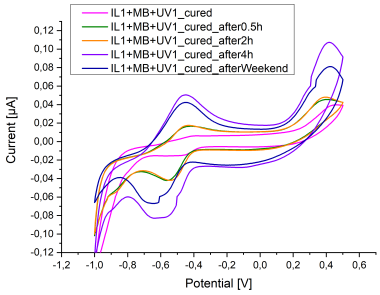

Figure 4.53. CV curves of the temperature sensitive layer, 30 min, 120 min and 240 min as well as three days after curing.

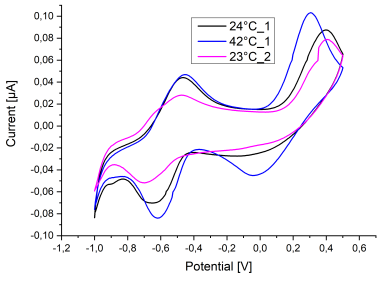

Figure 4.54. CV curve of methylene blue in **IL1** at different temperatures.

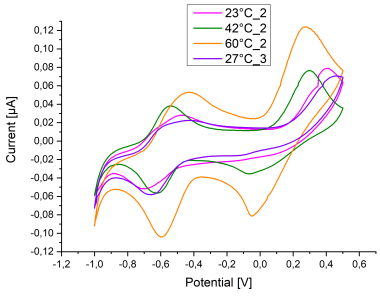

Figure 4.55. CV curves of methylene blue in **IL1** at elevated temperatures.

atures [184]. The CV measurements show that a sensitive layer comprising methylene blue instead of a ferrocene derivative is more stable and shows a similar temperature dependence, which is why for all further experiments methylene blue was chosen as a redox molecule.

Table 4.6. Oxidation and reduction potentials at several temperatures for the test sensor containing methylene blue as redox molecule in **IL1**.

Temperature (°C)	$E_{Ox.}$ (V)	$E_{Red.}$ (V)
24	-0.46629	-0.66262
42	-0.45114	-0.61731
23	-0.47129	-0.69793
42	-0.54184	-0-61731
60	-0.42598	-0.59723
27	-0.43106	-0.65762

However, the CV technique is also not the most suitable for the task at hand, i.e. to develop a flexible temperature sensor for IoT applications, since the measurement time is quite long. To decrease the measurement time, amperometric techniques are more appropriate, especially for these low power IoT applications, which require an output of data within seconds. Thus, switching to amperometric measurements can yield more stable and reproducible results as can be seen in the next paragraph.

4.4 Chronoamperometric Measurements

4.4.1 Chronoamperometric Experiments using Custom-made Measurement Electronics

Using the chronoamperometric measurement technique the sensors could be tested over longer times and for several heating and cooling cycles. Furthermore, instead of using a potentiostat the experiments were carried out with custom-made measurement electronics utilizing a NHS3152 NFC MCU by NXP Microelectronics. The NHS3152 has an embedded temperature sensor with a precision of $\pm$ 0.5°C, so that it provided the opportunity to record the resulting current and the reference temperature simultaneously with one device. In accordance with the CV experiments, described in the previous section, the applied voltage for the chronoamperometric measurements was chosen to be - 1.0 V, since at this potential the oxidation had taken place and a mass-transfer-limited region had been reached (the oxidation peak in the voltammograms occurred at approx. -0.6 V). To avoid charging processes on the electrode three measurements with a pulse length of 0.1 s were applied within 3 s, followed by a pause of 10 s. This is illustrated in figure 4.56.

The temperature was cycled automatically by the setup roughly between -20° and 60° (at this point which exact temperature was hit always depended upon the temperature in the lab). For the analysis of the data two differentiation are made: the data at the lowest temperature (approx. -20°C) is added to the cooling cycle and is depicted in blue, while the data at the highest temperature (approx. 60°C) is added to the heating cycle and depicted in red.
The previous experiments were all performed using only **IL1** as solvent. However, the melting point of **IL1** is -18°C which is for the desired temperature range of at least -20°C not sufficient. Since **IL2** has a melting point of -81°C a 4 : 1 mixture of **IL1** and **IL2** (sensor type 1) was used to prepare the first prototype. Furthermore, the pure **IL3** (sensor type 2) as well as a 1 : 3 mixture of **IL2** and **IL3** (sensor type 3) were used to assemble two more prototypes. In case of sensor

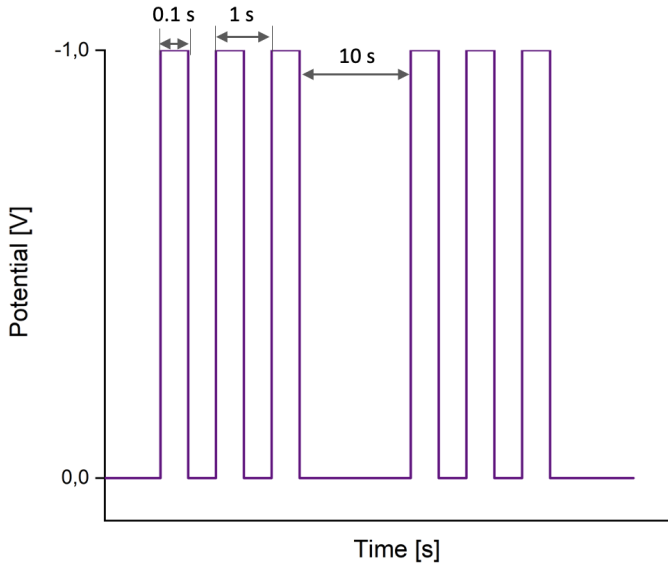

Figure 4.56. Potential step of the chronoamperometric measurements at -1.0 V with a pulse length of 0.1 s. Three pulses in a row were applied, followed by a pause of 10 s.

type 1, methylene blue (40 mM) was added as redox molecule. In sensor type 2 and 3, **IL3** was used as redox species and solvent simultaneously. All three sensor types were fixed onto the planar electrode system using the above described UV matrix.

4.4.1.1 Sensor Type 1: IL1 + IL2 + MB

Figure 4.57 shows the results of a type 1 sensor (comprising the mixture of **IL1** and **IL2**; see chapter 3.4.2.2) starting with a cooling cycle from 11.2°C downwards. The last heating cycle ended therefore at a temperature of 19.4°C. In total seven heating and seven cooling cycles were recorded. The temperature was varied between -14.2° and 55.2° in roughly 10° steps. Only the current values at stable temperatures were chosen and averaged for each single cycle ($N_{averg.} = 54 \pm 10$ measurements per temperature per cycle). At -14.2°C the average current is 396.7 ± 11.3 nA and at 55.2°C 1685.5 ± 26.3 nA. The lowest temperature is always counted for the cooling cycle, while the highest temperature always belongs to the heating cycle.

As displayed in figure 4.57 the resolution at the single temperatures are not always high enough to distinguish each temperature. Principally, the current values of the heating cycles are always lower than the ones of the cooling cycles. This might be due to supercooling phenomenon occurring during the cooling and heating cycles, meaning the IL stays in its liquid form beyond the freezing point. Due to the strong increase in viscosity during the cooling of IL, it might occur that no nucleus is formed that is necessary to start the crystallization. This results in a prolonged liquid phase until the IL solidifies and forms an amorphous (non-crystalline) solid phase. [128] However, if the temperature increases again the transition from solid to liquid occurs not at the same temperature as the solidification process and sometimes the heating of IL even only starts a kind of cold crystallization that yields in the formation of an amorphous glassy structure, resulting in a melting point clearly above the freezing/solidification point (can be up to 20 K

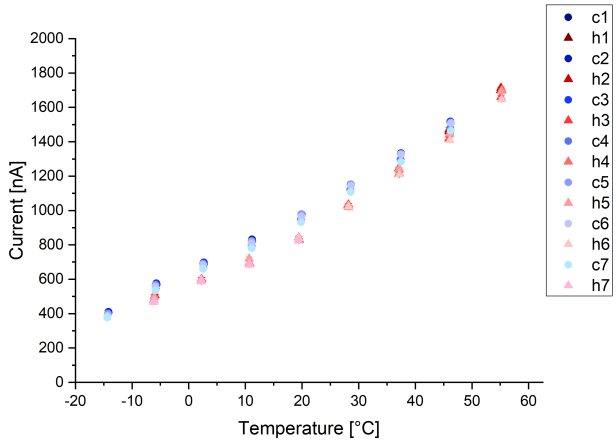

Figure 4.57. Chronoamperometric measurements at -1.0 V with a pulse length of 0.1 s from -14° to 55° using a methylene blue sensor type 1 for several cooling and heating cycles, starting from 11.2°C and decreasing further to complete the first half cooling cycle. The seventh heating cycles ends finally at a temperature of 19.4°C. The error bars lie within the marker size.

difference) [185, 186]. Since the cooling and heating between each temperature is done rather fast - approx. 10 K/min - it is probable that supercooling effects take place. According to Triolo et al. [186] crystallization occurs at much slower cooling rates of approx. 1.2 K/min. Applying these considerations to the presented results the sensitive layer stays in its liquid state from the highest to the coolest temperature during a cooling cycle. However, if the heating period starts a phase transition occurs that reduces the diffusion ability within the IL due to the formation of an amorphous phase and lowers therefore the current value compared to the one obtained during the cooling cycle. After reaching the highest temperature again the layer has returned its liquid state completely and the current values are again higher compared to the heating cycle. Examining the current values at the single temperatures more closely, it can be seen that the difference between cooling and heating increases up to a temperature of roughly 10°C (here, the current of the cooling cycles is higher by $\sim$ 14.5%), while afterwards the differences decreases again but are still observable. This suggests that at 10°C of the heating cycles the amorphous phase starts to dissolve again, but still influences the current measurements at 50°C.
Since a mixture of two ILs was used for this particular sensor and no DSC data are available, the exact thermal characteristics of the ILs are unknown. The freezing point of **IL1** is at -18°C, while **IL2** has a freezing point of -81°C, as mentioned before. The 4:1 ratio of **IL1** : **IL2** probably leads to a reduction of the freezing point of the mixture below -18°C, since a clear temperature dependence over the entire range can be observed. However, the found temperature characteristics of the mixture might suggest that the behavior of the layer is dominated by **IL1** which causes the supercooling effect, while the addition of **IL2** impedes the freezing of the layer.

If the cooling and heating cycles are plotted separately, the resolution improves enough to differentiate each single temperature. Additionally, the deviation of current at a single temperature over the seven heating and cooling cycles is rather small. This can be seen in figure 4.58 and 4.59.

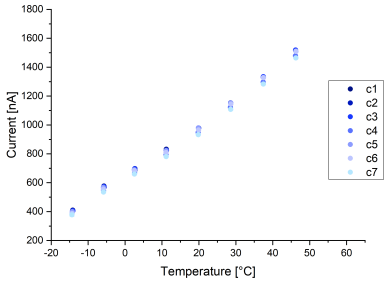

Figure 4.58. Chronoamperometric measurements ($N_{averg.} = 54 \pm 10$ measurements per temperature per cycle) from -14.2°C to 46.2°C showing only the results of the cooling cycles. The error bars lie within the marker size.

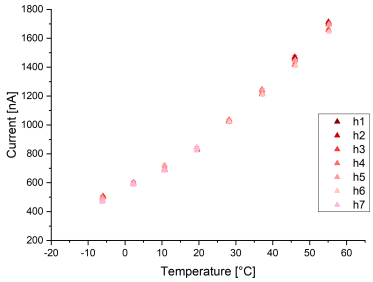

Figure 4.59. Chronoamperometric measurements ($N_{averg.} = 54 \pm 10$ measurements per temperature per cycle) from -5.9°C to 55.2°C showing only the results of the heating cycles. The error bars lie within the marker size.

Another feature that can be observed is the difference in linearity of the cooling and heating data. If the average current values are plotted against the temperature of either the cooling or the heating process (see figure 4.60 and 4.61), it can be seen that the cooling process shows a higher linearity, especially in the lower temperature regime. The r^2-value for the cooling cycle yields 0.9956 and for the heating cycle 0.9750, respectively . This is also consistent with the assumption of the supercooling phenomenon taking place.

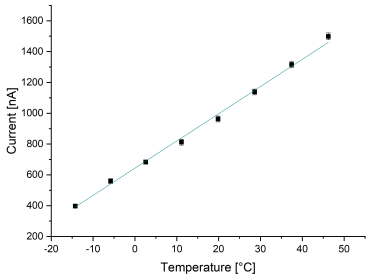

Figure 4.60. Average current data of the cooling cycle fitted with a linear equation and resulting in an r^2-value of 0.9956. The error bars lie within the marker size.

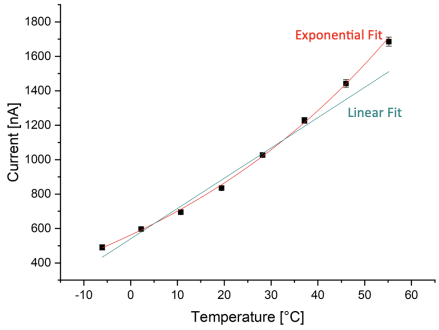

Figure 4.61. Average current data of the heating cycle fitted with a linear equation and an exponential equation, respectively. The linear fit results in an r^2-value of 0.9750, while the exponential fit yields $r^2 = 0.9981$. The error bars lie within the marker size.

Both fitting curves, however, have a similar slope of (17.7 ± 0.4) nA/°C and (17.6 ± 1.1) nA/°C for the cooling and heating cycles, respectively. In spite of that, the curve of the heating process indicates also that the relation between temperature and current might not be purely linear but rather having an exponential behavior. Therefore, the heating data was also fitted using an exponential expression, that results in $r^2 = 0.9981$. The exponential behavior will become more

obvious and clear in the next section (see 4.4.2) in which the three different layer compositions were tested at different pulse lengths using chronoamperometry.

4.4.1.2 Sensor Type 2: IL3

Since the resolution of a type 1 sensor is not high enough along the complete temperature regime a second IL-layer was investigated. Here, the pure 1-ethylimidazolium nitrate ([EIM][NO3], **IL3**) was used as redox molecule and transport medium simultaneously. However, this IL is not well known in literature, yet, which means that there are no information about its properties, e.g. melting point, viscosity, electrochemical window, available. As orientation for the electrochemical window the ionic liquid [EIM][NTF2] was used, since the cation is the same in both ILs and due to the negative applied potential the cation is of more interest. Thus, the cathodic limit is estimated to be around -0.8 V, which is considerably lower than the one for **IL1** (-2.5 V) and **IL2** (-2.4 V).
In a first experiment, the sensor was prepared as described previously (see section 3.4.2.2) using a cleanroom fabricated MEA and was measured using the custom-made measurement electronics in the same way as sensor type 1 ($N_{averg.} = 56 \pm 3$ measurements per temperature per cycle). Figure 4.62 shows the results and it can be seen that for higher temperatures (30°C to 60°C) the resolution improves quite strongly compared to sensor type 1, while below 20°C the current change is too small to be differentiated using a linear y-axis. Using a logarithmic scale on the y-axis, the change in current at the low temperatures is more clearly distinguishable (see figure 4.63). Additionally, the difference in current for the heating and cooling cycles can be observed for all temperatures between 0°C and 30°C, indicating the occurrence of supercooling effects. At temperatures below -10°C no change in current was measured anymore, which is why the data at -16°C was not considered at all and the lowest temperature used for analysis is -7°C.

The supercooling effect at 30°C is the most pronounced and the current of the cooling cycles is on average approx. 45% higher than the one of the heating cycles. Moreover, the variation of the single current values for the cooling cycles at this temperature is significant and yields an average $\pm$ 141 nA. This is due to a strong and continuous decrease of the current over time while the temperature is stable. Usually, the current at 30°C for a cooling cycle starts at $\sim$ 560 nA and ends at $\sim$ 200 nA, meaning at 30°C no stable current is achieved. On the contrary, the heating cycles show a stable behavior and yield at 30°C a standard deviation of 1.7 nA for each of the three heating cycles. Since the measurement time at each stable temperature at each cycle is the same, there has to be a "special" process taking place for the cooling cycles at 30°C that are not present for the heating cycles or at any other temperature. The observed behavior might be an indication of the freezing point of this IL, meaning at 30°C the IL starts to form a crystallized structure, which reduces the ability of the ions to diffuse towards the electrode. Since the formation of a solid structure does not take place from one second to another, the current decreases continuously over the time span at this temperature. The further reduction of temperature to 20°C in the next step supports the crystallization of the IL and the current decreases further, but is stable again for both cooling and heating cycles.

Considering only the temperature regime between 20°C and 60°C, the resolution of the temperatures are quite high. Figure 4.64 shows the averaged data points over all cycles (heating and cooling) as well as a linear and an exponential fit of the data. The previously described discrepancy at 30°C is represented by the quite large error bar for this data point. For all other temperatures the error bars lie within the marker size.
Both fits yield a r^2-value of 0.9978 and 0.9999 for the linear and exponential curve, respectively. However, the data point at 30°C deviate in both cases from the fit. According to the linear fit, the

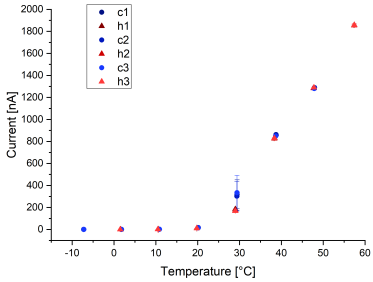

Figure 4.62. Results of the custom-made measurement electronic experiments using a sensor type 2 with [EIM][NO3] as redox molecule and transport medium simultaneously in a temperature range of -10°C to 60°C.

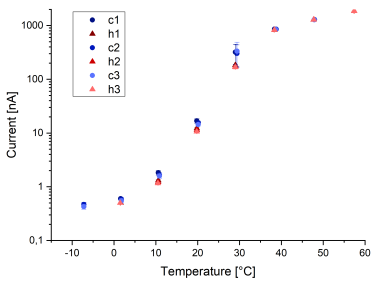

Figure 4.63. Logarithmic current scale of sensor type 2 to distinguish the change in current at temperatures below 20°C. Here, a supercooling effect for the low temperatures is observable.

slope at the high temperatures results in (48.9 ± 1.1) nA/°C and is almost three times higher than for sensor type 1. According to the presented results, this sensor type configuration is probably more feasible to be utilized at a higher temperature regime, starting above 30°C and covering temperatures well above 60°C (was not investigated in this work). Since the chosen temperature regime of this work was set to be -20°C to 60°C, a third senor type was fabricated.

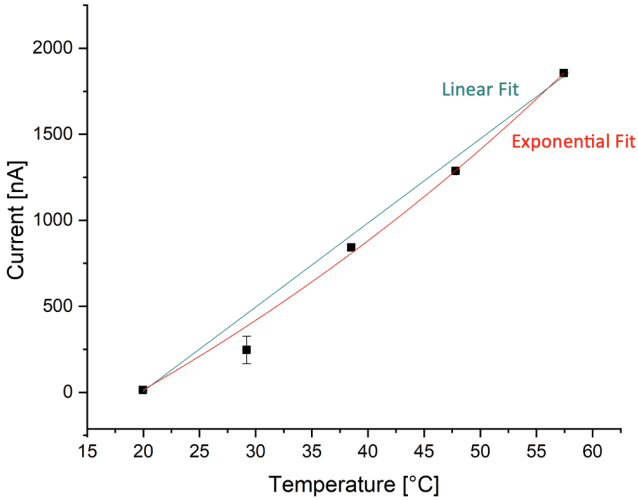

Figure 4.64. Linear and exponential fit of the averaged data (heating and cooling) in the temperature range of 20°C to 60°C.The slope of the linear fit yields (48.9 ± 1.1) nA/°C and is almost three times higher than the resolution of sensor type 1. The r^2-values result in 0.9978 and 0.9999, respectively, for the linear and exponential curves. The difference for cooling and heating at 30°C is represented by the error bar. For all other temperatures, the error bar lies within the marker size.

4.4.1.3 Sensor Type 3: IL3 + IL2

As indicated by the results of sensor type 2 the freezing point of **IL3** might lie around 30°C which is too high for the chosen temperature range. Therefore, a mixture of **IL3** und **IL2** (sensor type 3), in a ratio of 3 : 1 wt%, was investigated next, with the assumption that adding **IL2** will lower the freezing point onto a feasible level. As before, a first sensor was measured using the custom-made measurement electronics with the same settings as for the type 1 and 2 sensors. Figure 4.65 shows the respective results ($N_{averg.} = 58 \pm 5$ measurements per temperature per cycle).

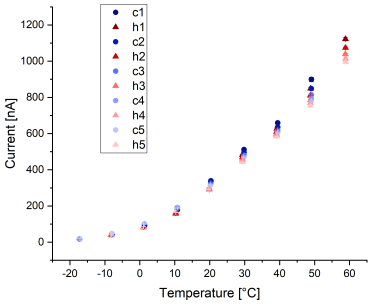

Figure 4.65. Results of custom-made measurement electronic experiments using a sensor type 3 consisting of a 3 : 1 wt% ratio of **IL3** and **IL2** in a temperature range of -20°C to 60°C ($N_{averg.} = 58 \pm 5$ measurements per temperature per cycle).

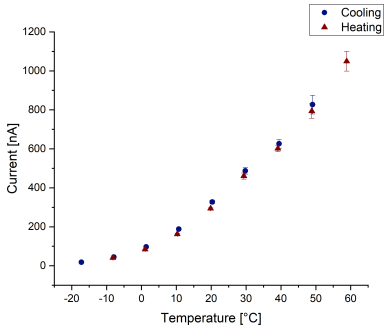

Figure 4.66. Average current data for all heating and cooling cycles. The error bars represent the deviation at the respective temperature for heating and cooling (if the error bar is not visible, it lies within the marker size).

Comparing these results with the ones of the sensor type 2 (see figure 4.62) it is obvious that the freezing point of **IL3** is lowered considerably to achieve distinguishable current values at the lower temperature regime. At -20°C the current of sensor type 3 is in average 18.5 nA, while for sensor type 2 the current reached its minimum at -7°C with 0.45 nA. At the same time, the absolute current values at 60°C are smaller by almost 40 % and reach at maximum 1049 nA, compared to 1856 nA at 60°C for sensor type 2 and 1686 nA for sensor type 1. Moreover, between 10°C and 50°C the effect of supercooling can also be recognized for sensor type 3, although not as strong as for sensor type 1 (see figure 4.57, which additionally used a different electrode geometry), but more significantly than for sensor type 2, which only showed a difference in heating and cooling for the values between 10°C and 30°C (visible for the logarithmic y-scale). Furthermore, the sensor shows a high enough resolution to distinguish each temperature over the entire chosen regime, which is an improvement compared to sensor types 1 and 2. While for sensor type 1 this differentiation was not possible due to the supercooling effect for the temperature regime of -10°C to 20°C, sensor type 3 shows a strong enough increase for each temperature step that the resolution is given over the entire temperature regime.
However, sensor type 3 shows another effect that was not as prominent for the other two sensor types, namely a significant decrease of current at the same temperature. This is visualized in figure 4.66 by the error bars at the temperature regime between 30°C and 60°C. For the temperature regime of 20°C to 50°C for the cooling cycles, as well as 30°C to 60°C for the heating cycles, a continuous decrease of current with increasing cycle number can be observed. Contrary to that, at the lower temperatures the opposite behavior is found, here the current increases with increasing cycle number, although it is not strictly continuous. The effect at the higher temperatures

might be explained with electrode fouling, at which the electrode surface is passivated due to the formation of a fouling agent. This fouling agent, probably a byproduct of the redox processes taking place at the electrode surface, reduces the electrode area at which further redox reactions can take place and therefore the current decreases. At lower temperatures another effect, e.g. the diffusion of the redox species towards the electrode, dominates the current behavior and therefore electrode fouling is not observable.
In contrast to sensor type 1, the temperature behavior for cooling and heating can be in both cases best described exponentially (not displayed). If only the temperature regime between 20°C and 60°C is considered, the data show a good linearity with r^2-values of 0.9951 and 0.9918 for cooling and heating, respectively (see figures 4.67 and 4.68). In the linear regime the sensitivity of sensor type 3 is comparable to sensor type 1 and lies with (16.3 ± 0.7) nA and (17.1 ± 0.8) nA slightly lower. However, the cooling cycles of sensor type 1 show a higher linearity over the entire temperature range, probably due to the presence of methylene blue as redox species. Following that, the sensitivity is not completely comparable between the two sensor types.
Comparing sensor type 2 and 3 shows that adding **IL2** in sensor type 3 influences the sensitivity as well as the behavior over the considered temperature range drastically. Although the amount of **IL2** is minor compared to **IL3**, the effect is considerable. On the one hand, the sensitivity of sensor type 3 is only 33% of that of sensor type 2 and on the other hand the sensitive temperature range is at least 10°C higher and reaches -20°C.

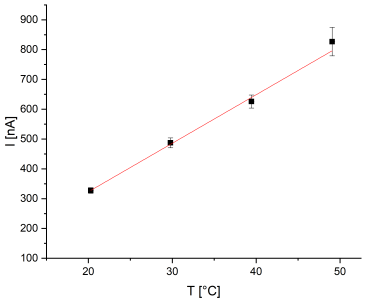

Figure 4.67. Linear fit of the average current data of the cooling cycles for the temperature regime between 20°C and 50°C (r^2: 0.9951).

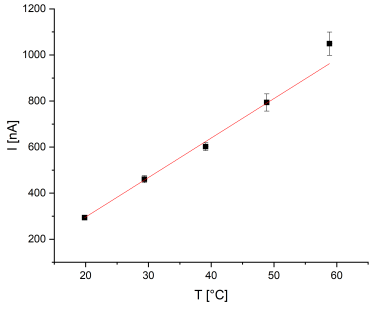

Figure 4.68. Linear fit of the average current data of the heating cycles for the temperature regime between 20°C and 60°C (r^2: 0.9918).

Table 4.7 gives an overview of the most important characteristics of the three sensor types described previously.

Table 4.7. Overview of the important characteristics of the three sensor types.

	I_{max} (nA)	I_{min} (nA)	Sensitivity + (nA/°C)		Supercooling (°C)
	Heating	Cooling *	Heating	Cooling	
Sensor Type 1	1686	397	17.6	17.7	-10 - 50
Sensor Type 2	1856	0.45	48.9		0 - 30
Sensor Type 3	1049	18.5	16.3	17.1	0 - 50

* For sensor type 2 the lowest temperature was -7°C, for sensor types 1 and 3 -20° C
+ For sensor types 2 and 3 only the temperature regime between 20°C and 60°C was used, for sensor type 1 the entire regime

4.4.2 Chronoamperometric Measurements Using Four Different Pulse Lengths

For a more detailed investigation the three different layer compositions were tested using four pulse lengths: 0.1 s, 0.5 s, 1.0 s and 10.0 s. The different pulse lengths, inter alia, were used to determine the highest resolution between the minimum and maximum temperature (around -20°C to 60°C). Applying the potential step for different time lengths, the thickness of the corresponding diffusion layer varies accordingly and thus, the resulting current. The chosen potential of - 1.0 V resulted in a mass-transfer-limited case, in which the redox species was reduced as soon as it arrived at the electrode and the current depended only on the diffusion velocity of this species. For longer pulse lengths, more redox molecules need to be transported towards the electrode, which becomes more difficult since the depletion zone increases close to the electrode surface. As a result, the current decreases for longer pulse lengths. The measurements were conducted using a potentiostat. Here, a potential of -1.0 V was applied for the different pulse lengths and the resulting current was recorded. Between two adjacent measurements a pause of 30 s was executed to avoid any charging of the electrodes or sensitive layer.
The respective sensor was fixed onto the automated temperature setup and connected to the potentiostat as described in section 3.5.2. For each sensor at each pulse length several hundreds (minimum 400) to a few thousand measurements (max. 3700) were recorded and analyzed. The analysis was done by self-developed python scripts that did several things:

- Filtering the 50 Hz noise out of the raw data using a 50 Hz notch filter
- Matching the filtered data of the chronoamperometric measurements to the temperature measurement of the reference thermometer
- Discarding the chronoamperometric measurements that were recorded at non stable temperatures, meaning between the increase or decrease of the temperature. This was done using a python script that compared each temperature with the temperature value of the last index. If the difference between the two temperatures was larger than 0.5°C the data point was discarded. Moreover, if the difference between two consecutive data points fulfilled this first requirement, it was in a second step checked if at least ten temperatures in a row satisfy this criteria. If this was not the case, these data points were also discarded.
- Averaging the data recorded at one stable temperature over several milliseconds, depending on the pulse length:
  - 0.1 s: average over 20 ms
  - 0.5 s: average over 20 ms
  - 1.0 s: average over 200 ms
  - 10.0 s: average over 2 s
- Differentiating between data recorded at a heating or a cooling cycle, respectively
- Plotting the respective data (current) against the temperature

4.4.2.1 Sensor Type 1: IL1 + IL2 + MB

The sensitive layer of the first sensor type comprised a mixture of **IL1** and **IL2** and methylene blue as redox molecule according to section 3.4.2.2. This solution was applied on top of a cleanroom fabricated MEA described in section 3.3.2.

The data for this sensor at a pulse length of 0.1 s is shown in figure 4.69. Similar to the previous section, data that belonged to the cooling cycles were colored in blue while the data points belonging to the heating cycles were colored in red. Figure 4.70 displays the average data point at each temperature for the heating and cooling cycles as well as the mean of that. As can be seen, the current increases in the negative for higher temperatures due to the negative applied potential and also shows a much higher variation there. The increase itself is of course mainly due to the change in viscosity with temperature. However, it is also displayed that with an increasing cycle number the overall current decreases. This behavior was not found for this sensor type using the custom-made measurement electronics (see chapter 4.4.1.1), however, two different sensor geometries were used, which makes a direct comparison difficult.
The shown data comprises 1069 measurements of which 826 were used for analysis. The rest was discarded due to the aforementioned reason, i.e. recorded at nonstable temperatures.

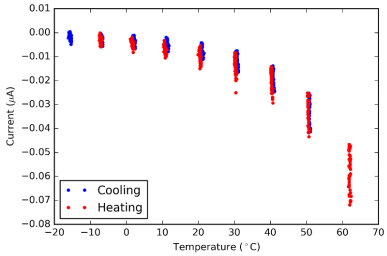

Figure 4.69. Sensor type 1 at a pulse length of 0.1 s for all cycles (826 data points). Each valid data point is shown. With increasing cycle number the current decreases.

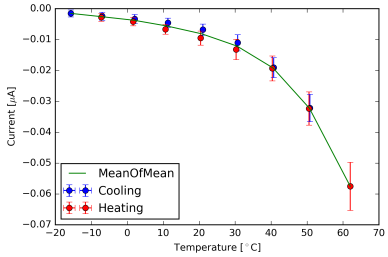

Figure 4.70. Sensor type 1 at a pulse length of 0.1 s displaying the average and standard deviation for the heating and cooling cycles, respectively, as well as the mean of those cycles.

The reason for the decrease in current over time (increasing cycle number) is not completely clear at that point. However, there are some considerations done to explain this finding or exclude some effects. Since the measurements were also conducted at temperatures below room temperature the humidity of the air could have condensed and be absorbed by the layer, although the measurement "chamber" was flushed with nitrogen all the time to prevent this. However, according to Seddon et al. [82] the absorption of water decreases the viscosity of ILs due to the formation of H-bonds with the anions and cations, leading to a reduction of the electrostatic attractions between the ions. A reduced viscosity would allow higher diffusion rates which would increase the current, which is not the case here. Furthermore, Anouti et al. [187] also states that a higher water content would lead to an increased conductivity, which also would result in higher currents not lower ones. Since the opposite is observed here, the water content can be assumed to not influence the performance significantly.
Due to the measurement itself, meaning, applying a potential repeatedly, an additional heating could occur. This could be estimated to: $1\ \mathrm{V} \cdot 0.07\ \mu\mathrm{A} = 0.07\ \mu\mathrm{W}$ for this sensor. Since one can say that 1 W heats up 1 g water 14 K per minute, the additional heating due the applied power in this case should be negligible. However, even if it would not be negligible, the effect should be the same over all cycles and therefore cannot explain the found behavior.
Another effect that could influence the current measurements is the occurrence of a temperature gradient along the z-axes of the sensor. Since the sensor is only heated from the bottom side the IL layer on the surface could experience a slightly different temperature than the IL layer close the electrodes. Due to the quite thin layer the gradient could become large for very high or low temperatures. Unfortunately, this cannot be ruled out with the data recorded here, but since the

setup was not changed during the measurements a potential temperature gradient should have the same influence over all cycles and not causing a constant decrease over time.

Besides the change in viscosity, that causes the change in current mainly, also the electrochemical double layer at the electrode-IL-interface is influenced by temperature. As discussed previously, the temperature dependence of the EDL is not fully understood, yet. However, literature presents elaborated insights that can be used to discuss the presented findings of this work. Here, the focus lies on the processes at the working electrode, since it limits the actions due to the fact that it is much smaller than the counter electrode.
According to Federov et al. [188] the ions of ILs form layers close to the electrode surface depending on its charging. In the presented experiments always a potential of -1 V was applied onto the electrode, meaning an excess of negatively charged electrons were located at the surface. This would lead to the formation of a cation-layer next to the electrode, probably oriented with their neutral alkyl chains away from the surface and with the charged ring towards the surface. Followed by a layer consisting of anions, then again cations and so on (multilayer; see figure 4.71 C) until in the bulk there are no excess charges left and the ions position themselves randomly. Further, it is possible that the charges provided by the electrode surface are not neutralized by only one layer of cations, so that a second layer of cations is build up to form a so called crowded structure (see, figure 4.71 A). The opposite arrangement could occur if a positive potential were applied onto the electrode. Figure 4.71 illustrates the packing and orientation of cations and anions close to the electrode surface.

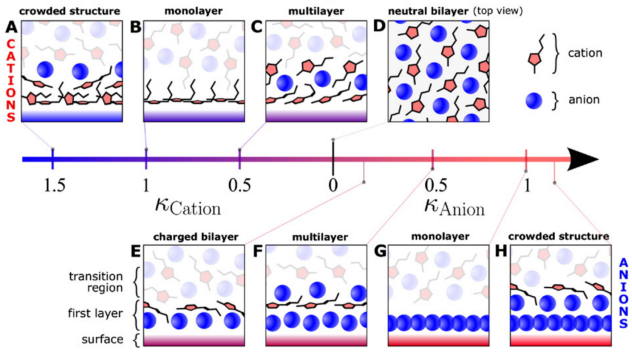

Figure 4.71. Schematics of the EDL structure in case of cathodic or anodic polarization of the electrode. The cations are represented as red pentagons with black tails and the anions are sketched as blue balls. The electrode surface is represented as colored rectangle depending on the charge. The formed structures are classified due to the packing of the ions as ionic bilayer (D, E), multilayer (C, F), monolayer (B, G) and crowded poly(a)morphic structures (A, H). The κ scale was defined as the normalized surface charge density by the maximum charge density that can be stored in a densely packed counter-ion monolayer. Here κ_{Cation} corresponds to negative surface charge densities and κ_{Anion} corresponds to positive surface charge densities. Image from [188].

In a freshly prepared or long rested sensor the ions of the IL are equally distributed throughout the layer (compare figure 4.71 D). By conducting the measurements and applying a potential several hundred times it can be assumed that either a multilayer or crowded structure forms over

time to compensate the excess charge onto the electrode surface. In between two measurements, where the potential is turned off again, the structure starts to "dissolve" just to be formed during the next measurement again. As described above, the pause between adjacent measurements was set to 30 s, which should not be enough time for the cations to diffuse far away from the electrode. Due to the numerous measurements conducted it is probable that the multilayer or crowded structure stays more or less intact causing the current to decrease over time. Additionally, the reduction of the methylene blue molecules take place due to the applied potential. For that to happen, the methylene blue molecules need to get close to the electrode as well which will become harder if a multilayer/crowded structure is formed already. Moreover, adding methylene blue into the IL mixture might cause a change of the physicochemical properties (e.g. viscosity behavior) of the ILs because the methylene blue needs to be considered as a kind of "impurity". Beyond that, two well-known effects that often lead to the degradation of sensors, i. a. electrode fouling and electrolyte poisoning, probably occurred during the measurements. Thereby, the surface of the electrode is reduced due to the formation of an fouling agent that passivates the electrode area and changes the composition of the electrolyte. In turn, the current decreases over time.
The above described effects are assumed to be responsible for the unstable behavior of the sensor found in the performed measurements. Although this needs a more detailed investigation, both experimentally and computationally, to really understand the events taking place during repeated chronoamperometric experiments. In case of the electrode fouling and electrolyte poisoning, especially the redox behavior of the chosen ILs need to be examined in greater detail. Furthermore, the sensitive layer was not protected by an additional passivation, which would be useful to reduce the influence of environmental conditions.

Considering only one or two cycles and computing the average current value for the heating and cooling cycles ($N_{averg.}$ = 4-5), respectively, an acceptable resolution between the temperatures can be found. Additionally, the standard deviation is much smaller and the errorbars lie mostly within the marker size as can be seen in figure 4.72. The green line represents the mean values of the averaged heating and cooling points at the respective temperature. However, at the low temperatures the resolution is not high enough to clearly distinguish between -15°C, -7°C and 2°C.

As can be seen from figure 4.72, the heating and cooling data differs slightly, similar as shown for the results in the previous section. A closer look at the actual data shows that although the temperature for the cooling cycles is always higher than the temperature for the heating cycle (except at -7°C), the current values of the cooling cycle are lower compared to the ones for the heating cycle at any temperature, except for -7°C. As mentioned above, the data at -15°C always counts for the cooling cycle, while the data at 62°C always counts for the heating cycle. Since each data point consists of four to five single measurements, table 4.8 shows only the average data of temperature and current for both, the heating and cooling cycles, as well as the standard deviation of the current values at each temperature.

In the previous section (4.4.1) the difference between the heating and cooling data was explained due to supercooling effects taking place, meaning that the freezing and melting point are not the same (although, thermodynamically this would be expected). Thereby, the melting point was assumed to be higher than the freezing point. Although, the sensitive layer is the same in both cases, the data does not show the same supercooling effects here, since the heating cycles always results in higher currents. In order to check if this is just the case for the two chosen cycles, the last two cycles of all the measurements were analyzed in the same way and plotted. As can be seen in figure 4.73 the general behavior is found to be the same as for the first two cycles. However, it can clearly be observed that the absolute current values reduced significantly

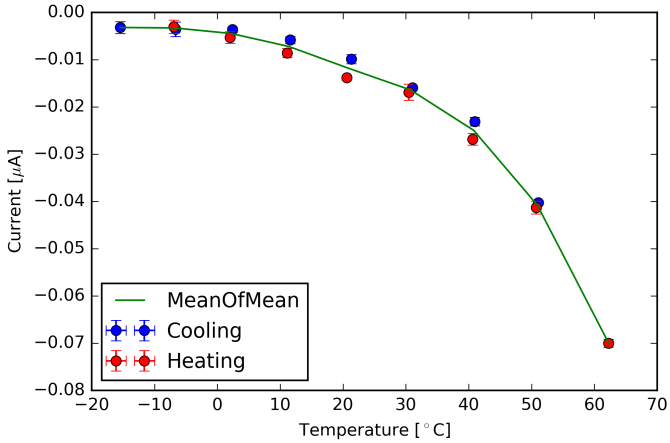

Figure 4.72. Data points of two complete cycles (-15°C – 60°C - -6°C) for a sensor type 1 at a pulse length of 0.1 s. Each temperature for heating and cooling contains 4-5 data points which were averaged. The error bars lie mostly within the marker size and represent the standard deviation of the data points. The green line displays the trend of the temperature dependence and is calculated as the mean of the cooling and heating points at each temperature.

Table 4.8. Averaged data ($N_{averg.} = 4$-5) of sensor type 1 at a pulse length of 0.1 s for the two heating and cooling cycles, respectively, shown in figure 4.72.

$T_{heat,ave.}$ (°C)	$I_{heat,ave.}$ (μA)	$I_{heat,std.}$ (μA)	$T_{cool,ave.}$(°C)	$I_{cool,ave.}$ (μA)	$I_{cool,std.}$ (μA)
			-15.4	$-3.19 \cdot 10^{-3}$	$1.27 \cdot 10^{-3}$
-6.9	$-3.01 \cdot 10^{-3}$	$1.41 \cdot 10^{-3}$	-6.7	$-3.56 \cdot 10^{-3}$	$1.55 \cdot 10^{-3}$
2.0	$-5.29 \cdot 10^{-3}$	$1.25 \cdot 10^{-3}$	2.4	$-3.63 \cdot 10^{-3}$	$5.33 \cdot 10^{-4}$
11.1	$-8.57 \cdot 10^{-3}$	$9.86 \cdot 10^{-4}$	11.6	$-5.84 \cdot 10^{-3}$	$7.71 \cdot 10^{-4}$
20.6	$-1.38 \cdot 10^{-2}$	$4.19 \cdot 10^{-4}$	21.3	$-9.87 \cdot 10^{-3}$	$9.65 \cdot 10^{-4}$
30.5	$-1.69 \cdot 10^{-2}$	$1.73 \cdot 10^{-3}$	31.1	$-1.60 \cdot 10^{-2}$	$4.41 \cdot 10^{-4}$
40.6	$-2.68 \cdot 10^{-2}$	$1.22 \cdot 10^{-3}$	41.0	$-2.31 \cdot 10^{-2}$	$9.06 \cdot 10^{-4}$
50.8	$-4.13 \cdot 10^{-2}$	$1.38 \cdot 10^{-3}$	51.1	$-4.03 \cdot 10^{-2}$	$2.99 \cdot 10^{-4}$
62.3	$-7.00 \cdot 10^{-2}$	$8.42 \cdot 10^{-4}$			

and reached only 50 nA at the highest temperature of 62°C, which, however, was also expected analyzing figure 4.69. Again, the error bars, representing the standard deviation of the single data points, lie within the marker size and seem to be smaller than for the first two cycles.
Since the sensor shows the same results at the beginning and the end of the measurements, the different behavior in the temperature regime of 2°C to 40°C compared to the sensor shown in the previous section needs another explanation. However, it is to be noted that the supercooling effects also take place at this sensor but they seem to be overruled by another effect that conceals the supercooling.

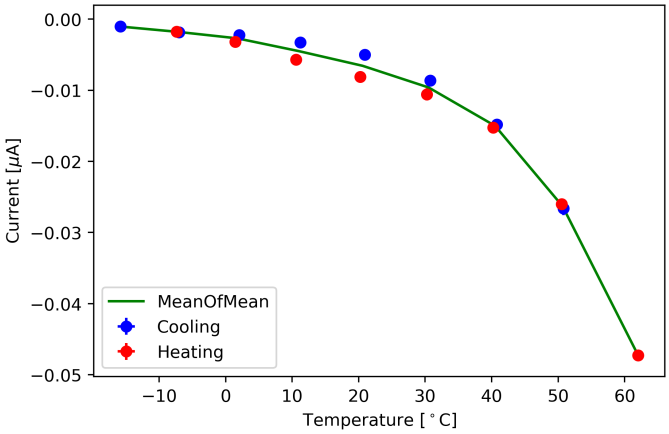

Figure 4.73. Data points of the last two complete cycles (-15°C – 60°C - -6°C) for a sensor type 1 at a pulse length of 0.1 s. Each temperature for heating and cooling contains 4-5 data points which were averaged. The error bars lie within the marker size and represent the standard deviation of the data points. The green line displays the trend of the temperature dependence and is calculated as the mean of the cooling and heating points at each temperature.

The main difference about the two used sensors (in this section and in the previous one) is the electrode size. The working electrode of the sensor presented in section 4.4.1 was defined by passivating a large area of the gold surface, so that only three small rectangles with a size of 50 μm x 500 μm ($A_{electrode}$ = 75,000 μm^2) were exposed to the sensitive layer, while the sensor used for the investigation of different pulse lengths, in this section, consisted of three circular microelectrodes with an opening of 80 μm in diameter ($A_{electrode}$ = 15,000 μm^2). The distance of the working electrodes to the counter electrode was approx. 200 μm for both sensor configurations.
The influence of the different electrode areas can be seen at once, if the absolute current values are compared. For the circular microelectrodes the current decreases drastically and only reaches values of 3 to 70 nA, while the other sensor showed values of 400 to 1700 nA. Furthermore, the arrangement of the three microelectrodes relative to each other differs for the two sensor layouts which results also in different sizes of the diffusion layer. It is assumed that for the laser ablated sensor, used in the experiments described in section 4.4.1, the three microelectrodes are separated widely enough so that their diffusion zones are not interacting with each other. This assumptions is based on the configuration of the sensor. The electrode openings have an area of (50 μm · 500 μm) · 3 = 75,000 μm^2, on which 2 μl of IL (+ UV matrix) mixture was applied.

Assuming further that the IL mixture was spread homogeneously over the electrode area, the thickness of the applied IL layer would be at maximum 26,7 nm. However, in this consideration the distance between the three electrodes is neglected, which means that the actual layer thickness is even less than 26,7 nm. Even if the IL layer would not be homogeneous due to H-bonds or other interionic forces, and therefore, the maximum height of the IL layer would be larger, the diffusion zones could not be large enough to influence each other.
The microelectrodes of the cleanroom fabricated MEAs are distant much less from each other and the area of the electrodes is smaller by a factor five [$(40^2 \cdot \pi)\ \mu m^2 \cdot 3 = 15{,}000\ \mu m^2$]. Considering the distance between the three electrode openings as well as the electrode area itself, an overall area of at least 28,300 μm^2 needs to be covered by 2 μl of the IL-UV matrix mixture, which results in a layer thickness of approx. 70 nm. However, the actual covered area was slightly larger and therefore, the thickness had to be less than 70 nm. Conclusively, the diffusion zones of this sensor are also too small to overlap. Additionally, it is also neglected that the cured UV matrix in both sensor configurations would probably inhibit the formation of a regular diffusion zone.
The significant decrease in current for the two sensor configurations is probably mainly due to the different electrode sizes. Furthermore, two different measurement devices (custom-made electronics vs. potentiostat) were used, which can cause generally differences in recordings. For a more detailed explanation of the findings and for example how the methylene blue contributes to all this or why the supercooling effect is reversed, more experimental and computational work needs to be done to achieve a clear insight on the molecular basis as well as on the EDL.

The same sensor was also measured at three more pulse lengths, i.e. 0.5 s, 1.0 s and 10.0 s. For the measurements at 0.5 s in total 3,716 measurements were conducted, of which 2,905 were recorded at stable temperatures. One cycle comprised approx. 38 data points, resulting in two to three measurements per temperature and cycle. While the absolute number of measured data points differs for 1.0 s (total: 1,197 measurements; at stable temperature: 869 measurements) and 10.s (total: 877 measurements; at stable temperatures: 625 measurements), the measurements per temperature and cycles stays constant.
The results are similar to the ones presented for the pulse length of 0.1 s. However, with increasing pulse length the absolute current value as well as the resolution between the single temperatures decreases significantly. This can be seen in figures 4.74 to 4.76, which also show that the differences in heating and cooling at a single temperature reduces and are hardly distinguishable any more at a pulse length of 10.0 s. Interestingly, the difference between heating and cooling shifts towards higher temperatures for longer pulse lengths, so that for the pulse length of 1.0 s only at 40°C and 50°C and for the pulse length of 10.0 s only at 50°C the difference is still observable. Furthermore, for the pulse lengths of 1.0 s and 10.0 s (see figures 4.75 and 4.76) the current values of the heating cycles are again higher than the ones for the cooling cycles, showing the supercooling effect.
Since the depletion zone close to the electrode surface increases with increasing pulse lengths, the resulting current and the resolution decreases and the single temperatures are not distinguishable anymore. While for a pulse length of 0.1 s the temperatures between -15°C and 2°C are not clearly differentiable, this temperature range increases with increasing pulse lengths. For 0.5 s, 1.0 s and 10.0 s only the temperature regime between 30°C and 60°C is dissolvable. This shows the temperature dependence of the viscosity clearly, because the higher thermal energy at elevated temperatures is needed to transport new redox molecules through the diffusion zone towards the electrode. Contrary to the measurements in the previous section, the sensitivity cannot be determined easily, since the dependency of current from temperature does not show a linear relation.

Additionally, the current for all three pulse lengths (0.5 s, 1.0 s, 10.0 s) decreases with increasing cycle number, similar to the trend displayed in figure 4.69 for a pulse length of 0.1 s. Figure 4.77 shows the averaged results of 2 cycles for all four pulse lengths in one graphic for direct comparison.

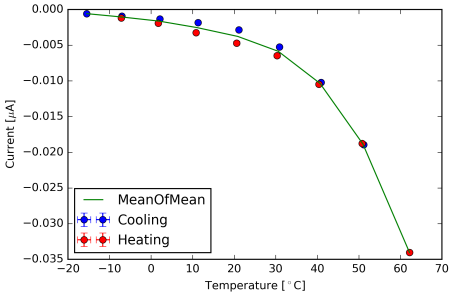

Figure 4.74. Data points of one complete cycle (-15°C – 60°C - -6°C) for a sensor type 1 at a pulse length of 0.5 s. Each temperature for heating and cooling contains 4-5 data points which were averaged. The error bars lie mostly within the marker size and represent the standard deviation of the data points. The green line displays the trend of the temperature dependence and is calculated as the mean of the cooling and heating points at each temperature.

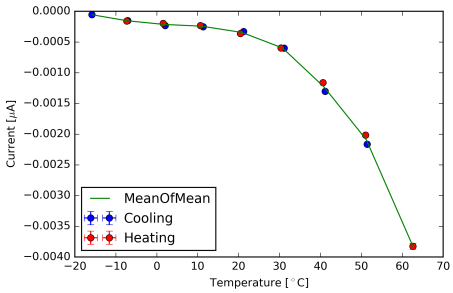

Figure 4.75. Data points of two complete cycles (-15°C – 60°C - -6°C) for a sensor type 1 at a pulse length of 1.0 s. Each temperature for heating and cooling contains 4-5 data points which were averaged. The error bars lie mostly within the marker size and represent the standard deviation of the data points. The green line displays the trend of the temperature dependence and is calculated as the mean of the cooling and heating points at each temperature.

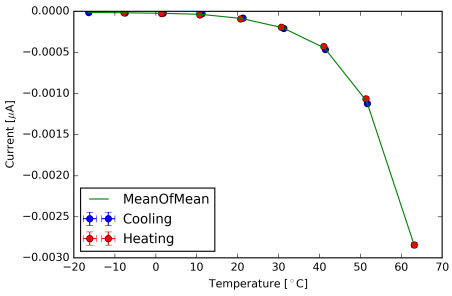

Figure 4.76. Data points of two complete cycles (-15°C – 60°C - -6°C) for a sensor type 1 at a pulse length of 10.0 s. Each temperature for heating and cooling contains 4-5 data points which were averaged. The error bars lie mostly within the marker size and represent the standard deviation of the data points. The green line displays the trend of the temperature dependence and is calculated as the mean of the cooling and heating points at each temperature.

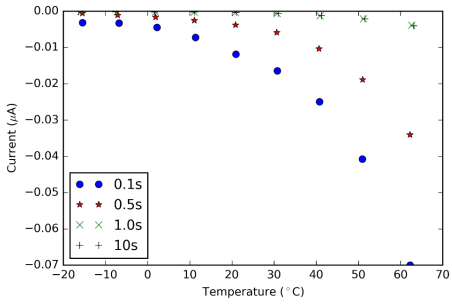

Figure 4.77. Results of the four different pulse lengths - 0.1 s, 0.5 s, 1.0 s and 10.0 s - over the complete temperature range plotted in one diagram for better comparison. It can be seen that the resolution decreases with increasing pulse length.

4.4.2.2 Sensor Type 2: IL3

In a next step, a second type 2 sensor was prepared and investigated using the chronoamperometric technique at four different pulse lengths. The analysis of the recorded data was done in the same way as described for sensor type 1. Here, 568 measurements were conducted in total at a pulse length of 0.1 s, of which 377 were recorded at stable temperatures. In the following the results of the measurements at 0.1 s are presented in detail.
In figure 4.78 the sensor behavior over all measurements is displayed. As can be seen the current decreases with increasing cycle number, similar as for the type 1 sensor. However, with **IL3** as redox species and solvent the absolute current values are much higher (by approx. 4 times) as for the previous sensor. Again, the current decreases with increasing cycle number due to the same effects that were described before, resulting in a too low resolution for the temperatures between -20°C and 30°C (see figure 4.79). Contrary to sensor type 1, the difference between the heating and cooling cycles represents the expected supercooling effect between 0°C and 30°C. This can be seen in figure 4.79, where the current values of the heating cycles are lower than the ones for the cooling cycles, which is the same behavior that was found when using the custom-made measurement electronics.

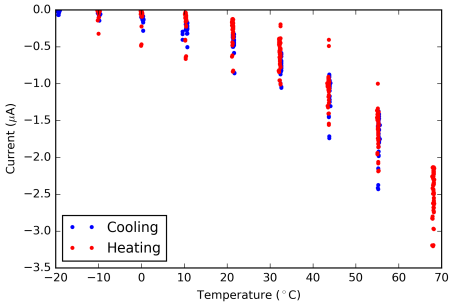

Figure 4.78. Sensor type 2 at a pulse length of 0.1 s for all cycles (377 data points). Each valid data point is shown. With increasing cycle number the current decreases.

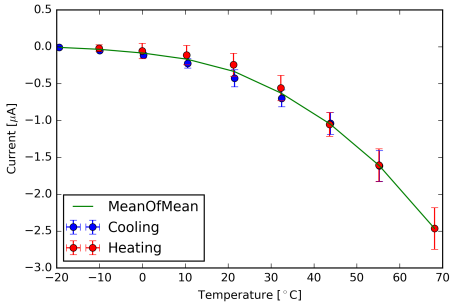

Figure 4.79. Sensor type 2 at a pulse length of 0.1 s displaying the average and standard deviation for the heating and cooling cycles, respectively, as well as the mean of those cycles for the entire data set.

However, considering only the data of the first two cycles the same behavior as for sensor type 1 is found, meaning the current values obtained during a heating cycle are higher as for the cooling cycle. Figure 4.80 represents this data. Furthermore, using only this data the resolution improves, but simultaneously, the difference between heating and cooling gets more pronounced for temperatures between -10°C and 20°C. As indicated by the data over all measurements, at some point the behavior of the sensitive layer changed and the heating values lie above the cooling ones. The analysis of the last two recorded cycles confirm this as can be seen in figure 4.81.

The change in behavior over all heating and cooling cycles suggests that the sensitive layer experiences a kind of transformation while the measurements are conducted. This transformation probably includes the alignment of the ions within the layer according to the applied potential. Since the cation (1-ethylimidazolium) has a quite short alkyl chain attached on one of the N-atoms of the imidazolium ring and a hydrogen atom on the second one the van der Waals forces can be assumed to be much lower than for the layer comprising **IL1** and **IL2**, while the ability to form H-bonds is increased simultaneously. Furthermore, the NO_3^- anion is quite small com-

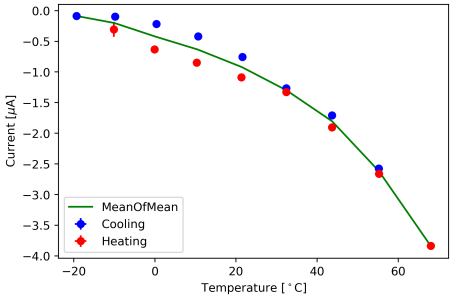

Figure 4.80. Sensor type 2 at a pulse length of 0.1 s displaying the average and standard deviation for the heating and cooling cycles, respectively, for two cycles at the beginning of the measurements in the temperature range of -20°C and 70°C. Each temperature comprises 4 - 5 data points for heating and cooling, respectively. The green solid line represents the mean of mean data of the heating and cooling cycles. The error bars lie within the marker size, except for the heating value at -10 °C. The behavior of the heating and cooling cycle is opposite to what can be found for the trend over all data (compare figure 4.81).

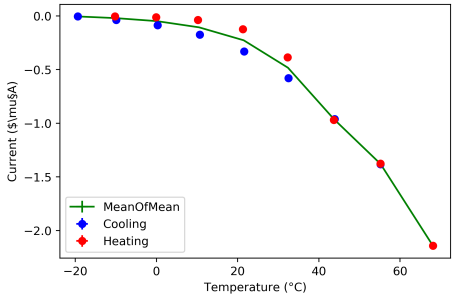

Figure 4.81. Sensor type 2 at a pulse length of 0.1 s displaying the average and standard deviation for the heating and cooling cycles, respectively, for the last two cycles in the temperature range of -20°C and 70°C. Each temperature comprises 4 - 5 data points for heating and cooling, respectively. The green solid line represents the mean of mean data of the heating and cooling cycles. The error bars lie within the marker size. Contrary to the beginning, here the supercooling effect can be observed.

pared to the NTf_2 anion, which might result in a denser packed layer. This is probably supported due to its ability to form stronger H-bonds than the NTf_2 anion. Additionally, the methylene blue in sensor type 1 can be seen as a kind of "impurity" for the ILs which also causes changes in their properties (e.g. viscosity behavior with changing temperature), which is not present in the sensitive layer of sensor type 2. Considering these differences in the layer composition and adding the effects taking place close to the electrode surface due to the applied potential (see schematics of the EDL structure, figure 4.71), the observed behavior might be explained.
Summarizing, the use of the pure **IL3**, which contains much smaller cations and anions and therefore experiences different van der Waals interactions as well as stronger H-bonds, the supercooling effect cannot be observed for the first cycles. With increasing cycle number the structure of the layer starts to transform which leads to a change in current behavior. This means in the beginning of the measurements the IL was not able to form an amorphous glassy structure due to the cold crystallization process that takes place during the heating cycle if supercooling effects occur. Over time the ions start to rearrange due to the applied potential and the ability to form a crystal structure is enhanced.

In contrast to the measurements shown in the previous section, using the custom-made electronics, the resolution of the measurements using the potentiostat at the low temperatures is high enough to differentiate between -20°C and -7°C. The absolute current values at 70°C are also significantly higher using the potentiostat and reached 2.46 μA (compared to 1.86 μA at 60°C, see table 4.7). At -20°C the current yield 8 nA and at -10°C 34 nA, while the measurements using the custom-made electronics resulted in 0.45 nA at -7°C. This comparison is based on the data of 0.1 s pulse length. Since for both measurements the same sensor geometry was used, i.e. the cleanroom fabricated MEA, this difference is attributed to the different measurement devices used to record the current data. Based on the analysis of the recorded data in the previous section, the freezing point of **IL3** was estimated to lie around 30°. This assumption is not strengthened by the data of this section, but it is also not falsified.

For the longer pulse lengths of 0.5 s (total number of measurements conducted: 411; at stable temperature: 294), 1.0 s (total number of measurements conducted: 647; at stable temperature: 474) and 10.0 s (total number of measurements conducted: 1,536; at stable temperature: 1,119) the supercooling effect can be observed from the beginning. Except for the temperatures around 40°C and 50°C at the pulse length of 10.0 s the heating and cooling values do not show such a significant difference compared to the results in figure 4.80 for the pulse length of 0.1 s. The relative large error bars at 40°C and 50°C at 10.0 s indicate that the measurements experienced some fluctuations during the recording. All results, for the other pulse length as well as a comparison between the recorded data for all pulse lengths, can be seen in figure 4.82 to 4.85.
The comparison of the four pulse length shows that the sensitivity of the sensor decreases with increasing pulse length, similar to the sensor type 1. However, at the temperatures of 30°C to 70°C the data of the pulse length at 0.5 s displays a steeper increase in current than the pulse length at 0.1 s and therefore also a higher resolution. With the available data it is not possible to drew any concrete conclusion which could explain this finding. Furthermore, the pulse lengths of 1.0 s and 10.0 s show a higher resolution for sensor type 2 than for type 1.

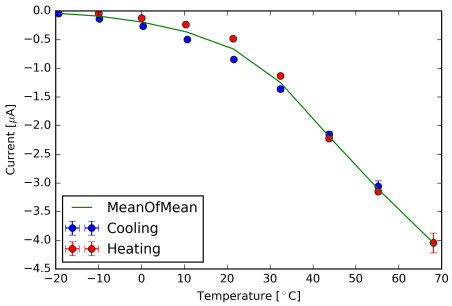

Figure 4.82. Data points of one complete cycle (-15°C – 70°C - -6°C) for a sensor type 2 at a pulse length of 0.5 s. Each temperature for heating and cooling contains 4-5 data points which were averaged. The error bars lie mostly within the marker size and represent the standard deviation of the data points. The green line displays the trend of the temperature dependence and is calculated as the mean of the cooling and heating points at each temperature.

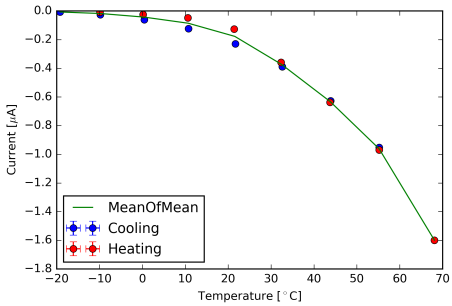

Figure 4.83. Data points of two complete cycles (-15°C – 70°C - -6°C) for a sensor type 2 at a pulse length of 1.0 s. Each temperature for heating and cooling contains 4-5 data points which were averaged. The error bars lie mostly within the marker size and represent the standard deviation of the data points. The green line displays the trend of the temperature dependence and is calculated as the mean of the cooling and heating points at each temperature.

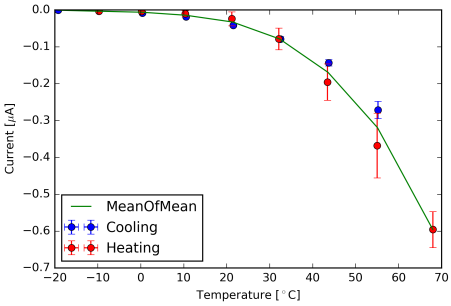

Figure 4.84. Data points of two complete cycles (-15°C – 70°C - -6°C) for a sensor type 2 at a pulse length of 10.0 s. Each temperature for heating and cooling contains 4-5 data points which were averaged. The error bars lie partly within the marker size and represent the standard deviation of the data points. The green line displays the trend of the temperature dependence and is calculated as the mean of the cooling and heating points at each temperature.

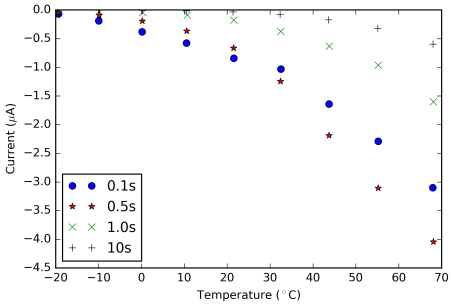

Figure 4.85. Results of the four different pulse lengths - 0.1 s, 0.5 s, 1.0 s and 10.0 s - over the complete temperature range (15°C – 70°C - -6°C) plotted in one diagram for better comparison. It can be seen that the resolution decreases with increasing pulse length. Furthermore, the pulse length of 0.5 s shows a steeper increase in current from 30 °C to 70°C compared to the pulse length of 0.1 s.

4.4.2.3 Sensor Type 3: IL3 + IL2

After the initial experiment, presented in section 4.4.1.3, a second sensor with the **IL3** and **IL2** mixture was prepared and measured at the four pulse lengths, 0.1 s, 0.5 s, 1.0 s and 10.0 s, using

the potentiostat. Again, the results for the pulse length at 0.1 s are shown in detail below and discussed. Figure 4.86 and 4.87 display all the valid data points at 0.1 s as well as the average current value for the heating and cooling cycles, respectively, at each temperature. The error bars indicate the standard deviation and lie within the marker size for the temperatures $\leq$ 20°C. In total, 1,437 measurements were conducted at this pulse length, of which 1,040 data points were recorded at stable temperatures. As before, the absolute current value decreases with increasing cycle number due to the aforementioned reasons. This was also observed in the sensor measured using the custom-made electronics. Comparing the two measurements, the same trend as for the sensor types 1 and 2 can be found. The absolute current values are much smaller when the potentiostat is used and ranges only from 1.85 nA to 115.65 nA, while for the custom-made measurement electronics values between 18.5 nA and 1,049 nA were reached in the investigated temperature regime. However, the relative change in current at a respective temperature is much higher for the measurements using the potentiostat (used data for the first five cycles with 0.1 s pulse length) than the custom-made electronics. For the latter, the current changes in average over the temperature regime by approx. 8%, while for the potentiostat measurements the change is up to 50% for the low temperatures (-20°C and -10°C) and between 20-40% for the higher ones.
In contrast to sensor type 2, the difference between the heating and cooling cycles is quite small. At 0°C and 10°C the heating value is higher than the cooling value, while at 20°C and 30°C the difference mainly results from a small shift in temperature at which the current was measured. For 40°C and 50°C, however, the heating values are lower than the cooling ones. Additionally, the absolute current values of sensor type 3 in these experiments are smaller by a factor 30 compared to sensor type 2, described previously. Both aspects represent the influence of **IL2** in this sensitive layer. While the addition of **IL2** provided the possibility to measure the entire chosen temperature range (compared to sensor type 2) using the custom-made electronics, the results of sensor type 3 using the potentiostat show a lower resolution.

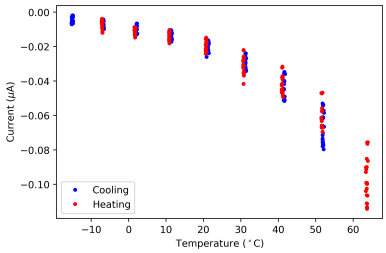

Figure 4.86. Sensor type 3 at a pulse length of 0.1 s for all cycles (1,040 data points). Each valid data point is shown. With increasing cycle number the current decreases.

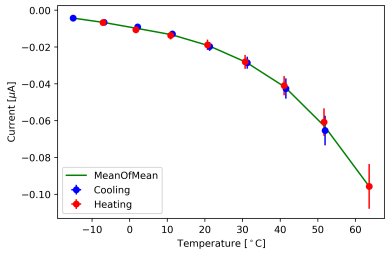

Figure 4.87. Sensor type 3 at a pulse length of 0.1 s displaying the average and standard deviation for the heating and cooling cycles, respectively, as well as the mean of those cycles for the entire data set.

The change from higher to lower current values with increasing temperature for the heating cycle compared to the cooling one can also be found for the data of only the first two cycles. There, the difference is even more pronounced and it can be assumed that this behavior can be attributed to the presence of **IL2** as described above. Since it is not clear how the single ions of two different ILs interact with each other, the results suggest that ions might have a different influence on the performance of the layer depending on the temperature. Since sensor type 2 implies that the freezing point of **IL3** lies around 30°C the higher heating values (compared to the cooling cycle) at the lower temperature regime for this sensor might be due to the presence

of **IL2**. For the higher temperatures, i. e. 40°C and 50 °C, the current values show a clear supercooling effect with lower heating values, which might come from the higher melting point of **IL3** (compared to the freezing temperature) and therefore suggests a greater influence of the behavior of this IL at higher temperatures.

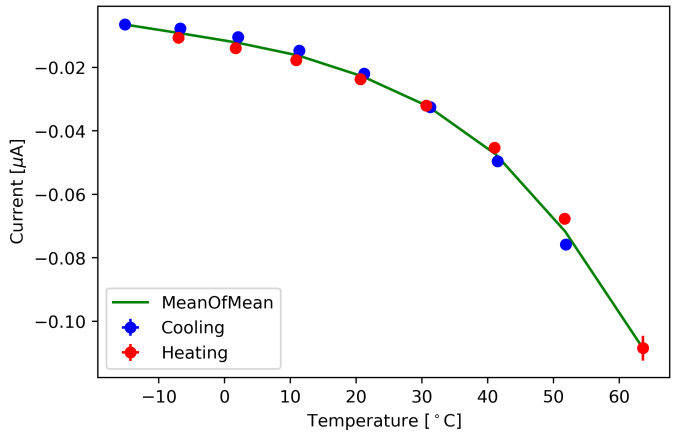

Figure 4.88. Sensor type 3 at a pulse length of 0.1 s displaying the average and standard deviation for the heating and cooling cycles, respectively, for two cycles in the temperature range of -20°C and 70°C. The green solid line represents the mean of mean data of the heating and cooling cycles. The error bars lie within the marker size, except for the heating value at -10 °C. The behavior of the heating and cooling cycle is opposite to what can be found for the trend over all data (compare figure 4.79).

Again, this sensor configuration was also measured at the pulse lengths of 0.5 s (total number of measurements conducted: 526; at stable temperature: 381), 1.0 s (total number of measurements conducted: 485; at stable temperature: 351) and 10.0 s (total number of measurements conducted: 263; at stable temperature: 189). For the pulse lengths of 1.0 s the supercooling effect is only observable at 40°C, while the results of 0.5 s and 10.0 s yields the same behavior found for the shortest pulse length (see figures 4.89 - 4.91). Also the difference in heating and cooling is more significant at 0 °C and 10°C for the pulse length of 1.0 s than for the others. Figure 4.92 displays the average current values of all four pulse lengths (first two cycles) and as for the other sensor types the sensitivity decreases significantly with increasing pulse length.

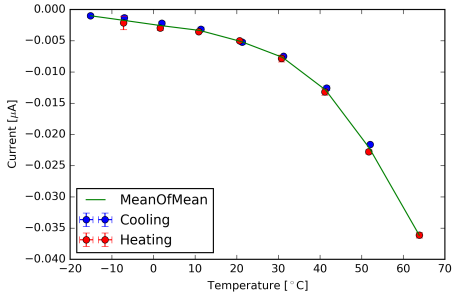

Figure 4.89. Data points of one complete cycles (-15°C – 70°C - -6°C) for a sensor type 3 at a pulse length of 0.5 s. Each temperature for heating and cooling contains 4-5 data points which were averaged. The error bars lie mostly within the marker size and represent the standard deviation of the data points. The green line displays the trend of the temperature dependence and is calculated as the mean of the cooling and heating points at each temperature.

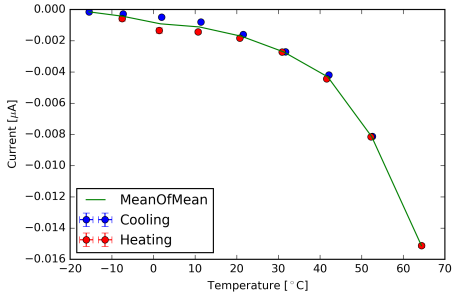

Figure 4.90. Data points of two complete cycles (-15°C – 70°C - -6°C) for a sensor type 3 at a pulse length of 1.0 s. Each temperature for heating and cooling contains 4-5 data points which were averaged. The error bars lie mostly within the marker size and represent the standard deviation of the data points. The green line displays the trend of the temperature dependence and is calculated as the mean of the cooling and heating points at each temperature.

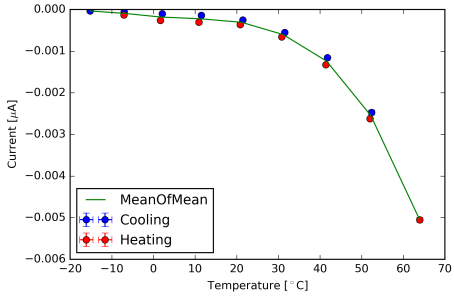

Figure 4.91. Data points of two complete cycles (-15°C – 70°C - -6°C) for a sensor type 3 at a pulse length of 10.0 s. Each temperature for heating and cooling contains 4-5 data points which were averaged. The error bars lie mostly within the marker size and represent the standard deviation of the data points. The green line displays the trend of the temperature dependence and is calculated as the mean of the cooling and heating points at each temperature.

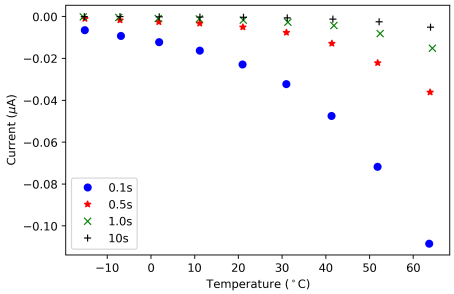

Figure 4.92. Results of the four different pulse lengths - 0.1 s, 0.5 s, 1.0 s and 10.0 s - over the complete temperature range (15°C – 70°C - -6°C) plotted in one diagram for better comparison. It can be seen that the resolution decreases with increasing pulse length.

5 Physical Models

In this chapter the results of the previously described temperature sensors are tried to correlate with physical models, e.g. Stokes-Einstein and Nernst-Einstein, which were described in chapter 2.3.4. Additionally, the Arrhenius equation is used to describe the viscosity behavior of the three sensor types. Finally, the Shoup-Szabo equation [171, 172] needs to be considered due to the used electrode arrangement. Combining these three aspects, an equation can be derived that fits the measured data to some aspect. However, this model does not consider the events taking place at the EDL or the porous UV-matrix that fixates the sensitive layer on top of the electrodes, which explains the deviation between the measured values and the values achieved by the model.
In a first step, the viscosity behavior of the used ionic liquids and their mixes were rheologically examined and analyzed using Arrhenius. In a second step, the above mentioned model was developed and validated using the recorded current data presented in the previous section. Finally, the obtained output data of the model, i.e. fitted viscosity data, was also analyzed using Arrhenius.

5.1 Viscosity Behavior of the Ionic Liquids Used for the Three Sensor Types

The change of viscosity with temperature is the basic phenomenon on which the function of the sensor relies. Therefore, the viscosity behavior between 20°C and 60°C for all three layer compositions were determined and the data were fitted according to the Arrhenius equation. In a second step, the viscosity behavior over a larger temperature regime (-10°C to 60°C) is discussed.

5.1.1 Determining the Activation Energy E_A and the Material Constant η_∞ of the Ionic Liquids Used for the Three Sensor Types

According to Okoturo et al. [69], which equation, Arrhenius or VFT, fits better can be obtained by plotting T^{-1} vs. $\ln(\eta)$. If this results in a linear relation Arrhenius can be applied. Therefore, in a first step of analyzing the viscosity behavior a respective plot was acquired. Next, the Arrhenius equation was fitted onto the measured data points and the material constant η_∞ as well as the activation energy E_A were determined. This is shown for sensor type 1 in figures 5.1 and 5.2. As can be seen, the data shows a good linear correlation ($r^2 > 0.9957$) and the resulting linear equation can be used to determine the material constant η_∞ and the activation energy E_A as well. Both values match the results of the fitting shown in figure 5.2 with $\eta_\infty = 9.17 \cdot 10^{-5}$ mPa s and $3.36 \cdot 10^{-5}$ mPa s and E_A = -3.44748 $\cdot 10^4$ J mol^{-1} and -3.70208 $\cdot 10^4$ J mol^{-1}, respectively.

The same analysis was done for the other two sensor types with similar results. Figures 5.3 and 5.4 as well as figures 5.5 and 5.6 show the results of the respective sensor types 2 and 3. Since the used IL mixtures (**IL1/IL2** and **IL3/IL2**) as well as the pure **IL3** are not investigated

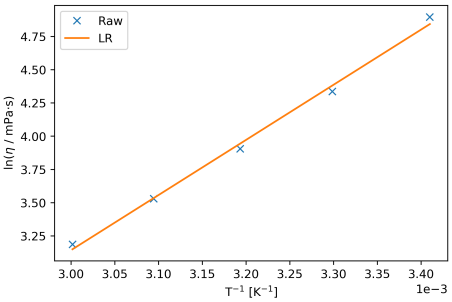

Figure 5.1. ln(η) vs. T^{-1} results for sensor type 1 in a good linear correlation ($r^2 > 0.9957$). Using the linear equation, η_∞ and E_A can be determined; $\eta_\infty = 9.17 \cdot 10^{-5}$ mPa s, E_A = -3.44748 · 10^4 J mol^{-1}.

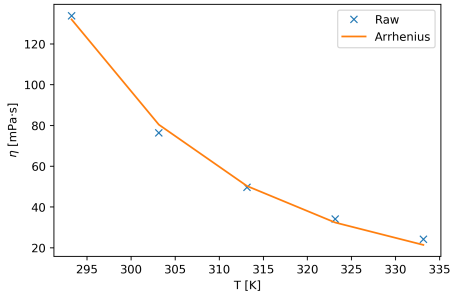

Figure 5.2. Plotting the Arrhenius equation ($\eta = \eta_\infty \cdot \exp(-E_A/RT)$) onto the measured viscosity data of sensor type 1, η_∞ and E_A can also be determined; $\eta_\infty = 3.36 \cdot 10^{-5}$ mPa s, E_A = -3.70208 · 10^4 J mol^{-1} ($r^2 > 0.9960$).

before, the obtained values cannot be matched with values reported in literature. However, the magnitude of η_∞ and E_A fits the literature values nicely.

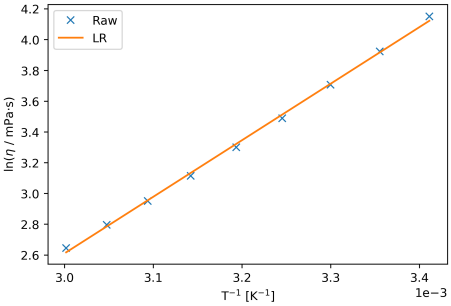

Figure 5.3. ln(η) vs. T^{-1} results for sensor type 2 in a good linear correlation ($r^2 > 0.9985$). Using the linear equation, η_∞ and E_A can be determined; $\eta_\infty = 2.22 \cdot 10^{-4}$ mPa s, E_A = -3.05556 · 10^4 J mol^{-1}.

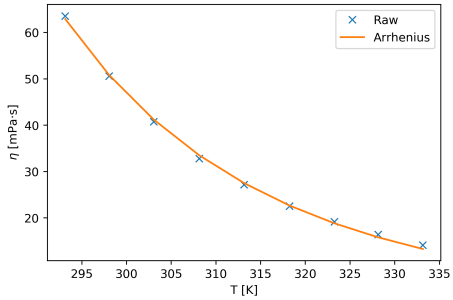

Figure 5.4. Plotting the Arrhenius equation ($\eta = \eta_\infty \cdot \exp(-E_A/RT)$) onto the measured viscosity data for sensor type 2, η_∞ and E_A can also be determined; $\eta_\infty = 1.50 \cdot 10^{-4}$ mPa s, E_A = -3.15606 · 10^4 J mol^{-1} ($r^2 > 0.9989$).

For sensor type 2 the activation energy E_A equals -30,555.6 J mol^{-1} and -31,560.6 J mol^{-1} while the material constant η_∞ corresponds to 2.22 · 10^{-4} mPa s and 1.50 · 10^{-4} mPa s according to the linear regression ($r^2 > 0.9985$) and the Arrhenius plot ($r^2 > 0.9989$), respectively. Similar values are found for sensor type 3. Here, E_A equals -30,241.3 J mol^{-1} and -31,794.4 J mol^{-1} while η_∞ yields 1.95 · 10^{-4} mPa s and 1.06 · 10^{-4} mPa s for the linear regression ($r^2 > 0.9965$) and Arrhenius ($r^2 > 0.9963$), respectively.
The material constant η_∞ and the activation energy E_A for the different sensor types as well as the two methods are summarized in table 5.1 in the temperature regime between 20°C and 60°C (293 K to 333 K).

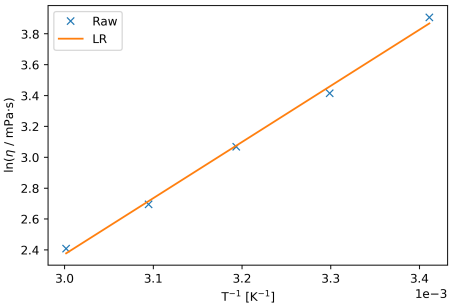

Figure 5.5. ln(η) vs. T^{-1} results for sensor type 3 in a good linear correlation ($r^2 > 0.9965$). Using the linear equation, η_∞ and E_A can be determined; $\eta_\infty = 1.95 \cdot 10^{-4}$ mPa s, E_A = -3.02413 · 10^4 J mol^{-1}.

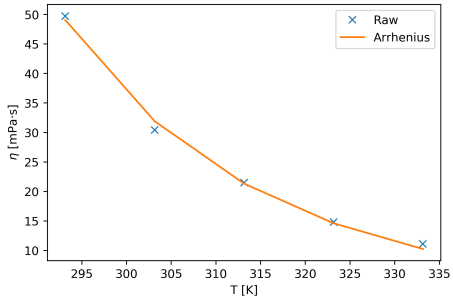

Figure 5.6. Plotting the Arrhenius equation ($\eta = \eta_\infty \cdot \exp(-E_A/RT)$) onto the measured viscosity data for sensor type 3, η_∞ and E_A can also be determined; $\eta_\infty = 1.06 \cdot 10^{-4}$ mPa s, E_A = -3.17944 · 10^4 J mol^{-1} ($r^2 > 0.9963$).

Table 5.1. Measured viscosity data with resulting material constants, E_A and η_∞, for Sensor types 1 - 3 in the temperature regime of 20°C to 60°C (293 K to 333 K).

		Arrhenius			**Linear Regression**		
	Sensor Type 1						
T (K)	$\eta_{meas.}$ (mPa s)	E_A (J mol^{-1})	η_∞ (mPa s)	r^2	E_A (J mol^{-1})	η_∞ (mPa s)	r^2
293.25	133.80 ± 1.97	-3.70208 · 10^4	3.36 · 10^{-5}	0.9960	-3.44748 · 10^4	9.17 · 10^{-5}	0.9957
303.15	76.39 ± 3.10						
313.15	49.71 ± 2.04						
323.15	34.15 ± 1.06						
333.15	24.21 ± 0.05						
	Senor Type 2						
T (K)	$\eta_{meas.}$ (mPa s)	E_A (J mol^{-1})	η_∞ (mPa s)	r^2	E_A (J mol^{-1})	η_∞ (mPa s)	r^2
293.15	63.54 ± 0.18	-3.15606 · 10^4	1.50· 10^{-4}	0.9989	-3.05556 · 10^4	2.22 · 10^{-4}	0.9985
298.05	50.60 ± 0.08						
303.05	40.47 ± 0.07						
308.15	32.78 ± 0.04						
313.15	27.13 ± 0.03						
318.25	22.54 ± 0.03						
323.25	19.13 ± 0.02						
328.15	16.39 ± 0.02						
333.15	14.09 ± 0.02						

	Senor Type 3						
T (K)	$\eta_{\mathbf{meas.}}$ (mPa s)	E_A (J mol^{-1})	η_∞ (mPa s)	r^2	E_A (J mol^{-1})	η_∞ (mPa s)	r^2
293.05	49.77 ± 0.12	-3.17944 · 10^4	1.06· 10^{-4}	0.9963	-3.02413 · 10^4	1.95 · 10^{-4}	0.9965
303.85	30.35 ± 0.20						
313.16	21.02 ± 0.06						
323.64	14.77 ± 0.04						
333.48	11.06 ± 0.04						

5.1.2 Investigation of the Viscosity Behavior over the Temperature Regime of -10°C to 60°C for the Ionic Liquids of All Three Sensor Types

In this section the viscosity behavior of the three IL mixtures is discussed. The viscosity was measured in several temperature regimes. Once, in the regime of 20°C to 60°C (293 K to 333 K) since at lower temperatures the condensation of moisture might influence the results. Since the chronoamperometric measurements were also conducted at temperatures down to -20°C (253 K) the viscosity was also obtained at such low temperatures. Furthermore, since the electrochemical experiments were done in heating and cooling cycles, the viscosity was also conducted for heating and cooling.

5.1.2.1 Sensor Type 1: IL1 + IL2

For the analysis above only the viscosity in the temperature regime of 20°C to 60°C (293 K to 333 K) are considered because below 20°C the condensation of moisture can influence the viscosity. However, since the current data was recorded at temperatures below 20°C, the viscosity was additionally examined at lower temperatures. Thereby, two main aspects can be observed: first, the linearity of the T^{-1} vs. $\ln(\eta)$ plot decreases significantly and a downward curvature can be observed, second, the absolute viscosity changes for a specific temperature significantly. This is shown in figures 5.7 and 5.8 for the IL mixture of sensor type 1. The linearity decreases from $r^2 > 0.9957$ to $r^2 > 0.9508$ since the viscosity at 20°C increases significantly from 133.8 mPa s to 326.6 mPa s and even further to 565.3 mPa s at 10°C. However, after heating up the temperature again to 20°C the viscosity value yields 275.9 mPa s and therefore, lies in between the starting value and the cooling value (see figure 5.8 Heat and Cool, respectively).

In literature the viscosity data is usually only given for one way, either heating or cooling, and therefore, it is not known if the found deviation is a common or a special phenomenon of the presented measurements. Furthermore, it was not possible to supply the measurement cup, in which the IL mixture was placed, with a nitrogen flow to prevent the influence of moisture. This might explain the in between value of 275.9 mPa s at 20°C since a higher amount of water in the IL mixture (condensed at 10°C) would lower the viscosity. However, it does not explain why the values between 30°C and 60°C show only a slight deviation (1 to 5 %) during the cooling cycle compared to the heating values while the viscosity at 20°C increases by a factor of 244 % upon cooling from 30°C to 20°C (see figure 5.8).

5.1.2.2 Sensor Type 2: IL3

To gain a better understanding of the viscosity behavior, **IL3** from sensor type 2 was thoroughly investigated. The advantage of this sensor type is the usage of a pure IL instead of a mixture

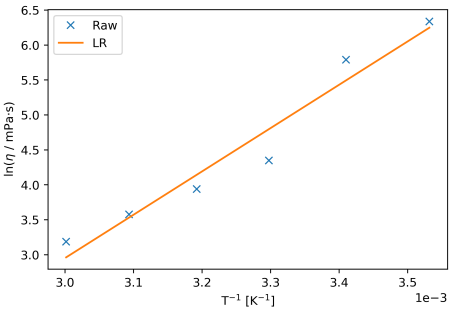

Figure 5.7. The $\ln(\eta)$ vs. T^{-1} plot for sensor type 1 shows a downward curvature and therefore a lower linearity ($r^2 > 0.9508$) for a temperature regime between 10°C and 60°C (compare figure 5.1). Here the cooling data (see figure 5.8 Cool) was used since the viscosity between 30°C and 60°C shows only a slight difference compared to the heating data.

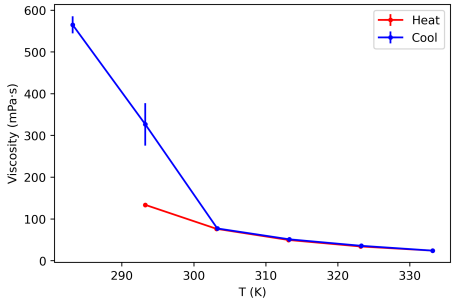

Figure 5.8. *Heat* represents the viscosity data that was measured by heating the IL mixture of sensor type 1 from 20°C to 60°C in 10°C steps. *Cool* represents the viscosity data of the cooling from 60°C to 10°C in increments of 10°C. At lower temperatures the viscosity differs significantly for the heating and cooling measurements, while the cooling data between 30°C and 60°C is only slightly higher than the heating data. If the temperature is increased again to 20°C the viscosity is still much higher than at the beginning with 275.9 mPa s (data point not shown).

of several ILs. Thereby, the influence of the viscosity due to interactions between cations and anions of two different ILs is eliminated. Figure 5.9 shows the viscosity data of the entire temperature regime. The measurements started at 20°C and the temperature was increased in 5°C steps up to 60°C (Heat). Afterwards the IL was directly cooled down to 20°C and from there the temperature was decreased in 5°C steps to -10°C (Cool). As can be seen, the temperature at 20°C differs only slightly after cooling down from 60°C. However, it has to be noted that the viscosity at 20°C was measured three times over 10 minutes after reaching this temperature and at each measurement the viscosity decreased further until a value of 64.74 mPa s was obtained. The significant decrease over this time at 20°C might be due to an inhomogeneous temperature distribution within the sample, which was leveled out over the first two measurements. Moreover, the standard deviation is much higher with 9.81 to 8.36 mPa s compared to the start value at the same temperature (see table 5.2).

Since it was noted that the sample needs some time to equilibrate at a new temperature, the same IL was measured again in the above shown temperature regime,with 30 minutes of equilibration at each new temperature. Furthermore, this time the temperature was increased and decreased in 10°C steps, starting again at 20°C. First the temperature was elevated up to 60°C and then decreased in 10°C steps down to -10°C. Thereby, a similar behavior as for the IL mixture of sensor type 1 was found (compare figure 5.8). The viscosity values for the temperatures between 30°C and 60°C lie almost within the standard deviation of the cooling measurements, while at 20°C the viscosity increases significantly higher than expected. Equilibrating the sample overnight at 20°C yields a viscosity of (51.74 ± 7.92) mPa s. Afterwards, the viscosity at the lower temperatures (10°C to -8°C) was measured. This is shown in figures 5.10 and 5.11 as well as in table 5.3.

Comparing the viscosity data of the measurements with and without equilibration time shows

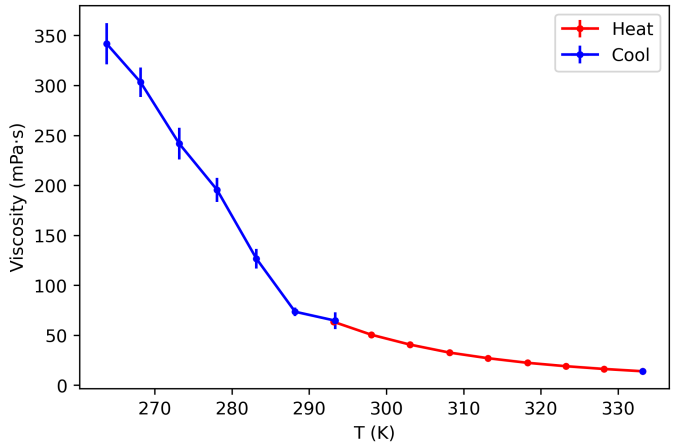

Figure 5.9. The viscosity data of sensor type 2 over the temperature regime of -10°C to 60°C (263 K to 333 K). Starting at 20°C and increasing the temperature in 5°C steps up to 60°C. From there the IL was cooled down in one step to 20°C (only the data point of the third measurement is shown) and then further in 5°C steps down to -10°C. The error bars for the heating data lie within the marker size.

Table 5.2. Viscosity data of **IL3** from sensor type 2 for the temperature regime of 20°C to 60°C (Heating) and afterwards from 60°C to 20°C in one step and further down to -9°C in smaller steps (Cooling).

	Heating	**Cooling**
T (K)	η (mPa s)	η (mPa s)
293.15	63.54 ± 0.18	-
298.05	50.60 ± 0.08	-
303.05	40.74 ± 0.07	-
308.15	32.78 ± 0.04	-
313.15	27.13 ± 0.03	-
318.25	22.54 ± 0.03	-
323.25	19.13 ± 0.02	-
328.15	16.39 ± 0.02	-
333.15	14.09 ± 0.02	-
293.35	-	79.13 ± 9.81 71.41 ± 8.46 64.74 ± 8.36
288.15	-	73.68 ± 4.25
283.15	-	126.8 ± 9.9
278.05	-	195.7 ± 12.0
273.15	-	241.9 ± 16.0
268.15	-	303.4 ± 14.7
263.75	-	341.9 ± 20.7

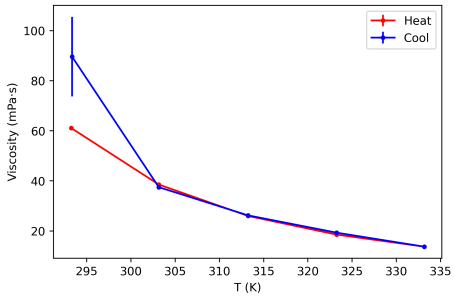

Figure 5.10. The viscosity data of sensor type 2 at the temperature regime of 20°C to 60°C (293 K to 333 K). At each new temperature the sample was equilibrated for 30 minutes before the measurement. The viscosity data of the cooling fits the data of the heating quite good between 30°C and 60°C (303 K to 333 K). However, the value at 20°C after cooling down is much higher than expected after 30 minutes equilibration time, but decreases even below the starting value over night (see figure 5.11). The error bars lie within the marker size for the temperatures between 20°C and 60°C (293 K to 333 K) for the heating and between 60°C and 30°C (333 K tot 303 K) for the cooling.

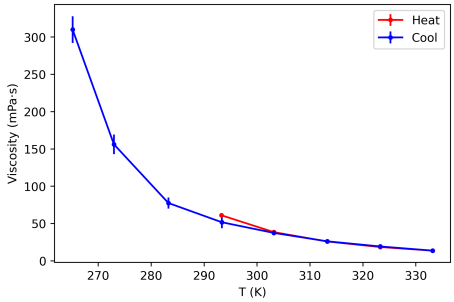

Figure 5.11. The viscosity data of sensor type 2 over the entire temperature regime (265 K to 333 K), showing the lower data point at 20°C for the cooling. The error bars lie within the marker size for the temperatures between 20°C and 60°C (293 K to 333 K) for the heating and between 60°C and 30°C (333 K to 303 K) for the cooling.

Table 5.3. Viscosity data of **IL3** from sensor type 2 for the temperature regime of 20°C to 60°C (Heating) and afterwards from 60°C to -10°C (Cooling). Before each measurement an equilibration time of 30 minutes was used.

	Heating (μA)	**Cooling**
Temperature (K)	η (mPa s)	η (mPa s)
293.25	61.12 ± 0.10	-
303.35	38.54 ± 0.05	-
313.25	25.97 ± 0.03	-
323.25	18.52 ± 0.02	-
333.15	13.72 ± 0.03	-
323.25	-	19.31 ± 0.52
313.25	-	26.21 ± 0.37
303.15	-	37.48 ± 0.26
293.35	-	83.56 ± 10.46 (30 minutes) 51.74 ± 7.92 (over night)
283.25	-	77.52 ± 7.35
272.95	-	156.3 ± 13.2
265.15	-	310.1 ± 17.9

a significant difference for the temperatures below 20°C, while for the temperatures between 20°C and 60°C (293 K to 333 K) the viscosity differs only slightly (see figure 5.12). The cooling without equilibration time was not measured for the temperature regime between 60°C and 20°C (333 K to 293 K). Since the viscosity below 20°C is always lower for the measurements with 30 minutes equilibration time, it is probable that the condensation of moisture into the IL sample is causing this behavior (see figure 5.13) .

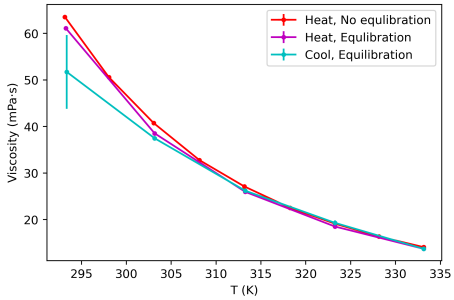

Figure 5.12. Comparison of the viscosity data with (heating and cooling) and without (only heating) equilibration time between 20°C and 60°C (293 K to 333 K) for sensor type 2. The error bars lie within the marker size for the temperatures between 20°C and 60°C (293 K to 333 K) for the heating and between 60°C and 30°C (333 K tot 303 K) for the cooling.

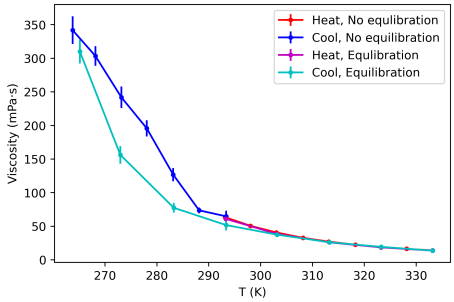

Figure 5.13. Comparison of the viscosity data with and without equilibration time of sensor type 2 over the entire temperature regime (265 K to 333 K). The error bars lie within the marker size for the temperatures between 20°C and 60°C (293 K to 333 K) for the heating and between 60°C and 30°C (333 K to 303 K) for the cooling.

5.1.2.3 Sensor Type 3: IL3 + IL2

The viscosity of the IL mixture of sensor type 3 was also determined in the temperature regime of -10°C to 60°C (263 K to 333 K) in 10°C steps. This time the measurements started at the lowest temperature (-7°C) and was then heated up. As for the other two sensor types, the standard deviation at the temperatures between 20°C and 60°C (293 K and 333 K) is quite small and lie within the marker size, while for the lower temperatures the viscosity itself and the standard deviation increases significantly (see figures 5.14 and 5.15 as well as table 5.4).

Since this IL mixture was used to lower the freezing point of the pure **IL3**, the obtained viscosity data of sensor type 2 and 3 were compared. It can be seen that the addition of **IL2** in a ratio of 1:3 lowered the viscosity about 23% between 20°C and 60°C (see figure 5.16). In the lower temperature regime the difference is much more significant as can be seen in figure 5.17. Here, the influence of **IL2** can be clearly observed due to the increase in viscosity of the mixture by a factor of 3.6 compared to the pure **IL3**. This might be due to the longer alkyl chain in **IL2** which has a greater impact at lower temperatures although it is the minor IL in the mixture.

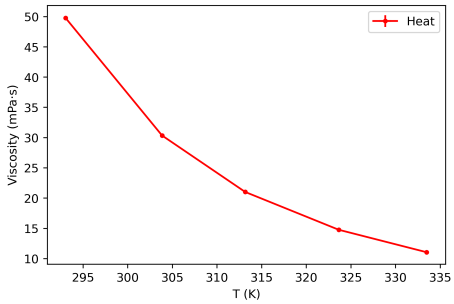

Figure 5.14. Viscosity data for the heating of the IL mixture of sensor type 3 between 20°C and 60°C. The error bars lie within the marker size.

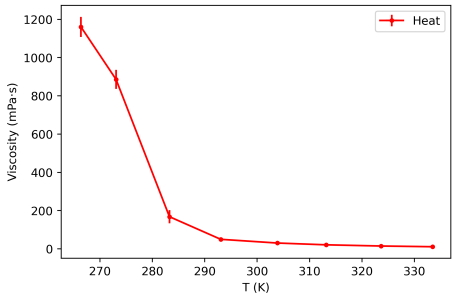

Figure 5.15. Viscosity data for the heating of the IL mixture of sensor type 3 over the entire temperature regime between -7°C and 60°C (266 K to 333 K). The error bars lie within the marker size for the temperatures between 20°C and 60°C (293 K to 333 K).

Table 5.4. Viscosity data of IL mixture from sensor type 3 for the temperature regime of -10°C to 60°C (Heating).

	Heating
T (K)	η (mPa s)
266.4	1,160 ± 53
273.1	886.0 ± 49.3
283.3	168.3 ± 24.6
293.1	49.77 ± 0.12
303.8	30.35 ± 0.20
313.2	21.02 ± 0.06
323.6	14.77 ± 0.04
333.5	11.06 ± 0.04

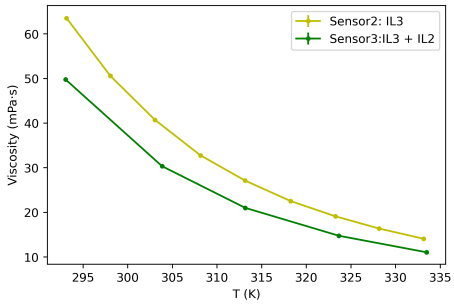

Figure 5.16. Comparison of the viscosity data of sensor types 2 and 3 between 20°C and 60°C. The error bars lie within the marker size.

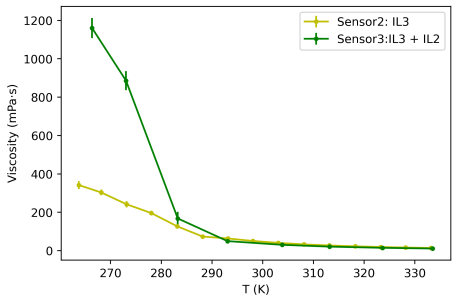

Figure 5.17. Comparison of the viscosity data of sensor types 2 and 3 over the entire temperature regime between -10°C and 60°C (266 K to 333 K). The error bars lie within the marker size for the temperatures between 20°C and 60°C (293 K to 333 K).

5.2 Correlation with Shoup-Szabo, Stokes-Einstein and Nernst-Einstein

The measurement principle of the developed temperature sensors discussed in the previous chapter 4.4 is assumed to be based mainly on the change of viscosity with temperature. In this chapter a model is developed that will describe the findings and confirm the assumption regarding the working principle. Therefore, the previously introduced equations of Shoup-Szabo, Stokes-Einstein and Nernst-Einstein will be used and combined to obtain fitted viscosity data at each measured temperature. Afterwards, this data is analyzed using Arrhenius to validate the developed equation.
The input data (current data) used in this chapter corresponds, if not stated otherwise, to the data discussed in chapter 4.4 for 1 or 2 heating and cooling cycles.

5.2.1 Developing a Model to Describe the Working Principle of the Temperature Sensors

As mentioned in chapter 2.4, the Shoup-Szabo equation [172] can be used to describe the chronoamperometric current at a microelectrode, since the redox process is dominated by radial diffusion towards the electrode and the electrode size is small enough. Since $\tau < 1$, f(τ) can be approximated as shown in equation 5.3.

$$i = 4nFDr_e c_0 f(\tau) \tag{5.1}$$

$$\tau = 4Dtr_e^{-2} \tag{5.2}$$

$$f(\tau) = 0.7854 + 0.8862\tau^{-\frac{1}{2}} + 0.2146\, e^{-0.7823\tau^{-\frac{1}{2}}} \tag{5.3}$$

Putting τ in f(τ) and afterwards f(τ) in i and simplifying the equation, i can be expressed as:

$$f(\tau) = 0.7854 + 0.8862 \cdot \frac{1}{2} \cdot r_e \cdot (Dt)^{-\frac{1}{2}} + 0.2146\, e^{-0.7823 \cdot \frac{1}{2} \cdot r_e \cdot (Dt)^{-\frac{1}{2}}} \tag{5.4}$$

$$i = 4 \cdot n \cdot F \cdot D \cdot r_e \cdot c_0\, (0.7854 + 0.4431 \cdot r_e \cdot (Dt)^{-\frac{1}{2}} + 0.2146\, e^{-0.3912 \cdot r_e \cdot (Dt)^{-\frac{1}{2}}} \tag{5.5}$$

$$\begin{aligned} i = {} & \underbrace{3.1416 \cdot n \cdot F \cdot r_e \cdot c_0}_{K1} \cdot D + \underbrace{1.7724 \cdot n \cdot F \cdot r_e^2 \cdot c_0}_{K2} \cdot D \cdot (Dt)^{-\frac{1}{2}} \\ & + \underbrace{0.8584 \cdot n \cdot F \cdot r_e \cdot c_0}_{K3} \cdot D \cdot e^{\underbrace{-0.3912 \cdot r_e}_{K4} \cdot (Dt)^{-\frac{1}{2}}} \end{aligned} \tag{5.6}$$

$$= K1D + \frac{K2D}{\sqrt{t}} \cdot D^{-\frac{1}{2}} + K3D \cdot e^{\frac{K4}{\sqrt{t}} \cdot D^{-\frac{1}{2}}} \tag{5.7}$$

with	n	=	number of transfererd electrons	1 or 2
	F	=	Faraday constant	96.485 C/mol = As/mol
	r_e	=	electrode radius	$40 \cdot 10^{-6}$ m
	c_0	=	concentration of redox species/IL	see table 5.9
	D	=	diffusion coefficient	approx. 10^{-13} m^2s^{-1}
	t	=	pulse length	0.1 s, 0.5 s, 1.0 s or 10.0 s

The number of transferred electrons as well as the concentration of the redox species varies between the different sensor types. While n is usually 1 or 2, depending if methylene blue was present, the exact concentration c_0 is not known since the IL functioned partially as redox species as well as solvent. However, to show if the above developed correlation is valid an estimated guess for c_0 is sufficient. For sensor type 1, which additionally contained the redox molecule methylene blue with a concentration of 0.4 mol l^{-1} (400 mol m^{-3}) , c_0 was initially set to 400 mol m^{-3}. However, the results of the fitting using equation 5.9 showed that with this concentration the viscosity at 20°C would be around 330 mPa s and therefore much higher than expected according to rheological measurements. Since this viscosity value seemed to be unrealistic at 20°C, the concentration c_0 was adjusted to $10^{2.4}$ mol m^{-3}, which results in a plausible viscosity value of 130 mPa s. The difference of the real concentration of methylene blue in sensor type 1 and the adjusted value for c_0 is probably due to the sensor geometry and setup. However, as can be seen below, the adjustment of c_0 does not compromise the validity of the developed equation 5.9. For the sensor types 2 and 3, c_0 was generally unknown since the used ILs were partly redox species and solvent at once and therefore, c_0 was determined by choosing it according to the resulting viscosity value at 20°C, which should be close to the viscosity value found by the rheological measurements for these ILs.
t corresponds to the four different pulse lengths (0.1 s, 0.5 s, 1.0 s and 10.0 s) used in the experiments described in the chapter before. Since these parameters vary, the self-defined constants, $K1$ - $K4$, vary as well and are given exemplarily for sensor type 1 at $t = 0.1$ s:

$$\begin{aligned} n &= 2 \\ c_0 &= 10^{2.4}\ \text{mol m}^{-3} \\ K1 &= 1.827 \cdot 10^4\ \text{As m}^{-2} \\ K2 &= 0.4124\ \text{As m}^{-1} \\ K3 &= 4.9930 \cdot 10^3\ \text{As m}^{-2} \\ K4 &= \text{-}4.694 \cdot 10^{-5}\ \text{m} \end{aligned}$$

In a next step, the Stokes-Einstein equation can be introduced, since this relates the diffusion of a dissolved molecule with the viscosity of the used solvent. As discussed in chapter 2.3.4 for ionic liquids the *Sutherland coefficient n* is 4 rather than 6 which corresponds to a sliding sphere behavior.

$$D = \frac{k_B T}{4\pi\eta r} \tag{5.8}$$

Here, D stands for the diffusion coefficient, k_B is the Boltzmann constant, T the absolute temperature, η the viscosity and r the radius of the molecule or the IL, respectively. This relation implies that a change in viscosity results in a change in the diffusion rate. Since the viscosity of fluids varies with temperature, the diffusion rate also depends on this quantity.
Substituting D in equation 5.7 with the above expression of the diffusion coefficient one obtains a direct relation of current and viscosity. Furthermore, it is necessary to consider the fractional Stokes-Einstein equation which introduces the exponent s on the relation of temperature and viscosity that are proportional to D (see equation 2.35).

$$i = K1 \cdot \frac{k_B}{4\pi R}\left(\frac{T}{\eta}\right)^s + \frac{1}{\sqrt{t}} \cdot K2 \cdot \left(\frac{k_B}{4\pi R}\left(\frac{T}{\eta}\right)^s\right)^{\frac{1}{2}} + K3 \cdot \frac{k_B}{4\pi R}\left(\frac{T}{\eta}\right)^s \cdot e^{\frac{1}{\sqrt{t}} \cdot K4 \cdot \left(\frac{k_B}{4\pi R}\left(\frac{T}{\eta}\right)^s\right)^{-\frac{1}{2}}} \tag{5.9}$$

A first step to evaluate equation 5.9 is to use the measured viscosity data, presented in the previous section, and calculate the corresponding current. If equation 5.9 is valid the calculated

current using this equation should be close to the recorded one. Since equation 5.9 consists of three terms, each term is calculated separately and summed up.

$$i = \underbrace{K1 \cdot \frac{k_B}{4\pi R}\left(\frac{T}{\eta}\right)^s}_{\text{Term1}} + \underbrace{\frac{1}{\sqrt{t}} \cdot K2 \cdot \left(\frac{k_B}{4\pi R}\left(\frac{T}{\eta}\right)^s\right)^{\frac{1}{2}}}_{\text{Term 2}} + \underbrace{K3 \cdot \frac{k_B}{4\pi R}\left(\frac{T}{\eta}\right)^s \cdot e^{\frac{1}{\sqrt{t}} \cdot K4 \cdot \left(\frac{k_B}{4\pi R}\left(\frac{T}{\eta}\right)^s\right)^{-\frac{1}{2}}}}_{\text{Term 3}} \tag{5.10}$$

To calculating each term for sensor type 1 the measured viscosity data is used for η at the respective temperature. As can be seen in table 5.5 the calculated current $i_{\text{calc.}}$ depends mainly on the second term of equation 5.10. To compare the calculated current with the measured one, the latter is given in the last column.

Table 5.5. Calculated values for the three terms, the summed up current of equation 5.10 and the measured current for sensor type 1 at a pulse length of 0.1 s.

T (K)	**Term 1** (A)	**Term 2** (A)	**Term 3** (A)	$i_{\text{calc.}}$ (A)	**T** (K)	$i_{\text{meas.}}$ (A)
293.3	$1.47 \cdot 10^{-12}$	$1.17 \cdot 10^{-8}$	0.00	$1.17 \cdot 10^{-8}$	294.1	$1.19 \cdot 10^{-8}$
303.2	$2.66 \cdot 10^{-12}$	$1.57 \cdot 10^{-8}$	0.00	$1.57 \cdot 10^{-8}$	303.9	$1.64 \cdot 10^{-8}$
313.2	$4.22 \cdot 10^{-12}$	$1.98 \cdot 10^{-8}$	0.00	$1.98 \cdot 10^{-8}$	314.0	$2.50 \cdot 10^{-8}$
323.2	$6.33 \cdot 10^{-12}$	$2.43 \cdot 10^{-8}$	0.00	$2.43 \cdot 10^{-8}$	324.1	$4.08 \cdot 10^{-8}$
333.2	$9.21 \cdot 10^{-12}$	$2.93 \cdot 10^{-8}$	0.00	$2.93 \cdot 10^{-8}$	335.4	$7.00 \cdot 10^{-8}$

The different temperature values presented in table 5.5 correspond in the first column with the temperatures at which the viscosity was rheologically measured and in the second last with the temperature of the current measurements. This needs to be considered if the current values are compared because they are in both cases temperature dependent.
Since the two current values, calculated and measured, are in good agreement with each other, equation 5.9 can be used to analyze the current data further. At first the temperature regime from 20°C to 60° was used to determine the viscosity based on the recorded current data. This particular temperature regime was chosen because the achieved values can be compared with viscosity data obtained at the same regime using a Brookfield rheometer. However, equation 5.9 is valid over the entire temperature range that was used in the chronoamperometrical experiments (see figures 5.21 to 5.23).

5.2.2 Analyzing the Developed Shoup-Szabo-Stokes-Einstein-Equation 5.9

Figure 5.18 shows the fit result of equation 5.9 for sensor type 1 at a pulse length of 0.1 s. Here, the exponent s is chosen to be 1.0. On the left y-axis the recorded (input data of the fitting) and calculated current data (see table 5.5) were plotted, while on the right y-axis the fitted viscosity data is shown.

As can be seen the fitted viscosity shows the expected temperature behavior in the regime of 20°C to 60° (293 K to 333 K) and results in reasonable absolute values due to the adjustment of the concentration c_0. Comparing the fitted and measured viscosity values shows that the fitted viscosity decreases faster for higher temperatures (see table 5.6 and figure 5.19).

Varying the exponent s of the fractional Stokes-Einstein equation between 0.8 and 1.0 while the rest of the parameters, e.g. c_0, is kept constant, shifts the absolute values to lower viscosities

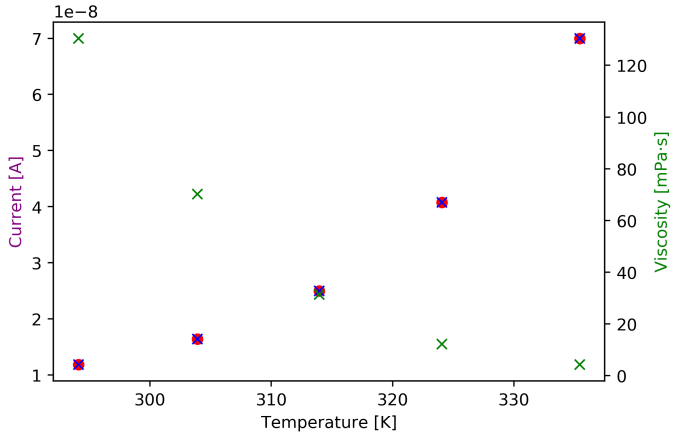

Figure 5.18. Plotting the measured current data of sensor type 1 with a pulse length of 0.1 s from 20°C to 60°C using equation 5.9 with an exponent $s = 1.00$. The resulting viscosity is in good agreement with the measured viscosity values. x represents the fitted viscosity while x stands for the recalculated current using equation 5.9 and the ■ represent the recorded current data.

Table 5.6. Comparing the fitted viscosity values achieved by the developed Shoup-Szabo-Stokes-Einstein equation (eq. 5.9) with $s = 1.0$ and the measured ones obtained using a Brookfield rheometer.

T (K)	$\eta_{\mathbf{fit}}$ (mPa s)	**T** (K)	$\eta_{\mathbf{meas.}}$ (mPa s)
294.1	130.4	293.3	133.8
303.9	70,25	303,2	76.39
314.0	31.41	313.2	49.71
324.1	12.15	323.2	34.15
335.4	4.27	333.2	24.21

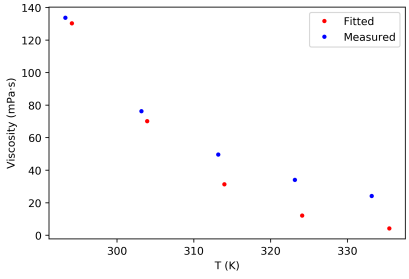

Figure 5.19. Comparing the fitted and measured viscosity of sensor type 1 with $s = 1.0$.

for lower s values. At lower temperatures the viscosity spread over a wider regime, e.g. at 294 K it varies from 130.4 mPa s for $s = 1.00$ to 106.4 mPa s for $s = 0.80$, while at higher temperatures the variation is smaller, from 4.27 mPa s ($s = 1.00$) to 1.43 mPa s ($s = 0.80$) at 335 K. The respective values can be found in table 5.7 and are plotted in figure 5.20. However, with the data at hand it is not possible to determine the exact value of s, which is why for all further plots s is kept at 1.0. Since the first step is to determine if the developed equation is valid and therefore, can be used to describe the developed temperature sensor, the estimation of s is sufficient at this point.

Table 5.7. Comparing the different viscosity values obtained by varying the fractional Stokes-Einstein exponent s.

T (K)	$\eta_{calc.}$ (mPa s) $s = 1.00$	$\eta_{calc.}$ (mPa s) $s = 0.95$	$\eta_{calc.}$ (mPa s) $s = 0.90$	$\eta_{calc.}$ (mPa s) $s = 0.85$	$\eta_{calc.}$ (mPa s) $s = 0.80$
294.1	130.4	125.0	119.1	113.0	106.4
303.9	70,25	65.04	59.70	54.25	48.71
314.0	31.41	27.83	24.32	20.93	17.67
324.1	12.15	10.22	8.44	6.81	5.35
335.4	4.27	3.39	2.63	1.98	1.43

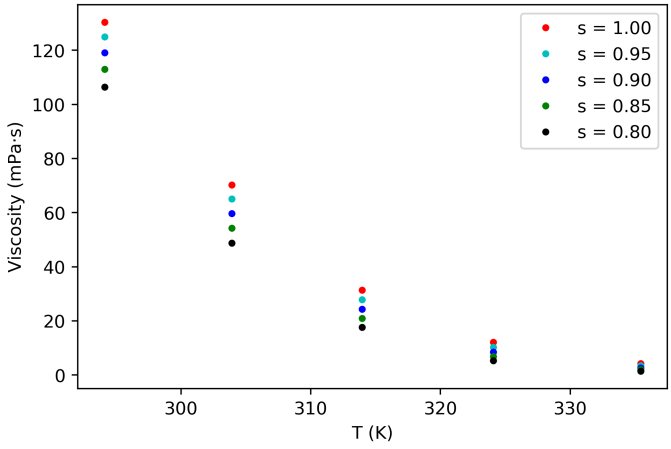

Figure 5.20. Varying the exponent s of the fractional Stokes-Einstein equation 5.9 from 0.80 to 1.00. As can be seen, the smaller the exponent the smaller the calculated viscosity.

As shown in figure 5.19 the fitted and measured viscosity differs significantly for higher temperatures. Since the two data sets are only partially comparable due to the different conditions under which the data were obtained, the comparison is insufficient to confirm the validity of the developed model. While the measured viscosity data were achieved by using a common rheometer with a cone-plate-geometry were only the respective IL/IL mix was investigated, the current data that were fed into the python fitting was obtained in a much more complex environment. At this point, this is not taken into consideration regarding the model. Especially two conditions were neglected so far. First, the porous UV-matrix that were used to fix the IL mixture on top of

the microelectrodes and second, the process occurring at the EDL. Since the fitted viscosity is based on the recorded current that was obtained during the chronoamperometric measurements both effects had influenced the resulting current values. However, with the present data the extent of this influence cannot be determined quantitatively, but the comparison to the measured viscosity values gives a qualitative indication.
Since the comparison of measured and fitted data is insufficient, for the following discussion the entire temperature range is considered. However, as can be seen, the results for the regime between 20°C and 60°C (293 K to 333 K) is the most reliable. There can be several reasons that explain these findings. First, the current (which is the input variable to obtain the viscosity) becomes very low at deep temperatures which in turn yields very high fitted viscosities. These high values might, as well as the very low current, indicate that the freezing point of the IL is reached and therefore a change of the physical state occurs, which is not considered by equation 5.9. Second, the neglected conditions induced due to the porous UV-matrix and the EDL processes might influence the measured current and therefore the results of the fitted viscosity. For sensor type 1 at a pulse length of 0.1 s the fitted viscosity show only a very slight increase at the low temperatures from 263 K to 253 K, which indicates that either the model is not valid for these low temperatures, the freezing point for this sensitive layer is reached or the input data is faulty. Since this behavior is not found for longer pulse lengths or the other sensor types, it is assumed that the model can be used for the entire temperature range and the found behavior for these two specific data points is faulty. To verify this assumption further, the current data of the last two complete heating-cooling cycles of pulse length 0.1 s were used as input data for the fitting (compare data presented in figure 4.73 in chapter 4.4.2.1). As can be seen with this data the viscosity fit is fine. The obtained viscosities for sensor type 1 are plotted in figures 5.21 over the entire temperature range (253 K - 333 K), in figure 5.22 for the range between 0°C and 60°C (273 K to 333 K) and in 5.23 between 20°C and 60°C (293 K to 333 K).

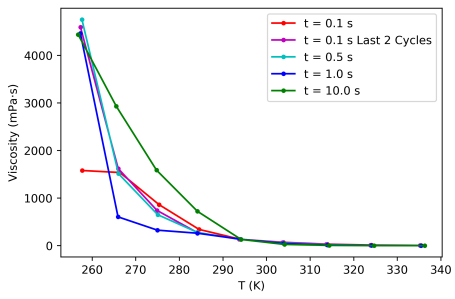

Figure 5.21. Plotting the fitted viscosity values for all pulse lengths of sensor type 1 over the entire temperature range from 253 K to 333 K.

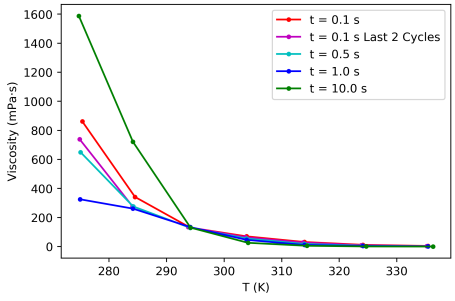

Figure 5.22. Plotting the fitted viscosity values for all pulse lengths of sensor type 1 for the temperature regime between 273 K to 333 K.

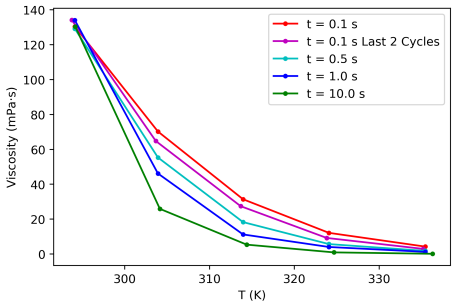

Figure 5.23. Plotting the fitted viscosity values for all pulse lengths of sensor type 1 for the temperature regime between 293 K to 333 K.

The reason that the viscosity at 20°C (293 K) is almost the same value for all pulse lengths is due to the estimation of c_0. For the pulse lengths of 0.1 s and 10.0 s the viscosity at 20°C was set to 130.41 mPa s and 130.40 mPa s, respectively, while for the pulse lengths of 0.5 s the viscosity is 129.17 mPa s and for 1.0 s as well as the last two cycles of 0.1 s the viscosity yields 134.07 mPa s and 134.18 mPa s, respectively. In the temperature regime of 20°C to 60°C (293 K to 333 K) the viscosity is always higher for shorter pulse lengths. The values for the last cycles of pulse length 0.1 s are also slightly below the data for the two cycles at the beginning of the measurements. This behavior differs for temperatures below 20°C, where the viscosities for the pulse lengths of 10.0 s is always higher than for the others. However, there is no consistent trend observable. The same behavior is found for sensor types 2 and 3. Figures 5.24 to 5.26 display the viscosity data for sensor type 2 in the three temperature regimes. c_0 was again chosen to result in a reasonable viscosity value at 20°C (293 K). For sensor type 2, this value ranges between 68.07 mPa s for a pulse length of 0.1 s and 58.69 mPa s for a pulse length of 10.0 s. The viscosity values for the pulse length of 0.1 s lie generally above the data for the longer pulse lengths in the temperature range of 20°C to 60°C (293 K to 333 K) and differ significantly (see figure 5.26). In the temperature regime below 20°C the viscosity data for the longer pulse lengths are always higher than for the shorter ones.
While the viscosity data for sensor type 1 at -20°C (253 K) is also quite similar for all pulse lengths and ranges from 4,591.9 mPa s to 4,753.6 mPa s for 0.5 s to 4,463.9 mPa s for 1.0 s and 4,438.8 mPa s for 10.0 s, the viscosity values of sensor type 2 at this temperature vary significantly from each other and increase with increasing pulse lengths. They range from 6,589.5 mPa s for 0.1 s to 13,574.9 mPa s for 0.5 s to 28,816.4 mPa s for 1.0 s and 56,634.1 mPa s for 10.0 s.

For sensor type 3 the values of c_0 were also adjusted to obtain similar viscosity values at 20°C (293 K). At a pulse length of 0.1 s and 0.5 s the viscosity was set to 55.47 mPa s and 55.39 mPa s, respectively, while at the pulse lengths of of 1.0 s and 10.0 s the viscosity yields 51.76 mPa s and 48.76 mPa s, respectively. Again, for the temperature regime of 20°C to 60°C (293 K to 333 K) the viscosity was always lower for longer pulse lengths. Below 20°C this trend was partly continued, especially for the pulse length of 10.0 s (see figure 5.28). Similar as for sensor type 2, the viscosity at -20°C (253 K) varies significantly for the different pulse lengths. However, for sensor type 3 the highest viscosity at this temperature was reached for the pulse lengths of 1.0 s, while for sensor type 2 the the viscosity increased strictly with increasing pulse length. The viscosity at this temperature for the pulse lengths of 0.1 s, 0.5 s and 10.0 s are 597.4 mPa s, 1,271.0 mPa s and 3,312.3 mPa s, respectively, while for the pulse length of 1.0 s the viscosity yields 5,828.9 mPa s.

The presented results indicate a dependency of viscosity and pulse length, which is physically not reasonable, since the viscosity is a material property that only depends on temperature (see

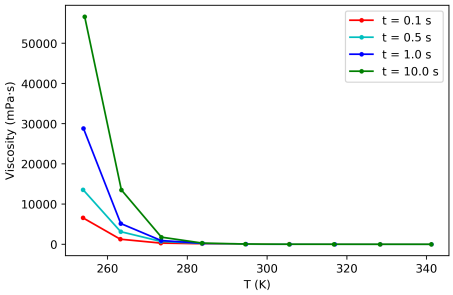

Figure 5.24. Plotting the fitted viscosity values for all pulse lengths of sensor type 2 over the entire temperature range from 253 K to 333 K.

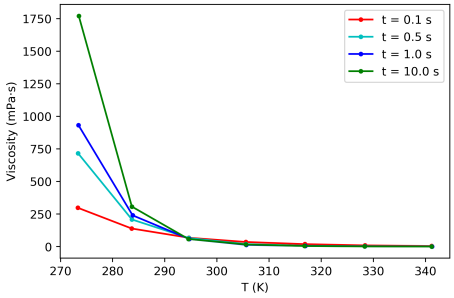

Figure 5.25. Plotting the fitted viscosity values for all pulse lengths of sensor type 2 for the temperature regime between 273 K to 333 K.

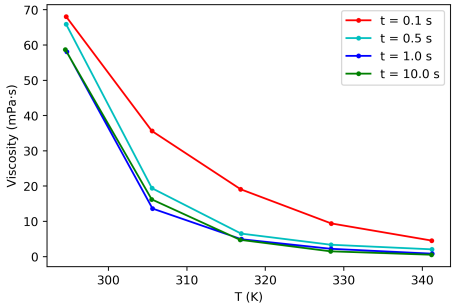

Figure 5.26. Plotting the fitted viscosity values for all pulse lengths of sensor type 2 for the temperature regime between 293 K to 333 K.

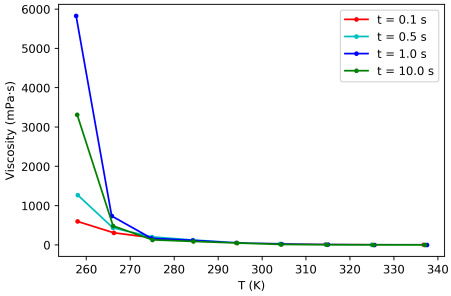

Figure 5.27. Plotting the fitted viscosity values for all pulse lengths of sensor type 3 over the entire temperature range from 253 K to 333 K.

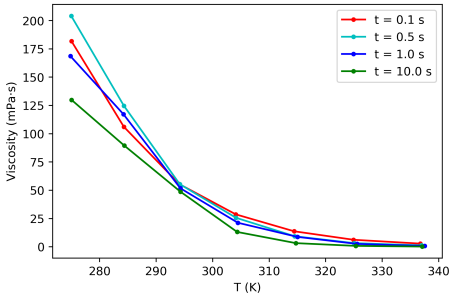

Figure 5.28. Plotting the fitted viscosity values for all pulse lengths of sensor type 3 for the temperature regime between 273 K to 333 K.

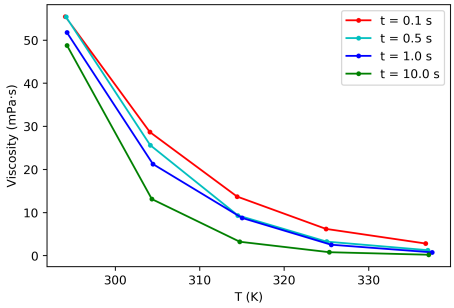

Figure 5.29. Plotting the fitted viscosity values for all pulse lengths of sensor type 3 for the temperature regime between 293 K to 333 K.

equation 2.15). However, considering Term 2 of equation 5.10 shows the relation of current with pulse length and viscosity.

$$i \sim \sqrt{\frac{1}{t} \cdot \frac{T}{\eta}} \tag{5.11}$$

where t is the pulse length, T the absolute temperature and η the viscosity. Since $\sqrt{\frac{T}{\eta}}$ should be a constant value at any given temperature, the variation in the above presented data is induced only by pulse length.
Contemplating the data at the lowest (253 K/-20°C) and the highest (333 K/60°C) temperature, the behavior of sensor type 1 is described quite well with equation 5.9. Using the data of the last cycles at a pulse length of 0.1 s, the fitted viscosity at -20°C (253 K) yields for (4,562.1 ± 124.9) mPa s. At 60°C (333 K) the fitted viscosity ranges from 4.27 mPa s to 0.15 mPa s for the pulse lengths of 0.1 s to 10.0 s, respectively, and decreases strictly with increasing pulse length. However, between the lowest and highest temperature the fitted viscosity for the different pulse length deviate strongly from each other for some temperatures. Especially, at 263 K (-10°C) and 273 K (0°C) the values for the pulse lengths of 1.0 s and 10.0 s differ significantly, while the data at 0.1 s and 0.5 s fit quite well at these temperatures. The neglected effects that are induced by the porous UV-matrix as well as the ones taking place at the EDL, which are not included into equation 5.9 might explain these inconsistencies.
For the sensor types 2 and 3 the same trend is found at 60°C (333 K) and the viscosity ranges from 4.55 mPa s to 0.53 mPa s and from 2.82 mPa s to 0.22 mPa s, respectively. However, at -20°C (253 K) the viscosity increases with increasing pulse length, although for sensor type 3 this trend is not completely consistent (see table 5.8). Considering the presented relation of current, pulse length and viscosity in equation 5.11, the pulse lengths has a stronger influence in the behavior of these sensor types compared to sensor type 1. This might be due to the presence of an additional redox species in the sensitive layer of sensor type 1, i.e. methylene blue or the fact that in sensor types 2 and 3 **IL 2** acts as solvent and redox species at the same time.

5.2.3 Using Arrhenius to Analyze the Fitted Viscosity Data

In a next step, the fitted viscosity values were analyzed in the same way the measured viscosity data was, as shown in chapter 5.1, using Arrhenius. It can be seen that the fitted viscosity data behaves accordingly. Using Arrhenius to determine the material constant η_∞ and the activation energy E_A for each pulse length (0.1 s, 0.5 s, 1.0 s and 10.0 s) of the three sensors shows on the one side a good agreement with Arrhenius over the entire temperature range, on the other side, however, the values of η_∞ and E_A differ significantly compared to the measured viscosity data. Especially the values of η_∞ decreased by several orders of magnitude, while E_A increased by a factor two to three. Again, this indicates that the developed model (equation 5.9) is neglecting the electrochemical processes taking place at the EDL as well as the impeded diffusion of the redox molecules towards the electrodes due to the porous UV-matrix. Furthermore, the observed supercooling effect discussed in chapter 4.4 as well as the electrode geometry are neglected.
Arrhenius can also be used to investigate the influence of c_0. As described before, the value of c_0 needed to be adjusted or guessed for sensor type 1 or 2 and 3, respectively, in order to obtain reasonable viscosity data. Furthermore, the concentration was also adjusted for the different pulse lengths since the viscosity at a certain temperature would increase with increasing pulse length with constant c_0. This also takes into account that with increasing pulse length the depletion zone at the electrode increases and therefore the concentration of redox molecules decreases. Additionally, the obstruction due to the porous UV-matrix might influence the concentration

Table 5.8. Comparison of recorded current data (average of heating and cooling over 2 cycles) with fitted viscosity data for all three sensor types at all pulse lengths showing the respective value for the lowest (253 K) and highest (333 K) temperature.

Pulse Length (s)	$i_{\text{meas.}}$ (μA)		η_{fit} (mPa s)	
Sensor Type 1	**T = 253 K**	**T = 333 K**	**T = 253 K**	**T = 333 K**
0.1	$3.19 \cdot 10^{-3}$	$7.00 \cdot 10^{-2}$	1,579.6	4.27
0.1 (last)	$1.05 \cdot 10^{-3}$	$4.73 \cdot 10^{-2}$	4,591.9	2.96
0.5	$0.58 \cdot 10^{-3}$	$3.41 \cdot 10^{-2}$	4,753.6	1.82
1.0	$5.59 \cdot 10^{-5}$	$3.83 \cdot 10^{-3}$	4,463.9	1.26
10.0	$1.40 \cdot 10^{-5}$	$2.84 \cdot 10^{-3}$	4,438.8	0.15
Sensor Type 2				
0.1	$8.69 \cdot 10^{-2}$	3.84	6,589.5	4.55
0.5	$4.29 \cdot 10^{-2}$	4.04	13,574.9	2.06
1.0	$7.39 \cdot 10^{-3}$	1.60	28,816.4	0.84
10.0	$1.67 \cdot 10^{-3}$	0.64	56,634.1	0.53
Sensor Type 3				
0.1	$6.51 \cdot 10^{-3}$	$1.08 \cdot 10^{-1}$	597.4	2.82
0.5	$1.00 \cdot 10^{-3}$	$3.61 \cdot 10^{-2}$	1,271.0	1.28
1.0	$0.15 \cdot 10^{-3}$	$1.51 \cdot 10^{-2}$	5,828.9	0.77
10.0	$3.48 \cdot 10^{-5}$	$5.05 \cdot 10^{-3}$	3,312.3	0.22

of the "bulk". Table 5.9 shows the chosen concentrations c_0 for the three sensor types at the different pulse lengths.

Table 5.9. c_0 for the three sensor types at the four pulse lengths used to fit the viscosity according to equation 5.9.

Pulse Length (s)	**Sensor Type 1** c_0 (mol m^{-3})	**Sensor Type 2** c_0 (mol m^{-3})	**Sensor Type 3** c_0 (mol m^{-3})
0.1	$10^{2.40}$	$10^{4.45}$	$10^{2.80}$
0.1 (last)	$10^{2.15}$	-	-
0.5	$10^{2.25}$	$10^{4.65}$	$10^{2.50}$
1.0	$10^{1.37}$	$10^{4.20}$	$10^{2.16}$
10.0	$10^{1.267}$	$10^{4.20}$	$10^{1.90}$

In case the chosen concentration c_0 would influence not only the fitted viscosity at a certain temperature, but also the validity of the model, it is expected that the results for E_A and η_∞ would differ depending on the input data (fitted viscosity data) to the Arrhenius fit. Table 5.10 represents the fitted viscosity data for Sensor type 1 at a pulse length of 0.1 s for $c_0 = 400$ mol m^{-3} and $c_0 = 10^{2.4}$ mol m^{-3}. As can be seen the values of E_A and η_∞ as well as r^2 are almost the same for the different concentrations.

This leads to the conclusion that the estimated guess for c_0 is at this point sufficient.
Since the fitted viscosity was determined over the entire temperature range, but shows a inconsistent behavior over this range, the Arrhenius analysis was also done for three temperature regimes: 20°C to 60°C (293 K to 333 K), 0°C to 60°C (273 K to 333 K) and -20°C to 60°C (253 K to 333 K). The obtained values for η_∞ and E_A as well as r^2 are shown for the Arrhenius plot and the linear regression in table 5.11. The best r^2 values are marked in green for better recognition. Additionally, the Arrhenius plot and linear regression are shown exemplarily for

Table 5.10. Fitted viscosity data with resulting E_A and η_∞ for Sensor type 1 at 0.1 s for two concentrations: $c_0 = 400$ mol m^{-3} and $c_0 = 10^{2.4}$ mol m^{-3}.

		Arrhenius			**Linear Regression**		
	$c_0 = 400$ mol m^{-3}						
T (K)	η_{fit} (mPa s)	E_A (J mol^{-1})	η_∞ (mPa s)	r^2	E_A (J mol^{-1})	η_∞ (mPa s)	r^2
294.1	330.7						
303.9	178.1						
314.0	79.65	$-5.483 \cdot 10^4$	$6.125 \cdot 10^{-8}$	0.99280	$-6.842 \cdot 10^4$	$2.779 \cdot 10^{-10}$	0.98734
324.1	30.80						
335.4	10.83						
	$c_0 = 10^{2.4}$ mol m^{-3}						
T (K)	η_{fit} (mPa s)	E_A (J mol^{-1})	η_∞ (mPa s)	r^2	E_A (J mol^{-1})	η_∞ (mPa s)	r^2
294.1	130.4						
303.9	70.25						
314.0	31.41	$-5.483 \cdot 10^4$	$2.417 \cdot 10^{-8}$	0.99280	$-6.841 \cdot 10^4$	$1.096 \cdot 10^{-10}$	0.98734
324.1	12.15						
335.4	4.271						

the pulse length of 0.1 s in the temperature range of 0°C to 60°C (273 K to 333 K) in figures 5.30 and 5.31.

Table 5.11. η_∞ and E_A for all pulse lengths of sensor type 1 for three temperature regimes.

	Arrhenius			**Linear Regression**		
T (K)	E_A (J mol^{-1})	η_∞ (mPa s)	**r**^{2}	E_A (J mol^{-1})	η_∞ (mPa s)	**r**^{2}
0.1 s						
293 - 333	$-5.483 \cdot 10^4$	$2.417 \cdot 10^{-8}$	0.99280	$-6.841 \cdot 10^4$	$1.096 \cdot 10^{-10}$	0.98734
273 - 333	$-6.554 \cdot 10^4$	$3.178 \cdot 10^{-10}$	0.99958	$-6.594 \cdot 10^4$	$2.781 \cdot 10^{-10}$	0.99473
253 - 333	$-3.068 \cdot 10^4$	$1.088 \cdot 10^{-3}$	0.90624	$-5.580 \cdot 10^4$	$8.769 \cdot 10^{-9}$	0.97138
0.5 s						
293 - 333	$-7.079 \cdot 10^4$	$3.482 \cdot 10^{-11}$	0.99653	$-8.605 \cdot 10^4$	$7.645 \cdot 10^{-14}$	0.99467
273 - 333	$-5.957 \cdot 10^4$	$3.021 \cdot 10^{-9}$	0.99933	$-7.441 \cdot 10^4$	$6.328 \cdot 10^{-12}$	0.98567
253 - 333	$-7.282 \cdot 10^4$	$8.148 \cdot 10^{-12}$	0.99832	$-6.842 \cdot 10^4$	$3.560 \cdot 10^{-11}$	0.98950
1.0 s						
293 - 333	$-8.576 \cdot 10^4$	$7.906 \cdot 10^{-14}$	0.99829	$-9.391 \cdot 10^4$	$2.035 \cdot 10^{-15}$	0.99799
273 - 333	$-3.833 \cdot 10^4$	$1.836 \cdot 10^{-5}$	0.93759	$-7.447 \cdot 10^4$	$4.567 \cdot 10^{-12}$	0.95819
253 - 333	$-1.222 \cdot 10^5$	$6.862 \cdot 10^{-22}$	0.99215	$-6.711 \cdot 10^4$	$4.353 \cdot 10^{-11}$	0.96324
10.0 s						
293 - 333	$-1.207 \cdot 10^5$	$4.867 \cdot 10^{-20}$	0.99999	$-1.318 \cdot 10^5$	$5.665 \cdot 10^{-22}$	0.99800
273 - 333	$-6.756 \cdot 10^4$	$2.307 \cdot 10^{-10}$	0.98652	$-1.184 \cdot 10^5$	$9{,}189 \cdot 10^{-20}$	0.98791
253 - 333	$-3.845 \cdot 10^4$	$6.956 \cdot 10^{-5}$	0.97894	$-9.348 \cdot 10^4$	$6.248 \cdot 10^{-16}$	0.94819

The r^2 values displayed in table 5.11 show that the temperature range for the best fit of Arrhenius and the linear regression varies for the four pulse lengths. Especially for the longer pulse

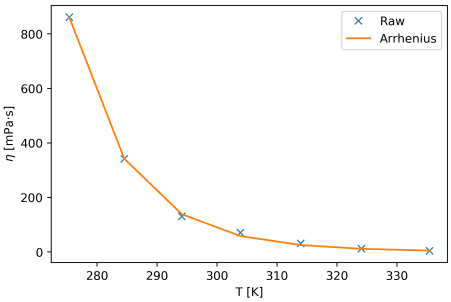

Figure 5.30. Plotting the Arrhenius equation ($\eta = \eta_\infty \cdot \exp(-E_A/RT)$) onto the measured viscosity data of sensor type 1, η_∞ and E_A can also be determined; $\eta_\infty = 3.17 \cdot 10^{-10}$ mPa s, E_A = -6.55372 $\cdot 10^4$ J mol^{-1} ($r^2 > 0.9996$).

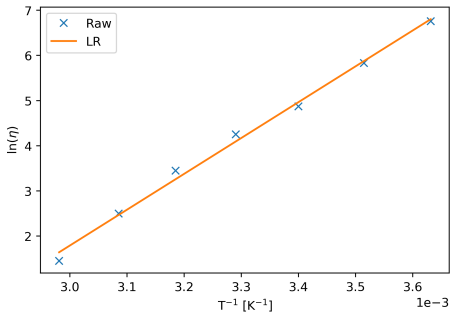

Figure 5.31. ln(η) vs. T^{-1} plot for the fitted viscosity of sensor type 1. It shows a good linear correlation ($r^2 > 0.9947$). Using the linear equation, η_∞ and E_A can be determined; $\eta_\infty = 2.78 \cdot 10^{-10}$ mPa s, E_A = -6.45140$\cdot 10^4$ J mol^{-1}.

lengths of 1.0 s and 10.0 s the fits for the temperature regime of 20°C to 60°C (293 K tot 333 K) yield a significantly higher r^2 value compared to the other two regimes. For the pulse length of 0.5 s the results differ for the Arrhenius plot and the linear regression. The Arrhenius plot shows for the regime of 0°C to 60°C (273 K to 333 K) a higher r^2 value, while the linear regression fits much better for 20°C to 60°C (293 K to 333 K). The pulse length of 0.1 s yields the highest correlation for 0°C to 60°C.

Furthermore, the material constant η_∞ and E_A are independent of the pulse lengths based on the Arrhenius equation. However, the data presented in table 5.11 show something different. The values for E_A and η_∞ increase and decrease with increasing pulse length, respectively, which indicates an influence of the pulse lengths on the results. This is expected, since the results are based on the recorded current data which decrease in absolute numbers with increasing pulse lengths. The average activation energy E_A, considering only the best fits, accounts to (-8.291 $\pm$ 2.39) $\cdot 10^4$ J mol^{-1} using the Arrhenius plot and (-9.640 $\pm$ 2.34) $\cdot 10^4$ J mol^{-1} according to the linear regression. These values are 224 % and 280 % higher than the determined activation energy values of the measured viscosity using a rheometer, respectively. The definition of the activation energy E_A in the context of viscosity is derived from thermodynamics, in which flow of a molecule or a group of them is seen as a local transition between one state (position before flowing) and another state (position after flow occurred) after overcoming an energy barrier. The larger E_A, the harder it is for the ions of the IL to move past each other. This might be due to their physical size as well as the strong intermolecular interactions, e.g. van-der-Waals-forces and H-bonds. [69,189] The significant increase in activation energy of the fitted viscosity values indicate that the flow of the IL molecules towards the electrode is impeded, probably due to the UV matrix which hinders the free flow of the ions additionally to the present intermolecular interactions as well as the electrochemical processes causing the electrochemical double layer at the electrode surface. In general, the data show that the activation energy increases with increasing pulse length, which indicates a secondary dependence on this quantity. On the other hand, the values of η_∞ expresses the viscosity at infinite temperature ($T \rightarrow \infty$) and represent the pure structural contribution of the ions to the viscosity, since the interactions which are present at room temperature are no longer effective at infinite temperature. The decrease of η_∞ by several orders of magnitude compared to the measured viscosity and the literature as well as the large range (between 10^{-9} and 10^{-22} mPa s), even for the best fits, over which the values spread,

indicate that there has to be other effects causing this drastic decrease.
One major effect causing the discrepancies is probably the very small dimensions of the temperature sensor which adds some boundary conditions to the model that are not considered here. The sensitive temperature layer of the sensor only consists of a 2 μl drop of the IL mixture, including the monomers of the UV matrix. Additionally, the dimensions of the temperature sensor were in the μm range, with electrode openings of 80 μm in diameter. This means, the dimensions of the temperature sensor were quite small which has a major impact for the model. In rheological measurements the bulk of the IL can be seen as infinite and equally over the entire measurement setup. For the chronoamperometric measurements the bulk of the IL is not infinite. First, the electrochemical processes taking place at the electrode surface form an electrochemical double layer, which comprises only one or two molecule layers, at which the concentration of the IL differs compared to the rest of the layer. Second, the bulk that comes behind the EDL is not infinite as it is for many other electrochemical setups, because the sensitive temperature layer is quite thin (approx. 130 - 150 μm). Third, the bulk is further restricted due to the porous UV-matrix which limits the diffusion and therefore the movement of the IL molecules. These limitations cause the values of η_∞ to decrease drastically compared to the values determined by the rheological measurements. In other words, the value of η_∞ is mainly determined by the spatial limitations of the sensor geometry which predominates all structural contributions of the ILs. This is supported by the fact that for longer pulse lengths, η_∞ decreases further than for shorter ones.

For the sensor types 2 and 3 the results are quite similar and show the same trends and behavior as described above for sensor type 1. The respective data is shown in tables 5.12 and 5.13.

Table 5.12. η_∞ and E_A for all pulse lengths of sensor type 2 for three temperature regimes.

	Arrhenius			**Linear Regression**		
T (K)	E_A (J mol^{-1})	η_∞ (mPa s)	$\mathbf{r}^2$	E_A (J mol^{-1})	η_∞ (mPa s)	$\mathbf{r}^2$
0.1 s						
293 - 333	$-4.553 \cdot 10^4$	$5.779 \cdot 10^{-7}$	0.99931	$-4.853 \cdot 10^4$	$1.774 \cdot 10^{-7}$	0.99778
273 - 333	$-4.659 \cdot 10^4$	$3.704 \cdot 10^{-7}$	0.99987	$-4.716 \cdot 10^4$	$2.960 \cdot 10^{-7}$	0.99881
253 - 333	$-9.624 \cdot 10^4$	$1.025 \cdot 10^{-16}$	0.99960	$-5.482 \cdot 10^4$	$9.762 \cdot 10^{-9}$	0.97722
0.5 s						
293 - 333	$-8.130 \cdot 10^4$	$2.532 \cdot 10^{-13}$	0.99871	$-6.266 \cdot 10^4$	$4.072 \cdot 10^{-10}$	0.97176
273 - 333	$-7.666 \cdot 10^4$	$1.609 \cdot 10^{-12}$	0.99996	$-6.936 \cdot 10^4$	$3.347 \cdot 10^{-11}$	0.98780
253 - 333	$-8.637 \cdot 10^4$	$2.295 \cdot 10^{-14}$	0.99999	$-7.292 \cdot 10^4$	$4.590 \cdot 10^{-12}$	0.99173
1.0 s						
293 - 333	$-9.503 \cdot 10^4$	$8.301 \cdot 10^{-16}$	0.99845	$-7.443 \cdot 10^4$	$3.087 \cdot 10^{-12}$	0.99097
273 - 333	$-8.511 \cdot 10^4$	$5.143 \cdot 10^{-14}$	0.99993	$-8.123 \cdot 10^4$	$2.441 \cdot 10^{-13}$	0.99414
253 - 333	$-1.021 \cdot 10^5$	$2.902 \cdot 10^{-17}$	0.99999	$-8.483 \cdot 10^4$	$2.990 \cdot 10^{-14}$	0.99464
10.0 s						
293 - 333	$-8.739 \cdot 10^4$	$1.855 \cdot 10^{-14}$	0.99997	$-8.488 \cdot 10^4$	$4.987 \cdot 10^{-14}$	0.99916
273 - 333	$-1.106 \cdot 10^5$	$1.345 \cdot 10^{-18}$	0.99998	$-9.263 \cdot 10^4$	$2.753 \cdot 10^{-15}$	0.99582
253 - 333	$-8.935 \cdot 10^4$	$2.485 \cdot 10^{-14}$	0.99937	$-9.602 \cdot 10^4$	$3.347 \cdot 10^{-16}$	0.99575

Conclusively, the discussed results show that the developed equation 5.9 generally can be used to describe the found behavior of the three sensor types. However, it also can be seen

Table 5.13. η_∞ and E_A for all pulse lengths of sensor type 3 for three temperature regimes.

	Arrhenius			**Linear Regression**		
T (K)	E_A (J mol^{-1})	η_∞ (mPa s)	$\mathbf{r}^2$	E_A (J mol^{-1})	η_∞ (mPa s)	$\mathbf{r}^2$
0.1 s						
293 - 333	-5.283· 10^4	2.312 · 10^{-8}	0.99824	-5.800 · 10^4	2.966· 10^{-9}	0.99752
273 - 333	-4.296 · 10^4	1.275 · 10^{-6}	0.99658	-5.236 · 10^4	2.487 · 10^{-8}	0.99213
253 - 333	-4.218 · 10^4	1.708· 10^{-6}	0.99877	-4.725 · 10^4	1.191 · 10^{-7}	0.99025
0.5 s						
293 - 333	-6.385 · 10^4	2.569· 10^{-10}	0.99636	-7.414 · 10^4	4.220 · 10^{-12}	0.99624
273 - 333	-4.541 · 10^4	4.955 · 10^{-7}	0.98800	-6.470 · 10^4	1.483 · 10^{-10}	0.98456
253 - 333	-6.780 · 10^4	2.368· 10^{-11}	0.99434	-5.947 · 10^4	6.665 · 10^{-10}	0.98805
1.0 s						
293 - 333	-6.737· 10^4	5.706· 10^{-11}	0.99870	-8.076 · 10^4	2.803 · 10^{-13}	0.99074
273 - 333	-4.169 · 10^4	2.101· 10^{-6}	0.97197	-6.736 · 10^4	4.356· 10^{-11}	0.97087
253 - 333	-1.431 · 10^5	5.615· 10^{-26}	0.99928	-5.947 · 10^4	6.665 · 10^{-10}	0.98805
10.0 s						
293 - 333	-9.886· 10^4	1.503· 10^{-16}	0.99987	-1.051 · 10^5	1.143 · 10^{-17}	0.99952
273 - 333	-4.166 · 10^4	1.672 · 10^{-6}	0.96204	8.301 · 10^4	4.638 · 10^{-14}	0.95963
253 - 333	-1.311 · 10^5	9.122· 10^{-24}	0.99870	-7.936 · 10^4	9.482 · 10^{-14}	0.97638

that equation 5.9 does not consider all boundary conditions and restrictions due to the sensor geometry since the resulting values for E_A and η_∞ vary significantly compared to the data found by analyzing rheologically recorded data of the ILs.

6 Summary & Outlook

In this work the development of a flexible and miniaturized temperature sensor based on different temperature sensitive materials was described. First, a sensitive layer composed of barium strontium titanate nanoparticles, that were synthesized by different methods, i.e. flash lamp sintering of BSTO sol-gel, synthesis of BSTO nanoparticles or nanocrystals by several routes, were investigated. All tested routes yielded to be unfeasible due to different reasons. The flash lamp sintering of a BSTO sol-gel did not result in a crystal BSTO layer since the expected peaks in the XRD measurement were not found. For the BSTO nanocrystals, the XRD measurements showed all the expected signals and indicated due to a peak broadening that the measured particles were in the nano-scale. However, literature showed that BSTO particles below a critical size of approx. 30 nm experience the loss of their temperature sensitive abilities. The obtained particles in this work had sizes around 10 nm, which made them not feasible for the indented application. Additionally, a complete coverage of the IDEs was not achieved with the tested suspensions, which would lead to a bad signal-to-noise-ratio in impedance experiments. Due to these results an alternative route using redox molecules dissolved in ionic liquids or pure ionic liquids as redox active species was investigated. Thereby, a relation between the measured current and temperature was obtained by using different measurement techniques, such as cyclic voltammetry and chronoamperometry.
First, a method to fixate the temperature sensitive layer onto a planar electrode system was investigated. Therefore, a mixture of two different monomers and a photoinitiator were added to the IL solution and cured by irradiation of UV light for several seconds causing a polymerization to occur and thereby forming a porous membrane. This membrane allows the redox molecules and IL still to diffuse throughout the layer but at the same time keeps the layer itself fixed upon the electrode surface.
Second, a variety of possible redox molecules were tested with the requirement of being stable over a longer period of time as well as a large number of redox cycles. Since ferrocene is a very prominent and well-known redox molecule, several derivatives were investigated. Unfortunately, all showed a high decomposition rate after the UV irradiation of the UV-matrix and stopped functioning after a few days. Another attempt was done by using a quinone-hydroquinone system, which turned out to be too complicated due to the additional acid-base equilibrium during the oxidation. Finally, methylene blue, also a common redox molecule, was tested and showed a stable behavior after the UV irradiation and several electrochemical measurements.
Although cyclic voltammetry is a sophisticated method to examine the stability and feasibility of different redox species, it is also a quite slow measurement technique and not suitable for the temperature sensor in mind. After improving the sensor itself by the above-mentioned steps, the measurement technique was changed towards chronoamperometry. Therefore, either custom-made electronics were used or a potentiostat, that allowed additionally to investigate the influence of different applied pulse lengths. Furthermore, the design of the sensor was improved from laser ablated, large gold electrodes which were manually passivated to achieve microelectrodes with a size of 50 μm x 500 μm to cleanroom fabricated MEAs with a diameter of 80 μm. Both, the measurement device as well as the sensor geometry showed an impact on the performance of the sensor. Especially the varying in pulse lengths leads to a change in resolution and sensitivity. The adjustment of the sensor geometry, however, shows an impact on the molecular

behavior of the sensitive layer.
In total, three different layer compositions were investigated closely. Sensor type 1 comprises methylene blue dissolved in a mixture of **IL1** and **IL2** as sensitive layer. To improve its sensitivity and resolution a third IL (1-ethylimidazolium nitrate; **IL3**) was tested that functions as redox species as well as solvent simultaneously (sensor type 2). However, this IL is not well known in literature, yet, and it turned out that the freezing point lies probably somewhere around 30°C. Finally, a mixture of **IL3** and **IL2** were examined (sensor type 3), in which the **IL3** still acted as redox molecule and solvent, while **IL2** was added to prevent the freezing of **IL3** and lower its freezing point.
All three sensor types were measured for numerous cycles between -20°C and 70°C with both measurement techniques (custom-made electronics and potentiostat at different pulse lengths) and show the same general behavior, namely a decrease in current with increasing cycle number as well as an decrease in current for increasing pulse lengths. The former was especially observed for the potentiostat measurements and only sensor type 3 showed this behavior for the measurements using the custom-made electronics. The main reason for this behavior is probably due to electrode fouling and electrolyte poisoning, but also some other effects, such as a temperature gradient along the z-axis and a change in the electrochemical double layer at the electrode-IL-interface could be influencing the temperature behavior of the sensors. The sensitivity and resolution for a pulse length of 0.1 s was found to be highest. Additionally, for all three sensor types supercooling effects were found. The supercooling phenomenon is especially visible for the MEA sensors that contain **IL3**. Sensor type 2, which only contains **IL3** and therefore quite small ions, needs time to rearrange the ions within the layer due to the applied potential and develop the ability to form a crystal structure with leads to supercooling effects. In comparison, sensor type 3, which contains a mixture of **IL3** and **IL2** also shows supercooling effects, although shifted along the temperature axis towards higher temperatures. For sensor type 1, which contains quite bulky ions (mixture of **IL1** and **IL2)**, no supercooling effects can be observed for the MEA sensor. This suggests that there is either another effect taking place that is stronger than the supercooling or the large NTf_2^- anion is preventing the formation of a crystal structure. This assumption is drawn due to the fact that the sensor type 1 shows a clear supercooling phenomenon for the laser ablated sensor geometry.
For all three sensor types the same effects were observed, i.e. decrease of current over time, supercooling effects, decrease of current for increasing pulse lengths. In order to understand and explain all of these findings in greater detail more experimental investigations are necessary. This includes an investigation about the performance of the temperature sensor in dependence of the methylene blue concentration within the ionic liquid or a mixture of ionic liquids as well as the general influence of the ion size and ion properties of the used ionic liquid. Since [EIM][NO3] (**IL3**) shows a quite interesting behavior and a good performance over the chosen temperature range using the potentiostat, a detailed characterization of its properties, e.g. melting/freezing point, electrochemical window as well as oxidation and reduction behavior needs to be determined to draw clear conclusions. Moreover, more general aspects need to be considered as already addressed in the previous sections, i.e. the influence of the additional heating due to the applied potential or the presence of a temperature gradient due to the measurement setup. To prevent the influence of other environmental conditions, e.g. the condensation of humidity at lower temperatures, an additional passivation layer should be found and applied on top of the sensitive layer. In addition, simulations of chronoamperometric measurements need to be performed to gain insights into the EDL structure formation as well as the ion behavior within the sensitive layer. Thereby, different electrode sizes, geometries as well as the arrangements and distances of the electrodes need to be investigated. On the other hand, the influence of the ion sizes onto the EDL structure and the occurrence of supercooling effects can give insights into

the function of the sensor and therefore, provide useful aspects for optimization according to various applications. Furthermore, the influence of the UV matrix can be modeled and different monomer concentrations can be investigated.

Bibliography

[1] Mohd Javaid, Abid Haleem, Shanay Rab, Ravi Pratap Singh, and Rajiv Suman. Sensors for daily life: A review. *Sensors International*, 2(July):100121, 2021.

[2] Hasan Hayat, Thomas Griffiths, Desmond Brennan, Richard P Lewis, Michael Barclay, Chris Weirman, Bruce Philip, and Justin R Searle. The state-of-the-art of sensors and environmental monitoring technologies in buildings. *Sensors (Switzerland)*, 19(17), 2019.

[3] Manir Suleiman, G. I. Saidu, M. I. Ilyasu, O. A. Adeboye, and M. Hamza. Ultrasonic Fluid Level Measuring Device. *International Journal of Research in Science*, 1(1):27, 2015.

[4] Eldar Musayev and Sait Eser Karlik. A novel liquid level detection method and its implementation. *Sensors and Actuators, A: Physical*, 109(1-2):21–24, 2003.

[5] C. M.A. Ashruf. Thin flexible pressure sensors. *Sensor Review*, 22(4):322–327, 2002.

[6] Thomas D. McGee. *Principles and Methods of Temperature Measurement*. John Wiley, & Son, Inc., New York, 1988.

[7] Peter R. N. Childs. *Practical Temperature Measurement*. Butterworth-Heinemann, Oxford, UK, 2001.

[8] Ronald Geballe. Note on "A thermometer based on Archimedes' principle," by George D. Nickas [Am. J. Phys. 5 7 , 845–846 (1989)] . *American Journal of Physics*, 59(1):90–90, 1991.

[9] Mattie Bell Fretwell. The Development of the Thermometer. *The Mathematics Teacher*, 30(2):80–83, 1937.

[10] Https://www.capgo.com/Resources/InterestStories/TempHistory/TempHistory.html. A Brief History of Temperature, 2013.

[11] Mark W. Zemansky and Richard H. Dittman. *Heat and Thermodynamics*. McGraw-Hill Companies, Inc., New York, 1997.

[12] Bureau International des Poids et Mesures - History of the SI.

[13] BIPM. BIPM - Resolution 1 of the 26th CGPM, 2006.

[14] Christos Goumopoulos. A high precision, wireless temperature measurement system for pervasive computing applications. *Sensors (Switzerland)*, 18(10), 2018.

[15] Zeeshan Ahmed. Role of quantum technologies in reshaping the future of temperature metrology. *Measurement: Sensors*, 18:2021–2024, 2021.

[16] Tomoyuki Yokota, Yusuke Inouea, Yuki Terakawaa, Jonathan Reedera, Martin Kaltenbrunnera, Taylor Wared, Kejia Yange, Kunihiko Mabuchif, Tomohiro Murakawag, Masaki Sekinoa, Walter Voitc, Tsuyoshi Sekitania, and Takao Someyaa. Ultraflexible, large-area, physiological temperature sensors for multipoint measurements. *Proceedings of the National Academy of Sciences of the United States of America*, 112(47):14533–14538, 2015.

[17] A R Zanatta, D Scoca, and F Alvarez. A suitable (wide-range + linear) temperature sensor based on Tm3+ ions. *Scientific Reports*, 7(1), 2017.

[18] Héctor Rodríguez, Margaret Williams, John S. Wilkes, and Robin D. Rogers. Ionic liquids for liquid-in-glass thermometers. *Green Chemistry*, 10(5):501–507, 2008.

[19] J V Nicholas and D R White. *Traceable Temperatures: An introduction to temperature measurement and calibration, 2nd edn*. John Wiley, & Sons, Inc., 2001.

[20] P. R.N. Childs, J. R. Greenwood, and C. a. Long. Review of temperature measurement. *Review of Scientific Instruments*, 71(8):2959–2978, 2000.

[21] Banqui Wu, John D. Holbrey, Ramana G. Reddy, and Robin D. Rogers. (12) Patent Application Publication (10) Pub . No .: US 2003 / 0124222 A1 Patent Application Publication, 2003.

[22] Ana B. Pereiro, Jose L. Legido, and Ana Rodríguez. Physical properties of ionic liquids based on 1-alkyl-3-methylimidazolium cation and hexafluorophosphate as anion and temperature dependence. *Journal of Chemical Thermodynamics*, 39(8):1168–1175, 2007.

[23] K. A. Kurnia, C. D. Wilfred, and T. Murugesan. Thermophysical properties of hydroxyl ammonium ionic liquids. *Journal of Chemical Thermodynamics*, 41(4):517–521, 2009.

[24] Normawati M. Yunus, M.I. Abdul Mutalib, Zakaria Man, Mohamad Azmi Bustam, and T. Murugesan. Thermophysical properties of 1-alkylpyridinium bis(trifluoromethylsulfonyl)imide ionic liquids. *J. Chem. Thermodynamics*, 42:491–495, 2010.

[25] Https://www.heraeus conamic.com/de/knowlegde base/properties. Thermische Eigenschaften von Quarzglas.

[26] A. J. Moulson and J. M. Herbert. *Electroceramics: Materials,Properties,Applications*. John Wiley, & Sons, Inc., 2nd editio edition, 2003.

[27] M. M. Vijatović, J. D. Bobić, and B. D. Stojanović. History and challenges of barium titanate: Part II. *Science of Sintering*, 40(3):235–244, 2008.

[28] Jun Su and Jun Zhang. Recent development on modification of synthesized barium titanate (BaTiO 3) and polymer/BaTiO 3 dielectric composites. *Journal of Materials Science: Materials in Electronics*, 30(3):1957–1975, 2019.

[29] Rui Hong Liang, Xian Lin Dong, Ying Chen, Fei Cao, and Yong Ling Wang. Effect of various dopants on the tunable and dielectric properties of Ba0.6Sr0.4TiO3 ceramics. *Ceramics International*, 31(8):1097–1101, 2005.

[30] Jong Yoon Ha, Ji Won Choi, Chong Yun Kang, Jin Sang Kim, Seok Jin Yoon, Doo Jin Choi, and Hyun Jai Kim. Improvement of dielectric loss of (Ba,Sr)(Ti,Zr)O3 ferroelectrics for tunable devices. *Journal of the European Ceramic Society*, 27(8-9 SPEC. ISS.):2747–2751, 2007.

[31] Wei Li, Zhijun Xu, Ruiqing Chu, Peng Fu, and Jigong Hao. Sol-gel synthesis and characterization of Ba(1-x)SrxTiO3 ceramics. *Journal of Alloys and Compounds*, 499(2):255–258, 2010.

[32] Hiroaki Matsumoto, Hiroshi Kakibayashi, Yoshihumi Taniguchi, I. Kuan Cheng, Ting Tai Lee, Ching Li Hu, Chun Te Lee, and Masayuki Fujimoto. Characterization of solid-state reaction of barium carbonate and titanium dioxide by spatially resolved electron energy loss spectroscopy. *Journal of the American Ceramic Society*, 96(8):2651–2656, 2013.

[33] Rouholah Ashiri. On the solid-state formation of BaTiO3 nanocrystals from mechanically activated BaCO3 and TiO2 powders: Innovative mechanochemical processing, the mechanism involved, and phase and nanostructure evolutions. *RSC Advances*, 6(21):17138–17150, 2016.

[34] Hiromichi Hayashi, Takashi Nakamura, and Takeo Ebina. In-situ Raman spectroscopy of BaTiO3 particles for tetragonal-cubic transformation. *Journal of Physics and Chemistry of Solids*, 74(7):957–962, 2013.

[35] J. L. Zhang, P. F. Ji, Y. Q. Wu, X. Zhao, Y. Q. Tan, and C. L. Wang. Strong piezoelectricity exhibited by large-grained BaTiO3 ceramics. *Applied Physics Letters*, 104(22), 2014.

[36] Theodor Schneller, Rainer Waser, Marija Kosec, and David Payne. *Chemical Solution Deposition of Functional Oxide Thin Films*. Springer-Verlag Wien, 2013.

[37] Y. Dimitriev, Y. Ivanova, and R. Iordanova. ChemInform Abstract: History of Sol-Gel Science and Technology. *ChemInform*, 40(12):181–192, 2009.

[38] Alain C Pierre. *Introduction to Sol-Gel Processing*. Springer Nature Switzerland AG, 2020.

[39] Robert W. Schwartz, Theodor Schneller, and Rainer Waser. Chemical solution deposition of electronic oxide films. *Comptes Rendus Chimie*, 7(5):433–461, 2004.

[40] Vadim G. Kessler, Gerald I. Spijksma, Gulaim A. Seisenbaeva, Sebastian Håkansson, Dave H.A. Blank, and Henny J.M. Bouwmeester. New insight in the role of modifying ligands in the sol-gel processing of metal alkoxide precursors: A possibility to approach new classes of materials. *Journal of Sol-Gel Science and Technology*, 40(2-3):163–179, 2006.

[41] Helmut Fric and Ulrich Schubert. Amine adducts of titanium tetraalkoxides. *New Journal of Chemistry*, 29(1):232–236, 2005.

[42] T. Kanata, T. Yoshikawa, and K. Kubota. Grain-size effects on dielectric phase transition of BaTiO3 ceramics. *Solid State Communications*, 62(11):765–767, 1987.

[43] J. F. Scott, H. M. Duiker, Paul D. Beale, B. Pouligny, K. Dimmler, M. Parris, D. Butler, and S. Eaton. Properties of ceramic KNO3 thin-film memories. *Physica B+C*, 150(1-2):160–167, 1988.

[44] Takuya Hoshina, Hirofumi Kakemoto, Takaaki Tsurumi, Satoshi Wada, and Masatomo Yashima. Size and temperature induced phase transition behaviors of barium titanate nanoparticles. *Journal of Applied Physics*, 99(5):1–9, 2006.

[45] Satoshi Wada, Aki Yazawa, Takuya Hoshina, Yoshikazu Kameshima, Hirofumi Kakemoto, Takaaki Tsurumi, and Yoshihiro Kuroiwa. Preparation of barium titanate nanoparticle sphere arrays and their dielectric properties. *IEEE Transactions on Ultrasonics, Ferroelectrics, and Frequency Control*, 55(9):1895–1898, 2008.

[46] Zhe Zhao, Vincenzo Buscaglia, Massimo Viviani, Maria Teresa Buscaglia, Liliana Mitoseriu, Andrea Testino, Mats Nygren, Mats Johnsson, and Paolo Nanni. Grain-size effects on the ferroelectric behavior of dense nanocrystalline BaTiO3 ceramics. *Physical Review B - Condensed Matter and Materials Physics*, 70(2), 2004.

[47] Kenji Uchino, Eiji Sadanaga, and Terukiyo Hirose. Dependence of the Crystal Structure on Particle Size in Barium Titanate. *Journal of the American Ceramic Society*, 72(8):1555–1558, 1989.

[48] Sjoerd A. Veldhuis, Wouter J.C. Vijselaar, Tomasz M. Stawski, and Johan E. Ten Elshof. Formation of nanocrystalline barium titanate in benzyl alcohol at room temperature. *Inorganic Chemistry*, 53(24):13188–13196, 2014.

[49] Kornelius Tetzner, Kurt A. Schroder, and Karlheinz Bock. Photonic curing of sol-gel derived HfO2 dielectrics for organic field-effect transistors. *Ceramics International*, 40(10):15753–15761, 2014.

[50] Hyun Jun Hwang, Soo Chul Lim, Kyung Chul Ok, Jin Seong Park, and Hak Sung Kim. Photonic sintering via flash white light combined with deep UV and NIR for SrTiO3 thin film vibration touch panel applications. *Nanotechnology*, 27(50), nov 2016.

[51] Suresh Kumar Garlapati, Julia Susanne Gebauer, Simone Dehm, Michael Bruns, Markus Winterer, Horst Hahn, and Subho Dasgupta. Room-Temperature Processing of Printed Oxide FETs Using Ultraviolet Photonic Curing. *Advanced Electronic Materials*, 3(9), sep 2017.

[52] Andreas Albrecht, Almudena Rivadeneyra, Alaa Abdellah, Paolo Lugli, and José F. Salmerón. Inkjet printing and photonic sintering of silver and copper oxide nanoparticles for ultra-low-cost conductive patterns. *J. Mater. Chem. C*, 4(16):3546–3554, 2016.

[53] P Walden. Über die Molekulargröße und elektrische Leitfähigkeit einiger geschmolzener Salze. *Bulletin de l'Académie Impériale des Sciences de St.-Pétersbourg VI série*, 8(6):405–422, 1914.

[54] John S. Wilkes. A short history of ionic liquids - From molten salts to neoteric solvents. *Green Chemistry*, 4(2):73–80, 2002.

[55] Patricia A. Hunt, Claire R. Ashworth, and Richard P. Matthews. Hydrogen bonding in ionic liquids. *Chemical Society Reviews*, 44(5):1257–1288, 2015.

[56] Robert Hayes, Gregory G. Warr, and Rob Atkin. Structure and Nanostructure in Ionic Liquids. *Chemical Reviews*, 115(13):6357–6426, 2015.

[57] Heiko Niedermeyer, Jason P. Hallett, Ignacio J. Villar-Garcia, Patricia a. Hunt, and Tom Welton. Mixtures of ionic liquids. *Chemical Society Reviews*, 41(23):7780–7802, 2012.

[58] Mario G. Del Pópolo and Gregory A. Voth. On the structure and dynamics of ionic liquids. *Journal of Physical Chemistry B*, 108(5):1744–1752, 2004.

[59] Patricia a. Hunt and Ian R. Gould. Structural Characterization of the 1-Butyl-3-methylimidazolium Chloride Ion Pair Using ab Initio Methods. *The Journal of Physical Chemistry A*, 110(6):2269–2282, feb 2006.

[60] Peter Wasserscheid and Tom Welton. *Ionic Liquids in Synthesis*. Wiley-VCH Verlag GmbH & Co. KGaA, oct 2002.

[61] Sergey a. Katsyuba, Elena E. Zvereva, Ana Vidiš, and Paul J. Dyson. Application of density functional theory and vibrational spectroscopy toward the rational design of ionic liquids. *Journal of Physical Chemistry A*, 111(2):352–370, 2007.

[62] Kenneth M. Dieter, Chester J. Dymek, Norman E. Heimer, John W. Rovang, and John S. Wilkes. Ionic Structure and Interactions in 1-Methyl-3-ethylimidazolium Chloride-AlCl3 Molten Salts. *Journal of the American Chemical Society*, 110(9):2722–2726, 1988.

[63] Kristina Noack, Peter S. Schulz, Natalia Paape, Johannes Kiefer, Peter Wasserscheid, and Alfred Leipertz. The role of the C2 position in interionic interactions of imidazolium based ionic liquids: A vibrational and NMR spectroscopic study. *Physical Chemistry Chemical Physics*, 12(42):14153–14161, 2010.

[64] Natalia V. Plechkova and Kenneth R. Seddon. Applications of ionic liquids in the chemical industry. *Chemical Society Reviews*, 37(1):123–150, 2008.

[65] Koichi Fumino and Ralf Ludwig. Analyzing the interaction energies between cation and anion in ionic liquids: The subtle balance between Coulomb forces and hydrogen bonding. *Journal of Molecular Liquids*, 192(June):94–102, 2014.

[66] Alpha a. Lee, Dominic Vella, Susan Perkin, and Alain Goriely. Are room-temperature ionic liquids dilute electrolytes? *Journal of Physical Chemistry Letters*, 6(1):159–163, 2015.

[67] Gregory Chatel, Jorge F.B. Pereira, Varun Debbeti, Hui Wang, and Robin D. Rogers. Mixing ionic liquids-"simple mixtures" or "double salts"? *Green Chemistry*, 16(4):2051–2083, 2014.

[68] Adrian Racki and Kamil Paduszyński. Recent Advances in the Modeling of Ionic Liquids Using Artificial Neural Networks. *Journal of Chemical Information and Modeling*, 65(7):3161–3175, 2025.

[69] O. O. Okoturo and T. J. VanderNoot. Temperature dependence of viscosity for room temperature ionic liquids. *Journal of Electroanalytical Chemistry*, 568(1-2):167–181, jul 2004.

[70] Mert Atilhan, Johan Jacquemin, David Rooney, Majeda Khraisheh, and Santiago Aparicio. Viscous behavior of imidazolium-based ionic liquids. *Industrial and Engineering Chemistry Research*, 52(47):16774–16785, 2013.

[71] J. Jacquemin, P. Husson, A. A.H. Padua, and V. Majer. Density and viscosity of several pure and water-saturated ionic liquids. *Green Chemistry*, 8(2):172–180, 2006.

[72] Hui Jin, Bernie O'Hare, Jing Dong, Sergei Arzhantsev, Gary A. Baker, James F. Wishart, Alan J. Benesi, and Mark Maroncelli. Physical properties of ionic liquids consisting of the 1-butyl-3- methylimidazolium cation with various anions and the bis(trifluoromethylsulfonyl)imide anion with various cations. *Journal of Physical Chemistry B*, 112(1):81–92, 2008.

[73] Mohammad Hadi Ghatee, Morteza Zare, Fatemeh Moosavi, and Amin Reza Zolghadr. Temperature-dependent density and viscosity of the ionic liquids 1-alkyl-3-methylimidazolium iodides: Experiment and molecular dynamics simulation. *Journal of Chemical and Engineering Data*, 55(9):3084–3088, sep 2010.

[74] Daisuke Tomida, Akibumi Kumagai, Satoshi Kenmochi, Kun Qiao, and Chiaki Yokoyama. Viscosity of 1-hexyl-3-methylimidazolium hexafluorophosphate and 1-octyl-3-methylimidazolium hexafluorophosphate at high pressure. *Journal of Chemical and Engineering Data*, 52(2):577–579, 2007.

[75] Daisuke Tomida, Satoshi Kenmochi, Takao Tsukada, Kun Qiao, Quanxi Bao, and Chiaki Yokoyama. Viscosity and thermal conductivity of 1-hexyl-3-methylimidazolium tetrafluoroborate and 1-Octyl-3-methylimidazolium tetrafluoroborate at pressures up to 20 MPa. *International Journal of Thermophysics*, 33(6):959–969, 2012.

[76] Thomas Rüther, Kenneth R. Harris, Michael D. Horne, Mitsuhiro Kanakubo, Theo Rodopoulos, Jean Pierre Veder, and Lawrence a. Woolf. Transport, electrochemical and thermophysical properties of two N-donor-functionalised ionic liquids. *Chemistry - A European Journal*, 19(52):17733–17744, 2013.

[77] Kenneth R. Harris, Mitsuhiro Kanakubo, Noriaki Tsuchihashi, Kazuyasu Ibuki, and Masakatsu Ueno. Effect of pressure on the transport properties of ionic liquids: 1-alkyl-3-methylimidazolium salts. *Journal of Physical Chemistry B*, 112(32):9830–9840, 2008.

[78] Kenneth R. Harris, Takashi Makino, and Mitsuhiro Kanakubo. Viscosity scaling of the self-diffusion and velocity cross-correlation coefficients of two functionalised ionic liquids and of their non-functionalized analogues. *Physical Chemistry Chemical Physics*, 16(19):9161–9170, 2014.

[79] Alok Rout, Satyabrata Mishra, and Nagarajan Ramanathan. Presence of a Molecular Ligand alters the Solvent Behavior of an Ionic Liquid: A Combined Physicochemical Properties, FTIR Spectroscopy and Dynamic Light Scattering Investigation. *ChemistrySelect*, 8(5), 2023.

[80] Mohammad Ebrahimi, Yaroslav Kobzar, Wojciech Kujawski, and Kateryna Fatyeyeva. New hydroxylammonium-based protic ionic liquids: Influence of cation and anion structure on thermal, viscosity and conductive properties. *Journal of Molecular Liquids*, 401(March):124574, 2024.

[81] Azra Sourjah, Agnieszka Mikus, Craig M. Forsyth, Wladyslaw Wieczorek, Luke A. O'Dell, and Jennifer M. Pringle. Physicochemical Properties of New Ionic Liquids and Plastic Crystal Based on Huckel Anions. *Chemistry - A European Journal*, 31(16), 2025.

[82] Kenneth R. Seddon, Annegret Stark, and María-José Torres. Influence of chloride, water, and organic solvents on the physical properties of ionic liquids. *Pure and Applied Chemistry*, 72(12):2275–2287, jan 2000.

[83] Pierre Bonhôte, Ana Paula Dias, Nicholas Papageorgiou, Kuppuswamy Kalyanasundaram, and Michael Grätzel. Hydrophobic, Highly Conductive Ambient-Temperature Molten Salts. *Inorganic Chemistry*, 35(5):1168–1178, 1996.

[84] Philipp Kölle and Richard Dronskowski. Hydrogen Bonding in the Crystal Structures of the Ionic Liquid Compounds Butyldimethylimidazolium Hydrogen Sulfate, Chloride, and Chloroferrate(II,III). *Inorganic Chemistry*, 43(9):2803–2809, 2004.

[85] Sérgio M. Urahata and Mauro C.C. Ribeiro. Structure of ionic liquids of 1-alkyl-3-methylimidazolium cations: A systematic computer simulation study. *Journal of Chemical Physics*, 120(4):1855–1863, 2004.

[86] Youngseon Shim and Hyung J. Kim. Dielectric relaxation, ion conductivity, solvent rotation, and solvation dynamics in a room-temperature ionic liquid. *Journal of Physical Chemistry B*, 112(35):11028–11038, 2008.

[87] Ioannis Skarmoutsos, Dimitris Dellis, Richard P. Matthews, Tom Welton, and Patricia a. Hunt. Hydrogen bonding in 1-butyl- and 1-ethyl-3-methylimidazolium chloride ionic liquids. *Journal of Physical Chemistry B*, 116(16):4921–4933, 2012.

[88] Stefan Zahn, Martin Brehm, Marc Brüssel, Oldamur Hollóczki, Miriam Kohagen, Sebastian Lehmann, Friedrich Malberg, Alfonso Sanmartin Pensado, Matthias Schöpke, Henry Weber, and Barbara Kirchner. Understanding ionic liquids from theoretical methods. *Journal of Molecular Liquids*, 192:71–76x, 2014.

[89] Nuno Dias, Karina Shimizu, Pedro Morgado, Eduardo J.M. Filipe, José N. Canongia Lopes, and Fabián Vaca Chávez. Charge templates in aromatic plus ionic liquid systems revisited: NMR experiments and molecular dynamics simulations. *Journal of Physical Chemistry B*, 118(21):5772–5780, 2014.

[90] Seiji Tsuzuki, Hiroyuki Tokuda, Kikuko Hayamizu, and Masayoshi Watanabe. Magnitude and directionality of interaction in ion pairs of ionic liquids: Relationship with ionic conductivity. *Journal of Physical Chemistry B*, 109(34):16474–16481, 2005.

[91] Elizabeth a. Turner, Cory C. Pye, and Robert D. Singer. Use of ab initio calculations toward the rational design of room temperature ionic liquids. *Journal of Physical Chemistry A*, 107(13):2277–2288, 2003.

[92] Thorsten Köddermann, Christiane Wertz, Andreas Heintz, and Ralf Ludwig. Ion-pair formation in the ionic liquid 1-ethyl-3-methylimidazolium bis(triflyl)imide as a function of temperature and concentration. *ChemPhysChem*, 7(9):1944–1949, 2006.

[93] Kenta Fujii, Shiro Seki, Shuhei Fukuda, Ryo Kanzaki, Toshiyuki Takamuku, Yasuhiro Umebayashi, and Shin Ichi Ishiguro. Anion conformation of low-viscosity room-temperature ionic liquid 1-ethyl-3-methylimidazolium bis(fluorosulfonyl) imide. *Journal of Physical Chemistry B*, 111(44):12829–12833, 2007.

[94] Nilesh R. Dhumal, Hyung J. Kim, and Johannes Kiefer. Molecular interactions in l-ethyl-3-methylimidazolium acetate ion pair: a density functional study. *Journal of Physical Chemistry A*, 113(38):10397–10404, 2009.

[95] Andrea Mele, Chieu D. Tran, and Silvia H. De Paoli Lacerda. The structure of a room-temperature ionic liquid with and without trace amounts of water: The role of C-H-O

and C-H-F interactions in 1-n-butyl-3-methylimidazolium tetrafluoroborate. *Angewandte Chemie - International Edition*, 42(36):4364–4366, 2003.

[96] Peter B. Hitchcock, Kenneth R. Seddon, and Thomas Welton. Hydrogen-bond acceptor abilities of tetrachlorometalate(II) complexes in ionic liquids. *Journal of the Chemical Society, Dalton Transactions*, -(17):2639–2643, 1993.

[97] Johannes Kiefer, Juergen Fries, and Alfred Leipertz. Experimental vibrational study of imidazolium-based ionic Liquids: Raman and infrared spectra of 1-ethyl-3methylimidazolium bis(trifluoromethylsulfonyl) imide and 1-ethyl-3-methylimidazolium ethylsulfate. *Applied Spectroscopy*, 61(12):1306–1311, 2007.

[98] Joseph Grondin, Jean Claude Lassègues, Dominique Cavagnat, Thierry Buffeteau, Patrik Johansson, and Roman Holomb. Revisited vibrational assignments of imidazolium-based ionic liquids. *Journal of Raman Spectroscopy*, 42(4):733–743, 2011.

[99] Jesse J. Allen, Sage R. Bowser, and Krishnan Damodaran. Molecular interactions in the ionic liquid emim acetate and water binary mixtures probed via NMR spin relaxation and exchange spectroscopy. *Physical Chemistry Chemical Physics*, 16(17):8078–8085, 2014.

[100] Ahmed Elaiwi, Peter B. Hitchcock, Kenneth R. Seddon, Narmatha Srinivasan, Yu May Tan, Thomas Welton, and Jalal a. Zora. Hydrogen bonding in imidazolium salts and its implications for ambient-temperature halogenoaluminate(III) ionic liquids. *Journal of the Chemical Society, Dalton Transactions*, -(21):3467–3472, 1995.

[101] John S. Wilkes and Michael J. Zaworotko. Air and water stable 1-ethyl-3-methylimidazolium based ionic liquids. *Journal of the Chemical Society, Chemical Communications*, -(13):965–967, 1992.

[102] Jairton Dupont, Paulo A. Z. Suarez, Roberto F. De Souza, Robert a. Burrow, and Jean-Pierre Kintzinger. C-H-π Interactions in 1-n-Butyl-3-methylimidazolium Tetraphenylborate Molten Salt: Solid and Solution Structures. *Chemistry - A European Journal*, 6(13):2377–2381, jul 2000.

[103] Christopher Hardacre, S. E.Jane McMath, Mark Nieuwenhuyzen, Daniel T. Bowron, and Alan K. Soper. Liquid structure of 1,3-dimethylimidazolium salts. *Journal of Physics Condensed Matter*, 15(1), 2003.

[104] Christopher Hardacre, John D. Holbrey, S. E.Jane McMath, Daniel T. Bowron, and Alan K. Soper. Structure of molten 1,3-dimethylimidazolium chloride using neutron diffraction. *Journal of Chemical Physics*, 118(1):273–278, 2003.

[105] Alexander Wulf, Ralf Ludwig, Padmanabhan Sasisanker, and Hermann Weingärtner. Molecular reorientation in ionic liquids: A comparative dielectric and magnetic relaxation study. *Chemical Physics Letters*, 439(4-6):323–326, 2007.

[106] Andreas P. Fröba, Peter Wasserscheid, Dirk Gerhard, Heiko Kremer, and Alfred Leipertz. Revealing the influence of the strength of Coulomb interactions on the viscosity and interfacial tension of ionic liquid cosolvent mixtures. *Journal of Physical Chemistry B*, 111(44):12817–12822, 2007.

[107] Vlad R. Vale, Stefan Will, Wolffram Schröer, and Bernd Rathke. The general phase behavior of mixtures of 1-alkyl-3-methylimidazolium bis[(trifluoromethyl)sulfonyl]amide ionic liquids with n-alkyl alcohols. *ChemPhysChem*, 13(7):1860–1867, 2012.

[108] Thomas Sonnleitner, David A Turton, Stefan Waselikowski, Johannes Hunger, Alexander Stoppa, Markus Walther, Klaas Wynne, and Richard Buchner. Dynamics of RTILs : a comparative dielectric and OKE study. *Journal of Molecular Liquids*, 192:19–25, 2014.

[109] Stephen Tait and Robert A. Osteryoung. Infrared study of ambient-temperature chloroaluminates as a function of melt acidity. *Inorganic Chemistry*, 23(25):4352–4360, 1984.

[110] Ala'a K. Abdul-Sada, Anthony M. Greenway, Peter B. Hitchcock, Thamer J. Mohammed, Kenneth R. Seddon, and Jalal a. Zora. Upon the structure of room temperature halogenoaluminate ionic liquids. *Journal of the Chemical Society, Chemical Communications*, -(24):1753–1754, 1986.

[111] Kenneth R Seddon, Annegret Stark, and María-José Torres. Viscosity and Density of 1-Alkyl-3-methylimidazolium Ionic Liquids. In *ACS Symposium Series*, volume 819, pages 34–49. American Chemical Society, may 2002.

[112] Hugo F.D. Almeida, José N.Canongia Lopes, Luís P.N. Rebelo, João A.P. Coutinho, Mara G. Freire, and Isabel M. Marrucho. Densities and viscosities of mixtures of two ionic liquids containing a common cation. *Journal of Chemical and Engineering Data*, 61(8):2828–2843, 2016.

[113] Catarina M.S.S. Neves, Kiki Adi Kurnia, João A.P. Coutinho, Isabel M. Marrucho, José N.Canongia Lopes, Mara G. Freire, and Luís Paulo N. Rebelo. Systematic study of the thermophysical properties of imidazolium-based ionic liquids with cyano-functionalized anions. *Journal of Physical Chemistry B*, 117(35):10271–10283, 2013.

[114] Nicole S.M. Vieira, Isabel Vázquez-Fernández, João M.M. Araújo, Natalia V. Plechkova, Kenneth R. Seddon, Luís P.N. Rebelo, and Ana B. Pereiro. Physicochemical Characterization of Ionic Liquid Binary Mixtures Containing 1-Butyl-3-methylimidazolium as the Common Cation †. *Journal of Chemical and Engineering Data*, 64(11):4891–4903, 2019.

[115] Kenneth R. Harris, Lawrence A. Woolf, and Mitsuhiro Kanakubo. Temperature and pressure dependence of the viscosity of the ionic liquid 1-butyl-3-methylimidazolium hexafluorophosphate. *Journal of Chemical and Engineering Data*, 50(5):1777–1782, 2005.

[116] C. S.G.P. Queirós, X. Paredes, T. F.S. Avelino, D. E.N. Bastos, M. Ferreira, F. J.V. Santos, A. F. Santos, M. L.M. Lopes, M. J.V. Lourenço, H. Pereira, and C. A. Nieto de Castro. The influence of water on the thermophysical properties of 1-ethyl-3-methylimidazolium acetate. *Journal of Molecular Liquids*, 297:111925, 2020.

[117] Hugo F.D. Almeida, José N.Canongia Lopes, Luís P.N. Rebelo, João A.P. Coutinho, Mara G. Freire, and Isabel M. Marrucho. Densities and viscosities of mixtures of two ionic liquids containing a common cation. *Journal of Chemical and Engineering Data*, 61(8):2828–2843, 2016.

[118] Thomas Koller, Michael H. Rausch, Peter S. Schulz, Markus Berger, Peter Wasserscheid, Ioannis G. Economou, Alfred Leipertz, and Andreas P. Fröba. Viscosity, interfacial tension, self-diffusion coefficient, density, and refractive index of the ionic liquid 1-ethyl-3-methylimidazolium tetracyanoborate as a function of temperature at atmospheric pressure. *Journal of Chemical and Engineering Data*, 57(3):828–835, 2012.

[119] C. Kolbeck, J. Lehmann, K. R.J. Lovelock, T. Cremer, N. Paape, P. Wasserscheid, a. P. Fröba, F. Maier, and H. P. Steinrück. Density and surface tension of ionic liquids. *Journal of Physical Chemistry B*, 114(51):17025–17036, 2010.

[120] Benjamin Hasse, Julia Lehmann, Daniel Assenbaum, Peter Wasserscheid, Alfred Leipertz, and Andreas Paul Fröba. Viscosity, interfacial tension, density, and refractive index of ionic liquids [EMIM][MeSO3], [EMIM][MeOHPO2], [EMIM][OcSO4], and [BBIM][NTf2] in dependence on temperature at atmospheric pressure. *Journal of Chemical and Engineering Data*, 54(9):2576–2583, 2009.

[121] Monika Geppert-Rybczyńska, Jochen K Lehmann, and Andreas Heintz. Physicochemical properties of two 1-alkyl-1-methylpyrrolidinium bis[(trifluoromethyl)sulfonyl]imide ionic liquids and of binary mixtures of 1-butyl-1-methylpyrrolidinium bis[(trifluoromethyl)sulfonyl]imide with methanol or acetonitrile. *Journal of Chemical Thermodynamics*, 71:171–181, 2014.

[122] Hugo F.D. Almeida, Helena Passos, José A. Lopes-Da-Silva, Ana M. Fernandes, Mara G. Freire, and João A.P. Coutinho. Thermophysical properties of five acetate-based ionic liquids. *Journal of Chemical and Engineering Data*, 57(11):3005–3013, 2012.

[123] Lara M. Galán Sánchez, Josep Ribé Espel, Ferdy Onink, G. Wytze Meindersma, and André B. De Haan. Density, viscosity, and surface tension of synthesis grade imidazolium,pyridinium, and pyrrolidinium based room temperature ionic liquids. *Journal of Chemical and Engineering Data*, 54(10):2803–2812, 2009.

[124] Andreas P. Fröba, Heiko Kremer, and Alfred Leipertz. Density, refractive index, interfacial tension, and viscosity of ionic liquids [EMIM][EtSO4], [EMIM][NTf2], [EMIM][N(CN) 2], and [OMA][NTf2] in dependence on temperature at atmospheric pressure. *Journal of Physical Chemistry B*, 112(39):12420–12430, 2008.

[125] Alexander Stoppa, Oliver Zech, Werner Kunz, and Richard Buchner. The conductivity of imidazolium-based ionic liquids from (-35 to 195) °c. A. variation of cations alkyl chain. *Journal of Chemical and Engineering Data*, 55(5):1768–1773, 2010.

[126] Hiroyuki Tokuda, Seiji Tsuzuki, Md Abu Bin Hasan Susan, Kikuko Hayamizu, and Masayoshi Watanabe. How ionic are room-temperature ionic liquids? An indicator of the physicochemical properties. *Journal of Physical Chemistry B*, 110(39):19593–19600, 2006.

[127] Yukihiro Yoshida, Osamu Baba, Carlos Larriba, and Gunzi Saito. Imidazolium-based ionic liquids formed with dicyanamide anion: Influence of cationic structure on ionic conductivity. *Journal of Physical Chemistry B*, 111(42):12204–12210, 2007.

[128] Maciej Galiński, Andrzej Lewandowski, and Izabela Stepniak. Ionic liquids as electrolytes. *Electrochimica Acta*, 51(26):5567–5580, 2006.

[129] Akihiro Noda, Kikuko Hayamizu, and Masayoshi Watanabe. Pulsed-gradient spin-echo 1H and 19F NMR ionic diffusion coefficient, viscosity, and ionic conductivity of non-chloroaluminate room-temperature ionic liquids. *Journal of Physical Chemistry B*, 105(20):4603–4610, 2001.

[130] Christian Schreiner, Sandra Zugmann, Robert Hartl, and Heiner J. Gores. Fractional walden rule for ionic liquids: Examples from recent measurements and a critique of the so-called ideal KCl line for the walden plot. *Journal of Chemical and Engineering Data*, 55(5):1784–1788, 2010.

[131] Kenneth R. Harris. Relations between the fractional stokes-einstein and Nernst-Einstein equations and velocity correlation coefficients in ionic liquids and molten salts. *Journal of Physical Chemistry B*, 114(29):9572–9577, 2010.

[132] Kenneth R. Harris. Can the transport properties of molten salts and ionic liquids be used to determine ion association? *Journal of Physical Chemistry B*, 120(47):12135–12147, 2016.

[133] Norikazu Ohtori, Yuta Kondo, Kenta Shintani, Tomohiro Murakami, Tamio Nobuta, and Yoshiki Ishii. The stokes-einstein relation for non-spherical molecular liquids. *Chemistry Letters*, 49(4):379–382, 2020.

[134] William Sutherland. LXXV. A dynamical theory of diffusion for non-electrolytes and the molecular mass of albumin. *The London, Edinburgh, and Dublin Philosophical Magazine and Journal of Science*, 9(54):781–785, 1905.

[135] Mikhail A. Vorotyntsev, Veronika A. Zinovyeva, and Michel Picquet. Diffusional transport in ionic liquids: Stokes-Einstein relation or "sliding sphere" model? Ferrocene (Fc) in imidazolium liquids. *Electrochimica Acta*, 55(18):5063–5070, 2010.

[136] Kenneth R. Harris. The fractional Stokes-Einstein equation: Application to Lennard-Jones, molecular, and ionic liquids. *Journal of Chemical Physics*, 131(5), 2009.

[137] Hiroyuki Tokuda, Kikuko Hayamizu, Kunikazu Ishii, Md Abu Bin Hasan Susan, and Masayoshi Watanabe. Physicochemical properties and structures of room temperature ionic liquids. 1. Variation of anionic species. *Journal of Physical Chemistry B*, 108(42):16593–16600, 2004.

[138] Kenneth R. Harris. Scaling the transport properties of molecular and ionic liquids. *Journal of Molecular Liquids*, 222:520–534, 2016.

[139] Mitsuhiro Kanakubo, Kenneth R. Harris, Noriaki Tsuchihashi, Kazuyasu Ibuki, and Masakatsu Ueno. Effect of pressure on transport properties of the ionic liquid 1-butyl-3-methylimidazolium hexafluorophosphate. *Journal of Physical Chemistry B*, 111(8):2062–2069, 2007.

[140] Oliver Zech, Alexander Stoppa, Richard Buchner, and Werner Kunz. The conductivity of imidazolium-based ionic liquids from (248 to 468) K. B. variation of the anion. *Journal of Chemical and Engineering Data*, 55(5):1774–1778, 2010.

[141] Philippe Hapiot and Corinne Lagrost. Electrochemical reactivity in room-temperature ionic liquids. *Chemical Reviews*, 108(7):2238–2264, 2008.

[142] H. Helmholtz. Studien über elektrische Grenzschichten. *Annalen der Physik und Chemie*, 7:22, 1879.

[143] M. Gouy. Sur la constitution de la charge électrique à la surface d'un électrolyte. *Journal de Physique Théorique et Appliquée*, 9(1):457–468, 1910.

[144] David Leonard Chapman. LI. A contribution to the theory of electrocapillarity . *The London, Edinburgh, and Dublin Philosophical Magazine and Journal of Science*, 25(148):475–481, 1913.

[145] Otto Stern. Zur Theorie der elektrolytischen Doppelschicht. *Berichte der Bunsengesellschaft für physikalische Chemie*, 30(21-22):508–516, 1924.

[146] Keith B. Oldham. A Gouy-Chapman-Stern model of the double layer at a (metal)/(ionic liquid) interface. *Journal of Electroanalytical Chemistry*, 613(2):131–138, 2008.

[147] Hainan Wang and Laurent Pilon. Accurate simulations of electric double layer capacitance of ultramicroelectrodes. *Journal of Physical Chemistry C*, 115(33):16711–16719, 2011.

[148] Eliezer Gileadi. *Physical Electrochemistry: Fundamentals, Techniques and Applications*. Wiley-VCH Verlag GmbH & Co. KGaA, Weinheim, 2011.

[149] Marisa C. Buzzeo, Russell G. Evans, and Richard G. Compton. Non-haloaluminate room-temperature ionic liquids in electrochemistry - A review. *ChemPhysChem*, 5(8):1106–1120, 2004.

[150] C. Nanjundiah, S. F. McDevitt, and V. R. Koch. Differential Capacitance Measurements in Solvent-Free Ionic Liquids at Hg and C Interfaces. *Journal of The Electrochemical Society*, 144(10):3392–3397, 1997.

[151] Alexei A. Kornyshev. Double-layer in ionic liquids: Paradigm change? *Journal of Physical Chemistry B*, 111(20):5545–5557, 2007.

[152] Maxim V. Fedorov and Alexei A. Kornyshev. Towards understanding the structure and capacitance of electrical double layer in ionic liquids. *Electrochimica Acta*, 53(23):6835–6840, 2008.

[153] Maxim V. Fedorov and Alexei A. Kornyshev. Ionic liquid near a charged wall: Structure and capacitance of electrical double layer. *Journal of Physical Chemistry B*, 112(38):11868–11872, 2008.

[154] M. V. Fedorov, N. Georgi, and A. A. Kornyshev. Double layer in ionic liquids: The nature of the camel shape of capacitance. *Electrochemistry Communications*, 12(2):296–299, 2010.

[155] N. Georgi, A. A. Kornyshev, and M. V. Fedorov. The anatomy of the double layer and capacitance in ionic liquids with anisotropic ions: Electrostriction vs. lattice saturation. *Journal of Electroanalytical Chemistry*, 649:261–267, 2010.

[156] Ming Chen, Zachary A.H. Goodwin, Guang Feng, and Alexei A. Kornyshev. On the temperature dependence of the double layer capacitance of ionic liquids. *Journal of Electroanalytical Chemistry*, 819:347–358, 2018.

[157] Yining Han, Shanghui Huang, and Tianying Yan. A mean-field theory on the differential capacitance of asymmetric ionic liquid electrolytes. *Journal of Physics Condensed Matter*, 26(28), 2014.

[158] Maxim V. Fedorov and Alexei A. Kornyshev. Ionic liquids at electrified interfaces. *Chemical Reviews*, 114(5):2978–3036, 2014.

[159] Marcel Drüschler, Natalia Borisenko, Jens Wallauer, Christian Winter, Benedikt Huber, Frank Endres, and Bernhard Roling. New insights into the interface between a single-crystalline metal electrode and an extremely pure ionic liquid: Slow interfacial processes

and the influence of temperature on interfacial dynamics. *Physical Chemistry Chemical Physics*, 14(15):5090–5099, 2012.

[160] Jenel Vatamanu, Oleg Borodin, and Grant D. Smith. Molecular simulations of the electric double layer structure, differential capacitance, and charging kinetics for N-methyl-N-propylpyrrolidinium bis(fluorosulfonyl)imide at graphite electrodes. *Journal of Physical Chemistry B*, 115(12):3073–3084, 2011.

[161] Jing Zhu and Xianwen Mao. Elucidating ionic liquids-mediated electrochemical interfaces for energy storage and electrocatalysis. *Materials Today Energy*, 51(May):101908, 2025.

[162] Vera Lockett, Mike Horne, Rossen Sedev, Theo Rodopoulos, and John Ralston. Differential capacitance of the double layer at the electrode/ionic liquids interface. *Physical Chemistry Chemical Physics*, 12(39):12499–12512, 2010.

[163] M. S. Loth, Brian Skinner, and B. I. Shklovskii. Anomalously large capacitance of an ionic liquid described by the restricted primitive model. *Physical Review E - Statistical, Nonlinear, and Soft Matter Physics*, 82(5):1–7, 2010.

[164] Allen J. Bard and Larry R. Faulkner. *Electrochemical methods, fundamentals and applications*. John Wiley, & Sons, Inc., 2001.

[165] Koichi Aoki. Theory of ultramicroelectrodes, 1993.

[166] Trevor J Davies and Richard G Compton. The cyclic and linear sweep voltammetry of regular and random arrays of microdisc electrodes: Theory. *Journal of Electroanalytical Chemistry*, 585(1):63–82, 2005.

[167] Trevor J Davies, Sarah Ward-Jones, Craig E Banks, Javier Del Campo, Roser Mas, Francesc Xavier Muñoz, and Richard G Compton. The cyclic and linear sweep voltammetry of regular arrays of microdisc electrodes: Fitting of experimental data. *Journal of Electroanalytical Chemistry*, 585(1):51–62, 2005.

[168] C. Amatore, J. M. Savéant, and D. Tessier. Charge transfer at partially blocked surfaces. A model for the case of microscopic active and inactive sites. *Journal of Electroanalytical Chemistry*, 147(1-2):39–51, 1983.

[169] Robert J Forster. Microelectrodes: New dimensions in electrochemistry, 1994.

[170] Peter J. Mahon and Keith B. Oldham. Diffusion-controlled chronoamperometry at a disk electrode. *Analytical Chemistry*, 77(18):6100–6101, sep 2005.

[171] Kamonwad Ngamchuea, Shaltiel Eloul, Kristina Tschulik, and Richard G Compton. Planar diffusion to macro disc electrodes—what electrode size is required for the Cottrell and Randles-Sevcik equations to apply quantitatively? *Journal of Solid State Electrochemistry*, 18(12):3251–3257, 2014.

[172] David Shoup and Attila Szabo. Chronoamperometry at an ensemble of microdisk electrodes. *Journal of Electroanalytical Chemistry*, 160(1-2):19–26, 1984.

[173] Alexander S. Barnes, Emma I. Rogers, Ian Streeter, Leigh Aldous, Christopher Hardacre, and Richard G. Compton. Extraction of electrode kinetic parameters from microdisc voltammetric data measured under transport conditions intermediate between steady-state

convergent and transient linear diffusion as typically applies to room temperature ionic liquids. *Journal of Physical Chemistry B*, 112(25):7560–7565, 2008.

[174] Phillipp Wachter, Christian Schreiner, Markus Zistler, Dirk Gerhard, Peter Wasserscheid, and Heiner J. Gores. A microelectrode study of triiodide diffusion coefficients in mixtures of room temperature ionic liquids, useful for dye-sensitised solar cells. *Microchimica Acta*, 160(1-2):125–133, 2008.

[175] Abdolmajid Moghtada and Rouholah Ashiri. Nanocrystals of XTiO3 (X = Ba, Sr, Ni, BaxTi1-x) materials obtained through a rapid one-step methodology at 50 °c. *Ultrasonics Sonochemistry*, 26:293–304, 2015.

[176] Charles M. Hansen. *Hansen solubility parameters: A user's handbook: Second edition*. CRC Press, 2007.

[177] Abdolmajid Moghtada and Rouholah Ashiri. Enhancing the formation of tetragonal phase in perovskite nanocrystals using an ultrasound assisted wet chemical method. *Ultrasonics Sonochemistry*, 33:141–149, 2016.

[178] Abdolmajid Moghtada, Ali Shahrouzianfar, and Rouholah Ashiri. Low-temperature ultrasound synthesis of nanocrystals CoTiO3without a calcination step: Effect of ultrasonic waves on formation of the crystal growth mechanism. *Advanced Powder Technology*, 28(4):1109–1117, 2017.

[179] A. Moghtada and R. Ashiri. Superiority of sonochemical processing method for the synthesis of barium titanate nanocrystals in contrast to the mechanochemical approach. *Ultrasonics Sonochemistry*, 41(September 2017):127–133, 2018.

[180] Sijia Liang. *Surface Acoustic Waves in Strain-Engineered Thin (K , Na) NbO 3 Films : From Basic Research to Application in Molecular Sensing Sijia Liang*. PhD thesis, Universität zu Köln, 2021.

[181] Tomasz M. Stawski, Sjoerd A. Veldhuis, Ole F. Göbel, Johan E. Ten Elshof, and Dave H.A. Blank. Effects of reaction medium on the phase synthesis and particle size evolution of BaTiO3. *Journal of the American Ceramic Society*, 93(10):3443–3448, 2010.

[182] F. Dumur. Recent advances on ferrocene-based photoinitiating systems Type I photo ini ti at o rs Type II pho t oiniti at o rs O xidatio n agent. *European Polymer Journal*, 147:110328, 2021.

[183] F. C. Schaefer and W. D. Zimmermann. Self-oxidation of Methylene Blue. *Nature*, 220(2):66–67, 1968.

[184] Reshu Sanan, Tejwant Singh Kang, and Rakesh Kumar Mahajan. Complexation, dimerisation and solubilisation of methylene blue in the presence of biamphiphilic ionic liquids: A detailed spectroscopic and electrochemical study. *Physical Chemistry Chemical Physics*, 16(12):5667–5677, mar 2014.

[185] Claudia Simona Stefan, Daniel Lemordant, Philippe Biensan, Clémence Siret, and Bénédicte Claude-Montigny. Thermal stability and crystallization of N-alkyl-N-alkylpyrrolidinium imides. *Journal of Thermal Analysis and Calorimetry*, 102(2):685–693, 2010.

[186] Alessandro Triolo, Andrea Mandanici, Olga Russina, Virginia Rodriguez-Mora, Maria Cutroni, Christopher Hardacre, Mark Nieuwenhuyzen, Hans Jurgen Bleif, Lukas Keller, and Miguel Angel Ramos. Thermodynamics, structure, and dynamics in room temperature ionic liquids: The case of 1-Butyl-3-methyl imidazolium hexafluorophosphate ([bmim][PF 6]). *Journal of Physical Chemistry B*, 110(42):21357–21364, 2006.

[187] Mérièm Anouti, Johan Jacquemin, and Patrice Porion. Transport properties investigation of aqueous protic ionic liquid solutions through conductivity, viscosity, and NMR self-diffusion measurements. *Journal of Physical Chemistry B*, 116(14):4228–4238, 2012.

[188] V. Ivaništšev, S. O'Connor, and M. V. Fedorov. Poly(a)morphic portrait of the electrical double layer in ionic liquids. *Electrochemistry Communications*, 48:61–64, 2014.

[189] Tatiana Budtova and Patrick Navard. Viscosity-temperature dependence and activation energy of cellulose solutions. *Nordic Pulp and Paper Research Journal*, 30(1):99–104, 2015.

Author's List of Patents

Stefanie Hamacher, Alexey Yakushenko, Saskia Roth, Andreas Offenhäusser. "Sensoranordnung, Verfahren zu seiner Herstellung sowie Verwendung der Sensoranordnung". DE 102019004120.8, field 13.06.2019.

Acknowledgments

Diese Arbeit hätte ohne die Unterstützung vieler toller Menschen niemals entstehen können! Deshalb geht mein Dank an alle, die mich in den Jahren meiner Promotion fachlich, inhaltlich, technisch und emotional unterstützt haben.
Zuerst geht mein Dank an Prof. Offenhäusser, der mir die Möglichkeit gab, weit außerhalb seines eigentlichen Forschungsgebiets meine Doktorarbeit anzufertigen. Darüber hinaus geht ein besonderer Dank an Dr. Alexey Yakushenko, der zunächst die Drittmittel für meine Promotion und dieses spannende Projekt akquiriert und meinen Fortschritt fachlich betreut hat. Danke Alexey, durch Dich habe ich viel fürs Leben gelernt!
Weiterhin gilt mein Dank auch Prof. Bernhard Wolfrum, der während meiner Promotionszeit an die TU München gewechselt ist und trotzdem regelmäßig für Diskussionen zur Verfügung stand. Außerdem habe ich es ihm zu verdanken, dass ich das Feld der funktionalen Tinten überhaupt kennenlernen durfte.
Ein weiterer besonderer Dank geht an Prof. Ulrich Simon für die Übernahme des Zweitgutachtens meiner Arbeit!

Des Weiteren danke ich meinem Mitstreiter, Christopher Beale, von ganzem Herzen für seine Unterstützung im Labor und darüber hinaus. Thanks a lot Chris, without you, my PhD time would have been much harder. We complemented each other in many ways and benefited from that. I wish you all the luck for your career and life and hope you will be happy!

Ein riesiges Dankeschön gehört auch meiner Auszubildenden Chemielaborantin Saskia Roth. Ich konnte mich immer auf Dich verlassen und Du warst eine riesige Unterstützung im Labor und hast nie aufgegeben, auch wenn es häufig nicht so lief wie wir das wollten. Vielen Dank und alles Gute für Deine Zukunft! Ich bin froh ein Teil davon zu sein!

Ein weiteres riesiges Dankeschön gebührt Dr. Stefan Achtsnicht, ohne ihn hätte ich die tausende von Daten niemals auswerten können. Danke für Deine unermüdliche Python-Programmierung und Unterstützung!

Ein weiterer großer Danke geht an Dr. Dirk Mayer für die Mitbetreuung meiner Arbeit und die Aufnahme in seine Arbeitsgruppe. Der Austausch in den Seminaren und die fachlichen Diskussionen haben meine Arbeit zum Großteil mit geformt.
Außerdem gebührt ein großes Dankeschön Prof. Roger Wördenweber und seinem Team (insb. Nico Wolf), die mich bei der Vermessung einiger BSTO-Proben unterstützt haben, ohne die ich nicht all die Erkenntnisse über meine hergestellten Nanokristalle hätte erlangen können.

Neben all der fachlichen Unterstützung braucht jede Promotion auch Menschen, die sich um das Drumherum kümmern. Dazu gehört Susanne Bippus, von der ich auf dem kleinen Dienstweg stets das bekommen habe, was ich gerade brauchte. Danke!
Ein weiterer toller Mensch, den ich durch meine Zeit am IBI-3 (damals noch ICS-8) kennenlernen durfte ist die gute Seele des Instituts Tina Breuer. Danke für zahlreiche Bestellungen und die Orga der Labore! Und vor allem danke für viele tolle Gespräche und Deine Klugheit!

Ein Riesendank geht auch an Elke Brauweiler-Reuters, die viele meiner BSTO-Versuche im REM vermessen hat und diesbezüglich alle Wünsche versucht hat zu erfüllen, die ich hatte. Liebe Elke, vielen Dank für Deine Unterstützung und alles Gute für Deine Zukunft!
In diesem Zusammenhang geht natürlich auch ein großes Dankeschön an Dr. Elmar Neumann, der immer mit Rat und Tat zur Seite stand, wenn die Dinge mit dem REM oder EDX nicht so klappten wie gehofft.
Ein weiterer Dank geht an Michael Prömpers, der im Reinraum die notwendigen MEAs für meine Messungen hergestellt hat und auch sonst für alle Fragen immer ansprechbar war.
Genauso dankbar bin ich Marko Banzet für seine Unterstützung, wenn es um den Tausch von Gasflaschen für den Plasmaofen ging.
Many thanks to all the colleagues I met during my time at the institute: Nouran, Sabrina, Silke, Lena, Kagithiri, Frano, Pengcheng, Johannes, Changtong, Gabriela, Timm, Bohdan, Pegah, Corinna, Erfan, Stella, Irina. I head a great time because of you!

Ein besonderer Danke geht auch viele FZJ-Kollegen, ohne die diese Arbeit nicht entstanden wäre. Dazu gehört die mechanische Werkstatt unter der Leitung von Jens Prigge. Vielen Dank Jens, Alex und Team, dass ich mir stets Werkzeug ausleihen und mit Sonderwünschen zu euch kommen konnte. Ihr habt meine Zeit sehr bereichert!
Vielen Dank liebe IT und Elektronikwerkstatt für den Support bei PC-Problemen, Softwarewünschen und dem individuellen Herstellen von Elektroniklösungen für meine Versuche. Ein besonderer Dank geht dabei an Sascha Thiele, Stefan Kirch, René Krebs und Nadine Neumann sowie an Norbert Wolters für die Entwicklung meines automatisierten Temperatur-Setups!
Ein großes Dankeschön geht auch an die Glasbläserei unter der Leitung von Andreas Schwaitzer, die sowohl einige tolle Einzelstücke für meine Forschung angefertigt haben, aber auch immer wieder meine Glaskolben von verkanteten Glasstopfen befreit haben.

Ein weiterer, sehr besonderer Dank geht an meine zahlreichen PhD-Kollegen im ganzen FZJ, mit denen ich gemeinsam im DocTeam arbeiten durfte. Thanks a lot for the great time, many fun events, such as the soccer tournament, and the devlopment of *JuDocs*. To discuss the many PhD issues that occur during such an intense phase helped me a lot to overcome some crises and down points during my PhD time.
Ich bin extrem dankbar, dass ich durch meine Arbeit im DocTeam die Möglichkeit hatte, *JuDocs* mit aufzubauen und hautnah miterleben konnte wie sich verschiedene Arbeitsgruppen zu einem Gesamtkonzept entwickelt haben. Dadurch habe ich auch meine ersten Erfahrungen in Punkte Gremienarbeit und übergreifende Zusammenarbeit sammeln können, für die ich bis heute sehr dankbar bin. Ein herzliches Dankeschön geht deshalb an Dr. Sabine Hanrath, Bettina Meenen, Natascha Haase, Dr. Sascha Pust, Prof. Markus Diesmann und Prof. Ingar Janzik. Vielen Dank für die vielen Einblicke und auch dafür, dass es *JuDocs* heute für alle Doktoranden gibt!

Die Arbeit an *JuDocs* hat mich exzellent auf meinen neuen Job bei PtJ vorbereitet. An dieser Stelle möchte ich auch einen großen Dank an meine Kolleginnen und Kollegen bei ESE loswerden. Wir sind zusammen ein großartiges Team und es macht mir große Freude jeden Tag mit euch zusammenzuarbeiten. Danke Martin für einige intensive Diskussionen bzgl. meiner Dissertation und die Programmierung in Python!

Nicht zuletzt möchte ich mich auch bei meinen Freunden und meiner Familie für ihre Unterstützung bedanken! Ohne euch alle wäre diese Arbeit niemals entstanden. Ein ganz besonderer Dank geht an meinen größten Kritiker und Unterstützer, Uli, sowie unsere Felldinos, die immer da sind, wenn ich sie brauche!

Ein weiterer Dank geht an die EFRE-Förderung der EU und des Landes NRW im Rahmen

“Europäischer Fonds für regionale Entwicklung,” für die Finanzierung des Projekts “EFRE-0800361 Packsense und damit meiner Forschung.

Band / Volume 288
Prediction of Magnetic Materials for Energy and Information Combining Data-Analytics and First-Principles Theory
R. Hilgers (2024), xv, 215 pp
ISBN: 978-3-95806-795-0

Band / Volume 289
Biodegradation and microbial upcycling of plastics
J. de Witt (2025), XVI, 259 pp
ISBN: 978-3-95806-804-9

Band / Volume 290
Practical Methods for Efficient Analytical Control in Superconducting Qubits
B. Li (2025), 202 pp
ISBN: 978-3-95806-807-0

Band / Volume 291
Ab initio investigation of topological magnetism in two-dimensional van der Waals heterostructures
N. Abuawwad (2025), xviii, 135 pp
ISBN: 978-3-95806-808-7

Band / Volume 292
Tolerance engineering of Pseudomonas for the efficient conversion and production of aldehydes
T. Lechtenberg (2025), XVI, 185 pp
ISBN: 978-3-95806-817-9

Band / Volume 293
Exploring the process window for production of itaconic, 2-hydroxyparaconic, and itatartaric acid with engineered *Ustilago* strains
P. Ernst (2025), x, 145 pp
ISBN: 978-3-95806-825-4

Band / Volume 294
Surface Plasmon Resonance Microscopy for the Characterization of Cell-Substrate Distances
J. Bednar (2025), xxiii, 187 pp
ISBN: 978-3-95806-830-8

Band / Volume 295
Microfluidic-MEA hybrid systems for electrophysiological recordings of neuronal co-cultures
J. Stevanović (2025), ix, 186 pp
ISBN: 978-3-95806-831-5

Band / Volume 296
Structural and Magnetic Properties of Biocompatible Iron Oxide Nanoparticles for Medical Applications
A. Nasser (2025), xii, 140 pp
ISBN: 978-3-95806-837-7

Band / Volume 297
Metabolic engineering of *Pseudomonas taiwanensis* for the improved production of styrene
J. Rönitz (2025), XII, 147 pp
ISBN: 978-3-95806-841-4

Band / Volume 298
Elucidation of anti-viral strategies in *Streptomyces*
B. U. Rackow (2025), xii, 148 pp
ISBN: 978-3-95806-842-1

Band / Volume 299
Ab initio investigations of spin-orbit functionalized graphene
D. Mazhjoo (2025), 163 pp
ISBN: 978-3-95806-847-6

Band / Volume 300
3D neural implants for* in vivo *applications
M. Jung (2025), xvi, 215 pp
ISBN: 978-3-95806-852-0

Band / Volume 301
Phonons in Magnetic Systems by means of Density- Functional Perturbation Theory
A. Neukirchen (2025), xviii, 195 pp
ISBN: 978-3-95806-853-7

Band / Volume 302
Optimal control and machine learning of quantum device dynamics
F. Preti (2025), iv, 211 pp
ISBN: 978-3-95806-856-8

Band / Volume 303
Development of a New, Miniaturized and Flexible Temperature Sensor
S. Hamacher (2025), XXII, 153 pp
ISBN: 978-3-95806-863-6

Weitere ***Schriften des Verlags im Forschungszentrum Jülich*** unter
http://wwwzb1.fz-juelich.de/verlagextern1/index.asp

Schlüsseltechnologien / Key Technologies
Band / Volume 303
ISBN 978-3-95806-863-6

Mitglied der Helmholtz-Gemeinschaft

JÜLICH
Forschungszentrum